Computational Nonlinear Vibration Analysis for Distributed Geometrical Nonlinearities in Structural Dynamics

Shuqing Lian

Department of Mechanical Engineering
Imperial College London

Submitted in part fulfilment of the requirements for the degree of
Doctor of Philosophy of Imperial College London
and the Diploma of Imperial College London

March 2022

To My Dear Parents and Loved Ones

Declaration

I hereby declare that except where specific reference is made to the work of others, the contents of this dissertation are original and have not been submitted in whole or in part for consideration for any other degree or qualification in this, or any other university. This dissertation is my own work which has been done after registration for the degree of Doctor of Philosophy at Imperial College London.

The copyright of this thesis rests with the author. Unless otherwise indicated, its contents are licensed under a Creative Commons Attribution-Non Commercial 4.0 International Licence (CC BY-NC).

Under this licence, you may copy and redistribute the material in any medium or format. You may also create and distribute modified versions of the work. This is on the condition that: you credit the author and do not use it, or any derivative works, for a commercial purpose.

When reusing or sharing this work, ensure you make the licence terms clear to others by naming the licence and linking to the licence text. Where a work has been adapted, you should indicate that the work has been changed and describe those changes.

Please seek permission from the copyright holder for uses of this work that are not included in this licence or permitted under UK Copyright Law.

Shuqing Lian
March 2022

Acknowledgements

First of all, I would like to express my deepest gratitude to my supervisor Dr Loïc Salles, for introducing me to the nonlinear vibration world. Without his guidance and constant support throughout my PhD years, this dissertation would have been unachievable.

I would also like to address my appreciations to my colleagues Fadi El Haddad and Alessandra Vizzaccaro for all the meetings and technical support.

I am also very grateful to the Engineering and Physical Sciences Research Council and Rolls-Royce plc for funding this work under the Industrial CASE Award scheme (Award No. 2155162).

I am thankful to my fellows from the Vibration University Technology Centre. The numerous discussions and all the cherished moments together are valuable.

This thesis is dedicated to my parents. For everything.

Abstract

The demand to reduce the impact of aviation on the environment is leading jet engine manufacturers to increase the fuel and propulsion efficiency of the engines. This in turn is pushing materials to their physical limits by undergoing increasingly higher thermo-mechanical loads. In this regime, blades and other engine components are subjected to large deformations generating nonlinearities that activate new failure mechanisms not dealt with before. Therefore, vibration analysis is essential to develop new methodologies for the accurate prediction of components' behaviour. This research focuses on investigating the effect of the distributed geometric nonlinearities and rotational speed on the dynamic behaviour of three-dimensional structures. The Green-Lagrange strain measures are employed in this research to express the nonlinear relationship between the displacement and the strain. The nonlinear algorithms used for the numerical simulations are developed based on the Finite Element Method combined with the Harmonic Balance method. The complex geometries are discretised by using the geometric exact three-dimensional solid elements. The forced response functions and the backbone curves for the steady-state response of the nonlinear system can be computed. The research aims to develop and validate methodologies for the identification and control of undesired vibration modes which will inform new design choices. Finite element modelling of the blades generally involves an immense number of degree-of-freedoms, which could be infeasible to compute. The reduced order modelling (ROM) techniques are crucial for achieving an accurate prediction of the nonlinear behaviour in an efficient way. Detailed computation strategies for the intrusive ROM methods are delivered. ROM techniques based on the linear and nonlinear mapping between the full model and the reduced basis are presented. The capabilities and limitations of both methods are assessed. The projection method based on the linear eigenmodes only has a slow converge to the full system. On the other hand, the quadratic manifold method with the static modal derivatives involved in the reduced coordinates provides a fast convergence.

Keywords: nonlinear vibration analysis, distributed geometric nonlinearities, rotational speed, Harmonic Balance Method, Nonlinear Normal Mode, Reduced Order Modelling.

Table of contents

List of figures **xv**

List of tables **xix**

1 Introduction **1**
1.1 Overview 1
1.2 Motivation and objectives 4
1.3 Outline of the thesis 6

2 State of Knowledge **9**
2.1 Nonlinear vibration of rotating system 9
2.2 Formulation of the problem 12
2.2.1 Formulation of the equations of motion 13
2.2.2 Finite strain theory 15
2.2.3 Finite element method 24
2.2.4 Damping 35
2.3 Numerical methods for nonlinear dynamics 36
2.3.1 Continuous-time systems 37
2.3.2 Dynamic analysis method 37
2.3.3 Continuation 43
2.4 Stability 46
2.4.1 Floquet theory 47
2.4.2 Poincaré map 48
2.4.3 Comparison of stability computational methods 49
2.4.4 Stability computation methods 50
2.4.5 Bifurcations 53
2.5 Nonlinear normal mode 56
2.6 Reduced order modelling 59

3 Finite Element Analysis of 3D Structures with Geometric Nonlinearity 63
3.1 Governing equation in the time domain for 3D Structure 64
3.1.1 Potential energy expression 65
3.1.2 Kinetic energy expression 72
3.1.3 Equation of motion for 3D structures with geometric nonlinearity . 72
3.1.4 Compressed Sparse Row 73
3.2 Effect of geometric nonlinearity on static deformation 74
3.3 Linear modal analysis 77
3.3.1 Eigenvalue problem of the finite element model 77
3.3.2 Analytical value 79
3.3.3 Convergence study 80
3.4 Dynamic analysis in frequency domain 82
3.4.1 Non-dimensionalization and scaling of the dynamics systems 83
3.4.2 Harmonic Balance Method with Alternating Fourier Transformation for forced vibration analysis 84
3.4.3 Computation method for NNMs using HBM 88
3.4.4 Numerical results 90
3.5 Concluding remarks 103

4 Application of Proposed Methods 105
4.1 Finite element analysis of Rotating Structures 106
4.1.1 Governing equation in the time domain 106
4.1.2 Kinetic energy expression 106
4.1.3 Equation of Motion for the Rotating 3D Structures 108
4.1.4 Linear modal analysis 109
4.1.5 Free and forced vibration analysis of the 3D rotating structure . . . 111
4.2 Structure with base excitation 114
4.2.1 Equation of motion in time domain 114
4.2.2 Simulation results for the experiment setup 115
4.3 Concluding remarks 119

5 Reduced order modelling based on intrusive method 121
5.1 Governing equations for a geometric nonlinear system 122
5.2 ROM using linear modes 123
5.2.1 Reduced equation of motion for 3D nonlinear structures 123
5.2.2 Harmonic balance method for vibration analysis 125
5.3 ROM with static modal derivatives and quadratic manifold 127

5.3.1 Static modal derivatives 128
5.3.2 Reduced equation of motion for 3D nonlinear structures 131
5.3.3 Harmonic balance method for vibration analysis 134
5.4 Numerical results 136
5.4.1 3D non-rotating clamped-clamped beam 137
5.4.2 Rotating 3D cantilevered beam 144
5.5 Concluding remarks 147

6 Conclusions and Future Works 149
6.1 Conclusions for research work 149
6.1.1 Conclusions on nonlinear modal analysis 149
6.1.2 Conclusions on the effect of rotation 151
6.1.3 Conclusions on the reduced order modelling techniques 152
6.2 Scientific contributions 153
6.3 Future works 153

References 155

Appendix A 3D Solid Elements in the Reference Coordinates 169
A.1 Shape functions of the 3D solid elements 169
A.1.1 4-node Tetrahedron Element 169
A.1.2 10-node Tetrahedron Element 170
A.1.3 8-node Hexahedron Element 170
A.1.4 20-node Hexahedron Element 171
A.2 Local derivative of the shape functions for the 3D solid elements 172
A.2.1 4-node Tetrahedron Element 172
A.2.2 10-node Tetrahedron Element 172
A.2.3 8-node Hexahedron Element 173
A.2.4 20-node Hexahedron Element 173

Appendix B Gaussian Quadrature for 3D Elements 175
B.1 3D tetrahedron element 175
B.2 3D hexahedron element 176

Appendix C Newton Direction Computation for Harmonic Balance Method 177

Appendix D Jacobian Matrix for the Reduced Equation of Motion in SMD 179

List of figures

1.1 *Example of a Campbell diagram to predict resonant crossings between the natural frequencies (red) and an engine order (black) around the operational range (green). Orange marker: resonance. Blue marker: flutter.* 3

2.1 *Configuration of a rotor blade and the co-ordinate system* 10
2.2 *Configurations used in geometrically nonlinear analysis in continuum mechanics: base configuration $\mathscr{B}$, reference configuration $\mathscr{R}_{ref}$ and current configuration $\mathscr{R}$* 16
2.3 *Schematic of Euler-Bernoulli Beam* 25
2.4 *Schematic of Timoshenko Beam* 28
2.5 *3D solid element types: (a) 4-node tetrahedron element, (b) 10-node tetrahedron element, (c) 8-node hexahedron element, (d) 20-node hexahedron element* 29
2.6 *Shape function and geometry of a single Euler-Bernoulli beam element* . . 32
2.7 *Poincaré section of periodic orbits* 42
2.8 *The prediction and correction step in the continuation scheme* 43
2.9 *Scenarios depicting how the Floquet multipliers leave the unit circle and the corresponding bifurcation types.* 53
2.10 (a) *Supercritical symmetry-breaking bifurcation*, (b) *Subcritical symmetry-breaking bifurcation [96].* 53
2.11 *Scenario in the vicinity of a cyclic-fold bifurcation point [96].* 54
2.12 *Two possible local scenarios at transcritical bifurcation point [96].* 55
2.13 (a) *Supercritical period-doubling bifurcation*, (b) *Subcritical period-doubling bifurcation [143].* 55
2.14 (a) *Schematic representation of the 2-DOF system example*, (b) *Two-dimensional invariant manifolds of system with the corresponding linear mode [67].* . . 58
2.15 *The classification of the reduction methods [130].* 60

3.1 *Transformation between physical and reference element.* 64
3.2 *Deformation of a 8-node hexahedron element with reduced integration subjected to bending moment.* 70
3.3 *Sparsity level of the linear stiffness matrix of the the 3D mesh.* 73
3.4 *Deformation of 3D cantilevered beam under static point load.* 75
3.5 *Force-displacement relationship in linear and nonlinear model.* 76
3.6 *Schematic of the cantilevered beam and the first three out-of-plane bending modes.* 76
3.7 *Cantilevered beam meshed with (a) Tetrahedron elements; (b) Hexahedron elements.* 78
3.8 *Hourglassing effect on the reduced-integration 8-node hexahedron element.* 79
3.9 *Cantilevered beams used for modal analysis.* 80
3.10 *Convergence of the finite element model with theoretical values.* 81
3.11 *Flowchart for the dynamic analysis of the structure.* 91
3.12 *The schematic model of the clamped-clamped beam.* 91
3.13 *Maximum displacement of the clamped-clamped beam: (–) numerical, (∘) Ribeiro's results, and (■) experimental data [165].* 92
3.14 *The schematic model the cantilevered beam.* 93
3.15 *First bending mode frequency response for various forcing amplitudes:* (x) *FE model with 3D solid elements, (∘) FE model with beam elements, (−−) VK model, (—) Inxt. model.* 93
3.16 *Second bending mode frequency response for various forcing amplitudes:* (x) *FE model with 3D solid elements, (∘) FE model with beam elements, (−−) VK model, (—) Inxt. model.* 94
3.17 *FEM mesh with HEX20 elements for numerical analysis.* 94
3.18 *FRF of the 3D cantilevered beam under periodic point load (1^{st} bending mode).* 96
3.19 *3D cantilevered beam under periodic point load around the 2^{nd} bending mode.* 97
3.20 *Backbone curves for the second bending mode with different number of harmonics used in HBM.* 97
3.21 *Computational time for points on the FRF plot.* 98
3.22 *Computational time with different time steps per period.* 98
3.23 *3D clamped-clamped beam model used for numerical analysis.* 99
3.24 *First 6 modes of the 3D clamped-clamped beam.* 100
3.25 *FRF of the 3D clamped-clamped beam under periodic point load in y direction.* 101
3.26 *Fourier coefficient for u_y at the load point.* 101
3.27 *Computational time with different harmonics in HBM ($N_t = 32$).* 102

3.28 *FRF of the clamped-clamped beam under periodic point load in both x and y direction.* 103

4.1 Rotating structure within the co-rotating reference system. 107
4.2 *Rotating cantilevered beam with centre of rotation 10 cm apart from the clamped end.* 110
4.3 *Effect of rotational speed on the linear vibration modes.* 111
4.4 *Backbone curves and FRF plots of the first bending mode for various rotational speed.* 112
4.5 *Backbone curves and FRF plots of the second bending mode for various rotational speed.* 113
4.6 *3D cantilevered beam under periodic base excitation.* 114
4.7 *Dynamic response of the cantilevered beam under base excitation.* 116
4.8 *Dynamic response of the cantilevered beam from the numerical simulation with* $Y = 7.25$ *mm.* 117
4.9 *Dynamic response of the cantilevered beam with* $Y = 7.25$ *mm and* $\omega = 0.965\omega_n$ *(zoomed): (a) absolute response, (b) relative response.* 117
4.10 *Upward frequency sweep of the cantilevered beam at different base excitation magnitudes.* 118
4.11 *Dynamic response of the cantilevered beam with extreme amplitude in one period of oscillation.* 118

5.1 *Time to compute the coefficient tensors with different number of reduced basis selected.* 127
5.2 *Time to compute* $\boldsymbol{\Theta}_{ij}$ *with different number of reduced basis selected in linear projection method.* 129
5.3 *Linear modes* $\boldsymbol{\phi}$ *of the cantilevered beam and the corresponding modal derivatives* $\boldsymbol{\Theta}$. 130
5.4 *Effect of rotational speed on the modal derivative* $\boldsymbol{\Theta}_{23}$ 130
5.5 *Time to compute the coefficient tensors with different number of reduced basis selected in SMD-QM.* 136
5.6 *The clamped-clamped beam under investigation in [131].* 137
5.7 *Convergence of the nonlinear ROM methods. Blue: ICE, orange: SMD-QM, red: MD, green: DNF, black: full FEM model.* 138

5.8 *FRFs of the clamped-clamped beam with $F = 1500$ N. Full FEM model (black) compared to ROMs obtained with the ICE method (purple), the DNF method (red), the MD method (blue), and the SMD-QM (light green). PF: pitchfork bifurcation point. NS: Neimark–Sacker bifurcation.* 139
5.9 *Zoomed views of Figure 5.8. Full FEM model (black), ICE (purple), DNF (red), MD (blue), and SMD-QM (light green).* 139
5.10 *Convergence of the SMD-QM and the linear approach with the full FE model.* 140
5.11 *Response of the reduced basis $\hat{\boldsymbol{q}}$ in odd harmonics ($r = 3$).* 141
5.12 *Computation time taken for the dynamic analysis.* 142
5.13 *Comparison of the results from the SMD-QM approach and the full FEM with $F_x = F_y = 500 \cdot \cos(\omega t)$.* 142
5.14 *Fourier coefficients in $\tilde{\boldsymbol{q}}$ with $r = 1$.* 143
5.15 *Fourier coefficients in $\tilde{\boldsymbol{q}}$ with $r = 2$.* 143
5.16 *FRF of the first bending mode from the SMD-QM model and the full FEM for a rotating cantilevered beam.* 144
5.17 *Dynamic shape of the cantilevered beam.* 145
5.18 *Fourier coefficients in $\tilde{\boldsymbol{q}}$ with $r = 3$.* 145
5.19 *3D cantilevered beam: FRF of the first bending mode from the ROM based on linear subspaces ($r = 20$).* 146
5.20 *FRF of the second bending mode from the SMD-QM model and the full FEM for a rotating cantilevered beam ($\Omega_x = 1400$ RPM).* 147

A.1 *Reference 4-node tetrahedron element.* 169
A.2 *Reference 10-node tetrahedron element.* 170
A.3 *Reference 8-node hexahedron element.* 170
A.4 *Reference 8-node hexahedron element.* 171

List of tables

2.1 *Finite strain measures used in geometrically nonlinear analysis* [14] 19
2.2 *Conjugate stress measures for the selected finite strain measures* [14] . . . 21
2.3 *Beam boundary conditions* 27

3.1 *Gaussian points required for stiffness matrix.* 70
3.2 *Gaussian points required for mass matrix.* 72
3.3 *Natural frequencies (Hz) of the first three out-of-plane bending modes for cantilevered beam.* 78
3.4 *Computational time for the pre-processing steps* 95

B.1 *Gaussian quadrature points and the weights for 3D tetrahedron element.* . . 175
B.2 *Gaussian quadrature points and the weights for 3D hexahedron element.* . . 176

Chapter 1

Introduction

1.1 Overview

In the last couple of decades, the global awareness of climate change and the economic impact of high fuel consumption and low propulsion efficiency in the aviation industry have led to major changes in manufacturing practices in the design stages [102]. Aero engines to attain high fuel efficiency requires sustained operations at an increasingly higher temperature using lightweight materials [51]. This poses a structural integrity challenge from a vibration analysis standpoint whereby components become ever more sensitive to fatigue failure and structural instabilities. From a cost perspective, the ability to simulate dynamic vibration behaviours at the design stage can reduce the cost of expensive prototyping and testing, as well as enable simulations of high rotational speeds, dynamic loads, and rotor-dynamic effect [74] which would be difficult or impractical to test otherwise. Therefore, the ability to model accurately the dynamic behaviours becomes imperative in the vibration analysis of safety-critical components.

Vibration analysis involves identifying the natural frequencies and modes of a system to predict various performance attributes, i.e. stability and forced response changes of the system. Numerical simulations of structural behaviour play an important role in dynamic analysis nowadays. The mathematical models used in the numerical simulations can be divided into two categories: linear and nonlinear. For a linear system, the modal superposition theorem applies, which makes the study of linear systems much simpler. The main characteristics of the modal response are its mode shapes, natural frequencies, and modal damping [37, 41]. While it is much easier to analyse such a system, a linear system finds limited applications in the real world. The classical linear dynamic analysis can generally only capture an approximation of the real system, hence nonlinear dynamic analysis becomes

of greater significance to increase the accuracy of the predicted performance of a system. Nonlinear systems are those for which the principle of superposition does not hold due to the coupling of modes, internal resonance, and shifting of natural frequencies. The main sources of nonlinearities derive from inertial forces, material, and geometrical nonlinearities. Inertial forces such as friction nonlinearity are due to the nonlinear function of the displacement and velocity, e.g. Coulomb friction or hysteric damping. This has a significant effect on the dynamic behaviour of a system as it can lead to structural changes from the intended design. Hence the shifts in the natural frequencies might arise leading to a significant reduction in the HCF (High Cycle Fatigue) component lifetime [178]. Material nonlinearity is associated with the material's nonlinear strain-stress relationship. In the case of a superalloy, commonly used for components under a high sustained thermo-mechanical load, this refers to the plastic behaviour associated with large strain deformations [177]. More recently, engine manufacturers have been opting for composite materials as substitutes for traditional Titanium and other alloys for fan blades. In this case, the viscoelastic behaviour of polymer matrices is also the cause of the nonlinear dynamics of a system [173]. Geometrical nonlinearities, in particular, arise due to large displacements and solid rotations and thus the nonlinear strain-displacement relations [17]. This is generally the case when large-amplitude vibrations generate large displacements such that the geometrical curvature of the blade does not deform linearly with displacement. Large deformation can be observed especially on the lightweight blades. Beyond these major sources of nonlinearities in the system, others can occur from structural changes due to material damages such as crack nucleation and propagation [118].

The excitation force of the blades is mainly caused by the aerodynamic flow, which has a frequency proportional to the rotational speed with an integer factor. The interface contact between the blade tip and the casing is another source of excitation. The integer multiples of the rotational speed are also known as the engine order. The resonances of the blades can be identified from the Campbell diagram, Figure 1.1. For a blade operating at a rotational speed with an engine order that coincides with its natural frequency, resonance would occur. This type of resonance needs to be avoided to prevent damage. Linear modal analysis is used to compute the natural frequencies of the blades. Fluttering is a common phenomenon caused by the unstable interaction between the aerodynamic flow and structural dynamics. The self-excited vibration of the blades can cause blades loss or HCF. Turbomachinery flutter is often found at frequencies very close to a blade mode frequency because the structural forces dominate. The risk of fluttering can be evaluated by computing the unsteady flow due to the blade mode shape. The logarithmic decrement of the blade motion for each aeroelastic

mode is then used as a risk indicator.

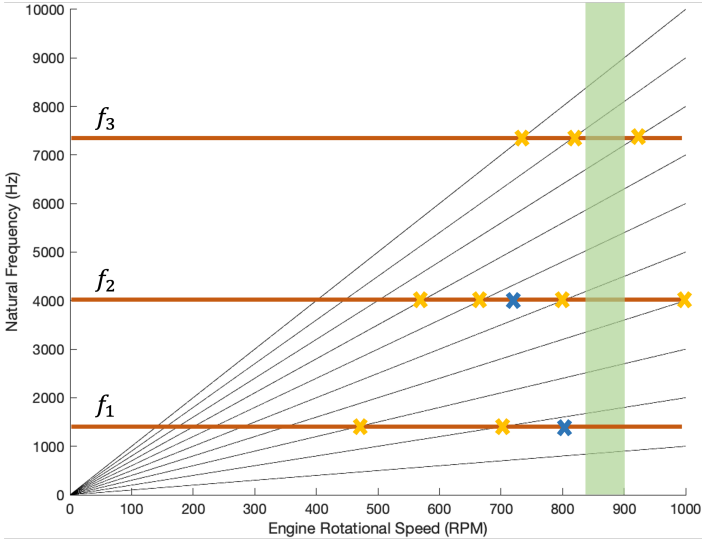


Fig. 1.1 *Example of a Campbell diagram to predict resonant crossings between the natural frequencies (red) and an engine order (black) around the operational range (green). Orange marker: resonance. Blue marker: flutter.*

In the design-analysis cycle of complex structural systems such as rotorcraft, aircraft, and ground vehicles, it is necessary to thoroughly understand their vibratory response. If the vibration of interest is restricted to small neighbourhoods of the static equilibrium positions, then the assumption of a linear system can generally be made. The corresponding analysis procedure is then greatly simplified, through the use of modern tools such as Finite Element Analysis and Linear Modal Analysis. In contrast, when the amplitudes of oscillation are large, beyond the scale of linearisation, or when a system behaves inherently nonlinearly with respect to its equilibrium configuration, then nonlinear equations of motion must be used for the model. The nonlinear dynamic analysis involves simulations of the structure behaviour to enable engineers to predict various performance attributes, avoiding the use of expensive physical prototypes and thus reducing the time of the design process. The continuum behaviour of the structure described at an infinite number of points is approximated in terms of a finite number of points by applying the Finite Element Methods (FEM). In the linear modal analysis, the invariant mode shapes and natural frequencies of a structure can be used to reduce the behaviour of the structure to the mode(s) of interest responding to a given excitation. This approach can be extended to the nonlinear regime in the nonlinear modal analysis. Once the amplitude-dependent mode shapes and natural frequencies are defined, the nonlinear behaviour of the structure subjected to periodic excitation can be approximated.

The nonlinear modes are computed by applying a continuation algorithm on the conservative system to find the periodic orbits. Multi-harmonic balance method [111] has been widely used as a tool for frequency analysis of the structural dynamics for the steady-state nonlinear dynamic solution, such as whole engine wind-milling and forced response of aero-mechanics structures. Other commonly used analysis tools for computing the periodic solutions are Shooting Method [91], Orthogonal Collocation Method [16], Time Finite Element Method [59], Poincaré Map Method [90], etc. Unlike the linear system, there exist multiple solutions in a nonlinear system. While some are stable and others are unstable, which indicates that a significant change in a system response could occur should the unstable solution be used. The Lyapunov and Poincare stability definitions [13] in the context of local stability for a steady-state periodic solution are widely used.

Real system presents multiple degrees of freedom (DOF) often coupled together leading to modal interactions and energy exchange between modes, in addition to nonlinear problems such as natural frequency shifts, sub-harmonics, limit cycles, and more. The computational resources that would need to be employed to solve such complex systems would be impractical. Model order reduction methods can reduce the number of unknowns in a large model, in order to facilitate faster solutions. This becomes essential when dealing with large-scale and complex engineering structures, which would otherwise be computationally infeasible. Commonly implemented ROM (Reduced Order Modeling) techniques are: the Hurty/Craig-Bampton method for contact nonlinearities [76], the projection-based methods [50, 61, 163], the invariant manifold based methods [129, 156], and so on.

1.2 Motivation and objectives

The time evolution of the dynamic response of the structure consists of two parts: the transient response and the steady-state response. The transient response is the temporary response of a system to a change from an equilibrium state. The steady state is reached when the system is settled. The dynamic features at the steady state are of the most interest in the early design stage. The natural frequencies and the corresponding modes of vibration can help to make the design away from the danger zone. In this research, the simplification of the structure with three-dimensional (3D) solid elements is applied. The 3D finite element model is sufficient to obtain a realistic representation of the nonlinear dynamic behaviour of a system. For instance engine blades, aircraft wings, bridges, and robotic arms all make use of this assumption in order to obtain solutions at a much faster rate. Unlike the 1D and

2D elements, 3D solid elements do not rely on limiting assumptions on the amplitude of vibration. The exact representation of geometric nonlinearities can hence be achieved. In comparison to the linear approximation, the nonlinear modal analysis of the 3D finite element model can provide more useful information such as modal interaction, bifurcation, stability, etc. The main objective of this thesis is to extend the nonlinear modal analysis techniques to an industrial framework. With the implementation of the ROM techniques, the nonlinear analysis techniques can be applied to large-scale systems. The solution of the steady-state response can then be sought within a much shorter computational time. The ROM techniques can not only preserve the nonlinear dynamic information of the full Finite Element (FE) system but also isolate the dynamic features of a particular mode or modal interactions from all the rest.

In summary, the work presented in this thesis is focused on the following objectives:

- To develop an in-depth understanding of the current state of knowledge and the physical phenomenon involved in the blade vibrations of jet engines.
- To develop a suitable modelling methodology for the 3D systems applicable to the engine blades, including both the distributed geometric nonlinearities and the rotational effect.
- To compute the nonlinear responses of the rotating geometrically nonlinear structures via the Harmonic Balance Method (HBM) combined with the 3D finite element model.
- To carry out an exploratory investigation of potential methodologies to generate reduced order models.
- To implement the intrusive ROM methods into the numerical model and investigate the limitations and the capabilities of the techniques.

The scientific objectives listed above are aimed at developing suitable numerical models for the nonlinear analysis of dynamic systems. The effects of geometric nonlinearities and rotation on the 3D structures are both considered. The distributed nonlinearities within the systems lead to complex dynamic behaviours, such as internal resonance and energy localisation due to the evolution of non-similar modes or bifurcations [101]. The dynamic behaviour of the full FE model is expressed as a boundary value problem containing nonlinear differential equations. The steady-state response of the full FE model is computed by using the HBM combined with the Newton-Raphson solver. In an industrial context, the periodic solutions of the nonlinear system are usually sought through time-integration schemes. The

frequency-domain method employed in this work requires less CPU time while providing accurate results. It can be very beneficial when parametric studies are carried out or when more complicated models are used. While the finite differences method is widely used in commercial software to estimate the Jacobian terms in nonlinear systems, the methodology for the analytical derivation of the Jacobian terms is proposed in this research. This ensures improved accuracy and faster convergence. The studies of the ROM methods are to provide guidelines and suggestions on the performance of different methods. The dynamic behaviour caused by the distributed nonlinearities, like internal resonance and energy localisation due to the evolution of non-similar modes or bifurcations [101], need to be captured accurately by the reduced models. The ability to reproduce the exact rotational effect on the nonlinear systems is also required. The implementation of the ROM methods in an intuitive way makes the fast computation for the large-scale application of the model feasible.

1.3 Outline of the thesis

The present thesis is organised as following:

- ***Chapter 2:*** Previous works done on the vibration analysis of the rotating structures are reviewed. The finite strain theory in continuum mechanics for geometric nonlinearity is introduced. Different nonlinear strain measures due to large deformation are studied and compared. Different theories used in the finite element vibration analysis and the formulation of equations of motion derived from the energy approach are presented. The state of knowledge about the existing numerical methods used for nonlinear vibration analysis is also provided. Finally, the state of the art in the computation of ROMs for nonlinear systems is surveyed.

- ***Chapter 3:*** Non-rotating 3D structures with geometric nonlinearities are considered in this chapter. Detailed numerical formulations for constructing the finite element equations with the 3D solid elements are presented. The performances of different 3D solid elements are investigated. The methodology for solving the dynamic equations by using the HBM is provided. The formulations for computing the backbone curves based on the extended energy balance method are also derived. The nonlinear dynamic response of the geometric nonlinear systems is demonstrated by using nonlinear modal analysis. The effects of the geometric nonlinear terms are studied on both static and dynamic analysis of the 3D test cases.

- ***Chapter 4:*** The proposed methodologies for nonlinear analysis are implemented onto the 3D rotating structure. The effects of rotational speed on the dynamic behaviour

of the nonlinear systems are discussed. Formulations for structures undergoing base excitation are also presented. The numerical simulation results are validated by the experimental data.

- ***Chapter 5:*** Two projection-based ROM methods are proposed. The convergence and computational cost for both methods are demonstrated. ROM with static modal derivatives and quadratic manifold is selected. The ability of the reduced system on capturing the features of nonlinear behaviours and the effect of rotations are discussed.

Chapter 2

State of Knowledge

2.1 Nonlinear vibration of rotating system

Vibration analysis of a rotating system provides a very important tool for studying the dynamic behaviour of the mechanical systems, such as rotors, turbine blades, aeroplane propellers, etc. Being able to simulate the global dynamic behaviour of rotating machines is necessary for early design stage and health monitoring of the machineries. Large rotations in a structure are described by the stretch in the shape due to the elasticity of the structure from the centrifugal forces associated to the rigid body motion of the beam. Vibration characteristics of a rotating structure, i.e. natural frequencies and mode shapes, vary significantly from the non-rotating status when undergoing high rotating speed. This is due to the increase in the overall stiffness of the structure introduced by the centrifugal forces. Relationship between the rotating and non-rotating frequencies for rotating structures was first studied by Southwell and Gough [137]. The Southwell equation was used to provide natural frequency estimates, however it has limitation on predicting natural frequencies for high angular velocities. More research on numerical methods have been carried afterwards to improve the accuracy of the natural frequency's estimation and to obtain the mode shapes [39, 123, 132, 167].

As shown in Figure 2.1, the deformation of a rotating blade can be considered as a combination of chordwise displacement (i.e. lag and lead), flapwise displacement and torsional deformation. Research employ beam formulations focus on the linear bending in a single plane are widely used due to its simplicity of formulation, ease of implementation and less requirement on computational power. However the geometric nonlinear terms, which are truncated from the linear modelling, play an important role in dynamic analysis when structures undergo large deformation. Works with the use of nonlinear models and full three-dimensional rotation models have also been attempted by many researchers for more

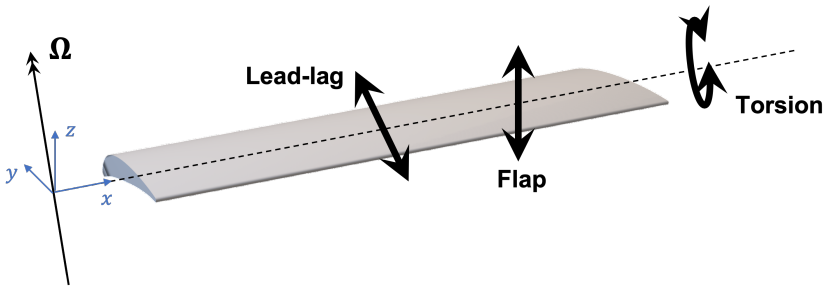


Fig. 2.1 *Configuration of a rotor blade and the co-ordinate system*

accurate results. In this section, linear modelling works are reviewed first, followed by the nonlinear modelling methods.

Hodges and Rutkowski [54] quantified the accuracy between different finite element (FE) model characteristics on the solutions of a free vibration Euler-Bernoulli beam around a fixed axis. Both uniform and tapered beam were investigated. The results of this research demonstrated that for a given accuracy level, FE model with fewer higher-order elements requires less computational power than a model with a finer mesh but lower-order elements. Chung and Yoo [27] presented a finite element analysis for a rotating cantilever beam with stretch deformation instead of the conventional axial deformation. The coupled stretch and chordwise deformations as well as the uncoupled flapwise deformation were used to describe the motion of a rotating cantilever beam. This method can improve the accuracy of the classical linear Cartesian modelling method. Banerjee [6, 7] used the dynamic stiffness method on tapered Euler-Bernouill beams. The dynamic stiffness matrix was developed using the Frobenius method of solution of the governing differential equation in power series. Unlike the finite element method, the shape function used in the dynamic stiffness is exact, and is generally obtained from the analytical solution of the governing equations. Hence the results are independent of the number of elements in the analysis. The author proposed that the method could offer an accurate method for free-vibration analysis of rotating uniform beams with one single element. Similarly, Gunda et al. [46] used the Euler-Bernouill's theory on tapered rotating beams with only transverse displacements. The research developed a Fourier-p supplement to the finite element method. Results showed agreement between different methods by using less degree of freedoms than other methods. Bazoune and Khulief [11] investigated the effect of introducing an angle of rotation and hub radius on the in-plane (lead-lag) and out-of-plane (flapping) modes of free vibration of a tapered Timoshenko beam

with uniform rotation. The research provided insights in the natural frequency response with respect to rotational speed, hub radius and setting angle. Explicit expressions of Southwell coefficients with setting angle, hub radius and taper ratios considered were first introduced for the uniform Timoshenko beam. Bulk research were also carried on investigating the effect of various parameters on the natural frequencies of a rotating beam, i.e. pre-twist angle [172, 36], cross-section variation [78], root offset [39], tipped mass [53, 167], rotational inertia [171] etc. Lin and Hsiao [83] showed the effect of rotational forces, such as coriolis, on the response of the natural frequency of a linear Timoshenko beam with varying angular velocity, hub radius and slenderness ratio. Results of the research show that the Coriolis force effect on the natural frequency is small for linear elastic beam with a coupled behaviour between the axial and transverse vibrations. An approach to extend the method to non-uniform rotating beams with discontinuities was also proposed. Combescure et al. [28] show the possibility of performing dynamic analysis of complex rotating machines using both the refined 3D shell models and 2D Fourier finite beam elements model.

The research so far referenced have been focused on the analysis of linear model, we now turn our focus on the nonlinear model research carried out on the topic of rotating structures. Turhan and Bulut [151] analysed the vibration behaviour of a rotating Bernouilli-Euler beam with nonlinear curvature and geometric nonlinearities, showing a softening behaviour proportional to the applied rotational speed. Using the nonlinear normal modes, the authors Pesheck, Pierre and Shaw [108] derived a reduced order model for rotating beams. The beam considered here was a simplified model of a rotating beam based on a von Kármán formulation. It is an idealized model for a rotor blade with motion dominated by transverse vibrations perpendicular to the plane of rotations. The analysis used an isotropic, uniform cantilever beam at constant rotational speed. Nonlinear axial strain has been included in the model causing axial-transverse strain coupling. The approach showed a very good approximation of the nonlinear modes of vibration and captured the internal resonant frequencies between the transverse and the axial modes. Tian et al. [148] proposed a modified variational method for nonlinear vibration analysis of rotating beams including Coriolis effects. Coriolis effects arise from the coupling among various modes of deformation. The effects can be significant for beams with small hub radius, large slenderness ratio and high rotating speed. A branch of research on higher order model for pre-twisted, laminated composite rotating beams using linear theory has been carried out by Chandiramani, Shete and Librescu [25, 26]. The investigation hypothesised a parabolic relationship between shear strain and wall thickness instead of a more traditional uniform variation. Free and forced vibrations were studied using the Galerkin method and derived using Hamilton's principle. Of particular

interest was the significant response difference between the more traditional beam theory and first order shear deformation theory (FSDT) for varying levels of pre-twist, rotational speed and hub radius. Bazoune et al. [12] analysed a rotating tapered Timoshenko's beam with bending, axial and torsional displacements with two modal reduction schemes. Time responses based on sinusoidal and impulse force were then compared. A bending-torsional model for double tapered beams model was developed by Oxgumus and Kaya [99]. This accounted for the flapwise bending displacements of the Timoshenko's beam and neglected any effect of Coriolis. The effects of the rotational speed and taper ratio on the nonlinear natural frequency response was then investigated. Shell elements were first used by Leissa for vibration analysis of rotating blade [82]. The influence of rotating speed, pre-twist and stagger angle were studied. Kee and Shin [65] investigated the dynamic characteristics of rotating composite blades with eighteen-node solid-shell finite element which shows good correlation with the experimental data.

This research focuses on the nonlinear vibration analysis of the rotating structure by using three dimensional solid elements. This enables the accurate dynamic analysis of rotating structures with more advanced configurations, i.e. large curvatures and twists, and large deformations.

2.2 Formulation of the problem

In order to solve the practical engineering problems and to study the actual response of the structures due to the application of force or other external excitations, computer simulations of the structure behaviour are required. Continuum models (mathematical idealisation) of the actual structures can be developed with expressions as ordinary differential equations (ODE) or partial differential equations (PDE) in space-time, describing the kinetics and kinematics of the structure based on the fundamental physical laws and the constitutive laws. Continuum mechanics of the structures deals with the behaviour of the solid continua, i.e. vector and tensor fields such as displacements, strain and stress. In continuum mechanics, finite strain theory (section 2.2.2) deals with systems undergoing large deformation, i.e. arbitrarily large rotations and strains. Structures are continuous systems and, as such systems, PDEs are used to mathematically formulate structure dynamic problems which involves functions of several variables. The derivation of the equation of motion for dynamic problems is introduced in section 2.2.1. Finite element method is the most popular technique used to solved the PDEs in structure dynamics by discretising the complex mechanical systems and structures in space. Details of the algorithms used are discussed in section 2.2.3.

2.2.1 Formulation of the equations of motion

Dynamic Equilibrium

Equation of motion of any dynamic system can be formulated based on the Newton's second law: *The change of motion is proportional to the motive force impressed; and is made in the direction of the right line in which the force is impressed.*

$$\sum_{j=1}^{N} f_{ij} - m_i a_i = 0 \tag{2.1}$$

Equation (2.1) shows the dynamic force equilibrium of the free body based on Newton's second law, where $-m_i a_i$ is regarded as the inertia force.

Principle of Virtual Displacement

In 1715, Johann Bernoulli first systematized the virtual work principle and made explicit the concept of infinitesimal displacement. The principle of virtual displacement states that 'if a system, which is in equilibrium under the action of a set of forces, is subjected to a virtual displacement $\boldsymbol{\delta u}$, then the total work done by the forces $\boldsymbol{f}$ will be zero' [110], i.e. Equation (2.2). $\boldsymbol{\delta u}$ are the infinitesimal variations from the equilibrium position of the system, not the true displacement.

$$\sum_{i=1}^{N} (f_i - m_i a_i) \cdot \boldsymbol{\delta u} = 0 \tag{2.2}$$

The advantage of applying energy principles over Newton's method is that only applied forces and inertia forces need to be considered, i.e. this overcomes the problem of vectorial addition of forces in complex system.

Consider a body Ω with boundary $\Gamma \equiv \Gamma_u + \Gamma_t$. Displacements $\boldsymbol{u}$ are specified on the displacement boundary Γ_u, and the internal traction per unit surface, $\boldsymbol{t}$, on the traction boundary Γ_t. Balance of linear momentum equations (Equation (2.3)) and the Neumann boundary condition (Equation (2.4)) yields the strong form of the momentum balance equations:

$$\sigma_{ij,j} + \rho b_i - \rho \ddot{u}_i = 0 \quad \text{on } \Omega, \tag{2.3}$$

$$\sigma_{ij} n_j = t_i \quad \text{on } \Gamma_t \tag{2.4}$$

where $\boldsymbol{\sigma}$ represents the stress tensor, $\rho \boldsymbol{b}$ is the internal body force per unit volume and n_j denotes the outward normal vector to Γ_t. Consider a virtual displacement field $\boldsymbol{\delta u}$ applied

continuously and bounded over Ω and $\delta \boldsymbol{u} = 0$ on the displacement boundary Γ_u. Multiply Equation (2.3) with the virtual displacement field δu_i and integrate over the body yields the weak form of the momentum balance equation or the principle of virtual work (Equation (2.5)):

$$\int_\Omega \left(\sigma_{ij,j} + \rho \boldsymbol{b} - \rho \ddot{u}_i\right) \cdot \delta u_i \mathrm{d}\Omega = 0$$

$$\Rightarrow \int_\Omega \left(\sigma_{ij} \cdot \delta u_{i,j} - \rho \boldsymbol{b} \cdot \delta u_i + \rho \ddot{u}_i \cdot \delta u_i\right) \mathrm{d}\Omega = \int_{\Gamma_t} \boldsymbol{t} \cdot \delta u_i \mathrm{d}\Gamma$$

$$\int \boldsymbol{\sigma} : \delta \boldsymbol{\varepsilon} \, \mathrm{d}\Omega + \int \rho \ddot{\boldsymbol{u}} \cdot \delta \boldsymbol{u} \, \mathrm{d}\Omega = \int \rho \boldsymbol{b} \cdot \delta \boldsymbol{u} \, \mathrm{d}\Omega + \int \boldsymbol{t} \cdot \delta \boldsymbol{u} \, \mathrm{d}\Gamma \tag{2.5}$$

Hamilton's Principle

The scalar product of two vectors involved in Equation (2.2) can be avoided by using Hamilton's principle, which uses scalar energy quantities only. Equation (2.6) is the mathematical statements of Hamilton's principle [49]:

$$\int_{t1}^{t2} (\delta T - \delta V + \delta W_{nc}) \, \mathrm{d}t = 0 \tag{2.6}$$

where T stands for the kinetic energy of the system, V stands for the potential energy of the system and δW_{nc} stands for the virtual work done by the non-conservative forces. The only interested potential energy in this research is the strain energy U. Hamilton's principle can be applied on both discrete and continuous systems.

Euler–Lagrange's Equation of Motion

When Hamilton's principle (Equation (2.6)) is applied to discrete systems, it can be expressed in a more convenient way [110]:

$$\frac{\mathrm{d}}{\mathrm{d}t}\left(\frac{\partial T}{\partial \dot{q}_j}\right) - \frac{\partial T}{\partial q_j} + \frac{\partial U}{\partial q_j} = Q_j, \qquad j = 1, 2, ..., n \tag{2.7}$$

Euler–Lagrange equation shows the Euler–Lagrange's equation for the multi-degree of freedom system, where $q_j \, (j = 1, 2, ..., n)$ stands for the n independent displacements and Q_j are generalised forces. T and U are the kinetic and strain energy. The kinetic energy and the

strain energy can be written in the discrete form as:

$$T = \frac{1}{2}\{\dot{\boldsymbol{u}}\}^{\mathsf{T}}[\mathbf{M}]\{\dot{\boldsymbol{u}}\} \qquad (2.8)$$
$$U = \frac{1}{2}\{\boldsymbol{u}\}^{\mathsf{T}}[\mathbf{K}]\{\boldsymbol{u}\}$$

where $\{\boldsymbol{u}\}$ and $\{\dot{\boldsymbol{u}}\}$ are the column vector of system displacements and velocities. $[\mathbf{M}]$ and $[\mathbf{K}]$ are the mass and stiffness matrix. Using Equation (2.7), the Euler–Lagrange's equations of motion in the matrix form can be derived as shown in Equation (2.9), with $[\mathbf{C}]$ standing for the damping matrix and $\{\boldsymbol{F}\}$ standing for the excitation force vector.

$$[\mathbf{M}]\{\ddot{\boldsymbol{u}}\} + [\mathbf{C}]\{\dot{\boldsymbol{u}}\} + [\mathbf{K}]\{\boldsymbol{u}\} = \{\boldsymbol{F}\} \qquad (2.9)$$

2.2.2 Finite strain theory

Material and geometric nonlinearities are the two sources of nonlinearity existing in the analysis of solid continua. Material nonlinearity occurs when the stress-strain constitutive law is nonlinear, whereas the geometric nonlinearity occurs when change in geometry has an effect on the load deformation behaviour [18]. In continuum mechanics, finite strain theory deals with deformation problems which involve large strains and large rotations of the material body particles when compared to the material body dimensions. There is a significant difference between the initial (reference, undeformed) configuration and the current (deformed) configuration of the continuum model, as shown in Figure 2.2. Hence the assumptions in the infinitesimal strain theory, i.e. small displacement and small displacement gradient when compared to the unity, can no longer be used to simplify or to linearise the continuum mechanics equations.

In mechanics, kinematics deals with the motion and deformation of a body without reference to the cause, and kinetics studies the internal forces within a body and their relationships to a body's motion. Both kinematics and kinetics are important when studying and understanding the nature of motion. In this section, nonlinear continuum mechanics is reviewed from both perspectives.

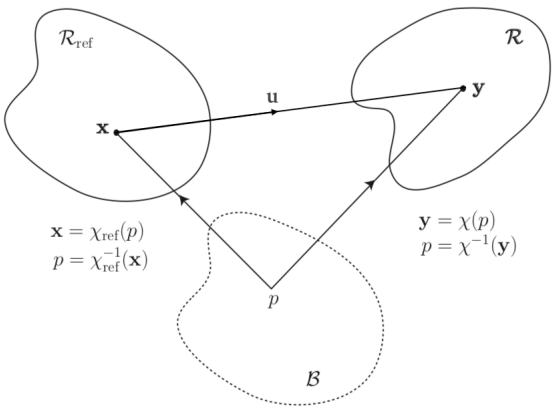


Fig. 2.2 *Configurations used in geometrically nonlinear analysis in continuum mechanics: base configuration $\mathscr{B}$, reference configuration $\mathscr{R}_{ref}$ and current configuration $\mathscr{R}$*

Deformation Measures

In continuum model, the actual structure can be mathematically treated as a continuum body $\mathscr{B}$, composed of a set of particles p. The region $\mathscr{R}$ occupied by the configuration χ of the body at specific time under certain condition is the set of locations $\mathbf{y}$ of all the particles in space. As shown in Figure 2.2, $\mathscr{R} = \chi(\mathscr{B},t)$ and $\mathbf{y} = \chi(p,t)$. A reference configuration χ_{ref} of the body $\mathscr{B}$ may be needed sometimes for geometric studies, $\mathscr{R}_{ref} = \chi_{ref}(\mathscr{B},t)$ and $\mathbf{x} = \chi_{ref}(p,t)$. Configurations during the response analysis are linked by a Cartesian coordinate systems. Material coordinates $\mathbf{x}$ tracks the base configuration whereas the spatial coordinates $\mathbf{y}$ tracks all others by classical continuum mechanics conventions.

Total Lagrangian descriptions and *Updated Lagrangian* descriptions are the two mostly used kinematic descriptions in continuum-based finite element analysis to handle geometrically nonlinear problems in solid or structure mechanics. In Total Lagrangian descriptions, the base and the reference configurations coalesce and remain fixed. Motion and deformation of a body over time are described with respect to its initial configuration. This description is primarily used in solid mechanics with finite displacements and strains. In Updated Lagrangian descriptions, the reference configuration is constantly updated throughout the solution process. This formulation is widely used to handle solid mechanics with large displacements or strains or flow-like behaviours [14]. Total Lagrangian descriptions are used in this research as the initial/undeformed configuration is time independent and satisfies the

boundary conditions.

In this chapter, we shall consider the fixed reference configuration only. The displacement field $\mathbf{u}$ is a vector field which maps the positions of all the particles in the reference configuration to the deformed configuration.

$$\mathbf{u}(\mathbf{x},t) = \mathbf{y}(\mathbf{x},t) - \mathbf{x} \tag{2.10}$$

The partial derivative of the displacement vector $\mathbf{u}$ with respect to the material/reference coordinates $\nabla_{\mathbf{x}}\mathbf{u}$, yields the material displacement gradient tensor $\mathbf{F}$:

$$\nabla_{\mathbf{x}}\mathbf{u}(\mathbf{x},t) = \frac{\partial \mathbf{u}}{\partial \mathbf{x}} = \frac{\partial \mathbf{y}(\mathbf{x},t)}{\partial \mathbf{x}} - \mathbf{I} = \mathbf{F} - \mathbf{I} \tag{2.11}$$

The displacement gradient tensor $\mathbf{F}$ (Equation (2.12)) maps an infinitesimal undeformed material fiber $d\mathbf{x}$ into its location $d\mathbf{y}$ in the deformed configuration, and is used to study the deformation in the immediate neighbourhood of $d\mathbf{x}$ [3].

$$\mathbf{F} = \frac{\partial \mathbf{u}}{\partial \mathbf{x}} + \mathbf{I} = \begin{bmatrix} 1 + \dfrac{\partial \mathbf{u}_1}{\partial \mathbf{x}_1} & \dfrac{\partial \mathbf{u}_1}{\partial \mathbf{x}_2} & \dfrac{\partial \mathbf{u}_1}{\partial \mathbf{x}_3} \\ \dfrac{\partial \mathbf{u}_2}{\partial \mathbf{x}_1} & 1 + \dfrac{\partial \mathbf{u}_2}{\partial \mathbf{x}_2} & \dfrac{\partial \mathbf{u}_2}{\partial \mathbf{x}_3} \\ \dfrac{\partial \mathbf{u}_3}{\partial \mathbf{x}_1} & \dfrac{\partial \mathbf{u}_3}{\partial \mathbf{x}_2} & 1 + \dfrac{\partial \mathbf{u}_3}{\partial \mathbf{x}_3} \end{bmatrix} \tag{2.12}$$

This is a one-to-one mapping between $d\mathbf{x}$ and $d\mathbf{y}$, thus $\mathbf{F}$ can be decomposed, using the polar decomposition theorem, into a product of two second-order tensors [150]. As shown in Equation (2.13), where $\mathbf{R}$ is a proper orthogonal rotation tensor, i.e. $\det(\mathbf{R}) = 1$ and $\mathbf{R}^{\intercal} = \mathbf{R}^{-1}$; $\mathbf{U}$ and $\mathbf{V}$ are the symmetrical right and left stretch tensors respectively. Hence the body particle motion can be expressed as a pure deformation followed by a rigid rotation (Lagrangian form) or as a rigid rotation followed by a pure deformation (Eulerian form).

$$\mathbf{F} = \mathbf{R}\mathbf{U} = \mathbf{V}\mathbf{R} \tag{2.13}$$

$\mathbf{U}$ and $\mathbf{V}$ share the same eigenvalues, λ_i, which are called the principal stretches, but different eigenvectors or principal directions. Polar decomposition are very tedious to compute as eigenanalysis is required. The right and left Cauchy-Green deformation tensors, named after Augustin Louis Cauchy and George Green, are often used as measures of stretch. The two

rotation-independent tensors, $\mathbf{C}_R$ and $\mathbf{C}_L$, , are defined in terms of $\mathbf{U}^2$ and $\mathbf{V}^2$ respectively, with eigenvalues of ${\lambda_i}^2$ (Equation (2.14)).

$$\mathbf{C}_R = \mathbf{F}^\intercal \mathbf{F} = \mathbf{U}^2, \quad \mathbf{C}_L = \mathbf{F}\mathbf{F}^\intercal = \mathbf{V}^2 \tag{2.14}$$

When modelling materials that are path dependent, the time derivative of the deformation gradient, $\dot{\mathbf{F}}$, need to be calculated.

$$\dot{\mathbf{F}} = \frac{\partial \mathbf{F}}{\partial t} = \frac{\partial}{\partial t}\frac{\partial \mathbf{y}(\mathbf{x},t)}{\partial \mathbf{x}} = \frac{\partial \mathbf{v}(\mathbf{x},t)}{\partial \mathbf{x}} = \frac{\partial \mathbf{v}(\mathbf{x},t)}{\partial \mathbf{y}}\frac{\partial \mathbf{y}}{\partial \mathbf{x}} = \mathbf{L}\cdot\mathbf{F} \tag{2.15}$$

$\mathbf{L}$ in Equation (2.15) and (2.16) is the spatial velocity gradient, which can be expressed as sum of the rate of deformation tensor $\mathbf{D}$ and the spin tensor $\mathbf{W}$. The symmetric rate of deformation tensor (Equation (2.17)) calculates the rate of stretching of line elements and the antisymmetric spin tensor (Equation (2.18)) tells the rate of rotation or vorticity of the motion. Both tensors are the commonly used quantities in continuum mechanics.

$$\mathbf{L} = \frac{\partial \mathbf{v}(\mathbf{x},t)}{\partial \mathbf{y}} = \mathbf{W} + \mathbf{D} \tag{2.16}$$

$$\mathbf{D} = \frac{1}{2}(\mathbf{L} + \mathbf{L}^\intercal) \tag{2.17}$$

$$\mathbf{W} = \frac{1}{2}(\mathbf{L} - \mathbf{L}^\intercal) \tag{2.18}$$

Strain Measures

Strain is a measure for the non-rigid part of the deformation. When undergoing a geometrically nonlinear deformation process, continuum bodies will exhibit large strains. Definition of strain is not unique. Table 2.1 lists the different ways in which these large strain can be measured in Lagrangian form. Since a pure rotation does not induce any strains onto the body, it is often preferable to use rotation-independent measures of deformation in continuum mechanics. The strain measures listed in the table are all rotation-independent. The corresponding Eulerian form of the strain measures can be converted by substituting $\mathbf{U}$ with $\mathbf{V}$. The Lagrange strain tensor quantifies the change in length and direction of an infinitesimal material fibre, while the Eulerian form holds the same physical significance but computes the strain of an infinitesimal material fibre from its orientation after deformation.

The stretch tensor $\mathbf{U}$ is very difficult to compute due to the polar decomposition. As shown in Table 2.1, the Green-Lagrange and Almansi strain measures are the only two measures which can avoid solving eigen-problems. Green-Lagrange strain measures are used in this research

to describe the nonlinear geometric effect for structures undergoing finite deformation. Substituting the Equation (2.12) into Equation (2.14), yields the explicit expression for the Green-Lagrange strain tensor:

$$\boldsymbol{\varepsilon}^G = \frac{1}{2}\left(\mathbf{U}^2 - \mathbf{I}\right) \quad or \quad \varepsilon_{ij}^G = \frac{1}{2}\left(\frac{\partial \mathbf{u}_i}{\partial \mathbf{x}_j} + \frac{\partial \mathbf{u}_j}{\partial \mathbf{x}_i} + \frac{\partial \mathbf{u}_k}{\partial \mathbf{x}_i}\frac{\partial \mathbf{u}_k}{\partial \mathbf{x}_j}\right) \tag{2.19}$$

The strain used in the infinitesimal strain theory, also called small strain theory, is obtained when neglecting all the nonlinear parts of the Green-Lagrange strain measures. The linear small strain tensor as shown in Equation (2.20) depends on the displacement gradient tensor $\mathbf{F}$, hence the rotations. The inaccuracy of the tensor grows with the amount of rotation, which makes it not suitable for cases involving large rotations.

$$\boldsymbol{\varepsilon} = \frac{1}{2}\left(\mathbf{F} + \mathbf{F}^\intercal\right) - \mathbf{I} \quad or \quad \varepsilon_{ij} = \frac{1}{2}\left(u_{i,j} + u_{j,i}\right) \tag{2.20}$$

Strain Measures	**Tensor Form**	**Comments**
Green-Lagrange	$\frac{1}{2}\left(\mathbf{U}^2 - \mathbf{I}\right)$	Widely used in the geometrically nonlinear finite element analysis. Easy to compute. No eigenanalysis required.
Biot	$\mathbf{U} - \mathbf{I}$	Not too commonly employed. Eigenanalysis required to get $\mathbf{U}$.
Hencky	$\log\left(\mathbf{U}\right)$	Prone to singularities in FEM computations due to zero strain. Often used in finite strain elastoplasticity. Eigenanalysis required.
Swainger	$\mathbf{I} - \mathbf{U}^{-1}$	Rarely used in Lagrangian form. Eigenanalysis required to get $\mathbf{U}$.
Almansi-Lagrange	$\frac{1}{2}\left(\mathbf{I} - \mathbf{U}^{-2}\right)$	Eulerian version is more popular. Inversion of $\mathbf{C}_R$ required, no eigenanalysis required to get $\mathbf{U}$.
Midpoint	$2\left(\mathbf{U} - \mathbf{I}\right)\left(\mathbf{I} + \mathbf{U}\right)^{-1}$	log-free approximation to Hencky strain or logarithmic strain. Eigenanalysis to get $\mathbf{U}$ and an inversion required.
Bazant	$\frac{1}{2}\left(\mathbf{U} - \mathbf{U}^{-1}\right)$	log-free approximation to Hencky strain or logarithmic strain. Eigenanalysis to get $\mathbf{U}$ and an inversion required.

Table 2.1 *Finite strain measures used in geometrically nonlinear analysis* [14]

Stress Measures

In geometrically nonlinear structural analysis, second-order or higher partial differential equations are involved in the mathematical models. The governing differential equations

along with the initial or boundary conditions are referred to as the strong form of the problem. The high order partial differential equations would require high smoothness of the solutions, hence not desirable. In the principle of virtual work approach, the weak form of the problem involves integrals of the strong form differential equations, which reduces the order of the governing equations. The work conjugates of stress and strain tensors need to be defined to give the accurate energy density, δW^0, for weak formulation as shown in Equation (2.21), where $\boldsymbol{\varepsilon}$ stands for the strain matrix of choice and $\boldsymbol{\tau}$ is the work conjugate stress matrix to $\delta\boldsymbol{\varepsilon}$.

$$\delta W^0 = \boldsymbol{\tau} : \delta\boldsymbol{\varepsilon} \tag{2.21}$$

While each strain definition can find application in different situations, Cauchy or True Stress is generally acknowledged to have a better physical interpretation than any other stress definitions. Cauchy stress $\underline{\sigma}$ is the force per unit area of material in the current (deformed) configuration, which reflects the actual stress happening in the material. However its work-conjugate strain is not commonly used in FEM analysis. Cauchy stress can be recovered later in FEM analysis for engineering interests.

For an elastic material the power generated by internal stress over the configuration can be expressed as:

$$\int \underline{\sigma} : \mathbf{L}\,\mathrm{d}V = \int J\underline{\sigma} : (\mathbf{D}+\mathbf{W})\,\mathrm{d}V_0 = \int J\underline{\sigma} : \mathbf{D}\,\mathrm{d}V_0 \tag{2.22}$$

Where J is the Jacobian of the elastic deformation between the reference/undeformed volume V_0 and the current/deformed volume V. Since pure rotation does not induce any power into the system, the spin tensor $\mathbf{W}$ is removed in Equation (2.22). With the definition of Green-Lagrange strain and $\dot{\mathbf{F}}$ given in Equation (2.19) and (2.15), respectively, the rate of the Green-Lagrange strain can be derived as:

$$\dot{\boldsymbol{\varepsilon}}^G = \frac{1}{2}\left(\dot{\mathbf{F}}^\mathsf{T}\cdot\mathbf{F} + \mathbf{F}^\mathsf{T}\cdot\dot{\mathbf{F}}\right) = \frac{1}{2}\mathbf{F}^\mathsf{T}\cdot(\mathbf{L}+\mathbf{L}^\mathsf{T})\cdot\mathbf{F} = \mathbf{F}^\mathsf{T}\cdot\mathbf{D}\cdot\mathbf{F} \tag{2.23}$$

Thus,

$$\mathbf{D} = \mathbf{F}^{-\mathsf{T}}\cdot\dot{\boldsymbol{\varepsilon}}^G\cdot\mathbf{F}^{-1} \tag{2.24}$$

The work rate per unit reference volume becomes:

$$\delta W^0 = J\underline{\sigma} : \mathbf{D} = J\underline{\sigma} : \mathbf{F}^{-\mathsf{T}}\cdot\dot{\boldsymbol{\varepsilon}}^G\cdot\mathbf{F}^{-1} = J\mathbf{F}^{-1}\underline{\sigma}\mathbf{F}^{-\mathsf{T}} : \dot{\boldsymbol{\varepsilon}}^G \tag{2.25}$$

Hence the conjugate stress of the Green-Lagrange strain, usually referred to as second Piola–Kirchhoff stress, is derived:

$$\boldsymbol{S} = J\mathbf{F}^{-1}\underline{\boldsymbol{\sigma}}\mathbf{F}^{-\mathsf{T}} \tag{2.26}$$

The weak form of the equations of motion as shown in Equation (2.5) can thus be expressed in terms of Green-Lagrange strain and second Piola–Kirchhoff stress as:

$$\int \boldsymbol{S} : \delta\boldsymbol{\varepsilon}^G \,\mathrm{d}\Omega + \int \rho\ddot{\boldsymbol{u}} \cdot \delta\boldsymbol{u} \,\mathrm{d}\Omega = \int \rho\boldsymbol{b} \cdot \delta\boldsymbol{u} \,\mathrm{d}\Omega + \int \boldsymbol{t} \cdot \delta\boldsymbol{u} \,\mathrm{d}\Gamma \tag{2.27}$$

Same derivation steps can be applied on other strain measures to compute the stress conjugates. Table 2.2 lists the conjugate stress measures corresponding to the existed or commonly used finite strain measures in continuum mechanics. In contrast to the Cauchy stress tensor, second Piola–Kirchhoff stress tensors express the stress relative to the reference (undeformed) configuration. Balance of angular momentum requires the symmetry of the Cauchy stress tensor, i.e. $\underline{\boldsymbol{\sigma}}^{\mathsf{T}} = \underline{\boldsymbol{\sigma}}$. The second Piola–Kirchhoff stress is therefore also symmetric.

Strain Measures	**Conjugate Stress Tensor**	**Comments**
Green-Lagrange	$J\mathbf{F}^{-1}\underline{\boldsymbol{\sigma}}\mathbf{F}^{-\mathsf{T}}$	Second Piola-Kirchoff tensor $\underline{\boldsymbol{\sigma}}$ "pulled back" to the reference configuration
Biot	$\frac{1}{2}J\left(\mathbf{U}^{-1}\underline{\boldsymbol{\sigma}}^R + \underline{\boldsymbol{\sigma}}^R\mathbf{U}^{-1}\right)$	Biot stress or Jaumann stress $\underline{\boldsymbol{\sigma}}^R = \mathbf{R}^{\mathsf{T}}\underline{\boldsymbol{\sigma}}\mathbf{R}$
Hencky	Isotropic material: $\underline{\boldsymbol{\sigma}}^R$	Hencky stress Extremely complicated for anisotropic material.
Swainger	$\frac{1}{2}J\left(\mathbf{U}\underline{\boldsymbol{\sigma}}^R + \underline{\boldsymbol{\sigma}}^R\mathbf{U}\right)$	Swainger stress Rarely used
Almansi-Lagrange	$J\mathbf{F}^{\mathsf{T}}\underline{\boldsymbol{\sigma}}\mathbf{F}$	Almansi stress

Table 2.2 *Conjugate stress measures for the selected finite strain measures* [14]

Constitutive Relationships

The mechanical properties of an isotropic material subject to loading depends on its microstructural physical properties such as internal constitution of the material of the continuum body. Constitutive equations describe different kinds of stress-strain response to different loading conditions [176]. A range of constitutive models are available for the wide variety of materials encountered in the analysis problem. Metals and superalloy materials, commonly

used in the aerospace industry due to their high thermo-mechanical load capabilities, are typically modelled through a linear stress-strain relationship, such as Hooke's law. Equation (2.28) shows the index expression for Hooke's Law, with C_{ijkl} being the component of the constitutive 4th order tensor. This model is valid up to the yield stress, where the accumulation of plastic dislocations in the material microstructure becomes significant enough to lead to plastic slip in the material. Any further stress on the material generates a nonlinear strain response, a strain rate dependent elasto-plastic constitutive model then needs to be applied [69].

$$\begin{aligned} \psi(\varepsilon) &= \frac{1}{2} C_{ijkl}\, \varepsilon_{ij}\, \varepsilon_{kl} \\ \sigma_{ij} &= C_{ijkl}\, \varepsilon_{kl} \end{aligned} \tag{2.28}$$

In order to increase the propulsive efficiency of aircraft and the need for lighter and stronger materials, significant advancements have been made in the mechanical properties of composite materials. These are generally sandwich structure of polymeric and ceramic materials, layered on each other using orthogonal fibre directions. This practice ensures the strength of the material in the direction of the fibre while maintaining isotropic properties in the other directions.The mechanical behaviour of such structures are highly dependent on the placement of the different layers as well as the materials used for the matrix and fibre. Generally, the Young's modulus tends to be somewhere between that of the fibre and matrix, while significantly increasing the strength of the material compared to the fibre or resin alone [20]. Guo et al. [47] reviewed the typical constitutive models used in finite element analysis on composites such as the continuum damage model [75] for predicting the stiffness degradation and modelling damage evolution; mixture theory model [38] for nonlinear behaviour of composite at high strain; multi-scale model [43] for more efficient microstructural analysis, and so on.

In this research, we focus on homogeneous materials only and are not going deep on composites. For many metallic materials, such as steel, aluminium or titanium, the assumption of Green elasticity or hyper-elasticity is valid. In hyper-elastic material, the constitutive relationship is defined by a strain energy function ψ, Equation (2.29), which does not depend on the deformation history or the rate of deformation.

$$\sigma_{ij}(\boldsymbol{\varepsilon}) = \frac{\mathrm{d}\psi(\boldsymbol{\varepsilon})}{\mathrm{d}\varepsilon_{ij}} \tag{2.29}$$

The strain energy or energy density function, ψ, describes the potential energy stored in the body. For isotropic material, i.e. the response of the material is indifferent from the

directions, ψ can be introduced, which depends on the invariants (I_C, II_C, III_C) of the Cauchy Green strain tensor, $\mathbf{C}$ [166]. The strain invariants are in terms of λ_i, which is the principal stretch of the deformation.

$$\begin{aligned} I_C &= \mathrm{tr}\,\mathbf{C} = \lambda_1^2 + \lambda_2^2 + \lambda_3^2 \\ II_C &= \frac{1}{2}\left[(\mathrm{tr}\,\mathbf{C})^2 - \mathrm{tr}\,(\mathbf{C})^2\right] = \lambda_1^2\lambda_2^2 + \lambda_2^2\lambda_3^2 + \lambda_3^2\lambda_1^2 \\ III_C &= \det(\mathbf{C}) = \lambda_1^2\lambda_2^2\lambda_3^2 \end{aligned} \tag{2.30}$$

For an isotropic hyper-elastic material, the second Piola-Kirchoff tensor can be expressed as:

$$\boldsymbol{S} = \frac{\mathrm{d}\psi(I_C, II_C, III_C)}{\mathrm{d}\boldsymbol{\varepsilon}^G} = 2\frac{\mathrm{d}\psi(I_C, II_C, III_C)}{\mathrm{d}\mathbf{C}}$$

$$\boldsymbol{S} = 2\left[\left(\frac{\partial\psi}{\partial I_C} + I_C\frac{\partial\psi}{\partial II_C}\right)\mathbf{I} - \frac{\partial\psi}{\partial II_C}\mathbf{C} + III_C\frac{\partial\psi}{\partial III_C}\mathbf{C}^{-1}\right] \tag{2.31}$$

The strain energy function in hyper-elastic material can be formulated by following different material models. The choice of material model depends on its applications and available experimental data to determine the material parameters. Examples of hyper-elastic models are: Mooney–Rivlin solid [87] with ψ as a linear function of I_C and II_C; the Yeoh model [170] for incompressible, nonlinear elastic materials with a cubic strain energy function in terms of I_C only; the Ogden material model [98] for modelling the nonlinear stress–strain behaviour of complex materials such as rubbers and polymers with ψ expressed in terms of the principal stretches, λ_i; the linear Saint Venant–Kirchhoff material law [52] and the nonlinear Neo-Hookean model [68] for isotropic materials undergoing large deformations; the Gent model [42] which is a phenomenological model of rubber elasticity based on the concept of limiting chain extensibility, etc.

Saint Venant–Kirchhoff model (Equation (2.32)) is the simplest hyperelastic model with the stress and strain relationship modelled by using Hooke's generalised law. It is an extension of the linear elastic material model to the nonlinear regime. The model is often used for metallic structures undergoing large deformation. In this research, the material nonlinearities are not included. The deformation of the material is assumed to be within the elastic regime. The linear Saint Venant–Kirchhoff model is selected for the finite element analysis due to its

simplicity to implement and compute.

$$\psi\left(\boldsymbol{\varepsilon}^G\right) = \frac{\lambda}{2}\operatorname{tr}\left(\boldsymbol{\varepsilon}^G\right)^2 + \mu\operatorname{tr}\left((\boldsymbol{\varepsilon}^G)^2\right)$$
$$\boldsymbol{S} = \lambda\operatorname{tr}\left(\boldsymbol{\varepsilon}^G\right)\mathbf{I} + 2\mu\boldsymbol{\varepsilon}^G \tag{2.32}$$

μ and λ are the Lamé constants, which can be computed in terms of Young's modulus E and Poisson's ratio ν of the material:

$$\lambda = \frac{\nu E}{(1+\nu)(1-2\nu)}, \qquad \mu = \frac{E}{2(1+\nu)} \tag{2.33}$$

2.2.3 Finite element method

Having defined the kinematics and the constitutive law of the system, the equation of motion containing the PDEs can be derived. The equation can be solved by using variational approach. In Finite Element Method, solutions of the PDEs are approximated by linear combination of independent functions. In this section, different commonly used theories in the finite element modelling for structure dynamics are explicated. Examples of finite element discretisation with Euler-Bernoulli beam elements and three-dimensional solid elements are shown. Modal analysis of the FE model, which provides important information of the dynamical behaviour of structures, i.e. the natural frequencies and vibration modes, is also presented.

Algorithms used in Finite Element Modelling

Section 2.2.1 shows that the equations of motion of the structures can be formulated based on the energy functions of the system, consisting of the strain energies, the kinetic energies, virtual work done by the applying loads and the dissipation functions. 1D Beam elements are heavily used in several industries to provide valuable insights into the behaviour of the structures with much less effort than more complex models, i.e. solids and shells. It can be used as a simple model to calculate the load-carrying and deflection characteristics of beams. The nonlinear dynamic response of a long, slender beam has been the subject of many theoretical and experimental efforts due to the fact that engineering structures like rotor blades, aeroplane wings, etc., can be modelled as a beam-like slender member. However beam element has its limitations in accuracy of the results and in representing complex structures. Three-dimensional (3D) solid elements, on the other hand, provide a better approximation to the dynamic behaviour of the structure, yet the complexity of the algorithms can become significant. Other algorithms used in the finite element analysis include Föppl–von Kármán

equations [154] for deflections of a thin flat plate, 2D shell elements for modelling shell/solid structures or crack propagation [174, 144], etc. The 2D shell elements allow modelling of thin features with fewer mesh elements than solid elements, hence requiring less computational power.

The Euler-Bernoulli beam theory and the Timoshenko beam theory have been widely used for the analysis of the distribution of stresses and displacements in the beam element [125, 160, 145, 97]. In this section, the two mostly used beam theories that evaluate the static and dynamic characteristics of the beam element are introduced. The derivation of the energy functions are presented. For simplicity of explanation, the small strain tensor is used in both cases. Commonly used 3D solid elements are also discussed in details.

Euler-Bernoulli Beam Theory In structure mechanics, a beam is a structure element which has one of its dimensions much larger than the other two. Cross sections of the beam do not deform significantly under the effect of the external forces. Shear forces and bending moments within the beam due to the applied loads induce the internal stresses, strains and deflections of the beam.

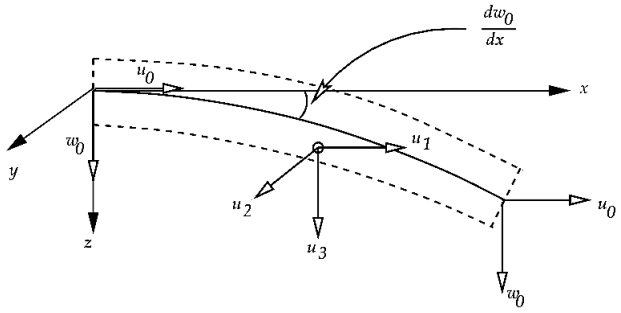


Fig. 2.3 *Schematic of Euler-Bernoulli Beam*

Euler–Bernoulli beam theory is used to describe the physical behaviour of the beam under loads. Figure 2.3 shows the schematic of the Euler-Bernoulli beam model based on the following assumptions [158]:

- Cross-sections of the beam do not deform during bending.
- Plane section remain in plane.
- Long slender beam, i.e. shear deformation can be neglected. Normal fibres of the beam axis remain normal to the neutral axis during the deformation.
- For small deflection, the bending moment M is proportional to the curvature.

w is the deflection of the beam, depends on both the space and the time. For small deflection, the stress distribution over the cross-section area of the beam can be expressed as:

$$\sigma_x = E\varepsilon_{xx} = E\frac{\partial}{\partial x}\left(-\frac{\partial w}{\partial x}z\right) = -E\frac{\partial^2 w}{\partial x^2}z \tag{2.34}$$

Hence the energy expressions for the Euler–Bernoulli beam elements are:

$$\begin{aligned} T &= \frac{1}{2}\int_L \rho A\left(\frac{\partial w}{\partial t}\right)^2 \mathrm{d}x \\ U &= \frac{1}{2}\int_L EI\left(\frac{\partial^2 w}{\partial x^2}\right)^2 \mathrm{d}x \\ \delta W_{nc} &= \int_L p(x,t)\,\delta w\,\mathrm{d}x \end{aligned} \tag{2.35}$$

where A is the cross-section area of the beam, L is the length of the beam, ρ is the material density of the beam and $p(x,t)$ is the external force applied on the beam. Assuming uniform material Young's modulus E, constant second moment of area I and uniform mass distribution along the beam. Substitute Equation set (2.35) into Equation (2.6) and integrate by parts, yield the strong form of the governing equation along the beam and its boundary conditions at both ends:

$$\begin{aligned} & EI\frac{\partial^4 w}{\partial x^4} + \rho A\frac{\partial^2 w}{\partial t^2} = p(x,t) \\ \text{with either} \quad & w = 0 \quad \text{or} \quad EI\frac{\partial^3 w}{\partial x^3} = 0 \\ \text{and either} \quad & \frac{\partial w}{\partial x} = 0 \quad \text{or} \quad EI\frac{\partial^2 w}{\partial x^2} = 0 \end{aligned} \tag{2.36}$$

The vanishing of w and $\frac{\partial w}{\partial x}$ represents the vanishing of displacement and rotation at the beam ends respectively. Consider the stress distribution over the cross-section area of the beam, the moment M about the y-axis is:

$$M = -\int_A \sigma_x z\,\mathrm{d}A = EI\frac{\partial^2 w}{\partial x^2} \tag{2.37}$$

Moment equilibrium of a beam element yields the shear force expression:

$$Q = -\frac{\partial M}{\partial x} = -EI\frac{\partial^3 w}{\partial x^3} \tag{2.38}$$

Hence $EI\left(\partial^2 w/\partial x^2\right) = 0$ in the boundary conditions indicates the vanishing of the bending moment and vanishing of $EI\left(\partial^3 w/\partial x^3\right)$ represents the vanishing of the shear force at the beam ends. The boundary conditions for a beam are defined in Table 2.3, where the boundary conditions consist of displacements or rotations are called geometric boundary conditions and the ones consist of forces or moments are called natural boundary conditions.

Free end	$w = 0 \quad M = 0$
Clamped end	$w = 0 \quad \partial w/\partial x = 0$
Simply supported	$Q = 0 \quad M = 0$

Table 2.3 *Beam boundary conditions*

Energy balance of the principle of virtual work (Equation 2.5) yields the weak form of the governing equation:

$$\begin{aligned} &\int \boldsymbol{\sigma} : \delta\boldsymbol{\varepsilon}\,\mathrm{d}\Omega + \int \rho\ddot{\boldsymbol{u}} \cdot \delta\boldsymbol{u}\,\mathrm{d}\Omega = \int \rho\boldsymbol{b} \cdot \delta\boldsymbol{u}\,\mathrm{d}\Omega + \int \boldsymbol{t} \cdot \delta\boldsymbol{u}\,\mathrm{d}\Gamma \\ &\Rightarrow EI \int_L \left(\frac{\partial^2 w}{\partial x^2} \frac{\partial^2 (\delta w)}{\partial x^2} \right) \mathrm{d}x + \rho A \int_L \left(\frac{\partial^2 w}{\partial t^2}\, \delta w \right) \mathrm{d}x = \int_L q(x,t) \cdot \delta w\,\mathrm{d}x \end{aligned} \tag{2.39}$$

where $q(x,t)$ is force per unit length applied on the beam.

Timoshenko Beam Theory The Euler-Bernoulli Beam theory for bending vibrations tends to give higher frequency values than those obtained by experiments, especially when analysing slender beam at higher frequencies and deep beams at low frequencies [146]. Rayleigh improved the theory in 1877 by including the rotary inertia effects of the cross-sections of the beam [116]. Timoshenko further extended the theory after Rayleigh in 1921 to include the effects of transverse shear in the mathematical model [149].

Figure 2.4 shows the schematic of Timoshenko beam element, where ϕ_x is the rotation of the cross-section at position x and γ_{xy} is the shear strain due to out-of-plane warping. The shear stress τ_{xy} and the shear strain varies over the cross-section. The numerical factor κ is introduced to cope with the variation over the area. Value of κ depends on the shape of the cross-section area [29].

$$\tau_{xy} = \kappa G \gamma_{xy} \tag{2.40}$$

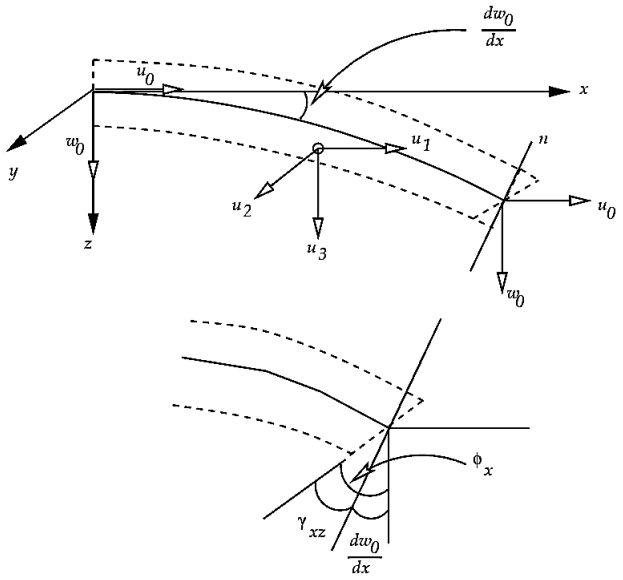


Fig. 2.4 *Schematic of Timoshenko Beam*

where G is the shear modulus and τ_{xy} is the average shear stress. Hence the energy expressions of the Timoshenko beam elements are:

$$
\begin{aligned}
T &= \frac{1}{2}\int_L \rho A \left(\frac{\partial w}{\partial t}\right)^2 \mathrm{d}x + \frac{1}{2}\int_L \rho I \left(\frac{\partial \phi_x}{\partial t}\right)^2 \mathrm{d}x \\
U &= \frac{1}{2}\int_L EI \left(\frac{\partial \phi_x}{\partial x}\right)^2 \mathrm{d}x + \frac{1}{2}\int_L \kappa AG \left(\frac{\partial w}{\partial x} - \phi_x\right)^2 \mathrm{d}x \\
\delta W_{nc} &= \int_L p(x,t)\,\delta w \,\mathrm{d}x
\end{aligned}
\tag{2.41}
$$

where A is the cross-section area of the beam, L is the length of the beam, ρ is the material density of the beam and $p(x,t)$ is the external force applied on the beam. Substitute Equation set (2.41) into Hamilton's Principle (Equation (2.6)) yields the strong form of the governing equations along the beam and its boundary conditions at both ends:

$$
\begin{aligned}
&\kappa AG \frac{\partial^2 w}{\partial x^2} - \kappa AG \frac{\partial \phi_x}{\partial x} - \rho A \frac{\partial^2 w}{\partial t^2} + p(x,t) = 0 \\
&\kappa AG \frac{\partial w}{\partial x} + EI \frac{\partial^2 \phi_x}{\partial x^2} - \kappa AG\,\phi_x - \rho I \frac{\partial^2 \phi_x}{\partial t^2} = 0 \\
&\text{with either} \quad w = 0 \quad \text{or} \quad \kappa AG \left(\frac{\partial w}{\partial x} - \phi_x\right) = 0 \\
&\text{and either} \quad \phi_x = 0 \quad \text{or} \quad EI \frac{\partial \phi_x}{\partial x} = 0
\end{aligned}
\tag{2.42}
$$

$w = 0$ and $\phi_x = 0$ represent the vanishing of displacement and rotation at the beam ends respectively and vanishing of $EI(\partial\phi_x/\partial x)$ or $\kappa AG\left(\frac{\partial w}{\partial x} - \phi_x\right)$ indicates the vanishing of bending moment or shear force at the ends. Boundary conditions for the beam are defined as shown in Table 2.3.

In three-dimensional beam theories, both out-of-plane and in-plane warpings are considered. For beams with isotropic materials and solid cross sections, Timoshenko shear deformable beam theory are practically equivalent to three-dimensional beam theories [157].

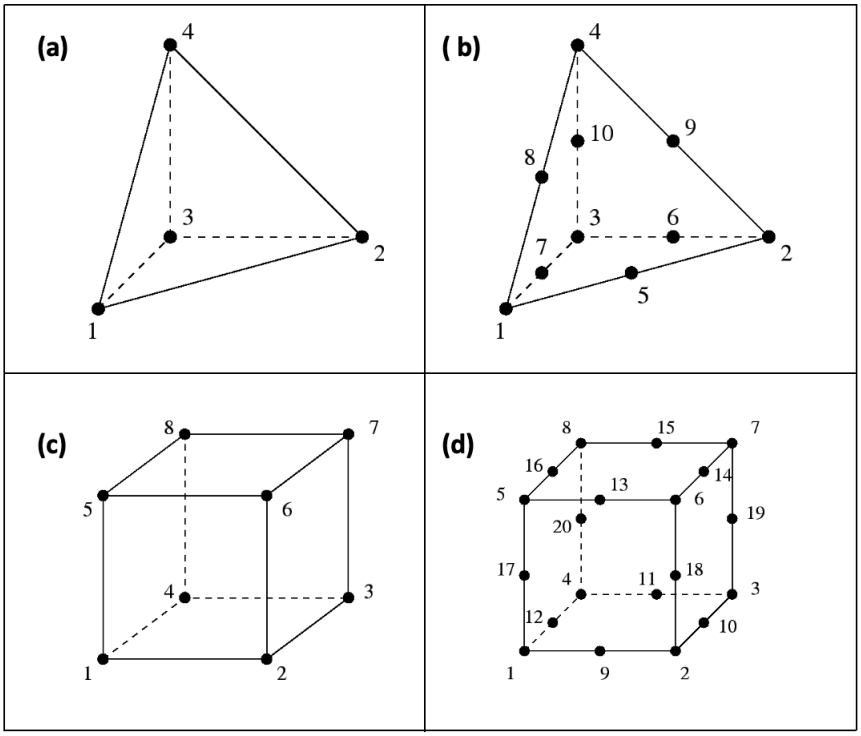


Fig. 2.5 *3D solid element types: (a) 4-node tetrahedron element, (b) 10-node tetrahedron element, (c) 8-node hexahedron element, (d) 20-node hexahedron element*

Three-Dimensional Solid Elements One of the most common elements used in solid finite element structural analysis are the 3D solid elements, such as hexahedron and tetrahedron. These are widely used due to the simple representations of field variables using cartesian coordinates. A 3D solid element state can be fully described using the six stress components (3 normal and 3 shear stresses) with each node having three translational DOFs. Each movement of the node can be considered as a sum of translations along the x, y and z axis of the system. The element can thus deform in all three directions in space. In practice

these elements have material properties and boundary conditions assigned to element faces and node, therefore deforming the solid element when arbitrary loads are applied. However, unlike the 1D beam elements as introduced in the previous sections, 3D solid elements do not find application where there are applied moments to the structure.

Since the research is interested in the nonlinear dynamic behaviour of complex structure, 3D solid elements are used. Figure 2.5 shows the four 3D solid elements types used in this research, these are also the most commonly used element types in other research. The surface of the element can be straight or curved depends on the element type. The first-order 4-node tetrahedron element has the simplest form compared to the others. Although simulations with this element involve very straightforward algorithms, it is not suited for structural calculations. Unless a large number of elements in the mesh is used, the results generated are too stiff compared to reality, especially in bending [5]. A solid element with more nodes on it gives a better representation of the structure, hence a better approximation of the dynamic behaviour. However, this comes with a significant increase in demand for computer resources.

Finite Element Displacement Method

As shown in equations (2.36) and (2.42), in order to obtain the dynamic response of the structures, partial differential equations of motion with appropriate boundary conditions needs to be solved. The analytical solutions to the equations can be difficult to achieve in some situations. In this section, solving method for obtaining the approximation solutions to Hamilton's principle is introduced. The strategy involves using a finite element discretisation of continuum mechanics equations.

Rayleigh-Ritz Method

Rayleigh-Ritz method (or the Galerkin method) is one of the most widely used methods on solving boundary value problems. The Rayleigh-Ritz method approximates the solution with a series of assumed functions that satisfies kinematic boundary conditions. The approximate solutions to the equations of motion can be expressed in the finite expansion form shown in Equation (2.43):

$$\bar{\boldsymbol{u}}^n(\boldsymbol{x},t) = \sum_{i=1}^{n} N_i(\boldsymbol{x})\, u_i^n(t) \tag{2.43}$$

The continuous system with infinite number of degree-of-freedoms (DOFs) is reduced to a discrete system with n DOFs in the Rayleigh-Ritz method. The field variable $\bar{\boldsymbol{u}}$ and its derivatives are expressed as the sum of shape functions $N_i(\boldsymbol{x})$ multiplying their corresponding amplitudes u_i. $N_i(\boldsymbol{x})$ are the pre-described space-dependent functions that satisfying the

boundary conditions. Since the equations of motion involve the derivatives of $\bar{\boldsymbol{u}}$ with respect to physical coordinates $\boldsymbol{x}$, $N_i(\boldsymbol{x})$ should be continuous and linear independent. If the equations of motion involve the derivatives up to order p, function $N_i(\boldsymbol{x})$ should have derivatives up to order $(p-1)$ to satisfy the convergence criteria. The amplitudes $u_i(t)$ are the unknown functions of time, t, which can be found by substituting the approximate solution (Equation (2.43)) into the equations of motion.

Since the system is discrete, Euler-Lagrange's equation of motion (Equation (2.7)) can be used instead of Hamilton's principle, yields the matrix form of:

$$[\mathbf{M}]\{\ddot{\boldsymbol{u}}^n\} + [\mathbf{C}]\{\dot{\boldsymbol{u}}^n\} + [\mathbf{K}]\{\boldsymbol{u}^n\} = \{\boldsymbol{F}\} \tag{2.44}$$

with $\{\boldsymbol{u}^n\} = \{u_1^n \quad u_2^n \quad \cdots \quad u_n^n\}^\mathsf{T}$.

Finite Element Discretisation

Finite element displacement method can be used to construct the pre-described functions $N_i(\boldsymbol{x})$ in Rayleigh-Ritz method. The structure is assigned with a set of node points associated with given number of DOFs (i.e. displacements, slope, etc.). The region between each pair of the adjacent nodes is referred to as an element. During the finite element analysis, the energy expression of each element is evaluated first and then add the contribution from the elements together. The pre-described functions over an element are called shape functions. A set of shape functions are constructed. Each shape function needs to be continuous along the element and has a unit value for one DOF of the element and zero value for all the other DOFs. As mentioned, all the element shape functions need to satisfy the geometric boundary conditions and have continuous derivatives up to order $(p-1)$. In the Rayleigh-Ritz method (Equation (2.43)), convergence is obtained as the number of the pre-described functions $N_i(\boldsymbol{x})$ increased. Rate of convergence can be increased by increasing the number of elements, hence the nodes and shape functions.

The methodology used for derivation of the mass and stiffness matrix for the 1D Euler-Bernoulli beam element will be presented next. The matrices can then be substituted into Equation (2.44) to obtain the matrix form of the equation of motion.

§ *Example of finite element discretisation with Euler-Bernoulli beam element:*

For each Euler-Bernoulli beam element, two DOFs are assigned to each node, i.e. the displacement and the slope. In total there are four (2×2) DOFs, therefore four shape functions are required. C^1-smoothness Hermitian shape functions are used as second order

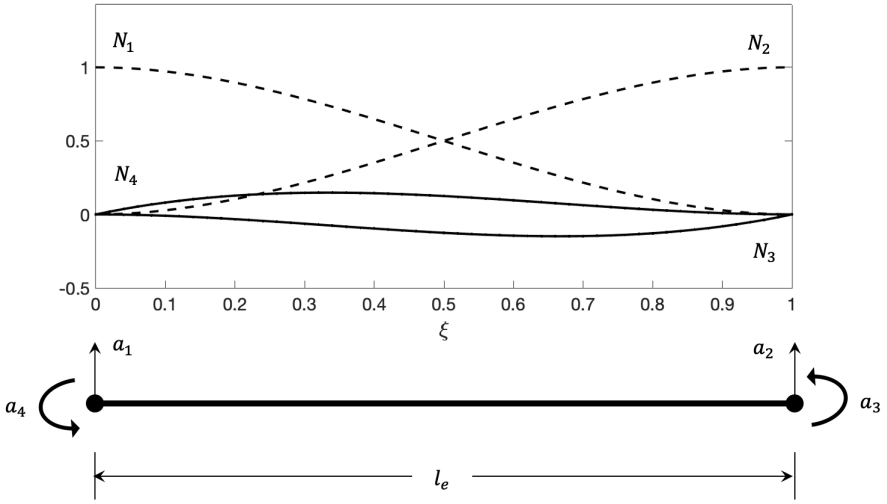


Fig. 2.6 *Shape function and geometry of a single Euler-Bernoulli beam element*

derivatives are involved in the energy expressions (Equations (2.35)). Figure 2.6 shows the plots of the geometry and the shape functions of an Euler-Bernoulli beam element of length l_e. Rayleigh-Ritz method gives that the estimated solution $w(x,t)$ of each element to the equations of motion of the Euler-Bernoulli beam (Equation(2.39)) can be expressed as:

$$\boldsymbol{w}(x,t) = \sum_{i=1}^{4} N_i(x)\, a_{e,i}(t) = \mathbf{N}(x)\, \mathbf{a}_e(t) \tag{2.45}$$

where $\mathbf{N}(x) = [N_1\, N_2\, N_3\, N_4]$ is the vector of shape functions and $\mathbf{a}_e(t) = [a_1\, a_2\, a_3\, a_4]^\mathsf{T}$ is the column vector of nodal parameters in terms of time t. For simplicity, non-dimensional parameter $\xi = \dfrac{x - x_e}{l_e}$ is often used for element shape function N_i instead of x.

$$\begin{aligned} N_1(\xi) &= 2\xi^3 - 3\xi^2 + 1 \\ N_2(\xi) &= \xi^3 - 2\xi^2 + \xi \\ N_3(\xi) &= -2\xi^3 + 3\xi^2 \\ N_4(\xi) &= \xi^3 - \xi^2 \end{aligned} \tag{2.46}$$

Substitute the estimated solution (Equation (2.45)) into the energy expressions of the beam element (Equation (2.35)) yields:

$$\begin{aligned} T &= \frac{1}{2}\int_{l_e} \rho A \left(\mathbf{N}(x)\,\dot{\mathbf{a}}_e(t)\right)^2 \mathrm{d}x \\ &= \frac{1}{2}\{\dot{\mathbf{a}}_e\}^{\mathsf{T}} \cdot \int_{l_e} \mathbf{N}^{\mathsf{T}}(x)\,\rho A\,\mathbf{N}(x)\,\mathrm{d}x \cdot \{\dot{\mathbf{a}}_e\} \\ &= \frac{1}{2}\{\dot{\mathbf{a}}_e\}^{\mathsf{T}} \cdot \int_0^1 \mathbf{N}^{\mathsf{T}}(\xi)\,\rho A\,\mathbf{N}(\xi)\,\frac{\mathrm{d}x}{\mathrm{d}\xi}\,\mathrm{d}\xi \cdot \{\dot{\mathbf{a}}_e\} \end{aligned} \tag{2.47}$$

$$\begin{aligned} U &= \frac{1}{2}\int_{l_e} EI \left(\frac{\partial^2 \mathbf{N}(x)}{\partial x^2}\mathbf{a}_e(t)\right)^2 \mathrm{d}x \\ &= \frac{1}{2}\{\mathbf{a}_e\}^{\mathsf{T}} \cdot \int_{l_e} \left(\frac{\partial^2 \mathbf{N}(x)}{\partial x^2}\right)^{\mathsf{T}} EI \left(\frac{\partial^2 \mathbf{N}(x)}{\partial x^2}\right) \mathrm{d}x \cdot \{\mathbf{a}_e\} \\ &= \frac{1}{2}\{\mathbf{a}_e\}^{\mathsf{T}} \cdot \int_0^1 \left(\frac{\partial^2 \mathbf{N}(\xi)}{\partial x^2}\right)^{\mathsf{T}} EI \left(\frac{\partial^2 \mathbf{N}(\xi)}{\partial x^2}\right) \frac{\mathrm{d}x}{\mathrm{d}\xi}\,\mathrm{d}\xi \cdot \{\mathbf{a}_e\} \end{aligned} \tag{2.48}$$

Comparing Equation (2.47) and Equation (2.48) with Equation (2.8) yields the mass $[\mathbf{M}_e]$ and stiffness $[\mathbf{K}_e]$ matrix of the Euler-Bernoulli beam element. In the finite element analysis, both matrices are symmetric. Both the stiffness and mass matrices of each element need to be transferred back into the global domain of the structure to assemble the global matrices shown in Equation (2.44). The global displacement vector $\boldsymbol{u}$ can then be solved.

$$[\mathbf{M}_e] = \int_0^1 \mathbf{N}^{\mathsf{T}}(\xi)\,\rho A\,\mathbf{N}(\xi)\,l_e\,\mathrm{d}\xi \tag{2.49}$$

$$\begin{aligned} [\mathbf{K}_e] &= \int_0^1 \left(\frac{\partial^2 \mathbf{N}(\xi)}{\partial x^2}\right)^{\mathsf{T}} EI \left(\frac{\partial^2 \mathbf{N}(\xi)}{\partial x^2}\right) l_e\,\mathrm{d}\xi \\ &= \int_0^1 \frac{1}{{l_e}^3} \left(\frac{\partial^2 \mathbf{N}(\xi)}{\partial \xi^2}\right)^{\mathsf{T}} EI \left(\frac{\partial^2 \mathbf{N}(\xi)}{\partial \xi^2}\right) \mathrm{d}\xi \end{aligned} \tag{2.50}$$

Numerical Integration

As seen in the equations for mass and stiffness matrix, the matrix components are calculated from the integration of the expressions. The exact integrations can be tedious and impossible sometimes, therefore some numerical integration techniques can be used to calculate the numerical value of a definite integral, i.e. the Newton–Cotes formulas, which approximates the integral of a function by constructing interpolation functions with polynomials evaluated at equally spaced points within the domain, the Clenshaw–Curtis quadrature and the Gauss–Legendre quadrature (Equation (2.51)), which have unequal intervals between inter-

polation points x_i. In one dimensional case, a n-point Gauss–Legendre quadrature provides exact integral results for polynomials of degree $(2n-1)$ or less and in general is more accurate than Newton–Cotes formulas with the same number of interpolation points.

$$\int_{-1}^{+1} f(x)\,\mathrm{d}x = \sum_{i=1}^{n} w_i f(x_i) \tag{2.51}$$

For the Gauss–Legendre quadrature, integral with interval of $[a,b]$ needs to map to interval $[-1,+1]$. interpolation point x_i is the i-th root of the Legendre polynomials P_n and the weights w_i of the function $f(x_i)$ is defined as [1]:

$$w_i = \frac{2}{\left(1-x_i^2\right)\left[P_n'(x_i)\right]^2} \tag{2.52}$$

For the three-dimensional elements used in this research, integration needs to be applied over the volume. The elements in physical coordinates $\bar{\boldsymbol{X}} = (x,y,z)$ need to be mapped into a reference element (Appendix A) in coordinate $\bar{\boldsymbol{\xi}} = (\xi,\eta,\zeta)$. The integration is done on the reference element, and then transformed back into the physical element by a Jacobian matrix $[\mathrm{Jac}] = \frac{\partial \bar{\boldsymbol{X}}}{\partial \bar{\boldsymbol{\xi}}}$. The numerical integration of an arbitrary function $\mathbf{G}$, over the hexahedron element is given by:

$$\begin{aligned} \boldsymbol{I}_{Hex} &= \int \mathbf{G}(x,y,z)\,\mathrm{d}V \\ &= \int_{-1}^{+1}\int_{-1}^{+1}\int_{-1}^{+1} \mathbf{G}(\xi,\eta,\zeta)\,|\mathrm{Jac}(\xi_i,\eta_i,\zeta_i)|\,\mathrm{d}\xi\,\mathrm{d}\eta\,\mathrm{d}\zeta \end{aligned} \tag{2.53}$$

Since the product $\mathbf{G}$ and the determinant of $[\mathrm{Jac}]$ does not yield a polynomial in general. Thus, the Gauss–Legendre quadrature rule can be applied to approximate the triple integral $\boldsymbol{I}_{Hex}$ as:

$$\boldsymbol{I}_{Hex} = \sum_{i=1}^{n} \mathbf{G}(\xi_i,\eta_i,\zeta_i)\,|\mathrm{Jac}(\xi,\eta,\zeta)| \cdot w_i \tag{2.54}$$

(ξ_i,η_i,ζ_i) is the coordinate of the i-th Gaussian point and w_i is the corresponding weight. For the reference tetrahedron element with node coordinates of $(0,0,0)$, $(1,0,0)$, $(0,1,0)$ and $(0,0,1)$ in the reference coordinates. The numerical integration of $\mathbf{G}$ over the tetrahedron element is given by:

$$\boldsymbol{I}_{Tet} = \int_0^1 \int_0^{1-\eta} \int_0^{1-\xi-\eta} \mathbf{G}(\xi,\eta,\zeta)\,|\mathrm{Jac}(\xi,\eta,\zeta)|\mathrm{d}\xi\,\mathrm{d}\eta\,\mathrm{d}\zeta \tag{2.55}$$

The integral $\boldsymbol{I}_{Tet}$ can be transformed into an integral over the cube. Gaussian formulation can then be applied [115]. Many other methods have also been developed for computing the quadrature rules on tetrahedron element. Readers are referred to read [169], [164], [62] and [175] for further information. Details of the Gaussian quadrature points and the weights for the 3D elements used in this research can be found in Appendix B.

2.2.4 Damping

The equations of motion of free vibration of a viscously damped system can be expressed by:

$$[\mathbf{M}]\{\ddot{\boldsymbol{u}}\} + [\mathbf{C}]\{\dot{\boldsymbol{u}}\} + [\mathbf{K}]\{\boldsymbol{u}\} = 0 \tag{2.56}$$

In vibration problems, periodicity conditions for the displacement vectors in time are assumed, i.e. $\boldsymbol{u}(0) = \boldsymbol{u}(T) \wedge \dot{\boldsymbol{u}}(0) = \dot{\boldsymbol{u}}(T)$, one can make the ansatz $\boldsymbol{u}(t) = \boldsymbol{\phi}_k e^{i\omega_k t}$, $(k = 1, \ldots, N)$. The equation of free vibration of undamped structure yields the eigenvalue problem:

$$\boldsymbol{\Lambda}\mathbf{M}\boldsymbol{\Phi} = \mathbf{K}\boldsymbol{\Phi} \tag{2.57}$$

where $\boldsymbol{\Lambda} = \mathrm{diag}(\omega_1^2, \omega_2^2, \ldots, \omega_N^2)$ represents the collection of natural frequencies and the modal matrix $\boldsymbol{\Phi} = (\boldsymbol{\phi}_1, \boldsymbol{\phi}_2, \ldots, \boldsymbol{\phi}_N)$ is a collection of all the mode shape column vectors of the system. Eigenvectors corresponding to distinct eigenvalues of a symmetric matrix are mutually orthogonal to each other. The eigenvectors are normalised as:

$$\boldsymbol{\Phi}^{\mathsf{T}}\mathbf{M}\boldsymbol{\Phi} = \mathbf{I} \quad \textit{and} \quad \boldsymbol{\Phi}^{\mathsf{T}}\mathbf{K}\boldsymbol{\Phi} = \boldsymbol{\Lambda} \tag{2.58}$$

The motion of the linear system can be computed by superposing the normal modes $\boldsymbol{\phi}_k$. Damping in the vibrating structures can arise from diverse phenomena, i.e. internal friction forces, material viscoelasticity, inelastic material behaviour etc. In spite of a large amount of research, the understanding of damping forces in vibrating structures is not well developed due to the unclear physics behind the damping forces. Hence the damping matrix of the structural expressed in terms of $[\mathbf{M}]$ and $[\mathbf{K}]$ can be assumed to ensure that the system will still possess the classical normal modes $\boldsymbol{\Phi}$, i.e. Rayleigh damping matrix (Rayleigh, 1954) or Caughey damping matrix (Caughey and O'Kelly, 1965) [24]. Rayleigh damping or proportional damping (Equation (2.59)) is a special case of Caughey series (Equation (2.61)).

$$[\mathbf{C}] = \alpha[\mathbf{M}] + \beta[\mathbf{K}] \tag{2.59}$$

In Rayleigh damping matrix the system damping can be tuned by the two damping coefficients α and β, which depend on the damping ratio ζ. The damping ratio ζ_n for the n-th mode of the system at frequency ω_n is:

$$\zeta_n = \frac{1}{2}\left(\frac{\alpha}{\omega_n} + \beta\,\omega_n\right) \tag{2.60}$$

Equation (2.60) indicates that the Rayleigh damping generates higher damping ratios in the lower and higher frequency range, which is far from reality and not satisfactory if a broad frequency range needs to be analysed. If modal damping ratios are known for many modes from the experiments, $[\mathbf{C}]$ can be constructed as:

$$[\mathbf{C}] = [\mathbf{M}] \sum_{j=0}^{j=N-1} \left(\alpha_j \, [\mathbf{M}]^{-1} [\mathbf{K}]\right)^j \tag{2.61}$$

The damping coefficients α_j are linearly related to the damping ratios. The Caughey series is possibly the most general form of damping matrix under which the system will still possess classical normal modes. The numerical cost for this method to gain the explicit expression is prohibitive even for moderately large system.

2.3 Numerical methods for nonlinear dynamics

The equations of motion of dynamical systems are mathematically represented by a system of ordinary differential equations, as shown in the previous section. Engine blades aeroelastic stability and response problems are frequently governed by nonlinear differential equations with periodic coefficients. Nonlinear systems are those for which the principle of superposition does not hold. They are known to exhibit rich and complex dynamical behaviours, i.e. system multiple solutions, jumps, natural frequency shifts, coupling of modes, internal resonance, quasiperiodic oscillations, detached resonance curves, bifurcations and chaos [34]. Hence, nonlinear modelling and analysis is important in the design and optimization of modern structural systems. Consider the nonautonomous nonlinear dynamical systems with n DOFs governed by the equations of motion:

$$[\mathbf{M}]\{\ddot{\boldsymbol{u}}\} + [\mathbf{C}]\{\dot{\boldsymbol{u}}\} + [\mathbf{K}]\{\boldsymbol{u}\} + \{\boldsymbol{F}_{nl}\} = \{\boldsymbol{F}_{ext}\} \tag{2.62}$$

where $\mathbf{M}$, $\mathbf{C}$ and $\mathbf{K}$ are the mass, damping and stiffness matrices respectively, as mentioned in Section 2.2.1. Vectors $\boldsymbol{u}$, $\boldsymbol{F}_{nl}$ and $\boldsymbol{F}_{ext}$ represent the displacements, the nonlinear forces and the periodic external forces with frequency ω. The dots refer to the derivatives with

respect to time t. $\boldsymbol{F}_{nl}$ in general is a function of $\boldsymbol{u}$ and/or $\dot{\boldsymbol{u}}$.

The nonlinear ODE (Equation (2.62)) involved in the dynamic systems can be solved by using different algorithms and numerical methods (Section 2.3.2). Most of them build on a continuation procedure (Section 2.3.3). Non-dimensionalization and scaling of the dynamics systems are vital when running the dynamic analysis, especially when the parameters of interest come with significantly different amplitudes. The algorithms used are delivered in Section 3.4.1.

2.3.1 Continuous-time systems

A dynamic system is one whose state changes with time t. The evolution of the continuous-time system is governed by either an autonomous (Equation (2.63)) or a nonautonomous (Equation (2.64)) system of differential equations:

$$\dot{\mathbf{x}} = \mathbf{F}(\mathbf{x}; \mathbb{M}) \tag{2.63}$$

$$\dot{\mathbf{x}} = \mathbf{F}(\mathbf{x}, t; \mathbb{M}) \tag{2.64}$$

where $\mathbf{x}$ is a $2n$-dimensional vector describes the state of the system, $\mathbb{M}$ is a vector of control parameters and $\mathbf{F}$ is often referred to as a vector field, which describes the evolution of the system in the state space over the time interval. A solution to the dynamical system can be either constant or time varying. In the case of the dynamic behaviour analysis of the structures, only the steady state dynamic solutions i.e. periodic solutions, quasiperiodic solutions, chaos etc. are interested [96]. In the present research, only the steady-state periodic response of the system for periodic forcing is studied.

2.3.2 Dynamic analysis method

Brute-force approach [96] is the simplest numerical method to construct the periodic solution to the continuous-time system (Equation (2.63) and (2.64)), which involves the direct integration of the ODEs, Equation (2.66), from the initial condition until converge to an attractor, i.e. steady state condition. The convergence rate can be very slow for lightly damped system and some unstable solutions might be missing. Direct approaches in the time domain and frequency domain formulation are proposed to overcome these shortages. In this section, the approximation methods for the study of nonlinear nonautonomous systems described by

ODEs are presented.

$$\mathbf{x} = \begin{Bmatrix} \boldsymbol{u} \\ \dot{\boldsymbol{u}} \end{Bmatrix} \tag{2.65}$$

$$\dot{\mathbf{x}} = \begin{bmatrix} 0 & \mathbf{I} \\ -\mathbf{M}^{-1}\mathbf{K} & -\mathbf{M}^{-1}\mathbf{C} \end{bmatrix} \mathbf{x} - \mathbf{M}^{-1} \begin{Bmatrix} 0 \\ \boldsymbol{F}_{ext} - \boldsymbol{F}_{nl} \end{Bmatrix} \tag{2.66}$$

Time domain methods for predicting the nonlinear behaviour of systems i.e. shooting method [66], finite-difference schemes [103], Poincaré map method [31], orthogonal collocation [120], perturbation method [71] etc. provide an accurate solution in time history but requires large computational time, especially when applying to large systems with many DOFs. Therefore they are not good for parametric studies, but are rather effective for searching the response to particular excitations and with particular initial conditions. Shooting method can be used to solve boundary value problems, which requires numerous time integrations that can slow down the algorithm and is prone to ill conditioning. Finite-difference scheme is less sensitive to the initial conditions when compared to the shooting method, hence more suitable to determine highly unstable periodic solutions. Orthogonal collocation are sometimes used for bifurcation detection and tracking and have the ability to address stiffness problems. However it requires considerable memory space for the discretisation of the boundary value problems [64]. Perturbation method (Equation (2.67)), such as multiple scales and averaging, is applicable for only weakly nonlinear systems as it is based on a small parameter ε:

$$\mathbf{x} = \mathbf{x}_0 + \varepsilon\mathbf{x}_1 + \varepsilon^2\mathbf{x}_2 + \cdots \tag{2.67}$$

where, $\mathbf{x}_0$ represents the known solution to the exactly solvable initial problem and $\mathbf{x}_1$, $\mathbf{x}_2$, ... represent the higher-order terms which may be found iteratively by some systematic procedure. For small ε these higher-order terms in the series become successively smaller. The implementation of this method on a computer is difficult, especially when higher order solutions are needed.

Harmonic balance method (HBM) are the most popular frequency domain method used for calculating the periodic steady-state response. It provides a simpler and more systematic approach for steady-state analysis, which can deal with highly nonlinear systems with no ill or instability in the algorithm. Low orders of approximation would be sufficient to provide an accurate approximation for smooth nonlinearities [34]. Errors involved in this method are

introduced by the truncation of the Fourier series. HBM is often coupled with continuation schemes for parametric studies.

Harmonic Balance Method

Harmonic balance method (HBM) or multi-harmonic balance is the most widely used method for analysing the periodic solutions of nonlinear dynamic systems in frequency domain. It was first introduced by Krylov and Bogoliubov [77] while Urabe introduced the method for Fourier approximations truncated to several harmonics into the harmonic balance in 1960s [152] also employed in other studies [35].

Approximate the external periodic force $\boldsymbol{F}_{ext}$ and in Equation (2.62) with frequency ω by Fourier series truncated to the N_H-th harmonic.

$$\boldsymbol{F}_{ext}(\omega,t) = \frac{\mathbf{c}_0^f}{2} + \sum_{k=1}^{N_H} \left(\mathbf{s}_k^f \sin(k\omega t) + \mathbf{c}_k^f \cos(k\omega t) \right) \tag{2.68}$$

We expect the response $\boldsymbol{u}(t)$ to periodic excitation to be ω-periodic as well and it can be expressed as a truncated Fourier series to the N_H-th harmonic.

$$\boldsymbol{u}(t) = \frac{\mathbf{c}_0^x}{2} + \sum_{k=1}^{N_H} \left(\mathbf{s}_k^x \sin(k\omega t) + \mathbf{c}_k^x \cos(k\omega t) \right) \tag{2.69}$$

$$\dot{\boldsymbol{u}}(t) = \sum_{k=1}^{N_H} \left(-k\omega\, \mathbf{s}_k^x \sin(k\omega t) + k\omega\, \mathbf{c}_k^x \cos(k\omega t) \right) \tag{2.70}$$

$$\ddot{\boldsymbol{u}}(t) = \sum_{k=1}^{N_H} \left(-k^2\omega^2\, \mathbf{s}_k^x \cos(k\omega t) - k^2\omega^2\, \mathbf{c}_k^x \sin(k\omega t) \right) \tag{2.71}$$

The n-dimensional vector $\mathbf{s}_k$ and $\mathbf{c}_k$ are the Fourier coefficients related to the sine and cosine terms of each DOF respectively. Substitute Equation (2.68) to (2.71) into Equation (2.62), the equation of motion in time domain can be transformed into the frequency domain with the application of Galerkin projection methods.

$$\mathbf{R}(\omega, \tilde{\mathbf{q}}) \equiv \mathbf{Z}(\omega)\tilde{\mathbf{q}} + \tilde{\mathbf{b}}(\tilde{\mathbf{q}}) = 0 \tag{2.72}$$

Where $\tilde{\mathbf{b}}(\tilde{\mathbf{q}}) = \tilde{\mathbf{b}}_{nl}(\tilde{\mathbf{q}}) - \tilde{\mathbf{b}}_{ext}$, and $\mathbf{Z}$ is the $(2N_H+1)n \times (2N_H+1)n$ matrix describing the linear dynamics part of the system.

$$\mathbf{Z}(\omega) = \begin{bmatrix} \mathbf{K} & & & & \\ & \mathbf{K}-\omega^2\mathbf{M} & \omega\mathbf{C} & & \\ & -\omega\mathbf{C} & \mathbf{K}-\omega^2\mathbf{M} & & \\ & & & \ddots & \\ & & & \mathbf{K}-(\omega N_H)^2\mathbf{M} & \omega N_H\mathbf{C} \\ & & & -\omega N_H\mathbf{C} & \mathbf{K}-(\omega N_H)^2\mathbf{M} \end{bmatrix} \tag{2.73}$$

Fourier coefficients of $\boldsymbol{u}(t)$ and $\boldsymbol{F}_{ext}(\omega,t)$ are gathered into the $(2N_H+1)n$-dimensional vectors $\mathbf{z}$ and $\mathbf{b}_{ext}$.

$$\tilde{\mathbf{q}} = \begin{bmatrix} (\mathbf{c}_0^x)^\intercal & (\mathbf{c}_1^x)^\intercal & (\mathbf{s}_1^x)^\intercal & \cdots & (\mathbf{c}_{N_H}^x)^\intercal & (\mathbf{s}_{N_H}^x)^\intercal \end{bmatrix} \tag{2.74}$$

$$\tilde{\mathbf{b}}_{ext} = \begin{bmatrix} (\mathbf{c}_0^f)^\intercal & (\mathbf{c}_1^f)^\intercal & (\mathbf{s}_1^f)^\intercal & \cdots & (\mathbf{c}_{N_H}^f)^\intercal & (\mathbf{s}_{N_H}^f)^\intercal \end{bmatrix} \tag{2.75}$$

HBM has also been coupled with alternating Fourier transformation (AFT) by Cameron in 1989 [19] which considerably improved the HBM method. The AFT methodology computes the nonlinear term in time domain $\boldsymbol{F}_{nl}(\boldsymbol{u},\dot{\boldsymbol{u}})$ and then transfers it to the frequency domain $\tilde{\mathbf{b}}_{nl}(\tilde{\mathbf{q}})$ by Fourier transform. This method provides better approximation than the analytical description of nonlinear term in frequency domain.

$$\tilde{\mathbf{q}} \xrightarrow{\text{FFT}^{-1}} \boldsymbol{u}(t) \longrightarrow \boldsymbol{F}_{nl}(\boldsymbol{u},\dot{\boldsymbol{u}}) \xrightarrow{\text{FFT}} \tilde{\mathbf{b}}_{nl}(\tilde{\mathbf{q}}) \longrightarrow \tilde{\mathbf{b}}(\tilde{\mathbf{q}}) \tag{2.76}$$

Equation (2.72) can be solved iteratively by using Newton-Raphson procedure. This method is popular in numerical analysis to find the roots of nonlinear equations. At each iteration, an evaluation of $\tilde{\mathbf{b}}_{ext}$ and of the Jacobian matrix of the system $\frac{\partial \mathbf{R}}{\partial \tilde{\mathbf{q}}}$ have to be provided. The Jacobian matrix of the system computed through finite differences is computationally demanding, and as such it is generally attempted to avoid it.

Finite-difference Method

The time-domain approaches are trying to construct a periodic solution $\mathbf{x}(t;\boldsymbol{\eta})$ with a minimal period T for the autonomous and nonautonomous systems with initial condition $\mathbf{x}(0) = \boldsymbol{\eta}$. The time span to converge steady-state solution is reduced by enforcing periodic condition.

$$\mathbf{x}(T,\boldsymbol{\eta}) = \boldsymbol{\eta} \tag{2.77}$$

For convenience, change independent variable t to non-dimensional independent variable $\tau = \dfrac{t}{T}$, so that Equation (2.64) and (2.77) become:

$$\frac{\mathrm{d}\mathbf{x}}{\mathrm{d}\tau} = T\boldsymbol{F}(\mathbf{x}, T\tau; \mathbb{M}) \tag{2.78}$$

$$\mathbf{x}(1; \boldsymbol{\eta}, T) = \boldsymbol{\eta} \tag{2.79}$$

where $\mathbf{x}(\tau; \boldsymbol{\eta}, T)$ has the period unity. A set of uniform time steps is set for the finite-difference method, i.e. $(\tau_0 = 0,\ \tau_1 = h,\ \tau_2 = 2h,\ \ldots,\ \tau_N = Nh = 1)$. Hence apply the trapezoidal rule to Equation (2.78):

$$\mathbf{x}^{i+1} - \mathbf{x}^i = \frac{1}{2}hT\left[\boldsymbol{F}(\mathbf{x}^{i+1}, T\tau_{i+1}; \mathbb{M}) + \boldsymbol{F}(\mathbf{x}^i, T\tau_i; \mathbb{M})\right] \tag{2.80}$$

The periodic condition takes the form $\mathbf{x}^0 = \mathbf{x}^N$. Hence for the n-dimensional nonlinear system, Newton-Raphson scheme can be used for solving the nN equations (Equation (2.80)) to obtain the nN unknows i.e. $(\mathbf{x}^0,\ \mathbf{x}^1,\ \mathbf{x}^2,\ \ldots,\ \mathbf{x}^{N-1})$.

Shooting Method

Equation (2.64) and (2.77) represent the two-point boundary-value problem. The initial guess $(T, \boldsymbol{\eta}_0)$ for the periodic solution $(T, \boldsymbol{\eta})$ is established first, Newton-Raphson scheme can then be used to correct the initial guess as. The offset between the initial guess and the solution can be expressed as follows:

$$\delta\boldsymbol{\eta} = \boldsymbol{\eta} - \boldsymbol{\eta}_0 \tag{2.81}$$

Substitute into Equation (2.77),

$$\mathbf{x}(T, \boldsymbol{\eta}_0 + \delta\boldsymbol{\eta}) - (\boldsymbol{\eta}_0 + \delta\boldsymbol{\eta}) \simeq 0 \tag{2.82}$$

Expand in a Taylor series and retain only the linear terms in $\delta\boldsymbol{\eta}$ yields n algebraic equations to be solved for n unknown $\delta\boldsymbol{\eta}$:

$$\left[\frac{\partial\mathbf{x}}{\partial\boldsymbol{\eta}} - \mathbf{I}\right]\delta\boldsymbol{\eta} = \boldsymbol{\eta}_0 - \mathbf{x}(T, \boldsymbol{\eta}_0) \tag{2.83}$$

with δ represents a small parameter, the matrix $\frac{\partial\mathbf{x}}{\partial\boldsymbol{\eta}}$ can be evaluated at $\boldsymbol{\eta}_0$ as:

$$\left.\frac{\partial\mathbf{x}}{\partial\boldsymbol{\eta}}\right|_{\boldsymbol{\eta}=\boldsymbol{\eta}_0} = \frac{\mathbf{x}(T, \boldsymbol{\eta}_0 + \delta) - \mathbf{x}(T, \boldsymbol{\eta}_0)}{\delta} \tag{2.84}$$

Poincaré Map Method

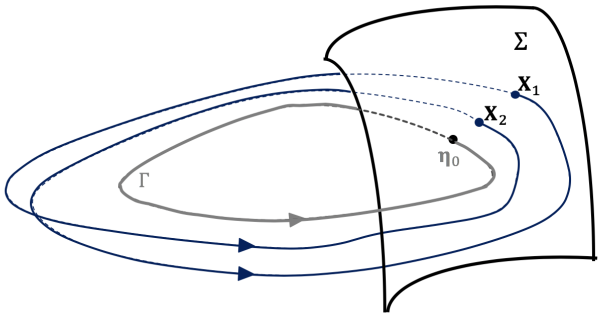


Fig. 2.7 *Poincaré section of periodic orbits*

As illustrated in Figure 2.7, Poincaré section Σ is a $(n-1)$-dimensional hypersurface in the state space that is transverse to the trajectory of the system of equations. Let the successive intersections of a trajectory with Σ be $\{\mathbf{X}_1, \mathbf{X}_2, \mathbf{X}_3, \cdots\}$. Poincaré map $\mathbf{P}$ maps the current intersection $\mathbf{X}_m$ to the subsequent intersection $\mathbf{X}_{m+1}$.

$$\mathbf{X}_{m+1} = \mathbf{P}(\mathbf{X}_m) \tag{2.85}$$

Consider a periodic solution $\mathbf{x}$ to the dynamic system with period T. The solution trajectory Γ initiated at $t = t_0$ from point $\boldsymbol{\eta}_0$ is represented as $\mathbf{x}(\boldsymbol{\eta}_0, t, t_0)$. The Poincaré map for the period orbit can be expressed as:

$$\mathbf{P}(\boldsymbol{\eta}) = \mathbf{x}(\boldsymbol{\eta}, t_0 + T, t_0) \tag{2.86}$$

$\boldsymbol{\eta}$ represents a point on the Poincaré section. Hence the periodic solution corresponds to a fixed point on an appropriately constructed one-sided Poincaré section. In autonomous systems (Equation (2.63)), the period T is not explicitly known in general. Different methods need to be used on constructing the Poincaré section Σ.

$$\mathbf{P}(\boldsymbol{\eta}_0) = \boldsymbol{\eta}_0 \tag{2.87}$$

For nonautonomous systems, the Poincaré map method is the same as the shooting method described above.

2.3.3 Continuation

Studying the evolution of periodic solutions $\mathbf{x}$ with respect to the frequency ω of the harmonic forcing $\boldsymbol{F}_{ext}$ or other control parameter α can be very useful. Continuation scheme provides algorithmic procedures to generate a continuum of periodic solution $\mathbf{x}(T;\alpha)$. Continuation algorithms are based on two main steps applied recursively for each point in the state-control space $(\mathbf{x},\alpha)$. A prediction point is guessed first based on the previous obtained points, then follows a correction step which provides the new point in the state-control space. The path following procedure in continuation scheme has long served as an useful theoretical tool to track the turning path of the solutions and find coexisting solutions for the same parameter value in many applications due to its versatility and robustness. In this chapter, different prediction and correction methods are introduced. Following notations as shown on Figure 2.8 are going to use:

- $\mathbf{y}^{(i)} = (\mathbf{x}^{(i)}, \alpha^{i})$: i-th converged point;
- $\mathbf{y}^{(i+1,0)} = (\mathbf{x}^{i+1,0}, \alpha^{(i+1,0)})$: prediction for $(i+1)$-th point;
- $\mathbf{y}^{(i+1,j)} = (\mathbf{x}^{(i+1,j)}, \alpha^{(i+1,j)}$: $(i+1)$-th point after j correction steps.

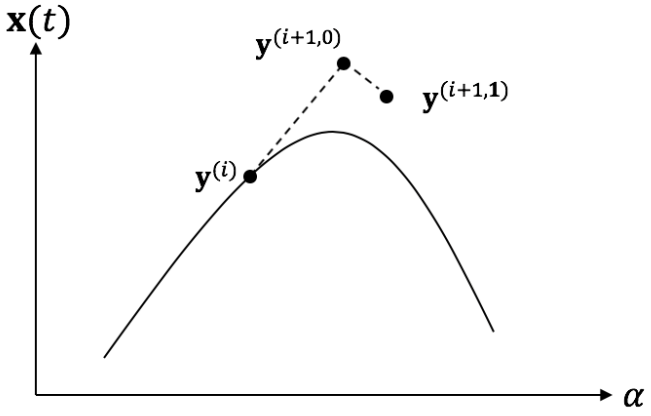


Fig. 2.8 *The prediction and correction step in the continuation scheme*

Prediction Methods

To predict a point in the state-space, a direction and a distance is needed. The step size $\Delta s^{(i+1)}$ is the distance between the converged points $\mathbf{y}^{(i)}$ and the predict point $(\mathbf{x}^{(i+1,0)}, \alpha^{(i+1,0)})$. The step size is determined and updated based on the converge rate during each continuation step.

$$\Delta s^{(i+1)} = \sqrt{(\mathbf{x}^{(i+1)} - \mathbf{x}^{(i)})^{\mathsf{T}}(\mathbf{x}^{(i+1)} - \mathbf{x}^{(i)}) + (\alpha^{(i+1)} - \alpha^{(i)})^2} \tag{2.88}$$

■ ***Secant Method:***

Two converged points in the previous step $(\mathbf{x}^{(i-1)}, \alpha^{i-1})$ and $(\mathbf{x}^{(i)}, \alpha^{(i)})$ are used to predict the point $(\mathbf{x}^{(i+1,0)}, \alpha^{(i+1,0)})$. This is a very cheap predictor but it does not suit paths with small curvature radii.

$$(\mathbf{x}^{(i+1,0)}, \alpha^{(i+1,0)}) = (\mathbf{x}^{(i)}, \alpha^{(i)}) + \Delta s^{i+1} \left((\mathbf{x}^{(i)}, \alpha^{(i)}) - (\mathbf{x}^{(i-1)}, \alpha^{i-1}) \right) \tag{2.89}$$

■ ***Tangent Method:***

Tangent predictor uses only one previous point $(\mathbf{x}^{(i)}, \alpha^{(i)})$ to predict $(\mathbf{x}^{(i+1,0)}, \alpha^{(i+1,0)})$ but requires the evaluation of the tangent vector, $\overrightarrow{t} = (\overrightarrow{t_{\mathbf{x}}}, t_\alpha)$, at $(\mathbf{x}^{(i)}, \alpha^{(i)})$ which can have a prohibitive cost.

$$\begin{cases} D_{\mathbf{x}}\mathbf{h}(\mathbf{x}^{(i)}, \alpha^{(i)})\overrightarrow{t_{\mathbf{x}}} + D_\alpha \mathbf{h}(\mathbf{x}^{(i)}, \alpha^{(i)}) t_\alpha = 0 \\ \overrightarrow{t_{\mathbf{x}}}^{\intercal}\, \overrightarrow{t_{\mathbf{x}}} + t_\alpha^2 = 1 \end{cases} \tag{2.90}$$

The tangent sign depends on the direction chosen to depict the curve. The prediction point is given as:

$$(\mathbf{x}^{(i+1,0)}, \alpha^{(i+1,0)}) = (\mathbf{x}^{(i)}, \alpha^{(i)}) + \Delta s^{i+1} (\overrightarrow{t_{\mathbf{x}}}, t_\alpha) \tag{2.91}$$

■ ***Lagrange Polynomials:***

Lagrange polynomial $\mathbf{P}$ of degree d together with $(d-1)$ previous points can also be used to predict the $(\mathbf{x}^{(i+1,0)}, \alpha^{(i+1,0)})$ point [63].

$$\mathbf{P}_d(s) = \sum_{k_0=0}^{d} \left(\prod_{\substack{k=0 \\ k \neq k_0}}^{d} \frac{(s - s^{(i-k)})}{s^{(i-k_0)} - s^{(i-k)}} \right) \mathbf{y}^{(i-k_0)} \tag{2.92}$$

$$\text{where,} \quad \begin{cases} s^{(i)} = 0 \\ s^{(i-k)} = s^{(i-k+1)} - \Delta s^{(i-k+1)} \end{cases}$$

Hence the predicted point can be obtained by substituting into the Lagrange polynomial $\mathbf{P}_d(s)$, i.e. $(\mathbf{x}^{(i+1,0)}, \alpha^{(i+1,0)}) = \mathbf{P}_d(s^{i+1}) = \mathbf{P}_d(\Delta s^{(i+1)})$.

Correction Methods

The correction step in continuation scheme is used to move the predicted point $(\mathbf{x}^{(i+1,0)}, \alpha^{(i+1,0)})$ towards to the converged point $\mathbf{y}^{(i+1)}$ which satisfies Equation (2.72).

$$(\mathbf{x}^{(i+1,j+1)}, \alpha^{(i+1,j+1)}) = (\mathbf{x}^{(i+1,j)} + \Delta\mathbf{x}, \alpha^{(i+1,j)} + \Delta\alpha) \tag{2.93}$$

$$\Rightarrow D_{\mathbf{x}}\mathbf{h}(\mathbf{x}^{(i+1,j)}, \alpha^{(i+1,j)})\Delta\mathbf{x} + D_{\alpha}\mathbf{h}(\mathbf{x}^{(i+1,j)}, \alpha^{(i+1,j)})\Delta\alpha = -\mathbf{h}(\mathbf{x}^{(i+1,j)}, \alpha^{(i+1,j)}) \tag{2.94}$$

Number of unknowns $(n(2N_H+1)+1)$ is greater than the number of equations $(n(2N_H+1))$ due to the $\Delta\alpha$. One more constrain needs to be added on top of Equation (2.94) to determine the correction point.

■ ***Constant Continuation Parameters:***

In this scheme, the scalar control parameter α is the continuation parameter, α is kept constant and equal to the predicted value. This algorithm fails to go pass the turning point in the state-control space.

$$\forall j \geq 1, \quad \alpha^{(i+1,j)} = \alpha^{(i+1,0)} \tag{2.95}$$

■ ***Arc Length Constraint:***

In this method, distance between the corrected points and the previous converged point is fixed. The arc-length method has the ability to pass turning points.

$$\forall j \geq 1, \quad \|\mathbf{x}^{(i+1,j+1)} - \mathbf{x}^{(i)}\|^2 + |\alpha^{(i+1,j+1)} - \alpha^{(i)}|^2 = (\Delta s^{(i+1)})^2 \tag{2.96}$$

■ ***Pseudo Arc Length Constraint:***

This method adds an orthogonality condition between the prediction vector $\mathbf{y}^{(I+1,0)-\mathbf{y}^{(i)}}$ and the corrected points.

$$\forall j \geq 1, \quad \Delta\mathbf{x}^{\intercal}(\mathbf{x}^{(i+1,0)} - \mathbf{x}^{(i)}) + \Delta\alpha^{\intercal}(\alpha^{(i+1,0)} - \alpha^{(i)}) = 0 \tag{2.97}$$

■ ***Moore-Penrose Pseudo-Inverse:***

Moore-Penrose pseudo-inverse matrix can be used to solve underconstrained systems $\underline{\underline{\mathbf{A}}}\mathbf{x} = \mathbf{b}$ where $\underline{\underline{\mathbf{A}}}$ has less rows than columns, i.e. Equation (2.94) [121]. Hence in this

case:

$$\underline{\underline{\mathbf{A}}} = \left[D_{\mathbf{x}}\mathbf{h}(\mathbf{x}^{(i+1,j)},\ \alpha^{(i+1,j)}), D_{\alpha}\mathbf{h}(\mathbf{x}^{(i+1,j)}, \alpha^{(i+1,j)})\right] \tag{2.98}$$

$$\underline{\mathbf{x}} = [\Delta\mathbf{x},\ \Delta\alpha]^{\mathsf{T}} \tag{2.99}$$

$$\underline{\mathbf{b}} = -\mathbf{h}(\mathbf{x}^{(i+1,j)}, \alpha^{(i+1,j)}) \tag{2.100}$$

The pseudo-inverse matrix $\underline{\underline{\mathbf{A}}}^{+}$ implicitly adds an orthogonality condition and is expressed as:

$$\underline{\underline{\mathbf{A}}}^{+} = \underline{\underline{\mathbf{A}}}^{\mathsf{T}}(\underline{\underline{\mathbf{A}\mathbf{A}}}^{\mathsf{T}})^{-1} \tag{2.101}$$

2.4 Stability

The local stability of dynamic system response is regarded as an important aspect of engineering interests. Concepts of stability of the solution $\mathbf{u}(t)$ to the continuous-time system (Equation (2.63) and (2.64)) can be defined as:

Lyapunov Stability: A solution is said to be Lyapunov stable if for any neighbouring solution $\mathbf{v}(t)$ at the initial time $t = t_0$, i.e. $\|\mathbf{u}-\mathbf{v}\| < \delta(\varepsilon)$, satisfies $\|\mathbf{u}-\mathbf{v}\| < \varepsilon$ for all $t > t_0$, where ε is a small positive number.

Asymptotic Stability: A solution is said to be asymptotically stable if it is Lyapunov stable and $\lim_{t\to\infty}\|\mathbf{u}-\mathbf{v}\| \to 0$.

Lagrange or Bounded Stability: A solution $\mathbf{u}(t)$ to the continuous-time system is said to be bounded stable if $\|\mathbf{u}\| \leq L$ for all t, where L is a finite positive number.

Poincaré Stability: A dynamic solution is said to satisfy Poincaré stability criteria if $\|\mathbf{u}(t = 0) - \mathbf{v}(t = \tau)\| < \delta(\varepsilon)$, and there exists $\|\mathbf{u}(t_1) - \mathbf{v}(t_2)\| < \varepsilon$. Poincaré stability exams the closeness of the two dynamic solution's trajectories or orbits in the state space.

Lyapunov stability and asymptotic stability criteria are typically used to study the stability of equilibrium solutions of Equation (2.63), i.e. $\dot{\mathbf{x}} = \boldsymbol{F}(\mathbf{x};\mathbb{M}) = 0$. For dynamic solutions, Poincaré stability is often used [96].

In this section, modal analysis for the nonlinear systems and different concepts of solution stability of the dynamic systems are discussed. Explicit schemes on how to determine the stability of dynamic solutions are explained. Different computational implementations for obtaining the stability of period solution of nonlinear problems are also compared.

2.4.1 Floquet theory

Floquet theory is a fundamental theory for most of stability analysis method. Consider the periodic solution set $\mathbf{X}(t)$, $\mathbf{x}_i$ are the n-linear independent solutions to the n-dimensional continuous-time system $\dot{\mathbf{x}} = \boldsymbol{F}(\mathbf{x};\mathbb{M})$ with least period T, then $\mathbf{X}(t+T)$ is also the solution to the system.

$$\mathbf{X}(t) = [\mathbf{x}_1(t)\ \mathbf{x}_2(t)\ \cdots\ \mathbf{x}_n(t)] \tag{2.102}$$

Let the periodic solution $\mathbf{X}(t)$ at $\mathbb{M} = \mathbb{M}_0$ be denoted by $\mathbf{X}_0(t)$. A small disturbance $\mathbf{y}(t)$ is superimposed on the periodic solution $\mathbf{X}_0(t)$, resulting in

$$\mathbf{x} = \mathbf{X}_0(t) + \mathbf{y}(t) \tag{2.103}$$

The stability of the periodic solution is determined by looking at the evolution of the perturbation. Substituting Equation (2.103) into Equation (2.63) yields:

$$\dot{\mathbf{X}}_0(t) + \dot{\mathbf{y}}(t) = \mathbf{F}(\mathbf{X}_0(t) + \mathbf{y}(t);\mathbb{M}_0) \tag{2.104}$$

Using Taylor's expansion at order 1 and considering the periodic solution $\dot{\mathbf{x}} = \dot{\mathbf{X}}_0 = 0$ yields:

$$\dot{\mathbf{y}}(t) = [D_{\mathbf{x}}\mathbf{F}(\mathbf{X}_0;\mathbb{M}_0)]\,\mathbf{y}(t) + \mathscr{O}(\|\mathbf{y}\|^2) \simeq \mathbf{A}(t;\mathbb{M}_0)\,\mathbf{y}(t) \tag{2.105}$$

where $[D_{\mathbf{x}}\mathbf{F}]$ is the Jacobian matrix $\frac{\partial \mathbf{F}}{\partial \mathbf{x}}$ evaluated along the periodic solution, hence $\mathbf{A}$ is periodic in time and has the same period T as $\mathbf{X}_0$. The stability analysis is local, as the disturbance $\mathbf{y}$ is linearised. Consider $\mathbf{Y}(t)$ as the fundamental matrix solution to Equation (2.105) with n-linear independent solutions y_i:

$$\mathbf{Y}(t) = [\mathbf{y}_1(t)\ \mathbf{y}_2(t)\ \cdots\ \mathbf{y}_n(t)] \tag{2.106}$$

Change t to $\tau = t + T$:

$$\frac{\mathrm{d}\mathbf{y}(\tau)}{\mathrm{d}\tau} \simeq \mathbf{A}(\tau - T;\mathbb{M}_0)\,\mathbf{y}(\tau) = \mathbf{A}(\tau;\mathbb{M}_0)\,\mathbf{y}(\tau) \tag{2.107}$$

Hence $\mathbf{Y}(t+T) = [\mathbf{y}_1(t+T)\ \mathbf{y}_2(t+T)\ \cdots\ \mathbf{y}_n(t+T)]$ is also a fundamental matrix solution. Since $\mathbf{y}_i(t)$ are the n-linearly independent solutions, the $\mathbf{y}_i(t+T)$ must be linear combinations of $\mathbf{y}_i(t)$:

$$\mathbf{Y}(t+T) = \mathbf{Y}(t)\Phi \tag{2.108}$$

If $\mathbf{Y}(0) = \mathbf{I}$, then $\Phi = \mathbf{Y}(T)$. The $n \times n$ monodromy matrix Φ is a Jacobian matrix for dynamic solution over one period. The state of perturbation $\mathbf{y}$ at each discrete time kT can be expressed as:

$$\mathbf{y}(kT) = \Phi^k \mathbf{y}(0) \tag{2.109}$$

The eigenvalues ρ_m $(m = 1, 2, ..., n)$ of the monodromy matrix is called the Floquet or characteristic multipliers. One of the Floquet multipliers associated with the periodic solution of an autonomous system is always unity. The stability of the periodic solution $\mathbf{X}_0(t)$ can be assessed directly from ρ_m:

- if $\forall m$, $|\rho_m| < 1$, then $\mathbf{y}(t) \xrightarrow{t \to \infty} 0$. The solution is asymptotically stable.
- if $\exists m$, $|\rho_m| > 1$, then $\mathbf{y}(t) \xrightarrow{t \to \infty} \infty$. The solution is unstable.
- if two or more $|\rho_m| = 1$, then nonlinear analysis is necessary to determine the stability of the solution, i.e. higher terms must retain in Equation (2.105).

γ_m are the Floquet or characteristic exponents, satisfying $\rho_m = e^{\gamma_m T}$. In general, both ρ_m and γ_m are complex quantities. The Floquet exponents can also be used to determine the solution stability:

- if $\forall m$, $\mathrm{Re}(\gamma_m) < 0$, then $\mathbf{y}(t) \xrightarrow{t \to \infty} 0$. The solution is asymptotically stable.
- if $\exists m$, $\mathrm{Re}(\gamma_m) > 0$, then $\mathbf{y}(t) \xrightarrow{t \to \infty} \infty$. The solution is unstable.

2.4.2 Poincaré map

As shown in the Poincaré map method section, the periodic solution corresponds to a fixed point on the Poincaré section (Figure 2.7).

$$\mathbf{P}(\boldsymbol{\eta}_0) = \boldsymbol{\eta}_0 \tag{2.110}$$

In the neighbourhood of the solution $\boldsymbol{\eta}_0$ on Σ, we have:

$$\mathbf{P}(\boldsymbol{\eta}_0 + \mathbf{v}) = \mathbf{P}(\boldsymbol{\eta}_0) + D_{\boldsymbol{\eta}}\mathbf{P}(\boldsymbol{\eta}_0)\,\mathbf{v} + \mathscr{O}(\|\mathbf{v}\|^2) \tag{2.111}$$

$\|\mathbf{v}\|$ represents the deviation from the fixed point on Σ. The stability of the fixed point reflects the stability of the solution, which can be determined by investigating the evolution of the deviation $\mathbf{v}$, i.e. by calculating the eigenvalues of the Jacobian matrix $D_{\boldsymbol{\eta}}\mathbf{P}$.

- if all of the eigenvalues are within the unit circle, then the solution is asymptotically stable.

- if any of the eigenvalues are outside of the unit circle, then the solution is unstable.
- if one or more of the eigenvalues lie on the unit circle, then nonlinear analysis is necessary to determine the stability of the solution, i.e. higher terms must retain in Equation (2.111).

2.4.3 Comparison of stability computational methods

The Floquet theory is the most popular approach for accessing the local stability of periodic solutions. Efficient numerical computation of the monodromy matrix Φ is the basis for the efficient numerical treatment of periodic systems. Different numerical methods for evaluating the monodromy matrix have been developed over the past. Hill's method [34] is the frequency-domain method for computing the monodromy matrix whereas 2n-pass numerical integration, matrix exponentials approximation [40], Newmark single-pass numerical integration [21], k-pass numerical integration [9], Chebyshev polynomials [133] and wavelet-Galerkin procedure [106] are the time-domain methods [105]. In time-domain methods, the monodromy matrix Φ can be obtained as a by-product of shooting continuation methods or computed by a time integration over one period. Explicit schemes on how to construct the monodromy matrix are shown in Section 2.4.

Peletan et al. [105] compare the accuracy and the computational time between different methods. There are vast differences in terms of CPU requirements, depending on the model and algorithms used. Most of the CPU time of the time-domain methods are spent on constructing the monodromy matrix, whereas for the frequency-domain methods, calculating the eigenvalues of the monodromy matrix requires most of the CPU time. Accuracy of the frequency-domain methods depends on the number of harmonics retained, hence time-domain methods tend to provide more satisfactory results than the frequency-domain methods. The non-physical Floquet multipliers obtained from the frequency-domain methods may lead to an inappropriate stability evaluation. Among the time-domain methods, single pass methods are much faster and Newmark single-pass algorithm appears to provide the best CPU performance. Fewer time steps per period would be sufficient to produce accurate results, due to the good stability of the implicit Newmark average acceleration scheme. However, as the system size or the number of DOF (n) increases, this method becomes less CPU efficient due to the n numerical integrations involved. This inefficiency can be avoided by applying model reduction techniques.

2.4.4 Stability computation methods

The explicit schemes on how to compute the monodromy matrix Φ, and thus determine the stability of the periodic solutions to the dynamic systems, are shown in this section. The stability computation methods shown are all based on the Floquet theory. Hill's method is a frequency-domain technique, which is usually combined with HBM in literature. Both Newmark time integration and matrix exponentiation are the time-domain techniques. Monodromy matrix calculated with these techniques can be computed as a by-product of time integration method and shooting method.

Hill's Method:

Hill's method is a variant of the Floquet theory used to evaluate local stability in frequency domain based on Fourier series. A periodic solution $\boldsymbol{u}(t)$ to the Equation (2.62) is perturbed with a periodic solution $\mathbf{y}(t)$ with an exponential decay:

$$\mathbf{p}(t) = \boldsymbol{u}(t) + e^{\lambda t}\mathbf{y}(t) \tag{2.112}$$

Substituting Equation (2.112) into Equation (2.62). Approximate the solution and the perturbation by using N_H-th order truncated Fourier series and apply Galerkin procedure as explained in Section 2.3.2 yields:

$$\mathbf{y}(t) \xrightarrow{\text{FFT}} \tilde{\boldsymbol{q}}_y \tag{2.113}$$

$$\mathbf{Z}\tilde{\boldsymbol{q}} + \left(\Delta_2\lambda^2 + \Delta_1\lambda + \mathbf{Z}\right) e^{\lambda t}\tilde{\boldsymbol{q}}_y = \mathbf{b}\left(\tilde{\boldsymbol{q}} + e^{\lambda t}\tilde{\boldsymbol{q}}_y\right) \tag{2.114}$$

with

$$\Delta_1 = \begin{bmatrix} \mathbf{C} & & & & \\ & \mathbf{C} & -2\omega\mathbf{M} & & \\ & 2\omega\mathbf{M} & \mathbf{C} & & \\ & & & \ddots & \\ & & & \mathbf{C} & -2N_H\omega\mathbf{M} \\ & & & 2N_H\omega\mathbf{M} & \mathbf{C} \end{bmatrix} \tag{2.115}$$

$$\Delta_2 = \mathbb{I}_{2N_H+1} \otimes \mathbf{M} \tag{2.116}$$

The right hand side of the Equation (2.114) can be approximated by using Taylor series expansion around **z**

$$\mathbf{b}\left(\tilde{\boldsymbol{q}}+e^{\lambda t}\tilde{\boldsymbol{q}}_y\right)=\mathbf{b}(\tilde{\boldsymbol{q}})+\frac{\partial \mathbf{b}}{\partial \tilde{\boldsymbol{q}}}\left(e^{\lambda t}\tilde{\boldsymbol{q}}_y\right) \tag{2.117}$$

Equation (2.72) gives that:

$$\mathbf{Z}-\frac{\partial \mathbf{b}}{\partial \tilde{\boldsymbol{q}}}=\frac{\partial \mathbf{R}}{\partial \tilde{\boldsymbol{q}}}=\mathbf{h}_z \tag{2.118}$$

Substitute Equation (2.117) and (2.118) into Equation (2.114) yields:

$$\left(\Delta_2\lambda^2+\Delta_1\lambda+\mathbf{h}_z\right)e^{\lambda t}\tilde{\boldsymbol{q}}_y=0 \tag{2.119}$$

Hence Hill's coefficients λ are thus the solutions of the quadratic eigenvalue problem. Only $2n$ of the $2n(2N_H+1)$ eigenvalues are the Floquet exponents γ_m, the other eigenvalues are spurious [88]. This raises the inaccuracy of Hill's method. Lazarus and Thomas then in 2010 proposed a technique to discriminate the non-physical exponents, i.e. Floquet exponents are the $2n$ eigenvalues with the smallest imaginary part in modulus [81].

Newmark Time Integration:

Assume the linear system (Equation (2.105)) is time-invariant between consecutive time instants t_k and t_{k+1}, i.e. matrix $\mathbf{A}(t;\mathbb{M}_0)$ is constant between this time interval. The Newmark implicit approximation formulas for the system at t_{k+1} are:

$$\dot{\mathbf{y}}_{k+1}=\dot{\mathbf{y}}_k+(1-\gamma)h\ddot{\mathbf{y}}_k+\gamma h\ddot{\mathbf{y}}_{k+1} \tag{2.120}$$

$$\mathbf{y}_{k+1}=\mathbf{y}_k+h\dot{\mathbf{y}}_k+h^2(\frac{1}{2}-\beta)\ddot{\mathbf{y}}_k+h^2\beta\ddot{\mathbf{y}}_{k+1} \tag{2.121}$$

where the algorithm parameters $\gamma=\frac{1}{2}$ and $\beta=\frac{1}{4}$, $h=t_{k+1}-t_k$ is the length of the time interval. The equations of linearised dynamic equilibrium at time t_k and t_{k+1} are:

$$\mathbf{M}\ddot{\mathbf{y}}_k=-\mathbf{C}_k\dot{\mathbf{y}}_k-\mathbf{K}_k\mathbf{y}_k \tag{2.122}$$

$$\mathbf{M}\ddot{\mathbf{y}}_{k+1}=-\mathbf{C}_{k+1}\dot{\mathbf{y}}_{k+1}-\mathbf{K}_{k+1}\mathbf{y}_{k+1} \tag{2.123}$$

Combine Equation (2.120) to (2.123) yields:

$$\begin{Bmatrix}\mathbf{y}\\ \dot{\mathbf{y}}\end{Bmatrix}_{k+1}=\mathbf{D}_k\begin{Bmatrix}\mathbf{y}\\ \dot{\mathbf{y}}\end{Bmatrix}_k \tag{2.124}$$

N is the number of time steps over one period T. The transition matrix $\mathbf{D}_k$ is computed as:

$$\begin{aligned}\mathbf{D}_k &= \mathbf{H}_1^{-1}\mathbf{H}_0 \\ &= \begin{bmatrix} \mathbf{M}+\beta h^2\mathbf{K}_{k+1} & \beta h^2\mathbf{C}_{k+1} \\ \gamma h\mathbf{K}_{k+1} & \mathbf{M}+\gamma h\mathbf{K}_{k+1} \end{bmatrix}^{-1} \begin{bmatrix} \mathbf{M}+(\frac{1}{2}-\beta)h^2\mathbf{K}_k & h\mathbf{M}-(\frac{1}{2}-\beta)h^2\mathbf{C}_k \\ -(1-\gamma)h\mathbf{K}_k & \mathbf{M}-(1-\gamma)h\mathbf{C}_k \end{bmatrix}\end{aligned} \tag{2.125}$$

The monodromy matrix Φ is computed by performing the products of all $\mathbf{D}_k$. Successive scale factor method α_k needs to be applied to avoid partial product overflow [21]:

$$\mathbf{C}_0 = \mathbf{I}, \tag{2.126}$$

$$\text{for } k = 1,\ldots,N, \text{ compute: } \begin{cases} \mathbf{C}_k^* = \mathbf{C}_{k-1}\mathbf{D}_k \\ \alpha_k = \|\mathbf{C}_k^*\| \\ \mathbf{C}_k = \alpha^{-1}\mathbf{C}_k^* \end{cases} \tag{2.127}$$

$$\text{Finally: } \Phi = \exp\left(\sum_{k=1}^{N}\log(\alpha_k)\right)\mathbf{C}_N \tag{2.128}$$

Matrix Exponentiation:

Assume the linear system (Equation (2.105)) is time-invariant between consecutive time instants t_k and t_{k+1}, hence:

$$\mathbf{y}_{k+1} = \exp(h\mathbf{A}_k)\mathbf{y}_k \tag{2.129}$$

where $\mathbf{A}_k$ is the system matrix in the time interval between t_k and t_{k+1}. The monodromy matrix Φ can then be computed as the product of the individual matrices.

$$\mathbf{y}_{N+1} = \prod_{k=1}^{N}\exp(h\mathbf{A}_k)\,\mathbf{y}_1 = \Phi\,\mathbf{y}_1 \tag{2.130}$$

The matrix exponential can be computed by using n-th order truncated Taylor series:

$$\exp(h\mathbf{A}_k) = \sum_{j=0}^{\infty}\frac{(h\mathbf{A}_k)^j}{j!} \simeq \sum_{j=0}^{n}\frac{(h\mathbf{A}_k)^j}{j!} \tag{2.131}$$

The monodromy matrix can then be obtained by computing the product of matrix exponentials. Algorithm with normalization of partial products needs to be applied at each step to avoid partial product overflow.

2.4.5 Bifurcations

In dynamical systems (Equation (2.63) and (2.64)), bifurcation occurs when a small smooth change made to the control parameter values $\mathbb{M}$ causes a sudden qualitative change in its behaviour. In continuous-time system, bifurcation occurs when the periodic solution loses stability. Figure 2.9 shows the different ways of how Floquet multipliers leave the unit circle, resulting in different types of bifurcation. Bifurcations in free vibrations give rise to new types of dynamic behaviour, they have significant effects on the dynamics of forced systems. Hence, the knowledge of the bifurcations offers important understanding on the dynamics of the structure. In this section different types of bifurcation are explained and methods on bifurcation detection and tracking are explicated.

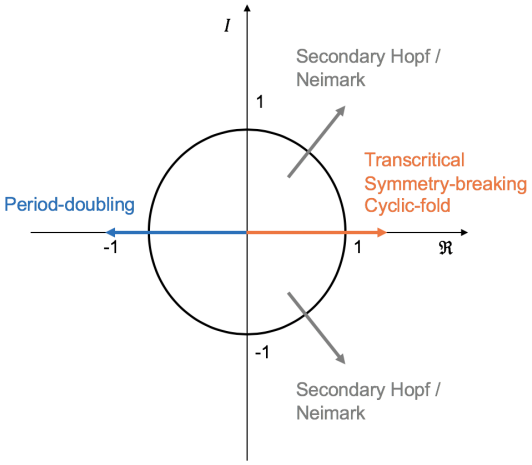


Fig. 2.9 *Scenarios depicting how the Floquet multipliers leave the unit circle and the corresponding bifurcation types.*

Symmetry-breaking bifurcation

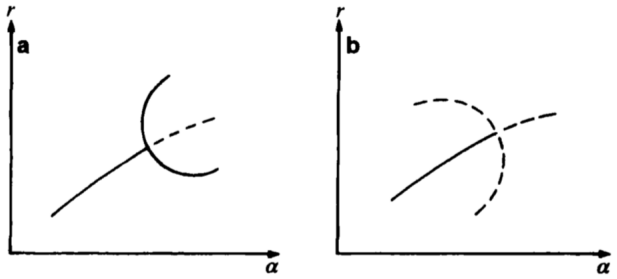


Fig. 2.10 (a) *Supercritical symmetry-breaking bifurcation*, (b) *Subcritical symmetry-breaking bifurcation [96].*

Symmetry breaking is a phenomenon in which small fluctuations acting on a system crossing a critical point (bifurcation point) decide the system's fate, by determining which branch of a bifurcation is taken. Figure 2.10 shows the scenario near the supercritical and subcritical symmetry-breaking bifurcation points, where branches of symmetric and asymmetric periodic solutions meet. r represents the amplitude of the periodic solution and α represents the scalar control parameter. The solid and broken lines correspond to stable and unstable periodic solutions, respectively. Supercritical symmetry-breaking bifurcation is considered as a continuous bifurcation, as the motion of the system evolves continuously onto another motion as a control parameter is varied. Subcritical symmetry-breaking bifurcation is an example of discontinuous bifurcation. Example of symmetry-breaking bifurcation can be found in [119], where the bifurcation occurs during the rubbing contact between rotor and stator components of the aeroengine.

Cyclic-fold Bifurcation

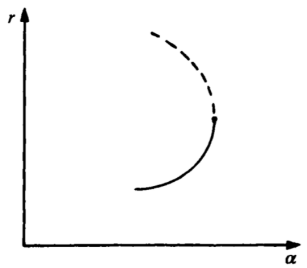


Fig. 2.11 *Scenario in the vicinity of a cyclic-fold bifurcation point [96].*

Figure 2.11 shows the scenario in the vicinity of a cyclic-fold bifurcation point or turning point ($\alpha = \alpha_c$). r represents the amplitude of the periodic solution and α represents the scalar control parameter. Cyclic-fold bifurcation is an example of discontinuous bifurcation, as there are no other solutions in the vicinity of the bifurcation point on the $\alpha > \alpha_c$ side, global considerations are necessary to determine the system behaviour on that side. Example of Cyclic-fold bifurcation can be found in [2]. The bifurcation occurs in nonlinear non-planar vibrations of geometrically imperfect cantilevered beams, which can be used to model the nonlinear dynamic response of the aeroengine blade.

Transcritical Bifurcation

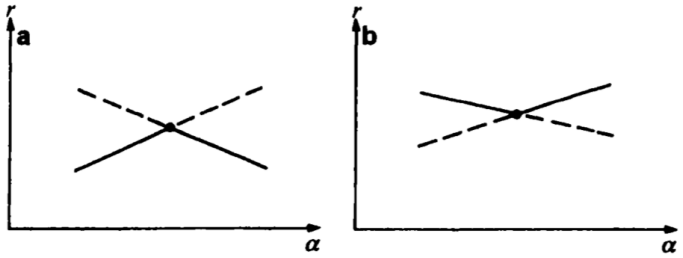


Fig. 2.12 *Two possible local scenarios at transcritical bifurcation point [96].*

A transcritical bifurcation leads to an exchange of stability as shown in Figure 2.12. Example of transcritical bifurcation can be found in [126], where the bifurcation occurs in harmonically excited mechanical system with rigid amplitude constraints. The response of linkages, gears, and fasteners with looseness can be modelled using an oscillator like this model.

Period-doubling Bifurcation or Flip Bifurcation

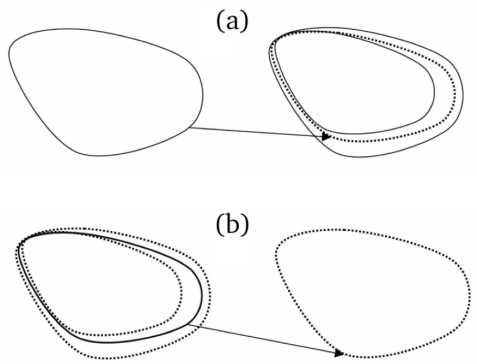


Fig. 2.13 (a) *Supercritical period-doubling bifurcation*, (b) *Subcritical period-doubling bifurcation [143].*

As illustrated in Figure 2.13, a period-doubling is a bifurcation whereby a τ-periodic orbit looses its stability as the parameter α crosses the critical value α_c, and at which point either a stable 2τ-periodic orbit emerges (supercritical) or an unstable 2τ-periodic orbit coalesces with τ-periodic orbit and is destroyed (subcritical). Global considerations are necessary to determine the system behaviour after the subcritical bifurcation. Example of period-doubling

bifurcation can be found in [112], where the bifurcation occurs in airfoil when the airspeed increases.

Secondary Hopf or Neimark–Sacker Bifurcation

Neimark–Sacker bifurcation occurs when two complex conjugate Floquet multipliers leave the unit circle away from the real axis. The bifurcating solution may be periodic or two-period quasiperiodic. In supercritical bifurcation, branch of stable periodic solutions continues as a branch of unstable periodic solutions and a branch of stable quasiperiodic solutions is created. In subcritical bifurcation, branch of stable periodic solutions continues as a branch of unstable periodic solutions and a branch of unstable quasiperiodic solutions is destroyed. Quasiperiodic oscillations are created or eliminated through Neimark bifurcations. Example of Neimark–Sacker bifurcation can also be found in [2], where the bifurcation occurs in nonlinear non-planar vibrations of geometrically imperfect cantilevered beams.

Bifurcation Detection and Tracking

To detect the bifurcation point, a test function is evaluated at each iteration of the numerical continuation process. Cyclic-fold bifurcation is characterized by a rank deficiency of 1 of the Jacobian matrix $\mathbf{h}_z$ of Equation (2.72) and $\mathbf{h}_\omega \notin \text{range}(\mathbf{h}_z)$. It can also be detected when the the tangent prediction related to the active parameter ω changes sign. The Jacobian matrix is rank deficient for branch point (BP) or transcritical bifurcations, with $\mathbf{h}_\omega \in \text{range}(\mathbf{h}_z)$. Turning points and branch points can be determined either through a direct method i.e. algorithm developed by Moore and Spence (1980) [89] or an indirect method i.e. by-product of continuation scheme. The direct methods are more expensive but more accurate. The Neimark bifurcation point can be detected when a pair of Floquet exponents crosses the imaginary axis as a pair of complex conjugates. Griewank and Reddien proposed a direct method on Hopf points detetion in 1983 [45]. Once a bifurcation point is detected, it can be tracked with respect to an additional parameter i.e. homotopy methods [159].

2.5 Nonlinear normal mode

For the autonomous n-dimensional nonlinear systems, the equation of motion in the matrix form can be expressed as:

$$[\mathbf{M}]\{\ddot{\boldsymbol{u}}\} + [\mathbf{C}]\{\dot{\boldsymbol{u}}\} + [\mathbf{K}]\{\boldsymbol{u}\} + \{\boldsymbol{F}_{nl}(\boldsymbol{u})\} = 0 \tag{2.132}$$

The dynamic characteristics of a structure are determined through the modes of vibration. Unlike in the linear conservative system, the vibration period varies with the vibration amplitude, and the oscillations can significantly deviate from harmonic in nonlinear systems. Although the periodic oscillations can still be found, the shape of the system varies along the period. The principle of superposition does not hold in the nonlinear systems, and the modal deflection shapes are no longer orthogonal to each other. Counterparts of the concept of linear eigenmodes shown in Section 2.2.4, which can be used to describe vibrational behaviour of nonlinear systems are tangent modes [138] and nonlinear normal modes (NNMs). In analogy to the linear theory, the resonances in the forced vibration occur in the neighbourhood of the free vibration oscillations [153]. Hence the NNMs from the free, undamped vibration systems can provide valuable information for understanding the system's behaviour in the nonlinear regime. In contrast to the linear system, the number of nonlinear modes in a discrete system can be more than the total number of DOFs and the nonlinear modes might not be neutrally stable due to the mode bifurcations.

NNMs depend on the energy of the system and are first defined in 1960s as "a vibration in unison of the conservative system" by Rosenberg [104], i.e. all nodes of the system moving with the same frequency and passing their equilibrium position simultaneously. This is an extension of the linear normal mode idea for the conservative systems with symmetric nonlinearities. Studies on NNMs were carried forward based on Rosenberg's definition [113, 114]. NNMs were established as a valuable tool for addressing the characteristics of the nonlinear system. Shaw and Pierre later extended Rosenberg's definition as "two-dimensional invariant manifold in phase space" [127, 128], Figure 2.14. The invariance property remains valid in the nonlinear case, i.e. once a motion is initiated in a particular nonlinear mode, it remains in it for all times. This extended the NNM concept to damped systems, systems affected by gyroscopic forces, and those with non-symmetric nonlinearities. A nonlinear mode occupies a general (curved) manifold, which is tangential to the hyperplanes spanned by the associated linear mode in the system's phase space at the equilibrium point. Based on the geometric arguments and the centre manifold technique [22], a single pair of state variables in linear modal coordinates are chosen as master coordinates. The remaining variables, the slave coordinates, are functionally related to the master coordinates through asymptotic expansions. Therefore, the system behaves like a nonlinear single-DOF system on the manifold.

Definition of the nonlinear normal modes can also be extended to include non-synchronous but periodic oscillations, such as the internal resonances [162]. Internal resonance occurs when the natural frequencies become commensurable, i.e. frequencies in integer ratios.

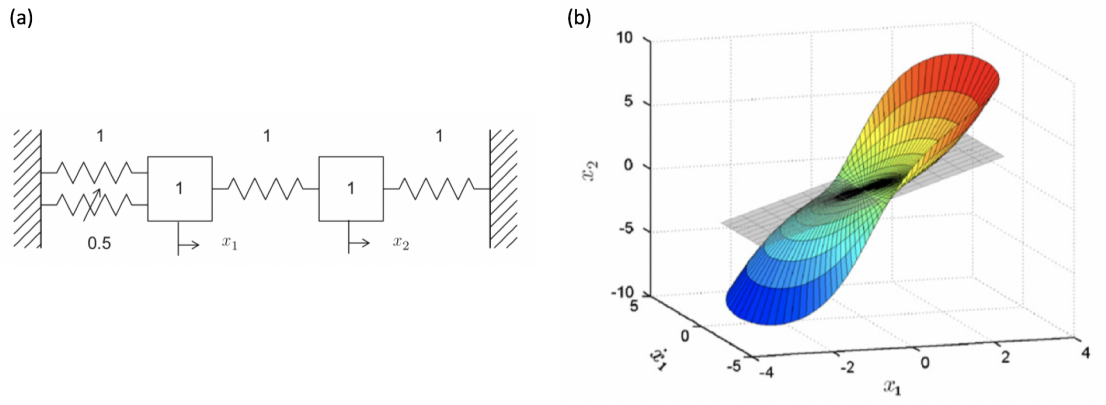


Fig. 2.14 (a) *Schematic representation of the 2-DOF system example*, (b) *Two-dimensional invariant manifolds of system with the corresponding linear mode [67].*

Energy starts to be exchanged between the relevant modes, and multimodal vibration can be observed [142]. This is a particular phenomena that arises in the nonlinear multi-degree-of-freedom system. Hence the invariant manifold approach based on a single mode expansion cannot cope with the internal resonances. The approach was then extended by Pesheck et al. [107] to the case of multi-mode manifolds. The dynamic models obtained were able to capture the coupling between modes of interest. For systems with strong and complex nonlinearities, the pairs of the master coordinates were transformed into the polar coordinates form, i.e. the Galerkin-based invariant manifold approach [107].

King et al. developed the energy-based NNM methodologies for the discrete and continuous systems to study the modal interaction [70]. Linear modal coordinates were used to construct the NNMs. Applications of the energy-based formulation are limited to the small motions. A direct method based on the method of normal forms and method of multiple scales were proposed by Nayfeh for constructing the NNMs of continuous systems [95]. Both methods are applicable to problems with internal resonances, with method of multiple scales appearing to be less computationally demanding. The multiple scales methods is a type of perturbation method, which considers the asymptotic expansions in terms of multiple independent time scales. Poincaré and Poincaré-Dulac theorems are fundamental for the normal form theory. The philosophy of the normal form is to seek a nonlinear coordinates that brings the equations of motion into the simplest possible form.

Slaat at al. proposed three mode types for reducing nonlinear dynamical system equations: tangent modes, modal derivatives, and static modes [135]. Tangent modes are the eigenmodes

obtained from the solution of an updated eigenvalue problem with the tangent stiffness $\mathbf{K}_T(\boldsymbol{\phi}_k)$ for the current deformation state:

$$\omega_k^2 \mathbf{M}\boldsymbol{\phi}_k = \mathbf{K}_T(\boldsymbol{\phi}_k)\boldsymbol{\phi}_k \tag{2.133}$$

where ψ_k stands for the k-th eigenmode and ω_k for the k-th natural frequency. The tangent stiffness matrix is the linearisation of the system at $t = t_0$

$$\mathbf{K}_T(\boldsymbol{\phi}_k) = \left.\frac{\partial([\mathbf{K}]\{\boldsymbol{u}\} + \{\boldsymbol{F}_{nl}\})}{\partial \boldsymbol{u}}\right|_{\boldsymbol{u}=\boldsymbol{u}_0} \tag{2.134}$$

Tangent modes are relatively simple to compute, but they do not account for internal resonances and can only be determined in the neighbourhood of a linear eigenfrequency. The concept of NNMs is more general in this case, but the numerical algorithms are more complex.

The extended definition of Rosenberg for NNMs is the one retained for the computation of NNMs in this research. The numerical method proposed in this research relies on two main techniques, namely the Extended Periodic Motion Concept (EPMC) and the arc-length continuation method. In the EPMC [122], an artificial viscous damping is introduced into the HBM equations to compensate the energy dissipated by the nonlinear forces. The modelling strategy can be applied to large systems with strong and complex nonlinearities. The complex nonlinear modes (CNM) investigated by Laxalde and Thouverez is another commonly used numerical method to compute the NNMs for non-conservative system with strong or non-smooth nonlinearities in large scale [80].

2.6 Reduced order modelling

After the spatial discretization of the governing PDEs using finite elements, a system of n-dimensional second order ODEs is obtained.

$$[\mathbf{M}]\{\ddot{\boldsymbol{u}}\} + [\mathbf{C}]\{\dot{\boldsymbol{u}}\} + [\mathbf{K}]\{\boldsymbol{u}\} + \{\boldsymbol{F}_{nl}(\boldsymbol{u})\} = \{\boldsymbol{F}_{ext}\} \tag{2.135}$$

Solution time of the system increases rapidly with the number of DOFs, n, in the system. For complex engineering structures with thousands or millions of DOFs in the FE model, the numerical analysis methods for solving the ODEs in the motion equations become impossible. Model order reduction methods are used to decrease the complexity and computational effort for solving the equations by reducing the number of DOFs ($r \ll n$) and allowing the frequency analysis, i.e. HBM, to be applied on large-scale applications. A computationally

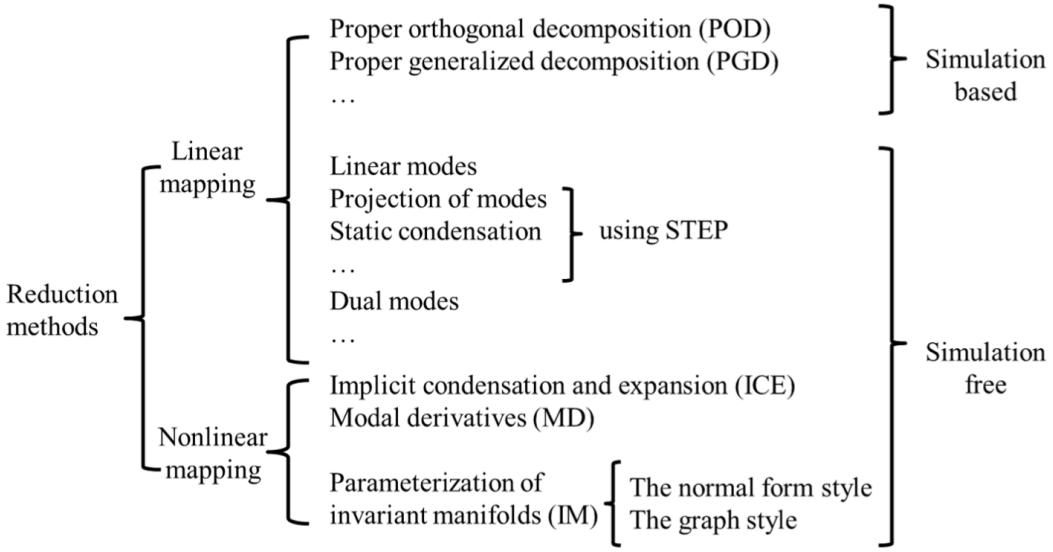


Fig. 2.15 *The classification of the reduction methods [130].*

efficient ROM model with good approximation of the full-order model and ability to retrieve nonlinear features is desired.

ROM techniques for finite element discretisation can be classified into two groups: intrusive and non-intrusive methods, also known as direct and indirect methods. Non-intrusive methods refer to the techniques which require output from a commercial finite element package, whereas the intrusive methods require full access to the code. In intrusive methods, nonlinear restoring forces are generally computed in the code by a direct projection of the full-order equations to a reduced eigenspace [130]. The ROM methods can be categorised into two groups based on the basis involved. Methods in the first group involves projection of linear mode, such as the proper orthogonal decomposition (POD) [33, 168]. The second group involves nonlinear mapping, such as the Implicit Condensation with Expansion (ICE) approach [141] and the modal derivatives (MD) [84]. Figure 2.15 shows the classification of the reduction methods summarised by Shen [130].

Generally speaking, each ROM operates a change of coordinates to obtain a reduced dynamics system of equations with reduced dimension. There is a wide range of projection-based model order reduction methods, where the physical coordinate vector $\boldsymbol{u} \in \mathbb{R}^n$ is approximated with a reduced coordinates $\hat{\boldsymbol{q}} \in \mathbb{R}^r$.

$$\boldsymbol{u}(t) \approx \boldsymbol{\Gamma}(\hat{\boldsymbol{q}}) \tag{2.136}$$

For the linear approaches, the function of $\boldsymbol{\Gamma}$ is expressed as $\boldsymbol{\Gamma} = \boldsymbol{V}\hat{\boldsymbol{q}}(t)$. The reduction matrix $\boldsymbol{V} \in \mathbb{R}^{n\times r}$ contains the linear projection subspace(s). The projection based ROM with nonlinear mapping, such as ICE and quadratic manifold (QM), $\boldsymbol{\Gamma}$ is a nonlinear function of $\hat{\boldsymbol{q}}$. The reduced basis can hence be computed as $\boldsymbol{V} = \frac{\partial \boldsymbol{\Gamma}}{\partial \hat{\boldsymbol{q}}}$. Introducing this transformation creates an approximation to the exact solution. The governing equation for the full FE model is reduced to:

$$\boldsymbol{V}^{\mathsf{T}}[\mathbf{M}]\{\ddot{\boldsymbol{\Gamma}}(\hat{\boldsymbol{q}})\} + \boldsymbol{V}^{\mathsf{T}}[\mathbf{C}]\{\dot{\boldsymbol{\Gamma}}(\hat{\boldsymbol{q}})\} + \boldsymbol{V}^{\mathsf{T}}[\mathbf{K}]\{\boldsymbol{\Gamma}(\hat{\boldsymbol{q}})\} + \boldsymbol{V}^{\mathsf{T}}\{\boldsymbol{F}_{nl}(\boldsymbol{\Gamma})\} = \boldsymbol{V}^{\mathsf{T}}\{\boldsymbol{F}_{ext}\} \tag{2.137}$$

The choice of the projection basis $\boldsymbol{V}$ is very critical in determining the accuracy of the reduced solution and the size of the basis is essential on determining the reduction in computation time. The projection of the nonlinear terms, $\boldsymbol{V}^{\mathsf{T}}\{\boldsymbol{F}_{ext}\}$, needs to be computed at each iteration during time integration of these equations, which causes a great computational cost. STiffness Evaluation Procedure (STEP) method and hyper-reduction methods such as Discrete Empirical Interpolation Method (DEIM), UDEIM or ECSW are the methods which can be applied to achieve a good speed up for fast evaluation. STEP was first proposed by Muravyov and Rizzi [92] in 2003. The nonlinear force are expressed in the polynomial form. The nonlinear modal stiffness coefficients for an arbitrary FE model are determined by prescribing selected static displacement to the FE model. DEIM [134] reduces the computational effort by simply evaluating the internal force at selected points of interest and interpolating the force at other points.

Modal reduction or truncation is the most common projection method where the transformation matrix is composed from a subset of linear eigenvectors $\boldsymbol{V} = \boldsymbol{\phi}_r$. The method is widely used in the linear structural dynamics. The modes of interest or the modes in the frequency band of the excitation frequency are selected as the reduced basis. For system with distributed nonlinearities, the function of mapping becomes complex due to the coupling between the modes. Modal derivatives (MDs) are defined from a second-order Taylor expansion of the nonlinear eigenvalue problem. It describes the change in the vibration mode $\boldsymbol{\phi}_i$ corresponding to a displacement given in the direction of $\boldsymbol{\phi}_j$. MDs form a nice augmentation of the reduction basis. MDs are used in the quadratic nonlinear mapping such as QM method. Modal reduction with modal derivatives, $\boldsymbol{V} = [\boldsymbol{\Phi}, \partial\boldsymbol{\Phi}]$, has been employed successfully for time integration of nonlinear solid dynamics in literature [8]. Low frequency modes are normally more excited and less damped than higher ones, thus making them the best candidates for reduction.

Conversely to the projection method, the invariant manifold methods based on the NNMs, such as the normal form approach [156] and the Shaw and Pierre approach [129], are also

widely used. In this case the phase space vector $\mathbf{x}$ of the first order equation shown in Equation (2.64) is approximated as a function of the invariant manifold coordinates $\boldsymbol{\eta}$:

$$\mathbf{x} \approx \hat{\mathbf{x}}(\boldsymbol{\eta}) \tag{2.138}$$

The reduced dynamics on the manifold are assumed to be known a priori, i.e. $\dot{\boldsymbol{\eta}} = \boldsymbol{r}(\boldsymbol{\eta})$. Equation (2.64) can then be re-written in terms of nonlinear mapping and the reduced dynamics:

$$\frac{\partial \hat{\mathbf{x}}}{\partial \boldsymbol{\eta}} \boldsymbol{r} = \mathbf{F}(\hat{\mathbf{x}}) \tag{2.139}$$

Other approaches for constructing a reduced dimensional subspace can also be found. Tangent modes [136], as shown in Section 2.5, are determined from the tangent modes in every time step. Therefore the method requires specific current deformation state. Ritz vectors are developed from load or displacement of a current state, which provides a good approximation of exact solutions but requires a fixed current state of deformation. Proper orthogonal decomposition [161] is a very effective method to construct low dimensional subspace and gives good results in structural time integration. However it is developed from a set of sample displacement vectors, priori knowledge of loads is required. Hence it is not suitable for the nonlinear dynamic cases as unexpected states of deformation or resonances are to be found. The implicit condensation and expansion (ICE) method [85, 86], sometimes also called the applied force method (AMF), relies on a serious of applied static force to construct the stress manifold. The new coordinates derived from the stress manifold are used to describe the dynamic behaviour instead of the modal coordinates. The method is very appealing to use on thin structures, as the geometric nonlinearities arising from the axial-bending coupling can be taken into account implicitly with ICE [55]. Hurty/Craig-Bampton method is a reduction method based on the splitting of the DOFs of the system into internal and boundary DOFs, which makes it particularly suitable for problems with localised contact nonlinearities [57].

In this research, the algorithms of two projection based ROM methods are presented and compared. The first method based on the projection on the linear modes only. The second method is based on the quadratic nonlinear mapping. MDs are augmented on top of the linear modes to approximate the displacement vector in the quadratic manifold method.

Chapter 3

Finite Element Analysis of 3D Structures with Geometric Nonlinearity

In this chapter, the finite element analysis is done on the 3D structure in both static and dynamic cases. The Green-Lagrange strain measures are employed to express the nonlinear relationship between displacement and strain. The governing equation in the time domain for the 3D structure with geometric nonlinearity is derived from the expressions of energy. FE matrices are yielded by applying the Euler–Lagrange equation to the energy expressions. 3D solid elements are used in the FE model and the characteristics of different element types are investigated. For the 3D solid element, the absence of the rotational degree of freedom on the nodes makes it suitable for structures with large displacement and rotation. The structure's material is assumed to be elastic, homogeneous, and isotropic. Linear 3D Saint Venant–Kirchhoff material law is applied for the constitutive relationship of the material and derivation of stress measure. The FE matrices derived are validated by comparing the results of the modal analysis with the analytical values computed from the Euler-Bernoulli Beam theory.

The investigation herein will make use of the AFT enhanced HBM method to numerically solve the dynamic equation of motion in the frequency domain. Dynamic analyses are done on both clamped-clamped beams and cantilevered beams with the equation of motion. Frequency Response Function (FRF) plot is used to show the response of the system to different excitation forces. The effect of the geometric nonlinear forces on the dynamic behaviour of the 3D structures can hence be studied and predicted. Unlike the formulations derived from the beam elements or other lower-order elements etc., the equation of motion derived in this chapter is applicable to 3D structures with complex shapes. However, the full FE model still has its limitation on applying to large structures even with the application of

the sparse matrix. The issue can be solved later by applying different ROM techniques to the full FE model.

3.1 Governing equation in the time domain for 3D Structure

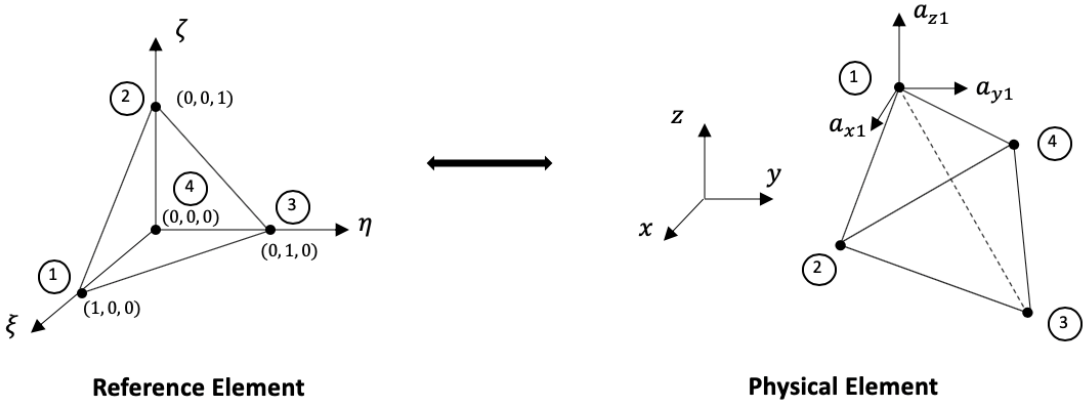


Fig. 3.1 *Transformation between physical and reference element.*

As discussed in section 2.2.3, FE models are obtained via a Galerkin discretisation of the governing partial differential equations (PDE) for the continuous systems. In 3D solid element, nodes are allowed to translate along the x, y, z axes, hence each node has 3 DOFs. The estimated displacement vector $\boldsymbol{u}_e$ of each element can be defined as in Equation (3.1), where $\mathbf{N}$ is the shape function matrix and $\mathbf{a}_e$ is the column vector of nodal displacement. n stands for the total number of nodes in the element and subscript e refers to elementary quantities.

$$\boldsymbol{u}_e\left(\bar{\boldsymbol{X}},t\right) = \left\{u_x \quad u_y \quad u_z\right\}^{\mathsf{T}} = \sum_{i=1}^{n} N_i\left(\bar{\boldsymbol{X}}\right) a_{e,i}\left(t\right) = \mathbf{N}\left(\bar{\boldsymbol{X}}\right)\cdot\mathbf{a}_e(t) \tag{3.1}$$

$$\textit{where}, \quad \mathbf{a}_e = \left\{a_{x1} \quad a_{y1} \quad a_{z1} \quad a_{x2} \quad a_{y2} \quad a_{z2} \quad \ldots \quad a_{xn} \quad a_{yn} \quad a_{zn}\right\}^{\mathsf{T}}$$

For each element, a set of Lagrange polynomial functions N_i is used as shape function set. The shape functions are defined and evaluated on each element in the physical coordinates $\bar{\boldsymbol{X}} = (x,y,z)$. For the convenience of computation, physical elements are all transformed into reference element as shown in Figure A.4. Shape functions of the reference element with coordinates $\bar{\boldsymbol{\xi}} = (\xi,\eta,\zeta)$ are used. For a tetrahedron solid element, for instance, the reference coordinates are defined in $[0,1]$ for each component. All field variables can hence

be expressed by the shape functions $N_i(\bar{\boldsymbol{\xi}})$ and the nodal coordinates $\hat{\boldsymbol{X}}_e$ or $\mathbf{a}_e$:

$$\boldsymbol{u}_e\left(\bar{\boldsymbol{\xi}}\right) = \left\{u_x \quad u_y \quad u_z\right\}^{\mathsf{T}} = \sum_{i=1}^{n} N_i\left(\bar{\boldsymbol{\xi}}\right) a_{e,i}(t) = \mathbf{N}\left(\bar{\boldsymbol{\xi}}\right) \mathbf{a}_e(t) \tag{3.2}$$

$$\bar{\boldsymbol{X}}\left(\bar{\boldsymbol{\xi}}\right) = \left\{x \quad y \quad z\right\}^{\mathsf{T}} = \sum_{i=1}^{n} N_i\left(\bar{\boldsymbol{\xi}}\right) \hat{\boldsymbol{X}}_{e,i} = \hat{\boldsymbol{X}}_e \boldsymbol{\Psi} \tag{3.3}$$

Where,

$$\mathbf{N}\left(\bar{\boldsymbol{\xi}}\right) = \begin{bmatrix} N_1 & 0 & 0 & N_2 & 0 & 0 & \cdots & N_n & 0 & 0 \\ 0 & N_1 & 0 & 0 & N_2 & 0 & \cdots & 0 & N_n & 0 \\ 0 & 0 & N_1 & 0 & 0 & N_2 & \cdots & 0 & 0 & N_n \end{bmatrix} \tag{3.4}$$

$$\hat{\boldsymbol{X}}_e = \begin{bmatrix} x_1 & x_2 & x_3 & \cdots & x_n \\ y_1 & y_2 & y_3 & \cdots & y_n \\ z_1 & z_2 & z_3 & \cdots & z_n \end{bmatrix} \tag{3.5}$$

$$\boldsymbol{\Psi} = \left\{N_1\left(\bar{\boldsymbol{\xi}}\right) \quad N_2\left(\bar{\boldsymbol{\xi}}\right) \quad N_3\left(\bar{\boldsymbol{\xi}}\right) \quad \ldots \quad N_n\left(\bar{\boldsymbol{\xi}}\right)\right\}^{\mathsf{T}} \tag{3.6}$$

Details of the shape function in the reference coordinates for the four 3D solid elements types shown in Figure 2.5 can be found in Appendix A. In the element level, the numbering sequence of the nodes is very important, but it varies between FE programs. Readers are advised to follow the numbering sequence shown in Appendix A to comply with the shape functions provided. For example, the first three nodes are addressed in anticlockwise direction when looking from the top of the 4-node tetrahedron element. If the incorrect node numbering sequence is followed, a distorted element will be defined. The matrix format of the equation of motion can be achieved by applying Euler–Lagrange equation (Equation (2.7)) onto the energy expressions of the system.

3.1.1 Potential energy expression

The potential energy of a dynamic system is due to the deformation of the structure. To calculate the strain energy, expressions of strain and stress tensors need to be derived. Geometric nonlinearity arises due to large displacements and solid rotations and thus the nonlinear strain-displacements relation. This is generally the case when large-amplitude vibrations generate large displacements such that the geometrical curvature of the blade does not deform linearly with displacement. Green-Lagrange strain measures are employed in this research to express the nonlinear strain. As discussed in section 2.2.2, the explicit expression of the tensor is shown in Equation (3.7). In Green-Lagrangian deformation tensor, partial derivative

of the displacement vector $\boldsymbol{u}$ are with respect to the material coordinates $\mathbf{X}$, i.e. the coordinate system of the undeformed configuration. This strain measure is independent of rigid body rotations, which makes it suitable for describing nonlinear geometric effect for structures undergoing finite deformation.

$$\varepsilon_{ij}^{G} = \frac{1}{2}\left(\frac{\partial u_i}{\partial X_i} + \frac{\partial u_j}{\partial X_j} + \frac{\partial u_k}{\partial X_i}\frac{\partial u_k}{\partial X_j}\right) \tag{3.7}$$

The Green strain vector $\boldsymbol{\varepsilon}^{G}$ can be decomposed into linear part $\boldsymbol{\varepsilon}_0$ and nonlinear part $\boldsymbol{\varepsilon}_1$, as shown in Equation 3.8.

$$\begin{aligned}
\boldsymbol{\varepsilon}^{G} &= \left\{\varepsilon_{xx} \quad \varepsilon_{yy} \quad \varepsilon_{zz} \quad 2\varepsilon_{yz} \quad 2\varepsilon_{xz} \quad 2\varepsilon_{xy}\right\}^{\mathsf{T}} \\
\boldsymbol{\varepsilon}^{G} &= \boldsymbol{\varepsilon}_0 + \boldsymbol{\varepsilon}_1 \\
&= \mathbf{B}_0(\xi,\eta,\zeta)\cdot\mathbf{a}_e + \frac{1}{2}\cdot\mathbf{B}_1(\boldsymbol{u}_e)\cdot\mathbf{a}_e
\end{aligned} \tag{3.8}$$

The increment of $\boldsymbol{\varepsilon}^{G}$ is derived as:

$$\mathrm{d}\boldsymbol{\varepsilon}^{G} = \left[\mathbf{B}_0(\xi,\eta,\zeta) + \mathbf{B}_1(\boldsymbol{u}_e)\right]\cdot\mathrm{d}\mathbf{a}_e \tag{3.9}$$

The matrices of derivatives of the shape function, $[\mathbf{B}_0]$ and $[\mathbf{B}_1]$, are expressed as:

$$[\mathbf{B}_0](\xi,\eta,\zeta) = \begin{bmatrix}
\frac{\partial N_1}{\partial x} & 0 & 0 & \dots & \dots & \dots & \frac{\partial N_n}{\partial x} & 0 & 0 \\
0 & \frac{\partial N_1}{\partial y} & 0 & \dots & \dots & \dots & 0 & \frac{\partial N_n}{\partial y} & 0 \\
0 & 0 & \frac{\partial N_1}{\partial z} & \dots & \dots & \dots & 0 & 0 & \frac{\partial N_n}{\partial z} \\
0 & \frac{\partial N_1}{\partial z} & \frac{\partial N_1}{\partial y} & \dots & \dots & \dots & 0 & \frac{\partial N_n}{\partial z} & \frac{\partial N_n}{\partial y} \\
\frac{\partial N_1}{\partial z} & 0 & \frac{\partial N_1}{\partial x} & \dots & \dots & \dots & \frac{\partial N_n}{\partial z} & 0 & \frac{\partial N_n}{\partial x} \\
\frac{\partial N_1}{\partial y} & \frac{\partial N_1}{\partial x} & 0 & \dots & \dots & \dots & \frac{\partial N_n}{\partial y} & \frac{\partial N_n}{\partial x} & 0
\end{bmatrix} \tag{3.10}$$

$$[\mathbf{B}_1(\boldsymbol{u}_e)] = [\mathbf{A}(\boldsymbol{u}_e)]\,[\mathbf{G}] \tag{3.11}$$

with,

$$[\mathbf{A}(\boldsymbol{u}_e)] = \begin{bmatrix} \frac{\partial u_x}{\partial x} & \frac{\partial u_y}{\partial x} & \frac{\partial u_z}{\partial x} & 0 & 0 & 0 & 0 & 0 & 0 \\ 0 & 0 & 0 & \frac{\partial u_x}{\partial y} & \frac{\partial u_y}{\partial y} & \frac{\partial u_z}{\partial y} & 0 & 0 & 0 \\ 0 & 0 & 0 & 0 & 0 & 0 & \frac{\partial u_x}{\partial z} & \frac{\partial u_y}{\partial z} & \frac{\partial u_z}{\partial z} \\ 0 & 0 & 0 & \frac{\partial u_x}{\partial z} & \frac{\partial u_y}{\partial z} & \frac{\partial u_z}{\partial z} & \frac{\partial u_x}{\partial y} & \frac{\partial u_y}{\partial y} & \frac{\partial u_z}{\partial y} \\ \frac{\partial u_x}{\partial z} & \frac{\partial u_y}{\partial z} & \frac{\partial u_z}{\partial z} & 0 & 0 & 0 & \frac{\partial u_x}{\partial x} & \frac{\partial u_y}{\partial x} & \frac{\partial u_z}{\partial x} \\ \frac{\partial u_x}{\partial y} & \frac{\partial u_y}{\partial y} & \frac{\partial u_z}{\partial y} & \frac{\partial u_x}{\partial x} & \frac{\partial u_y}{\partial x} & \frac{\partial u_z}{\partial x} & 0 & 0 & 0 \end{bmatrix} \tag{3.12}$$

$$[\mathbf{G}] = \begin{bmatrix} \frac{\partial N_1}{\partial x} \otimes \mathbf{I}_3 & \frac{\partial N_2}{\partial x} \otimes \mathbf{I}_3 & \ldots & \frac{\partial N_n}{\partial x} \otimes \mathbf{I}_3 \\ \frac{\partial N_1}{\partial y} \otimes \mathbf{I}_3 & \frac{\partial N_2}{\partial y} \otimes \mathbf{I}_3 & \ldots & \frac{\partial N_n}{\partial y} \otimes \mathbf{I}_3 \\ \frac{\partial N_1}{\partial z} \otimes \mathbf{I}_3 & \frac{\partial N_2}{\partial z} \otimes \mathbf{I}_3 & \ldots & \frac{\partial N_n}{\partial z} \otimes \mathbf{I}_3 \end{bmatrix} \tag{3.13}$$

The space derivative of the displacement terms in $[\mathbf{A}(\boldsymbol{u}_e)]$ are computed as:

$$[\mathbf{G}]\,\{\mathbf{a}_e\} = \begin{bmatrix} \frac{\partial u_x}{\partial x} & \frac{\partial u_y}{\partial x} & \frac{\partial u_z}{\partial x} & \frac{\partial u_x}{\partial y} & \frac{\partial u_y}{\partial y} & \frac{\partial u_z}{\partial y} & \frac{\partial u_x}{\partial z} & \frac{\partial u_y}{\partial z} & \frac{\partial u_z}{\partial z} \end{bmatrix} \tag{3.14}$$

In $[\mathbf{B}_0]$ and $[\mathbf{B}_1]$, the space derivative of the field tensor are carried out on the shape functions $N_i(\boldsymbol{\xi})$. With respect to Equation (3.3), the space derivative terms can be derived as:

$$\frac{\partial \boldsymbol{\Psi}}{\partial \bar{\boldsymbol{X}}} = \frac{\partial \boldsymbol{\Psi}}{\partial \bar{\boldsymbol{\xi}}} \frac{\partial \bar{\boldsymbol{\xi}}}{\partial \bar{\boldsymbol{X}}} = \frac{\partial \boldsymbol{\Psi}}{\partial \bar{\boldsymbol{\xi}}} \left[\frac{\partial \bar{\boldsymbol{X}}}{\partial \bar{\boldsymbol{\xi}}}\right]^{-1} = \frac{\partial \boldsymbol{\Psi}}{\partial \bar{\boldsymbol{\xi}}} \left[\hat{\boldsymbol{X}}_e \frac{\partial \boldsymbol{\Psi}}{\partial \bar{\boldsymbol{\xi}}}\right]^{-1} \tag{3.15}$$

$$\frac{\partial \boldsymbol{\Psi}}{\partial \bar{\boldsymbol{X}}} = \begin{bmatrix} \frac{\partial N_1}{\partial x} & \frac{\partial N_2}{\partial x} & \frac{\partial N_3}{\partial x} & \cdots & \frac{\partial N_n}{\partial x} \\ \frac{\partial N_1}{\partial y} & \frac{\partial N_2}{\partial y} & \frac{\partial N_3}{\partial y} & \cdots & \frac{\partial N_n}{\partial y} \\ \frac{\partial N_1}{\partial z} & \frac{\partial N_2}{\partial z} & \frac{\partial N_3}{\partial z} & \cdots & \frac{\partial N_n}{\partial z} \end{bmatrix}^{\mathsf{T}} \tag{3.16}$$

with $\frac{\partial \boldsymbol{\Psi}}{\partial \bar{\boldsymbol{\xi}}}$ denotes the local derivative of the shape functions and $\left[\frac{\partial \bar{\boldsymbol{X}}}{\partial \bar{\boldsymbol{\xi}}}\right] = \left[\hat{\boldsymbol{X}}_e \frac{\partial \boldsymbol{\Psi}}{\partial \bar{\boldsymbol{\xi}}}\right]$ is the Jacobian matrix. Details of the $\frac{\partial \boldsymbol{\Psi}}{\partial \bar{\boldsymbol{\xi}}}$ matrix for the commonly used 3D solid elements can be found in Appendix A.

Linear 3D Saint Venant–Kirchhoff material law (Equation 3.17) is used in this research for the constitutive relationship of the material and derivation of stress measure. $\mathbf{S}$ represents the second Piola-Kirchoff stress tensor, which is the work conjugate of the Green strain $\boldsymbol{\varepsilon}^G$. μ and λ are the Lamé constants. Hence the second Piola-Kirchoff stress vector in matrix form can be expressed as shown in Equation (3.18), with $[\mathbf{D}]$ representing the symmetric constitutive matrix.

$$\mathbf{S} = \lambda \operatorname{tr}(\mathbf{E})\mathbf{I} + 2\mu\mathbf{E} \tag{3.17}$$

$$\begin{aligned}\mathbf{S} &= \begin{Bmatrix}\sigma_{xx} & \sigma_{yy} & \sigma_{zz} & \tau_{yz} & \tau_{xz} & \tau_{xy}\end{Bmatrix}^{\mathsf{T}} = [\mathbf{D}]\,\boldsymbol{\varepsilon}^G \\ &= [\mathbf{D}]\left[\mathbf{B}_0 + \frac{1}{2}\mathbf{B}_1(\boldsymbol{u}_e)\right]\{\mathbf{a}_e\}\end{aligned} \tag{3.18}$$

With E and ν representing the Young's Modulus and Poisson's ratio of the material, respectively, the constitutive matrix $[\mathbf{D}]$ is computed as:

$$[\mathbf{D}] = \frac{E}{(1+\nu)(1-2\nu)}\begin{bmatrix} 1-\nu & \nu & \nu & 0 & 0 & 0 \\ \nu & 1-\nu & \nu & 0 & 0 & 0 \\ \nu & \nu & 1-\nu & 0 & 0 & 0 \\ 0 & 0 & 0 & \mu & 0 & 0 \\ 0 & 0 & 0 & 0 & \mu & 0 \\ 0 & 0 & 0 & 0 & 0 & \mu \end{bmatrix} \tag{3.19}$$

$$\mu = \frac{1-2\nu}{2}$$

The strain energy of the system can thus be expressed as:

$$\begin{aligned}U &= \frac{1}{2}\int \mathbf{S} : \boldsymbol{\varepsilon}^G \,\mathrm{d}V \\ &= \frac{1}{2}\cdot \mathbf{a}_e{}^{\mathsf{T}} \int \left[\mathbf{B}_0 + \frac{1}{2}\mathbf{B}_1(\boldsymbol{u}_e)\right]^{\mathsf{T}} [\mathbf{D}] \left[\mathbf{B}_0 + \frac{1}{2}\mathbf{B}_1(\boldsymbol{u}_e)\right] \mathrm{d}V\, \mathbf{a}_e\end{aligned} \tag{3.20}$$

V stands for the volume of the 3D element. Applying the Euler–Lagrange equation (Equation (2.7)) onto the strain energy equation yields the expression of the stiffness matrix of the 3D solid element $[\mathbf{K}_e]$, as shown in Equation (3.21). For a structure with geometric nonlinearity

taking into account, the stiffness matrix can be expressed as the sum of linear stiffness matrix $[\mathbf{K}_0^e]$ and nonlinear stiffness matrix $[\mathbf{K}_{nl}^e]$. Both $[\mathbf{K}_0^e]$ and $[\mathbf{K}_{nl}^e]$ are symmetric.

$$\begin{aligned}[\mathbf{K}_e] &= [\mathbf{K}_0^e] + [\mathbf{K}_{nl}^e] = \int \mathbf{S} : \mathrm{d}\boldsymbol{\varepsilon}^G \mathrm{d}V \\ &= \int [\mathbf{B}_0 + \mathbf{B}_1(\boldsymbol{u}_e)]^\mathsf{T} [\mathbf{D}] \left[\mathbf{B}_0 + \frac{1}{2}\mathbf{B}_1(\boldsymbol{u}_e)\right] \mathrm{d}V \end{aligned} \tag{3.21}$$

$$\textit{where}, \quad [\mathbf{K}_0^e] = \int [\mathbf{B}_0]^\mathsf{T} [\mathbf{D}] [\mathbf{B}_0] \, \mathrm{d}V \tag{3.22}$$

$$\begin{aligned}[\mathbf{K}_{nl}^e] &= \frac{1}{2}\int [\mathbf{B}_0]^\mathsf{T} [\mathbf{D}] [\mathbf{B}_1] \, \mathrm{d}V + \int [\mathbf{B}_1]^\mathsf{T} [\mathbf{D}] [\mathbf{B}_0] \, \mathrm{d}V + \frac{1}{2}\int [\mathbf{B}_1]^\mathsf{T} [\mathbf{D}] [\mathbf{B}_1] \, \mathrm{d}V \\ &= \frac{1}{2}[\mathbf{K}_1^e(\boldsymbol{u}_e)] + [\mathbf{K}_2^e(\boldsymbol{u}_e)] + \frac{1}{2}[\mathbf{K}_3^e(\boldsymbol{u}_e)] \end{aligned} \tag{3.23}$$

As discussed in section 2.2.3, the integral functions can be estimated by employing Gaussian quadrature rule. N is the total number of Gaussian Quadrature points. ξ_i, η_i and ζ_i are the quadrature points and w_i is the corresponding quadrature weight. The determinant of the Jacobian matrix $|\mathrm{Jac}\left(\bar{\boldsymbol{\xi}}\right)| = \frac{\mathrm{d}\bar{\boldsymbol{X}}}{\mathrm{d}\bar{\boldsymbol{\xi}}}$ is the volume ratio of the physical element to the reference element. The Jacobian matrix for each element can be computed as seen in Equation (3.15).

$$\begin{aligned}[\mathbf{K}_e] &= \int \left[\mathbf{B}_0 + \mathbf{B}_1(\boldsymbol{u}_e)\right]^\mathsf{T} [\mathbf{D}] \left[\mathbf{B}_0 + \frac{1}{2}\mathbf{B}_1(\boldsymbol{u}_e)\right] \mathrm{d}V \\ &= \sum_{i=1}^{N} \left[\mathbf{B}_0 + \mathbf{B}_1(\boldsymbol{u}_e)\right]^\mathsf{T} [\mathbf{D}] \left[\mathbf{B}_0 + \frac{1}{2}\mathbf{B}_1(\boldsymbol{u}_e)\right] |\mathrm{Jac}(\xi_i, \eta_i, \zeta_i)| \cdot w_i \end{aligned} \tag{3.24}$$

Table 3.1 shows the order of Equation (3.24) for each element type when substituting the derivatives of the shape functions into the equation. “TET4" indicates the 4-node linear tetrahedron element with nodes at the corners only, as shown in Appendix A, and “TET10" indicates the 10-node quadratic tetrahedron element with 6 more nodes at the mid of the edges. “HEX8" and “HEX20" represent the 8-node and 20-node hexahedron element, respectively. “HEX8" has shape function of order 3 and “HEX20" has shape function of order 4. The number of Gaussian Quadrature points needed for estimating the stiffness matrix is also listed in the table. Details of the Gaussian quadrature points and the weights can be found in Appendix B.

For the hexahedron elements, volumetric locking is likely to happen when material is incompressible, i.e. with Poisson’s ratio close to 0.5. This is due to the pressure build up within the element as a penalty to keep the volume constant. The elements end up behaving too stiff. Shear locking can also happen in “HEX8" due to the inability to bend of the edge

	TET4	TET10	HEX8	HEX20
Function order	0	4	8	12
No. of Gaussian points	1	11	1 $(1*1*1)$	8 $(2*2*2)$

Table 3.1 *Gaussian points required for stiffness matrix.*

[4]. This results in the development of the artificial shear strain when structures undergo bending. The locking issues for the hexahedron elements can be alleviated by introducing reduced-integration when computing the stiffness matrix [10]. Functions are integrated using an integration scheme that is one order less accurate than the standard scheme, as shown in Table 3.1. For “HEX8", only one Gaussian Quadrature point is used for integration. The point is located in the middle of the element. The reduced linear elements are very tolerant of distortion (Figure 3.2). When bending moment applying to the element, the stress element at the integration point remains zero. The bending mode becomes a zero-energy mode, hence the numerical problem of hourglassing occurs and the element ends up being too flexible. Hourglassing can be controlled by using more refined mesh and with at least one element used through the thickness, so that the integration point will not lie on the neutral axis of the beam. Selectively Reduced Integration [93, 58] and the B-bar [32, 56] method can also be used to cure the hourglass deformations. In these methods, the volumetric and deviatoric parts of the stiffness matrix are treated separately. In this research, locking effect is avoided by using a full reduced integration with hourglassing control for computing the stiffness matrix. The computational time is reduced, as less function evaluations are required.

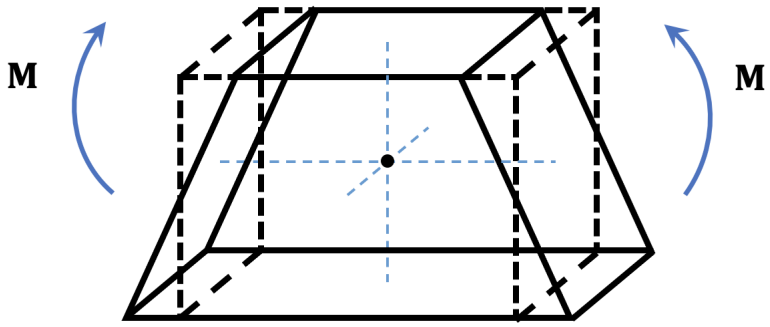


Fig. 3.2 *Deformation of a 8-node hexahedron element with reduced integration subjected to bending moment.*

Jacobian matrix of nonlinear force

The analytical Jacobian matrix is required when solving the nonlinear equations with Newton-Raphson's iteration method. The stiffness matrix $[\mathbf{K}_e]$ contribute to the total internal force in the dynamic equation, i.e. $\boldsymbol{F}^e = [\mathbf{K}_e]\,\mathbf{a}_e$, the Jacobian matrix can be derived as:

$$\frac{\partial \boldsymbol{F}^e(\boldsymbol{u}^e)}{\partial \mathbf{a}_e} = \int \frac{\partial\,[\mathbf{B}_0+\mathbf{B}_1(\boldsymbol{u}_e)]^\mathsf{T}}{\partial \mathbf{a}_e}\,\mathbf{S}\,\mathrm{d}V + \int [\mathbf{B}_0+\mathbf{B}_1(\boldsymbol{u}_e)]^\mathsf{T}\,\frac{\partial \mathbf{S}}{\partial \mathbf{a}_e} \tag{3.25}$$

$$\begin{aligned}\int \frac{\partial\,[\mathbf{B}_0+\mathbf{B}_1(\boldsymbol{u}_e)]^\mathsf{T}}{\partial \mathbf{a}_e}\,\mathbf{S}\,\mathrm{d}V &= \int_V \frac{\partial \mathbf{B}_1(\boldsymbol{u}_e)^\mathsf{T}}{\partial \mathbf{A}(\boldsymbol{u}_e)^\mathsf{T}}\cdot\frac{\partial \mathbf{A}(\boldsymbol{u}_e)^\mathsf{T}\mathbf{S}}{\partial \mathbf{G}\,\mathbf{a}_e}\cdot\frac{\partial \mathbf{G}\,\mathbf{a}_e}{\partial \mathbf{a}_e}\,\mathrm{d}V \\ &= \int [\mathbf{G}]^\mathsf{T}\,[\boldsymbol{\Sigma}(\mathbf{S})]\,[\mathbf{G}]\,\mathrm{d}V\end{aligned} \tag{3.26}$$

As stated in Equation (3.9) and (3.18), the derivative of $\mathbf{S}$ can be derived as:

$$\frac{\partial \mathbf{S}}{\partial \mathbf{a}_e} = [\mathbf{D}]\,\frac{\mathrm{d}\boldsymbol{\varepsilon}^G}{\mathrm{d}\mathbf{a}_e} = [\mathbf{D}]\,[\mathbf{B}_0+\mathbf{B}_1\,(\boldsymbol{u}_e)] \tag{3.27}$$

Hence,

$$\int_V [\mathbf{B}_0+\mathbf{B}_1(\boldsymbol{u}_e)]^\mathsf{T}\,\frac{\partial \mathbf{S}}{\partial \mathbf{a}_e}\,\mathrm{d}V = \int_V [\mathbf{B}_0+\mathbf{B}_1(\boldsymbol{u}_e)]^\mathsf{T}\,[\mathbf{D}]\,[\mathbf{B}_0+\mathbf{B}_1(\boldsymbol{u}_e)]\,\mathrm{d}V \tag{3.28}$$

Thus the Jacobian of the nonlinear force can be expressed as:

$$\begin{aligned}\frac{\partial \boldsymbol{F}^e_{nl}(\boldsymbol{u}_e)}{\partial \mathbf{a}_e} = &\int [\mathbf{B}_0]^\mathsf{T}\,[\mathbf{D}]\,[\mathbf{B}_1]\,\mathrm{d}V + \int [\mathbf{B}_1]^\mathsf{T}\,[\mathbf{D}]\,[\mathbf{B}_0]\,\mathrm{d}V \\ &+ \int [\mathbf{B}_1]^\mathsf{T}\,[\mathbf{D}]\,[\mathbf{B}_1]\,\mathrm{d}V + \int [\mathbf{G}]^\mathsf{T}\,[\boldsymbol{\Sigma}(\mathbf{S})]\,[\mathbf{G}]\,\mathrm{d}V\end{aligned} \tag{3.29}$$

with,

$$\boldsymbol{\Sigma}(\mathbf{S}) = \begin{bmatrix} \sigma_{xx}\otimes\mathbf{I}_3 & \tau_{xy}\otimes\mathbf{I}_3 & \tau_{xz}\otimes\mathbf{I}_3 \\ \tau_{xy}\otimes\mathbf{I}_3 & \sigma_{yy}\otimes\mathbf{I}_3 & \tau_{yz}\otimes\mathbf{I}_3 \\ \tau_{xz}\otimes\mathbf{I}_3 & \tau_{yz}\otimes\mathbf{I}_3 & \sigma_{zz}\otimes\mathbf{I}_3 \end{bmatrix} \tag{3.30}$$

3.1.2 Kinetic energy expression

The kinetic energy of the 3D solid element can be expressed as:

$$\begin{aligned} T &= \frac{1}{2}\int \left[\mathbf{N}\left(\bar{\boldsymbol{\xi}}\right)\cdot \dot{\mathbf{a}}_e(t)\right]^{\mathsf{T}} \rho \left[\mathbf{N}\left(\bar{\boldsymbol{\xi}}\right)\dot{\mathbf{a}}_e(t)\right] \mathrm{d}V \\ &= \frac{1}{2}\{\dot{\mathbf{a}}_e\}^{\mathsf{T}} \int \left[\mathbf{N}\left(\bar{\boldsymbol{\xi}}\right)\right]^{\mathsf{T}} \rho \left[\mathbf{N}\left(\bar{\boldsymbol{\xi}}\right)\right] \mathrm{d}V \{\dot{\mathbf{a}}_e\} \end{aligned} \tag{3.31}$$

Comparing Equations (3.31) with Equation (2.8) yields the symmetric mass matrix $[\mathbf{M}_e]$ of the 3D solid element. The integral function can be estimated by employing Gaussian quadrature rule as shown in Equation (3.32):

$$\begin{aligned} [\mathbf{M}_e] &= \rho \int \boldsymbol{N}^T(\bar{\boldsymbol{\xi}})\boldsymbol{N}(\bar{\boldsymbol{\xi}})\,\mathrm{d}V \\ &= \rho \int\int\int \boldsymbol{N}^T(\bar{\boldsymbol{\xi}})\boldsymbol{N}(\bar{\boldsymbol{\xi}})|\mathrm{Jac}\left(\bar{\boldsymbol{\xi}}\right)|\,\mathrm{d}\xi\,\mathrm{d}\eta\,\mathrm{d}\zeta \\ &= \sum_{i=1}^{N} \mathbf{N}^{\mathsf{T}}(\xi_i,\eta_i,\zeta_i)\,\rho\,\mathbf{N}(\xi_i,\eta_i,\zeta_i)\cdot|\mathrm{Jac}(\xi_i,\eta_i,\zeta_i)|\cdot w_i \end{aligned} \tag{3.32}$$

Table 3.2 lists the order of the highest order terms in Equation (3.32) for each element type when substituting the shape functions into the equation and the number of Gaussian Quadrature points needed for estimating the mass matrix. Details of the Gaussian quadrature points and the weights can be found in Appendix B.

	TET4	TET10	HEX8	HEX20
Function order	2	4	6	8
No. of Gaussian points	4	11	8 $(2*2*2)$	27 $(3*3*3)$

Table 3.2 *Gaussian points required for mass matrix.*

3.1.3 Equation of motion for 3D structures with geometric nonlinearity

The matrices of each element derived in the previous sections need to be transferred back into the global domain of the structure to assemble the global matrices shown in Equation (3.33). $[\mathbf{M}]$ is the global mass matrix and $[\mathbf{C}]$ is the global damping matrix. $[\mathbf{K}_0]$ stands for the global linear stiffness matrix and $[\mathbf{K}_{nl}]$ represents the global nonlinear stiffness matrix due to large strain. The nonlinear stiffness matrix can be expressed as sum of the nonlinearity terms $[\mathbf{K}_1]$, $[\mathbf{K}_2]$, and $[\mathbf{K}_3]$. $\{\boldsymbol{F}_{ext}\}$ is the harmonic excitation force vector. The element's nodal displacement vector $\{\mathbf{a}_e\}$ is transferred into the global response field tensor $\boldsymbol{u}$, with

$$\boldsymbol{u} = \left\{ u_1 \quad u_2 \quad u_3 \quad \cdots \quad u_{\text{DOF}} \right\}^{\mathsf{T}}.$$

$$[\mathbf{M}]\ddot{\boldsymbol{u}} + [\mathbf{C}]\dot{\boldsymbol{u}} + \left([\mathbf{K}_0] + \frac{1}{2}[\mathbf{K}_1(\boldsymbol{u})] + [\mathbf{K}_2(\boldsymbol{u})] + \frac{1}{2}[\mathbf{K}_3(\boldsymbol{u})] \right) \boldsymbol{u} = \{\boldsymbol{F}_{ext}(t)\}$$

$$[\mathbf{M}]\ddot{\boldsymbol{u}} + [\mathbf{C}]\dot{\boldsymbol{u}} + \left([\mathbf{K}_0] + [\mathbf{K}_{nl}(\boldsymbol{u})] \right) \boldsymbol{u} = \{\boldsymbol{F}_{ext}(t)\} \tag{3.33}$$

As discussed in section 2.2.4, damping matrix of the structural expressed in terms of $[\mathbf{M}]$ and $[\mathbf{K}]$ can be assumed to ensure that the system will still possess the classical normal modes, i.e. Rayleigh damping matrix. System damping can be tuned by the two damping coefficients α and β, which depend on the damping ratio ζ.

$$[\mathbf{C}] = \alpha [\mathbf{M}] + \beta [\mathbf{K}_0] \tag{3.34}$$

According to Equation (2.5), the harmonic excitation force vector should be derived as $\boldsymbol{F}_{ext}(t) = \int \mathbf{N}^{\mathsf{T}} \boldsymbol{q}(x,t)\, \mathrm{d}V$. The vector of external forces, $\boldsymbol{q}$, depends on the position of the applied load and on time. In this research, only point load is considered. Hence, for a system with N nodes in the mesh, $\{\boldsymbol{F}_{ext}(t)\}$ has the following form:

$$\{\boldsymbol{F}_{ext}(t)\} = \left\{ F_x^1 \quad F_y^1 \quad F_z^1 \quad F_x^2 \quad F_y^2 \quad F_z^2 \quad \cdots \quad F_x^N \quad F_y^N \quad F_z^N \right\}^{\mathsf{T}} \tag{3.35}$$

3.1.4 Compressed Sparse Row

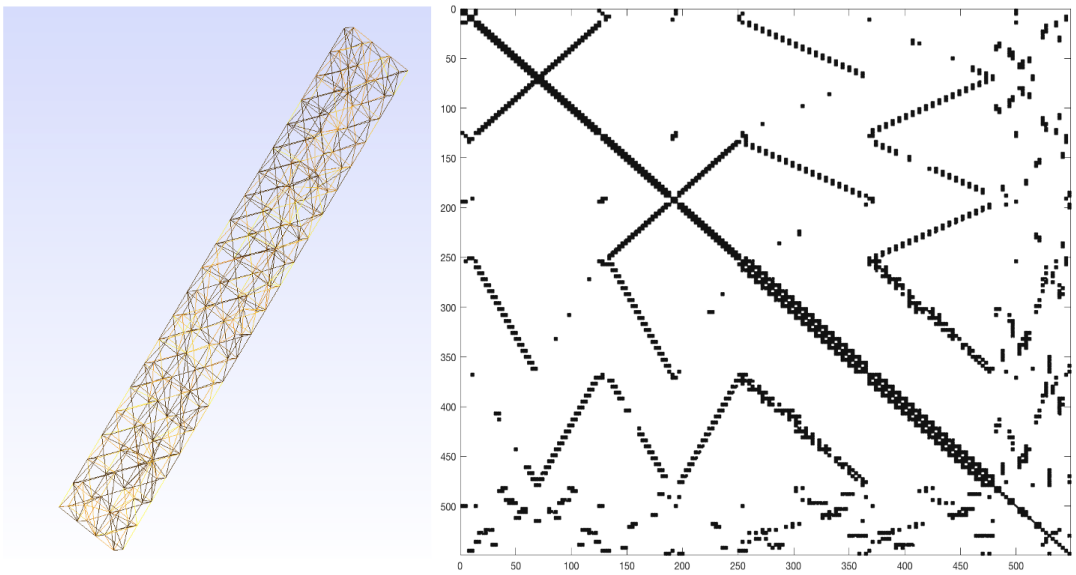


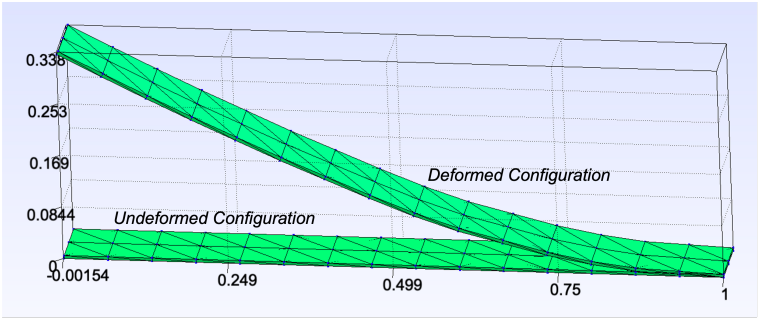
Fig. 3.3 *Sparsity level of the linear stiffness matrix of the the 3D mesh.*

One characteristic or advantage of the FEM is that the matrices generated have a high degree of sparsity (i.e. large number of zero elements as its entries). Figure 3.3 shows the linear stiffness matrix of a 3D mesh, with black squares representing the non-zero elements of the matrix. The mesh has 600 DOFs in total, hence the size of the stiffness matrix is (600×600). Since the computational requirements to analyse complex engineering structures can easily become unmanageable, FEM provides a memory efficient computational approach to investigate nonlinear behaviour. In the investigation herein presented the high level of sparsity gives us the choice to use Compressed Sparse Row (CSR) storage numerical method to reduce the computational burden to converge to a solution. Instead of processing and storing the dense matrices with a large amount of zeros, CSR format stores the dense matrix into three arrays, as illustrated in Equation (3.36). For a $m \times n$ dense matrix, $\{\mathbf{A}\}$ stores the values of all non-zero elements row-by-row and $\{\mathbf{JA}\}$ stores the corresponding column indices of the non-zero elements. These two arrays have length of the total number of the non-zeros in the matrix. Array $\{\mathbf{IA}\}$ with length of $m+1$, shows the accumulated number of non-zeros of each row plus one. i.e. the $(i+1)$-th element shows the total number of non-zeros from row 1 to row i plus one. The first element of the array is defaulted as 1. CSR format enables the computer to operate with sparse matrices more efficiently and to work with large sparse matrices that are infeasible in the dense format.

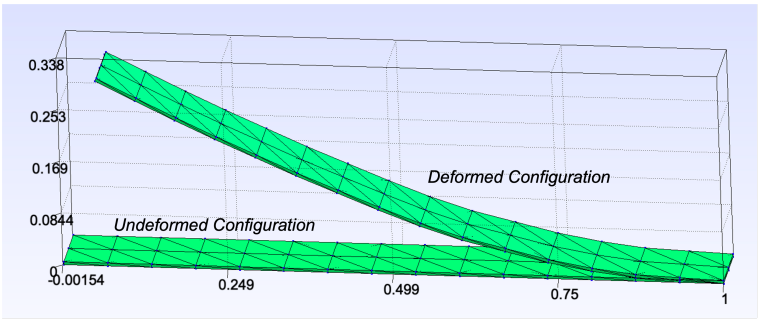
$$[\mathbf{M}] = \begin{bmatrix} 0 & 0 & 0 & 2 & 0 \\ 1 & 0 & 0 & 0 & 15 \\ 0 & 10 & 0 & 0 & 0 \\ 0 & 20 & 0 & 3 & 0 \end{bmatrix} \quad \Longrightarrow \quad \begin{aligned} \{\mathbf{A}\} &= \begin{Bmatrix} 2 & 1 & 15 & 10 & 20 & 3 \end{Bmatrix} \\ \{\mathbf{IA}\} &= \begin{Bmatrix} 1 & 2 & 4 & 5 & 7 \end{Bmatrix} \\ \{\mathbf{JA}\} &= \begin{Bmatrix} 4 & 1 & 5 & 2 & 2 & 4 \end{Bmatrix} \end{aligned} \tag{3.36}$$

3.2 Effect of geometric nonlinearity on static deformation

To show the effect of the nonlinear terms on the results of the analysis, a 3D cantilevered beam model with dimension of $5\text{mm} * 100\text{mm} * 1000\text{mm}$ is used. The point load of $\boldsymbol{F}_{ext} = 30000$ N is applied at the free end of the beam. The nonlinear beam used is made with homogeneous material of Young's Modulus $E = 104$ GPa, density $\rho = 4400\ \text{kg/m}^3$, and Poisson's ratio $\nu = 0.3$. Figure 3.4 shows the deformation of the 3D cantilevered beam under static point load. A total of 284 4-node tetrahedron elements are used in the FE model. Figure 3.4a shows the deformation of the 3D beam with consideration of only the linear part of the strain, i.e. $[\mathbf{K}_0]\,\boldsymbol{u} = \{\boldsymbol{F}_{ext}\}$, artifacts can be observed such as increase in volume. Figure 3.4b shows the simulation result with the full Green-Lagrange strain measure employed in the model, i.e. $([\mathbf{K}_0] + [\mathbf{K}_{nl}(\boldsymbol{u})])\,\boldsymbol{u} = \{\boldsymbol{F}_{ext}\}$. Newton-Raphson's iteration method [15] is used to solve the



(a) Linear Model



(b) Nonlinear Model

Fig. 3.4 *Deformation of 3D cantilevered beam under static point load.*

nonlinear equation. $\frac{\partial \boldsymbol{F}_{nl}(\boldsymbol{u}_n)}{\partial \boldsymbol{u}_n}$ can be computed as shown in Equation (3.29).

$$\text{For :} \qquad \boldsymbol{F}(\boldsymbol{u}) = \left([\mathbf{K}_0] + [\mathbf{K}_{nl}(\boldsymbol{u})]\right)\boldsymbol{u} - \{\boldsymbol{F}_{ext}\} = 0$$

$$\boldsymbol{u}_{n+1} = \boldsymbol{u}_n - \frac{\boldsymbol{F}(\boldsymbol{u}_n)}{\boldsymbol{F}'(\boldsymbol{u}_n)} \tag{3.37}$$

$$\text{with :} \quad \boldsymbol{F}'(\boldsymbol{u}_n) = [\mathbf{K}_0] + \frac{\partial \boldsymbol{F}_{nl}(\boldsymbol{u}_n)}{\partial \boldsymbol{u}_n} \tag{3.38}$$

The effect of the nonlinear part of the strain measure becomes significant when the response amplitude is large. Nonlinearities appear in all real systems, and trying to model systems undergoing large deformation with linear theory leads to erroneous solutions. Point loads with different magnitude are applied at the tip, the corresponding flapwise deflections are recorded. Figure 3.5 shows the comparison of the force-displacement relationship in both linear and nonlinear FEM models. When the maximum deflections reach above 30% of the total length, the approximations start to diverge from the real values in the linear FEM model. The deformation of the model under loading with nonlinear effect considered is also validated with the results generated from ABAQUS. It is worth mentioning that the linear model is still

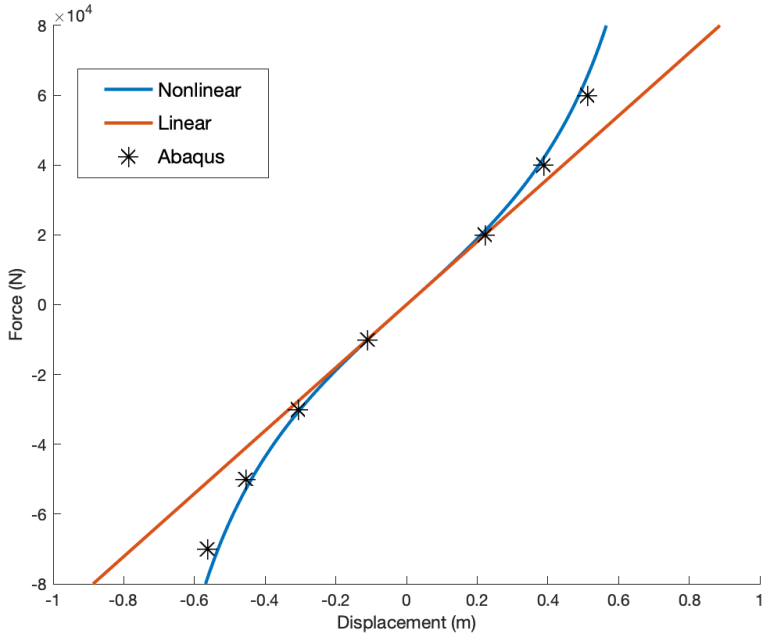


Fig. 3.5 *Force-displacement relationship in linear and nonlinear model.*

a good approximation tool for small deflections due to its simplicity to implement and less demand on the computing power.

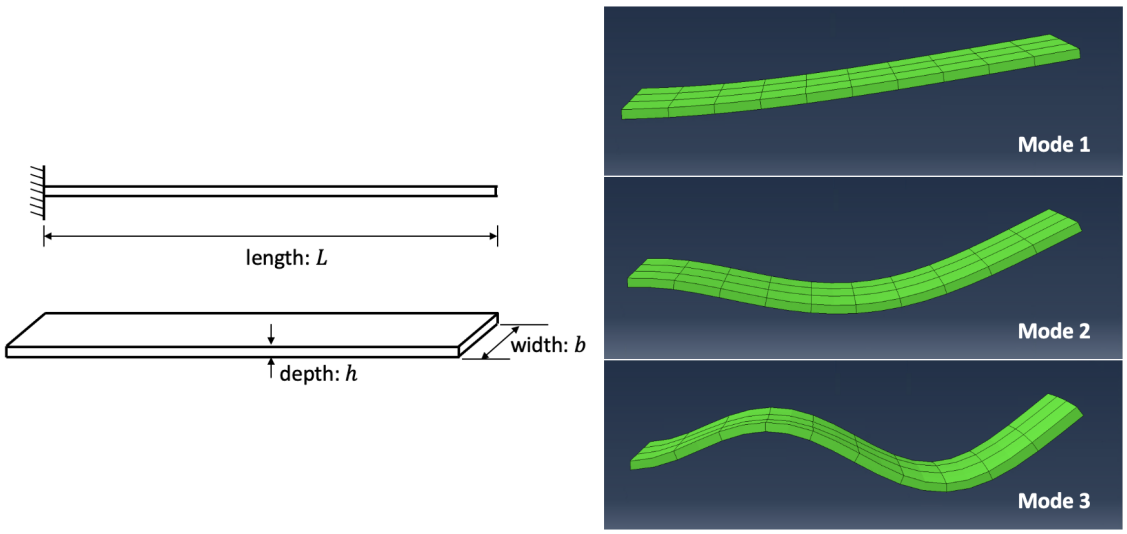


Fig. 3.6 *Schematic of the cantilevered beam and the first three out-of-plane bending modes.*

3.3 Linear modal analysis

In this section, the natural frequencies of a 3D cantilevered beam computed from the finite element model are compared with the results generated from the ABAQUS for validation. The first three out-of-plane bending modes of beams are investigated, Figure 3.6. In the FE model, choosing the appropriate element type is critical for obtaining accurate and reliable predictions. Characteristics of different element types are also discussed. The convergences of different element types to the analytical values generated from the Euler-Bernoulli beam theory are studied. Beams with different dimensions are used for investigation. Constant second moment of area I and uniform mass distribution along the beam is assumed. Rectangular cross-section is used for all cantilevered beams, hence I is computed as $I = \frac{bh^3}{12}$.

3.3.1 Eigenvalue problem of the finite element model

The free response of an undamped discretised mechanical systems is expressed as:

$$[\mathbf{M}]\,\ddot{\boldsymbol{u}} + \left([\mathbf{K}_0] + [\mathbf{K}_{nl}(\boldsymbol{u})]\right)\boldsymbol{u} = 0 \tag{3.39}$$

Harmonic motion is assumed for every point of the structure, hence $\ddot{\boldsymbol{u}} = \omega^2\boldsymbol{u}$. Resonance frequencies and the linear mode shapes of the FE model can be computed by solving the eigenvalue problem in Equation (3.40), where ω_i is the i-th angular frequency and vector $\boldsymbol{\phi}_i$ is the i-th linear mode shape.

$$\left([\mathbf{K}_0] - \omega_i^2\,[\mathbf{M}]\right)\{\boldsymbol{\phi}_i\} = 0 \quad \Rightarrow \quad \det\left([\mathbf{K}_0] - \omega_i^2\,[\mathbf{M}]\right) = 0 \tag{3.40}$$

In the current research, the matrices are stored in sparse format. The eigenvaule problem is solved by using Intel® oneAPI Math Kernel Library. The “mkl_sparse_d_gv" routine is used for computing the largest/smallest eigenvalues and the corresponding eigenvectors of a generalised eigenvalue problem, $\boldsymbol{A}\boldsymbol{x} = \lambda\,\boldsymbol{B}\boldsymbol{x}$. The generalised eigenvalue problem can be solved by using either the Krylov-Schur method [140, 139] or the subspace Iteration technique based on FEAST algorithm [109]. Both methods use subspace iteration algorithm in conjunction with the Rayleigh-Ritz procedure for computing partial eigensolution, i.e. calculation of a segment of eigenvalues and their corresponding eigenvectors for a large matrix. The Krylov subspace iteration approach are based on Lanczos Algorithm, which transforms the $(n \times n)$ matrix $\boldsymbol{A}$ into a $(m \times m)$ tridiagonal matrix $\boldsymbol{T} = \boldsymbol{V}^{\intercal}\boldsymbol{A}\boldsymbol{V}$, with $m \ll n$. The $(n \times m)$ matrix $\boldsymbol{V}$ consists of orthonormal subspaces. The FEAST algorithm is a type of contour integral-based eigensolvers for Hermitian matrix [60]. A subspace iteration is applied to a rational matrix function to filter the wanted eigenvalues from the unwanted ones.

With comparison to the Krylov-Schur method, the FEAST algorithm is more numerically stable and efficient. Since both the mass and stiffness matrices are symmetric in this research, the FEAST algorithm is selected.

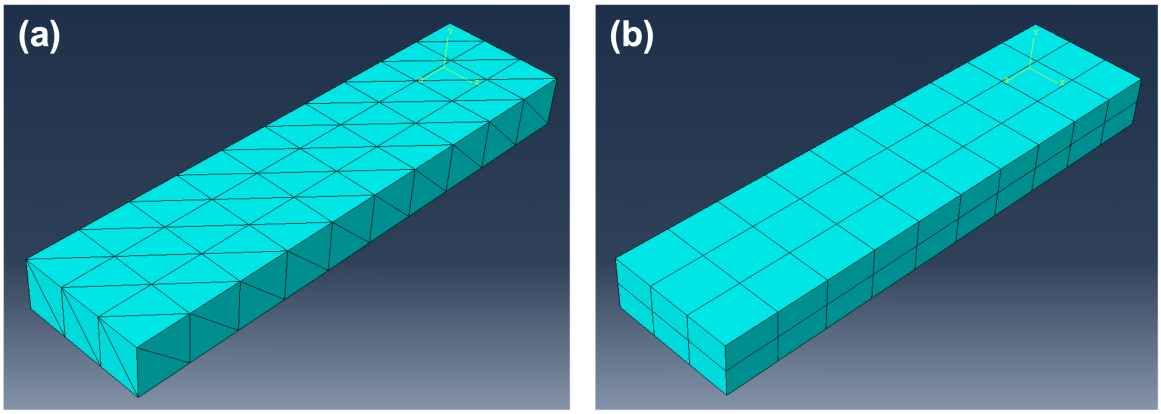


Fig. 3.7 *Cantilevered beam meshed with (a) Tetrahedron elements; (b) Hexahedron elements.*

	Element Number	**FE Model**			**ABAQUS**		
		ω_1	ω_2	ω_3	ω_1	ω_2	ω_3
TET4	352	122.58	725.16	1874.59	122.57	725.17	1874.60
TET10		79.20	476.17	1262.16	79.20	476.18	1262.20
HEX8	60	83.37	530.98	1388.35	83.36	531.00	1388.40
HEX8R		68.20	411.12	NaN	68.18	411.13	NaN
HEX20		79.20	475.13	1254.02	79.20	475.14	1254.00
HEX20R		79.04	473.94	1249.84	79.03	473.94	1249.80

Table 3.3 *Natural frequencies (Hz) of the first three out-of-plane bending modes for cantilevered beam.*

Table 3.3 lists the natural frequencies (Hz) of the first three out-of-plane bending modes of a cantilevered beam. The 3D beam has a dimension of $0.25m * 0.1m * 1m$. Homogeneous material with Young's Modulus $E = 104$ GPa, density $\rho = 4400$ kg/m^3, and Poisson's ratio $\nu = 0.3$ is assumed. Meshes with both tetrahedron and hexahedron elements, Figure 3.7, are investigated. The natural frequencies calculated from the FEM codes have a good match with the ABAQUS results for all element types. For the 20-node hexahedron case, the mesh with the reduced-integration elements (HEX20R) generates very similar results as with the full-integration element (HEX20). The full integration on the 8-node hexahedron element (HEX8)

can lead to the shear locking issue due to inability to bend the edge. The additional shear stress introduced makes the element appear to be stiffer. The development of the artificial shear strain can be alleviated by applying the reduced-integration technique (HEX8R). Hourglassing is observed on the third bending mode of HEX8R. The only one integration point used in the first-order element can result in the excitation of zero-strain deformation modes that produce highly spurious results. Figure 3.8 demonstrates the hourglassing effect on the third bending modes of HEX8R. The elements are severely deformed at the node of the bending mode, while the overall mesh section is undeformed. The problem of hourglassing can be controlled by using a more refined mesh.

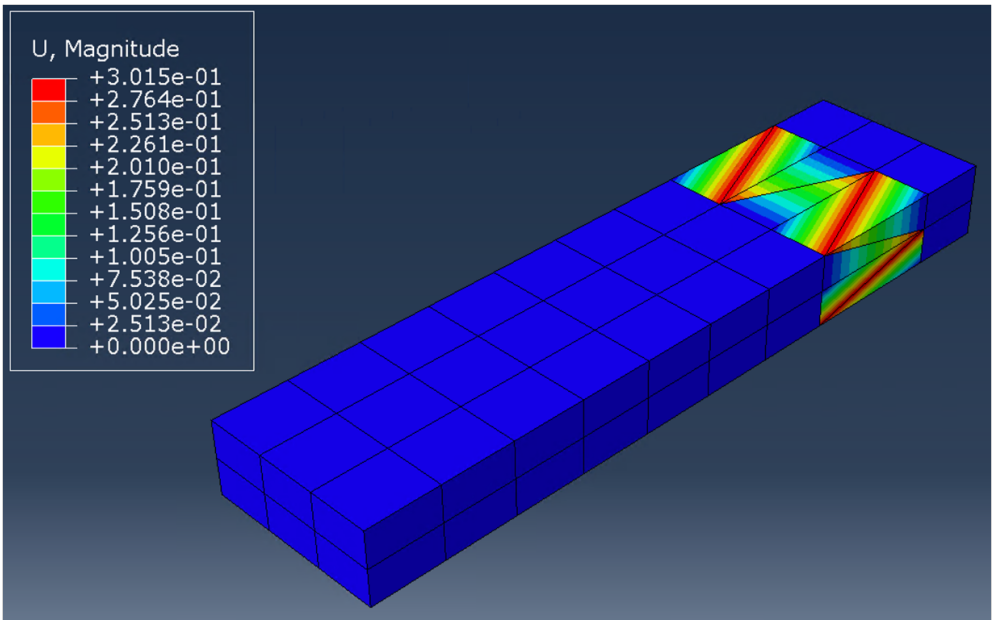


Fig. 3.8 *Hourglassing effect on the reduced-integration 8-node hexahedron element.*

3.3.2 Analytical value

Following Equation (2.36) in section 2.2.3, the free response of a free Euler-Bernoulli beam can be expressed as:

$$EI\frac{\partial^4 w}{\partial x^4} + \rho A\frac{\partial^2 w}{\partial t^2} = 0 \tag{3.41}$$

with A being the cross-section area of the beam, ρ and E being the density and Young's modulus of the material. The transverse displacement w can be expressed in a harmonic format of $w(x,t) = \mathrm{Re}[\hat{w}(x)e^{-i\omega t}]$ with ω being the frequency of vibration. Equation (3.42)

can be re-written as:

$$EI\frac{\partial^4 \hat{w}}{\partial x^4} + \omega^2 \rho A \hat{w} = 0 \tag{3.42}$$

The general solution is:

$$\hat{w} = A_1 \cosh(\beta x) + A_2 \sinh(\beta x) + A_3 \cos(\beta x) + A_4 \sin(\beta x) \tag{3.43}$$
$$with, \quad \beta := \left(\frac{\rho A \omega^2}{EI}\right)^{1/4}$$

Constants A_1, A_2, A_3 and A_4 can be defined by introducing boundary condition equations. For a cantilevered beam with boundary conditions shown in Table 2.3, the first three roots are $\beta_1 L = 0.596864\pi$, $\beta_2 L = 1.49418\pi$ and $\beta_3 L = 2.50025\pi$. Hence for a cantilevered beam with length L, the analytical value of the first three natural frequencies (rad/s) can be derived. Since the shear deformation is neglected in the Euler-Bernoulli beam theory, only out-of-plane bending modes can be computed.

$$\omega_1 = (1.875)^2\sqrt{\frac{EI}{\rho A L^4}}, \quad \omega_2 = (4.695)^2\sqrt{\frac{EI}{\rho A L^4}}, \quad \omega_3 = (7.855)^2\sqrt{\frac{EI}{\rho A L^4}} \tag{3.44}$$

3.3.3 Convergence study

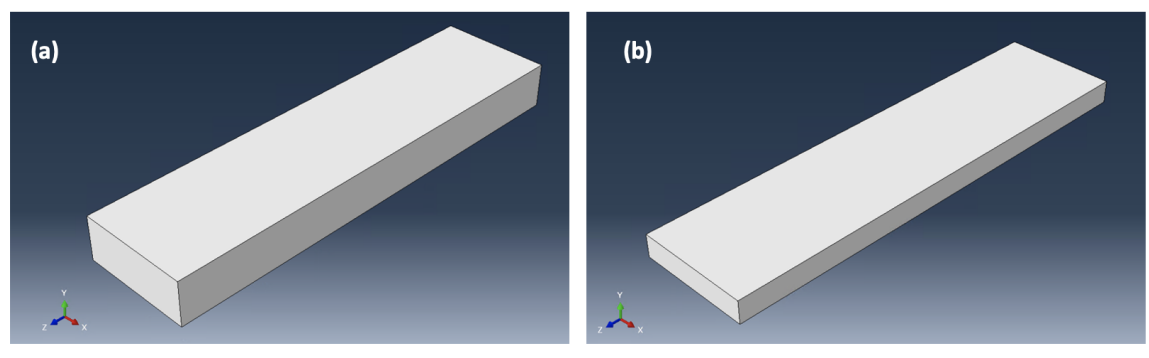
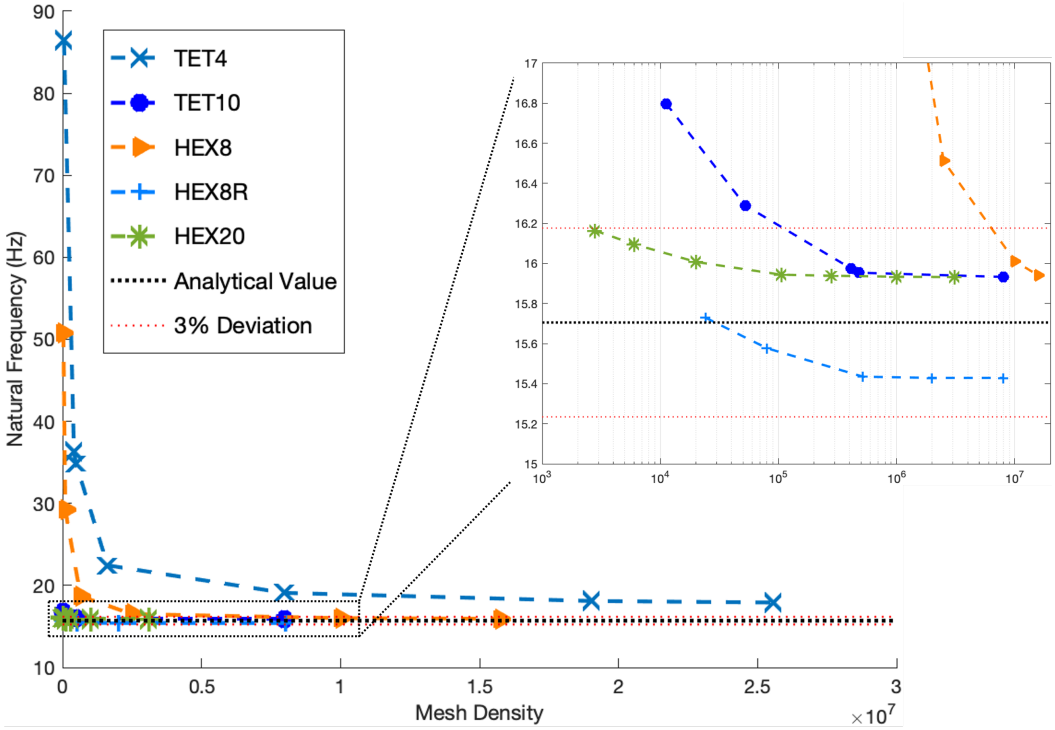
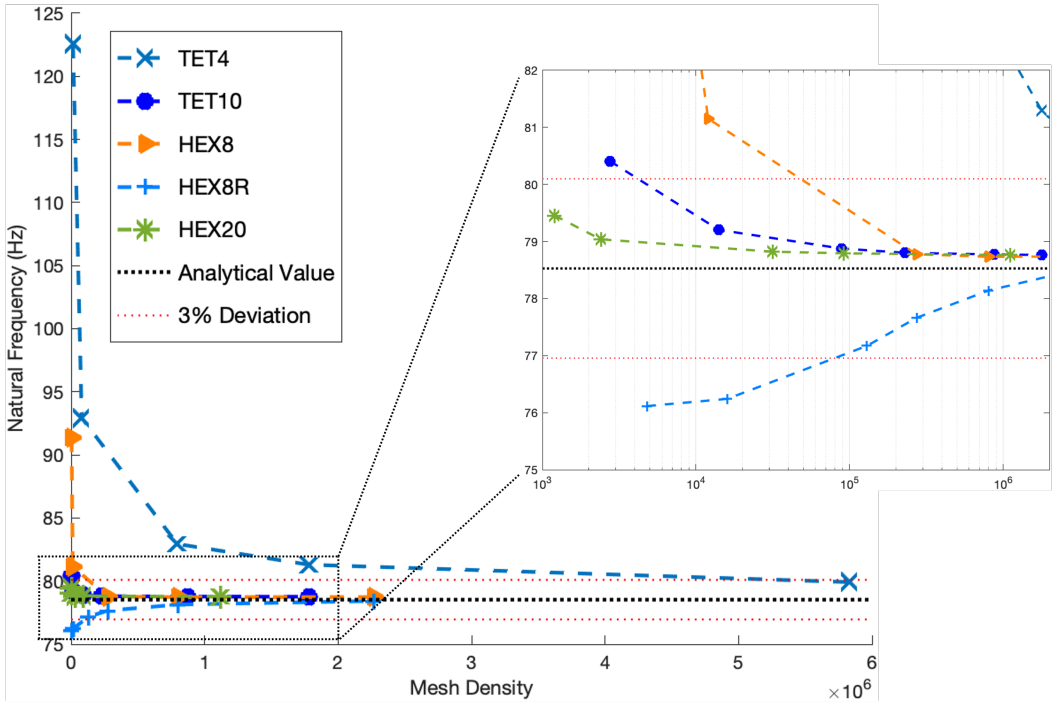


Fig. 3.9 *Cantilevered beams used for modal analysis.*

Two different cantilevered beams are used for the convergence study, as shown in Figure 3.9. The flat beam has a dimension of $(0.25m * 0.02m * 1m)$ and the deep one with a dimension of $(0.25m * 0.1m * 1m)$. Homogeneous material with Young's Modulus $E = 104$ GPa, density $\rho = 4400\ \mathrm{kg/m^3}$, and Poisson's ratio $\nu = 0.3$ is assumed. Figure 3.10 shows the convergence rate of different element types. The first out-of-plane bending frequencies computed from Equation (3.44) are used as reference values. The natural frequencies (Hz) yielded by using



(a) *Flat cantilevered beam* $(0.25m * 0.02m * 1m)$



(b) *Deep cantilevered beam* $(0.25m * 0.1m * 1m)$

Fig. 3.10 *Convergence of the finite element model with theoretical values.*

different mesh densities are compared with the analytical values. The mesh density indicates the number of element used per unit volume (m^3). The mathematical model assumes the perfect Euler-Bernoulli beam. Due to the nature of the 3D solid elements, the FE results will never be exactly the same as the analytical values. A relative 2-3% deviation between the FE results and their analytical counterparts is expected. For both beam cases, structures discretised with the first-order elements (TET4 and HEX8) are extremely stiff in the coarse mesh. The accuracies of the results increase with the refinement of the mesh. Since the edge of HEX8 can not be curved, multiple elements need to be applied on the depth edges of both beams. The convergence rate of HEX8 is better in the deep beam case. The reduced-integration elements (HEX8R) ease the shear locking problem of HEX8. To avoid the hourglassing effect, even number of elements are applied on the depth edge for the beam. Hence the integration points are not lying on the neutral axis of the beam. The TET4 elements are in general too stiff for structural calculations, unless using a very fine mesh. The convergence rate is the slowest among the others. Although TET4 has the simplest formulation, TET4 elements are not recommended for analysis. For the thin beam case, the tetrahedron elements tend to be too stiff for the problem. The convergence rates of the tetrahedron elements improve significantly in the deep beam case. TET10 elements can achieve good results with much lower mesh density. Since HEX20 and HEX20R generate very similar results, only the results of HEX20 are presented in the plots. The performance of HEX20 elements is good in both cases. Accurate results can be achieved with only few elements. The downside about the 20-node hexahedron element is that it has the most complicated formulation. For each element, 60 DOFs need to be considered in the equation. The computational time is increased when handling with large matrices.

3.4 Dynamic analysis in frequency domain

$$
\begin{aligned}
&[\mathbf{M}]\ddot{\boldsymbol{u}} + [\mathbf{C}]\dot{\boldsymbol{u}} + ([\mathbf{K}_0] + [\mathbf{K}_{nl}(\boldsymbol{u})])\,\boldsymbol{u} = \{\boldsymbol{F}_{ext}(\omega,t)\} \\
&\qquad\qquad \Downarrow \\
&[\mathbf{M}]\ddot{\boldsymbol{u}} + [\mathbf{C}]\dot{\boldsymbol{u}} + [\mathbf{K}_0]\,\boldsymbol{u} + \{\boldsymbol{F}_{nl}(\boldsymbol{u})\} = \{\boldsymbol{F}_{ext}(\omega,t)\}
\end{aligned}
\tag{3.45}
$$

The nonlinear ODE involved in the dynamic systems (Equation 3.45) can be solved by using harmonic balance method (HBM) coupled with Alternating Frequency Time (AFT) method [73]. Details of the algorithms in the simulation are reviewed in this section. The dynamic behaviours of the geometrically nonlinear beams undergoing forced frequency response are investigated.

3.4.1 Non-dimensionalization and scaling of the dynamics systems

With a dimensionless mathematical model, no physical quantities need to be assigned. Scaling of differential equations is a simple mathematical process, consisting of the chain rule for differentiation and some algebra. Traditionally, scaling was mainly used to identify small parameters in mathematical models. Nowadays, scaling is used in running numerical simulations, since scaling greatly simplifies the choice of input values and makes the simulation results more widely applicable. The dimensionless parameters in scaled models express ratios of physical effects rather than levels of individual effects. This simplification can increase the understanding of the physical problem as one can compare the impact of different parameters on the solutions easily. [79]

The equation of motion for the nonlinear dynamic systems as shown in Equation (3.45) needs to be scaled especially during the continuation stage. The independent variable time t is expressed as a dimensionless parameter $\tau = \omega_n t$, where ω_n is the fundamental frequency of the dynamic system. From the relationship between t and τ, we can have:

$$\omega_n = \frac{\mathrm{d}\tau}{\mathrm{d}t} \tag{3.46}$$

$$\dot{\boldsymbol{u}} = \frac{\mathrm{d}\boldsymbol{u}}{\mathrm{d}t} = \frac{\mathrm{d}\boldsymbol{u}}{\mathrm{d}\tau}\frac{\mathrm{d}\tau}{\mathrm{d}t} = \omega_n \frac{\mathrm{d}\boldsymbol{u}}{\mathrm{d}\tau} \tag{3.47}$$

$$\ddot{\boldsymbol{u}} = \frac{\mathrm{d}}{\mathrm{d}t}\frac{\mathrm{d}\boldsymbol{u}}{\mathrm{d}t} = \frac{\mathrm{d}}{\mathrm{d}\tau}\frac{\mathrm{d}\tau}{\mathrm{d}t}\left(\frac{\mathrm{d}\boldsymbol{u}}{\mathrm{d}\tau}\frac{\mathrm{d}\tau}{\mathrm{d}t}\right) = \omega_n^2 \frac{\mathrm{d}^2\boldsymbol{u}}{\mathrm{d}\tau^2} \tag{3.48}$$

The mass matrix in Equation (3.45) is scaled down by a factor of M_0, i.e. $[\hat{\mathbf{M}}] = \dfrac{[\mathbf{M}]}{M_0}$, and the response amplitude $\boldsymbol{u}$ is scaled down by a factor of A_0, i.e. $\{\hat{\boldsymbol{u}}\} = \dfrac{\{\boldsymbol{u}\}}{A_0}$. The scaled equation of motion can then be derived:

$$\begin{aligned}
[\mathbf{M}]\{\ddot{\boldsymbol{u}}\} + [\mathbf{C}]\{\dot{\boldsymbol{u}}\} + [\mathbf{K}_0]\{\boldsymbol{u}\} + \{\boldsymbol{F}_{nl}\} &= \{\boldsymbol{F}_{ext}\} \\
A_0 M_0 \omega_n^2 [\hat{\mathbf{M}}]\frac{\mathrm{d}^2\hat{\boldsymbol{u}}}{\mathrm{d}\tau^2} + A_0\,\omega_n [\mathbf{C}]\frac{\mathrm{d}\hat{\boldsymbol{u}}}{\mathrm{d}\tau} + A_0 [\mathbf{K}_0]\{\hat{\boldsymbol{u}}\} + \{\boldsymbol{F}_{nl}\} &= \{\boldsymbol{F}_{ext}\} \\
[\hat{\mathbf{M}}]\{\hat{\boldsymbol{u}}''\} + [\hat{\mathbf{C}}]\{\hat{\boldsymbol{u}}'\} + [\hat{\mathbf{K}}_0]\{\hat{\boldsymbol{u}}\} + \{\hat{\boldsymbol{F}}_{nl}\} &= \{\hat{\boldsymbol{F}}_{ext}\}
\end{aligned} \tag{3.49}$$

where $\{\cdot\}'$ represent the derivative of the parameter $\{\cdot\}$ with respect to τ. The scaled damping and stiffness matrix and the force vectors are:

$$[\hat{\mathbf{C}}] = \frac{[\mathbf{C}]}{M_0\,\omega_n}, \quad [\hat{\mathbf{K}}_0] = \frac{[\mathbf{K}_0]}{M_0\,\omega_n^2}, \quad \{\hat{\boldsymbol{F}}_{nl}\} = \frac{\{\boldsymbol{F}_{nl}\}}{A_0 M_0\,\omega_n^2}, \quad \{\hat{\boldsymbol{F}}_{ext}\} = \frac{\{\boldsymbol{F}_{ext}\}}{A_0\,cM_0\,\omega_n^2} \tag{3.50}$$

The Jacobian matrix of the scaled nonlinear force $\hat{\boldsymbol{F}}_{nl}$ is:

$$\frac{\partial \hat{\boldsymbol{F}}_{nl}}{\partial \hat{\boldsymbol{u}}} = \frac{\partial \boldsymbol{F}_{nl}(\boldsymbol{u})}{\partial \boldsymbol{u}} / \left(M_0\,\omega_n^2\right) \tag{3.51}$$

3.4.2 Harmonic Balance Method with Alternating Fourier Transformation for forced vibration analysis

HBM uses a linear combination of sinusoidal functions to build the solution. The dynamic response $\boldsymbol{u}$ to the periodic excitation is expected to be ω-periodic. As introduced in Section 2.3.2, the periodic vectors $\boldsymbol{u}$, $\boldsymbol{F}_{ext}$ and $\boldsymbol{F}_{nl}$ can be estimated as a truncated Fourier series to the N_H-th harmonic as shown in Equation (3.52). $\chi(\omega,t)$ represents the ω-periodic vectors. $\tilde{\chi}$ is the collection of all Fourier coefficients for all DOFs in the system.

$$\chi(\omega,t) = \frac{1}{2}\tilde{\chi}^{0,c} + \sum_{k=1}^{N_H} \tilde{\chi}^{k,c}\cos(n\omega t) + \tilde{\chi}^{k,s}\sin(k\omega t) \tag{3.52}$$

$$\tilde{\chi} = \left\{\tilde{\chi}^{0,c} \quad \tilde{\chi}^{1,c} \quad \tilde{\chi}^{1,s} \quad \tilde{\chi}^{2,c} \quad \tilde{\chi}^{2,s} \quad \ldots \quad \tilde{\chi}^{N_H,c} \quad \tilde{\chi}^{N_H,s}\right\} \tag{3.53}$$

The equation of motion in the time domain can hence be transformed into equation in frequency domain (Equation 3.54). The derivation of $\mathbf{Z}(\omega)$ can be found in Equation (2.73). Parameters $\tilde{\boldsymbol{q}}$, $\tilde{\boldsymbol{b}}_{nl}$ and $\tilde{\boldsymbol{b}}_{ext}$ are $\boldsymbol{u}$, $\boldsymbol{F}_{nl}$ and $\boldsymbol{F}_{ext}$ in frequency domain respectively. For a dynamic system, the variables in frequency domain have a size of $(2N_H+1)\times$ DOF. HBM is the most popular frequency domain method used for calculating the periodic steady-state response. It provides a simpler and more systematic approach for steady-state analysis, which can deal with highly nonlinear systems with no ill or instability in the algorithm. Low orders of approximation would be sufficient to provide an accurate approximation for smooth nonlinearities. Errors involved in this method are introduced by the truncation of the Fourier series.

$$\mathbf{R}(\omega,\tilde{\boldsymbol{q}}) \equiv \mathbf{Z}(\omega)\tilde{\boldsymbol{q}} + \tilde{\boldsymbol{b}}_{nl}(\tilde{\boldsymbol{q}}) - \tilde{\boldsymbol{b}}_{ext} = 0 \tag{3.54}$$

AFT methodology is used to compute $\tilde{\boldsymbol{b}}_{nl}$. The response $\tilde{\boldsymbol{q}}$ is transformed into time domain by applying Inverse Discrete Fourier Transform (IDFT). Discrete Fourier Transform (DFT) is then followed to compute the resulting nonlinear force in frequency domain $\tilde{\boldsymbol{b}}_{nl}$ as shown

in Equation 3.55.

$$\tilde{\boldsymbol{q}} \xrightarrow{\text{IDFT: } [\mathscr{F}]^{-1}} \underline{\boldsymbol{u}}(t) \xrightarrow{[\mathbf{K}_{nl}(\boldsymbol{u})]} \underline{\boldsymbol{F}}_{nl}(t) \xrightarrow{\text{DFT: } [\mathscr{F}]} \tilde{\boldsymbol{b}}_{nl}(\tilde{\boldsymbol{q}}) \tag{3.55}$$

In the Discrete Fourier Transform, vector of displacement in time domain $\underline{\boldsymbol{u}}$ has a length of $(\text{DOF} \times N_t)$, with N_t being the total number of samples taken per period in DFT.

$$\begin{aligned}\underline{\boldsymbol{u}} = \{&\left(u^1(t_1),\, u^1(t_2),\, ...,\, u^1(t_{Nt})\right) \quad \left(u^2(t_1),\, u^2(t_2),\, ...,\, u^2(t_{Nt})\right) \\ &... \quad \left(u^{\text{DOF}}(t_1),\, u^{\text{DOF}}(t_2),\, ...,\, u^{\text{DOF}}(t_{Nt})\right)\}\end{aligned} \tag{3.56}$$

The vector of nonlinear force in time domain $\underline{\boldsymbol{F}}_{nl}$ can be expressed in the same way as $\underline{\boldsymbol{u}}$.

$$\begin{aligned}\underline{\boldsymbol{F}}_{nl} = \{&\left(F^1_{nl}(t_1),\, F^1_{nl}(t_2),\, ...,\, F^1_{nl}(t_{Nt})\right) \quad \left(F^2_{nl}(t_1),\, F^2_{nl}(t_2),\, ...,\, F^2_{nl}(t_{Nt})\right) \\ &... \quad \left(F^{\text{DOF}}_{nl}(t_1),\, F^{\text{DOF}}_{nl}(t_2),\, ...,\, F^{\text{DOF}}_{nl}(t_{Nt})\right)\}\end{aligned} \tag{3.57}$$

The $(2N_H + 1) \times \text{DOF}$ vector of Fourier coefficients for the response is expressed as:

$$\tilde{\boldsymbol{q}} = \left\{(\mathbf{c}_0)^\mathsf{T} \quad (\mathbf{c}_1)^\mathsf{T} \quad (\mathbf{s}_1)^\mathsf{T} \quad \cdots \quad (\mathbf{c}_{N_H})^\mathsf{T} \quad (\mathbf{s}_{N_H})^\mathsf{T}\right\} \tag{3.58}$$

$$\begin{aligned}\textit{with}, \quad \mathbf{c}_k &= \left\{\tilde{q}^1_{k,c} \quad \tilde{q}^2_{k,c} \quad \tilde{q}^3_{k,c} \quad \cdots \quad \tilde{q}^{\text{DOF}}_{k,c}\right\}, \\ \mathbf{s}_k &= \left\{\tilde{q}^1_{k,s} \quad \tilde{q}^2_{k,s} \quad \tilde{q}^3_{k,s} \quad \cdots \quad \tilde{q}^{\text{DOF}}_{k,s}\right\}\end{aligned} \tag{3.59}$$

Similarly, the $(2N_H + 1) \times \text{DOF}$ vector of Fourier coefficients for the nonlinear force has the form of:

$$\tilde{\boldsymbol{b}}_{nl} = \left\{\tilde{\boldsymbol{b}}^{0,c}_{nl} \quad \tilde{\boldsymbol{b}}^{1,c}_{nl} \quad \tilde{\boldsymbol{b}}^{1,s}_{nl} \quad \cdots \quad \tilde{\boldsymbol{b}}^{N_H,c}_{nl} \quad \tilde{\boldsymbol{b}}^{N_H,s}_{nl}\right\}^\mathsf{T} \tag{3.60}$$

DFT $[\mathscr{F}]$ transforms variables from time domain into frequency domain, i.e. $\underline{\boldsymbol{u}}$ into $\tilde{\boldsymbol{q}}$. $[\mathscr{F}]$ is defines as:

$$\tilde{q}^i_{k,c} = \frac{2}{N_t} \times \sum_{n=0}^{N_t-1} \underline{u}^i(t_n) \cdot \cos\left(\frac{2\pi}{N_t} \cdot k \cdot n\right) \tag{3.61}$$

$$\tilde{q}^i_{k,s} = \frac{2}{N_t} \times \sum_{n=0}^{N_t-1} \underline{u}^i(t_n) \cdot \sin\left(\frac{2\pi}{N_t} \cdot k \cdot n\right) \tag{3.62}$$

The inverse of the transformation $[\mathscr{F}]^{-1}$ is defined as:

$$\underline{u}^i(t_n) = \frac{1}{2}c_0^i + \sum_{k=1}^{N_H} c_k^i \cdot \cos\left(\frac{2\pi}{N_t}\cdot k \cdot n\right) + \sum_{k=1}^{N_H} s_k^i \cdot \sin\left(\frac{2\pi}{N_t}\cdot k \cdot n\right) \tag{3.63}$$

The formulation in Equation (3.54) so far has $(2N_H+1)\times$ DOF equations and $(2N_H+1)\times$ DOF$+1$ unknowns, i.e. $(\omega,\tilde{\boldsymbol{q}})$. The system is underdetermined, one more constraint need to be added into the equations. Harmonic Balance Method (HBM) together with Arc-length continuation scheme (Equation (2.96)) is used in this research to calculate the periodic response of a nonlinear system:

$$r(\omega,\tilde{\boldsymbol{q}}) \equiv (\tilde{\boldsymbol{q}}-\tilde{\boldsymbol{q}}_0)\cdot(\tilde{\boldsymbol{q}}-\tilde{\boldsymbol{q}}_0) + (\omega-\omega_0)^2 - \Delta s^2 = 0 \tag{3.64}$$

where Δs is the continuation step size, $\tilde{\boldsymbol{q}}$ and ω are the predicted solution and frequency from $\tilde{\boldsymbol{q}}_0$ and ω_0. The equation of motion in frequency domain becomes:

$$\mathbf{F}(\omega,\tilde{\boldsymbol{q}}) = \begin{bmatrix} \boldsymbol{R}(\omega,\tilde{\boldsymbol{q}}) \\ r(\omega,\tilde{\boldsymbol{q}}) \end{bmatrix} = \begin{bmatrix} \mathbf{Z}(\omega)\tilde{\boldsymbol{q}} + \tilde{\boldsymbol{b}}_{nl}(\tilde{\boldsymbol{q}}) - \tilde{\boldsymbol{b}}_{ext} \\ (\tilde{\boldsymbol{q}}-\tilde{\boldsymbol{q}}_0)^2 + (\omega-\omega_0)^2 - \Delta s^2 \end{bmatrix} = 0 \tag{3.65}$$

The starting value for Δs is set to be 0.01, the value of Δs can be doubled or halved depending on the number of iteration used to solve Equation (3.65).

Solving the equation of motion in frequency domain

For $\boldsymbol{z} = \{\tilde{\boldsymbol{q}},\omega\}^\intercal$, equation $\mathbf{F}(\boldsymbol{z})$ can be solved by using Newton direction computation:

$$\mathbf{F}'(\boldsymbol{z}_0)\cdot\Delta\boldsymbol{z} = -\mathbf{F}(\boldsymbol{z}_0) \tag{3.66}$$

$$\Delta\boldsymbol{z} = \boldsymbol{z}_1 - \boldsymbol{z}_0 \tag{3.67}$$

$$\textit{where,}\quad \mathbf{F}'(\boldsymbol{z}) = \begin{bmatrix} \dfrac{\partial \boldsymbol{R}}{\partial \tilde{\boldsymbol{q}}} & \dfrac{\partial \boldsymbol{R}}{\partial \omega} \\ \dfrac{\partial r}{\partial \tilde{\boldsymbol{q}}} & \dfrac{\partial r}{\partial \omega} \end{bmatrix} = \begin{bmatrix} \mathbf{Z}(\omega) + \dfrac{\partial \tilde{\boldsymbol{b}}_{nl}}{\partial \tilde{\boldsymbol{q}}} & \dfrac{\partial \mathbf{Z}}{\partial \omega}\cdot\tilde{\boldsymbol{q}} \\ 2(\tilde{\boldsymbol{q}}-\tilde{\boldsymbol{q}}_0) & 2(\omega-\omega_0) \end{bmatrix} \tag{3.68}$$

With the expression of $[\mathscr{F}]$ and $[\mathscr{F}]^{-1}$ defined, the derivative of $\tilde{\boldsymbol{b}}_{nl}$ with respect to $\tilde{\boldsymbol{q}}$ can be computed as:

$$\begin{aligned}\frac{\partial \tilde{\boldsymbol{b}}_{nl}}{\partial \tilde{\boldsymbol{q}}} &= \frac{\partial \tilde{\boldsymbol{b}}_{nl}}{\partial \underline{\boldsymbol{F}}_{nl}} \frac{\partial \underline{\boldsymbol{F}}_{nl}}{\partial \underline{\boldsymbol{u}}} \frac{\partial \underline{\boldsymbol{u}}}{\partial \tilde{\boldsymbol{q}}} = [\mathscr{F}] \frac{\partial \underline{\boldsymbol{F}}_{nl}}{\partial \underline{\boldsymbol{u}}} [\mathscr{F}]^{-1} \\ &= \frac{2}{N_t} \times \sum_{n=0}^{N_t-1} \mathbf{P}(\tau) \otimes \frac{\partial \boldsymbol{F}_{nl}}{\partial \boldsymbol{u}}\bigg|_{t_n}\end{aligned} \tag{3.69}$$

$\otimes$ corresponds to the Kronecker tensor product. For $\tau = \frac{2\pi}{N_t} \cdot t_n$, the matrix $\mathbf{P}$ is computed as:

$$\mathbf{P} = \begin{bmatrix} \frac{1}{2} & \cos(\tau) & \sin(\tau) & \cos(2\tau) & \sin(2\tau) & \dots & \cos(N_H\tau) & \sin(N_H\tau) \\ \frac{\cos(\tau)}{2} & \cos(\tau)\cos(\tau) & \dots & \dots & \dots & \dots & \dots & \sin(N_H\tau)\cos(\tau) \\ \frac{\sin(\tau)}{2} & \cos(\tau)\sin(\tau) & \dots & \dots & \dots & \dots & \dots & \sin(N_H\tau)\sin(\tau) \\ \frac{\cos(2\tau)}{2} & \cos(\tau)\cos(2\tau) & \dots & \dots & \dots & \dots & \dots & \sin(N_H\tau)\cos(2\tau) \\ \frac{\sin(2\tau)}{2} & \cos(\tau)\sin(2\tau) & \dots & \dots & \dots & \dots & \dots & \sin(N_H\tau)\sin(2\tau) \\ \vdots & & & & \vdots & & & \vdots \\ \frac{\cos(N_H\tau)}{2} & \dots & \dots & \dots & \dots & \dots & \dots & \sin(N_H\tau)\cos(N_H\tau) \\ \frac{\sin(N_H\tau)}{2} & \dots & \dots & \dots & \dots & \dots & \dots & \sin(N_H\tau)\sin(N_H\tau) \end{bmatrix} \tag{3.70}$$

$\left[\frac{\partial \mathbf{Z}}{\partial \omega}\right]$ with a dimension of $((2N_H+1)\times \text{DOF}) * ((2N_H+1)\times \text{DOF})$ is computed as:

$$\frac{\partial \mathbf{Z}}{\partial \omega} = \begin{bmatrix} O_{DOF\times DOF} & & & & & \\ & -2\omega\mathbf{M} & \mathbf{C} & & & \\ & -\mathbf{C} & -2\omega\mathbf{M} & & & \\ & & & \ddots & & \\ & & & & -2\omega(N_H)^2\cdot\mathbf{M} & N_H\cdot\mathbf{C} \\ & & & & -N_H\cdot\mathbf{C} & -2\omega(N_H)^2\cdot\mathbf{M} \end{bmatrix} \tag{3.71}$$

With all the matrices defined, the Newton direction computation, i.e. Equation (3.66), is performed in the code by using the Intel® oneAPI Math Kernel Library PARDISO package.

The software package used is a high-performance and robust tool for solving large sparse linear systems of equations. To apply the HBM on the normalised system, Equation (3.49), the non-dimentionalised parameters $\hat{\boldsymbol{u}}$, $[\hat{\mathbf{M}}]$, $[\hat{\mathbf{C}}]$, $[\hat{\mathbf{K}}_0]$,$\{\hat{\boldsymbol{F}}_{nl}\}$, $\{\hat{\boldsymbol{F}}_{ext}\}$, and $\frac{\partial \hat{\boldsymbol{F}}_{nl}}{\partial \hat{\boldsymbol{u}}}$ are used instead. The physical parameters are substituted with the non-dimentionalised parameters by following the relationships shown in Equations (3.50) and (3.51).

3.4.3 Computation method for NNMs using HBM

In nonlinear systems, the vibration period varies with the vibration amplitude, and the oscillations can significantly deviate from harmonic. The superposition principle is not valid in nonlinear systems, and the modal deflection shapes are no longer orthogonal to each other. NNMs are the counterparts of the concept of linear eigenmodes, which can be used to describe vibrational behaviour of nonlinear systems. In analogy to the linear theory, the resonances in the forced vibration occur in the neighbourhood of the free vibration oscillations [153]. Hence the NNMs from the free, undamped vibration systems can provide valuable information for understanding the system's behaviour in the nonlinear regime. In this research, the Extend Periodic Motion Concept (EPMC) approach is used to compute the NNMs [72]. This method can also be used in computing damped NNMs in non-conservative systems. For the autonomous n-dimensional nonlinear systems, the equation of motion in the matrix form can be expressed as:

$$[\mathbf{M}]\{\ddot{\boldsymbol{u}}\} - \zeta[\mathbf{K}]\{\dot{\boldsymbol{u}}\} + [\mathbf{K}]\{\boldsymbol{u}\} + \{\boldsymbol{F}_{nl}\} = 0 \tag{3.72}$$

where $-\zeta[\mathbf{K}]$ is the artificial negative damping term introduced into the system. For the finite systems with only geometric nonlinearities included, ζ negligible. Unlike linear normal mode, the nonlinear mode shapes and resonance frequencies are modal energy-dependent. Hence the response tensor $\boldsymbol{u}$ is expressed in terms of modal amplitude α and mass-normalised modal displacement $\tilde{\boldsymbol{q}}$:

$$\boldsymbol{u}(\omega,t) = \frac{\alpha}{2}\tilde{\boldsymbol{q}}^{0,c} + \alpha\sum_{n=1}^{N_H}\tilde{\boldsymbol{q}}^{n,c}\cos(n\omega t) + \tilde{\boldsymbol{q}}^{n,s}\sin(n\omega t) \tag{3.73}$$

HBM coupled with AFT method is used to solve the equations generated by EPMC approach, Equation (3.74) and (3.75). Arc-length continuation scheme is applied. The derivation of

$\mathbf{Z}(\omega)$ can be found in Equation (2.73), with $\mathbf{C} = -\zeta\,[\mathbf{K}]$.

$$\boldsymbol{R}_1(\alpha,\zeta,\omega,\tilde{\boldsymbol{q}}) = \alpha\,\mathbf{Z}(\zeta,\omega)\,\tilde{\boldsymbol{q}} + \tilde{\mathbf{b}}_{nl}(\alpha\tilde{\boldsymbol{q}}) - \tilde{\mathbf{b}}_{ext} = 0 \tag{3.74}$$

$$\boldsymbol{R}_2(\alpha,\zeta,\omega,\tilde{\boldsymbol{q}}) = (\tilde{\boldsymbol{q}}-\tilde{\boldsymbol{q}}_0)^2 + (\omega-\omega_0)^2 + (\zeta-\zeta_0)^2 + (\alpha-\alpha_0)^2 - \Delta s^2 = 0 \tag{3.75}$$

Since two more unknowns are involved in the equations, additional constraints need to be added. Equation (3.76) ensures a positive modal amplitude α.

$$\boldsymbol{R}_3(\tilde{\boldsymbol{q}}) = \tilde{\boldsymbol{q}}^{\mathsf{T}}\,[\mathbf{I}_{2N_H+1}\otimes\mathbf{M}]\,\tilde{\boldsymbol{q}} - 1 = 0 \tag{3.76}$$

Phase constraint needs to be added to ensure the uniqueness of the periodic solution. The simplest way for the phase condition can be done by imposing a random Fourier coefficient equal to zero, i.e. $\tilde{\boldsymbol{q}}(i) = 0$. However this can cause numerical problems at some specific points. For a system with cubic nonlinearity, by imposing the amplitude of $\cos(3\omega t)$ equal to zero would cause problems when computing the NNM and make the continuation diverge. A more general phase condition that works independently with the nonlinearities is needed. Seydel [124] proposed the following phase condition in time domain:

$$\int_0^T \boldsymbol{u}_0^{\mathsf{T}}(t)\,\dot{\boldsymbol{u}}(t) = 0 \tag{3.77}$$

with $\boldsymbol{u}_0$ denotes the displacement vector at the end of the previous continuation step, i.e. $\tilde{\boldsymbol{q}}_0 \xrightarrow{[\mathscr{F}]^{-1}} \boldsymbol{u}_0$. The phase condition can hence be expressed as:

$$\boldsymbol{R}_4(\tilde{\boldsymbol{q}}) = \sum_{n=1}^{N_H} n\cdot\{\tilde{\boldsymbol{q}}_0^{n,c}\}^{\mathsf{T}}\{\tilde{\boldsymbol{q}}^{n,s}\} - n\cdot\{\tilde{\boldsymbol{q}}_0^{n,s}\}^{\mathsf{T}}\{\tilde{\boldsymbol{q}}^{n,c}\} \tag{3.78}$$

For $\boldsymbol{z} = \{\tilde{\boldsymbol{q}},\omega,\alpha,\zeta\}^{\mathsf{T}}$, the equation of motion in frequency domain becomes:

$$\mathbf{F}(\boldsymbol{z}) = \begin{bmatrix} \boldsymbol{R}_1(\alpha,\zeta,\omega,\tilde{\boldsymbol{q}}) \\ \boldsymbol{R}_2(\alpha,\zeta,\omega,\tilde{\boldsymbol{q}}) \\ \boldsymbol{R}_3(\tilde{\boldsymbol{q}}) \\ \boldsymbol{R}_4(\tilde{\boldsymbol{q}}) \end{bmatrix} = 0 \tag{3.79}$$

The Jacobian matrix $\mathbf{F}'(\boldsymbol{z})$ is:

$$\mathbf{F}'(\boldsymbol{z}) = \begin{bmatrix} \partial \boldsymbol{R}_1/\partial \tilde{\boldsymbol{q}} & \partial \boldsymbol{R}_1/\partial \omega & \partial \boldsymbol{R}_1/\partial \alpha & \partial \boldsymbol{R}_1/\partial \zeta \\ \partial \boldsymbol{R}_2/\partial \tilde{\boldsymbol{q}} & \partial \boldsymbol{R}_2/\partial \omega & \partial \boldsymbol{R}_2/\partial \alpha & \partial \boldsymbol{R}_2/\partial \zeta \\ \partial \boldsymbol{R}_3/\partial \tilde{\boldsymbol{q}} & 0 & 0 & 0 \\ \partial \boldsymbol{R}_4/\partial \tilde{\boldsymbol{q}} & 0 & 0 & 0 \end{bmatrix} \tag{3.80}$$

where,

$$\begin{aligned}
&\partial \boldsymbol{R}_1/\partial \tilde{\boldsymbol{q}} = \alpha \mathbf{Z}(\zeta,\omega) + \alpha \frac{\partial \tilde{\boldsymbol{b}}_{nl}}{\partial(\alpha \tilde{\boldsymbol{q}})} && \partial \boldsymbol{R}_2/\partial \tilde{\boldsymbol{q}} = 2(\tilde{\boldsymbol{q}} - \tilde{\boldsymbol{q}}_0) \\
&\partial \boldsymbol{R}_1/\partial \omega = \alpha \frac{\partial \mathbf{Z}}{\partial \omega} \cdot \tilde{\boldsymbol{q}} && \partial \boldsymbol{R}_2/\partial \omega = 2(\omega - \omega_0) \\
&\partial \boldsymbol{R}_1/\partial \alpha = \mathbf{Z}(\zeta,\omega)\tilde{\boldsymbol{q}} + \frac{\partial \tilde{\boldsymbol{b}}_{nl}}{\partial(\alpha \tilde{\boldsymbol{q}})} \tilde{\boldsymbol{q}} && \partial \boldsymbol{R}_2/\partial \alpha = 2(\zeta - \zeta_0) \\
&\partial \boldsymbol{R}_1/\partial \zeta = \alpha \frac{\partial \mathbf{Z}}{\partial \zeta} \cdot \tilde{\boldsymbol{q}} && \partial \boldsymbol{R}_2/\partial \zeta = 2(\alpha - \alpha_0) \\
&\partial \boldsymbol{R}_4/\partial \tilde{\boldsymbol{q}} = \left\{ O_{DOF} \quad -\tilde{\boldsymbol{q}}_0^{1,s} \quad \tilde{\boldsymbol{q}}_0^{1,c} \quad -2\cdot\tilde{\boldsymbol{q}}_0^{2,s} \quad 2\cdot\tilde{\boldsymbol{q}}_0^{2,c} \quad \ldots \quad -N_H\cdot\tilde{\boldsymbol{q}}_0^{N_H,s} \quad N_H\cdot\tilde{\boldsymbol{q}}_0^{N_H,c} \right\} \\
&\partial \boldsymbol{R}_3/\partial \tilde{\boldsymbol{q}} = 2\cdot[\mathbf{I}_{2N_H+1} \otimes \mathbf{M}]\,\tilde{\boldsymbol{q}}
\end{aligned} \tag{3.81}$$

3.4.4 Numerical results

In the previous sections, the mathematical model used on computing the nonlinear dynamic behaviour of the 3D structures is explained in details. 3D solid elements are used in the FE model to capture the geometric nonlinearities within the system. In order to demonstrate the validity of the procedure followed, the dynamic results generated from the FE model are compared with the benchmarks used in literatures. The effect of geometric nonlinearity on the dynamic behaviour of the structure is studied on two different cases. The first example is a cantilevered beam with a harmonic excitation force applied at the tip. The second model is a clamped-clamped beam with a force applied in the middle. The square cross-section of the beam leads to the presence of the modal coupling through internal resonance. The forced frequency responses of the bending modes for both models are studied. Figure 3.11 depicts the procedures involved when generating the points on the nonlinear FRF plot. Details of the algorithms used in the Newton direction computation for HBM can be found in Appendix

C. A total of 5 harmonics, i.e. $N_H = 5$, is considered in the HBM method. 32 samples per period are taken, i.e. $N_t = 32$, for the $\mathscr{F}$ and $\mathscr{F}^{\intercal}$ functions in AFT.

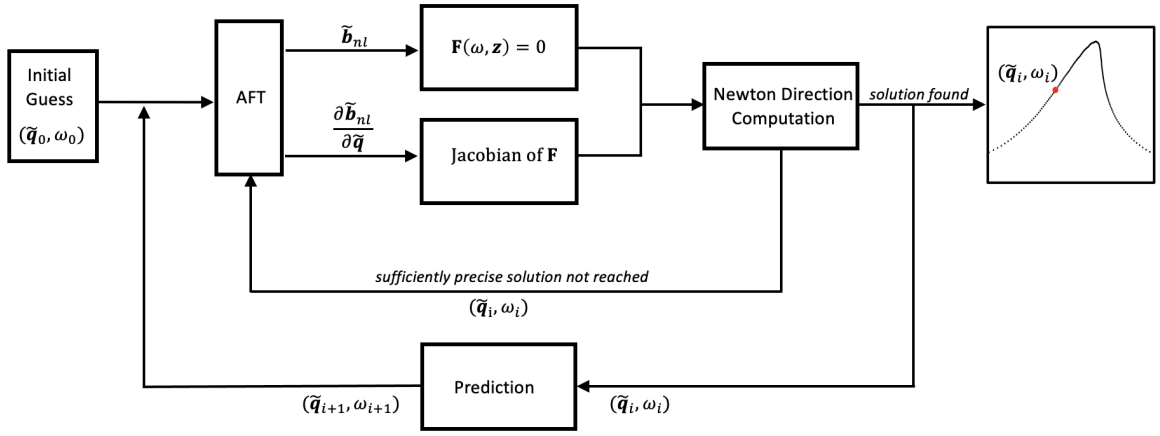
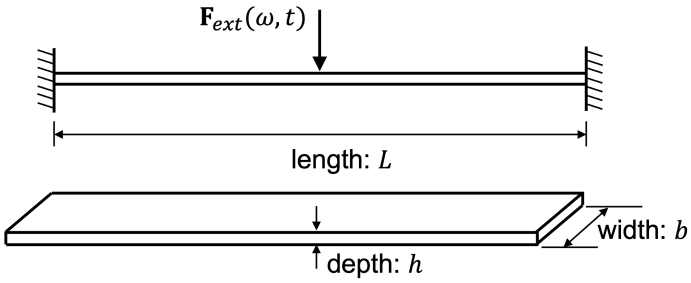


Fig. 3.11 *Flowchart for the dynamic analysis of the structure.*

In the FE model, the boundary conditions for the nodes on the fixed end/ends need to be imposed in the final assembled system of equations in FEM. For a clamped node n, the boundary conditions are $u_x^n = u_y^n = u_z^n = 0$. In this research, the rows and columns corresponding to the boundary nodes are all removed from the global system. For a system with N DOFs and n boundary nodes, the total free DOFs used in the simulation is $(N - 3n)$. Other commonly used methods for boundary conditions in FEM are Lagrange multipliers [23] and penalty method [179]. The advantages of the elimination method used are that it can preserve the symmetry of the mass and stiffness matrix and that fewer DOFs are considered in the simulation. The positive definite matrices are preferred in the sparse matrix solver for fast convergence.

Validation of the FE model with literatures



Parameters	
$b\ (mm)$	20
$h\ (mm)$	2
$L\ (mm)$	406
$E\ (GPa)$	71.72
$\rho\ (kg/m^3)$	2800
ν	0.33

Fig. 3.12 *The schematic model of the clamped-clamped beam.*

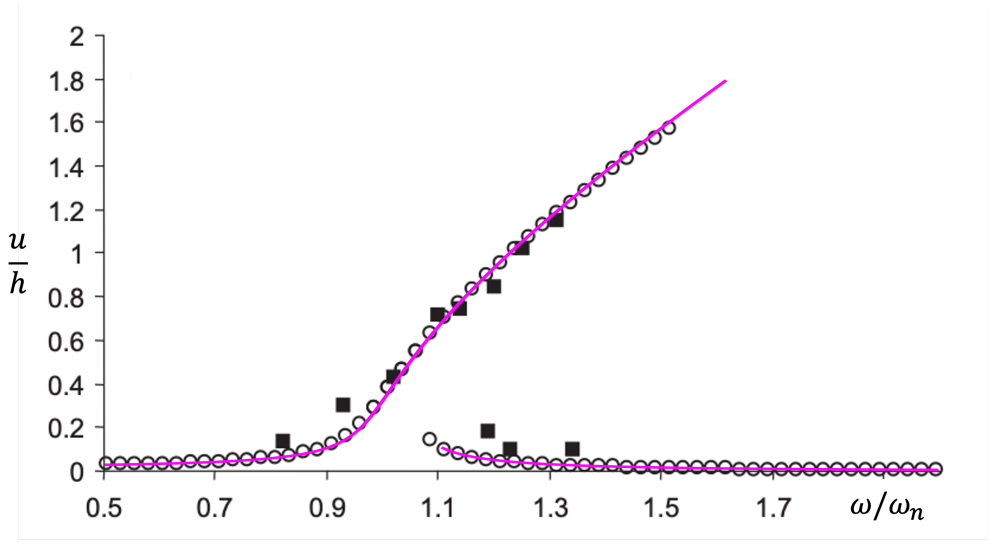
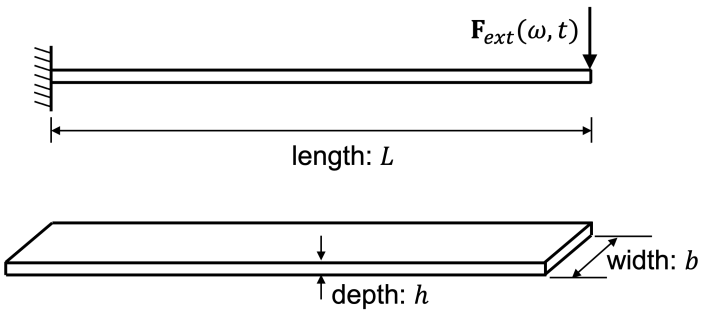


Fig. 3.13 *Maximum displacement of the clamped-clamped beam: (–) numerical, (○) Ribeiro's results, and (■) experimental data [165].*

The geometrically nonlinear periodic vibrations of an elastic and isotropic clamped-clamped beam are studied first. Figure 3.12 shows the schematic model of the 3D beam used in the study. The physical parameters and the material properties are also listed. A point harmonic force with amplitude of 0.134 N was applied at the middle of the beam. In Ribeiro's paper [117], the nonlinear vibrations of the beam are obtained by using the *p*-version, hierarchical finite element methods. An algorithm based on the shooting method is applied to solve the equations of motion. Figure 3.13 shows the comparison of the numerical result generated by the proposed methodology, Ribeiro's results, and the experimental data [165]. HEX20 elements are selected for the FE mesh used in the proposed methodology. In Figure 3.13, the vertical axis gives the maximum response u of the beam attained divided by the thickness h. The frequency on the horizontal axis is normalised by the linear natural frequency $\omega_n = 415.247$ rad/s. The computational results show in the figure are for the undamped beam. A good agreement between the proposed methodology, Ribeiro's results, and the experimental values is attained. Stiffening effect on the first bending mode can be observed in all cases.

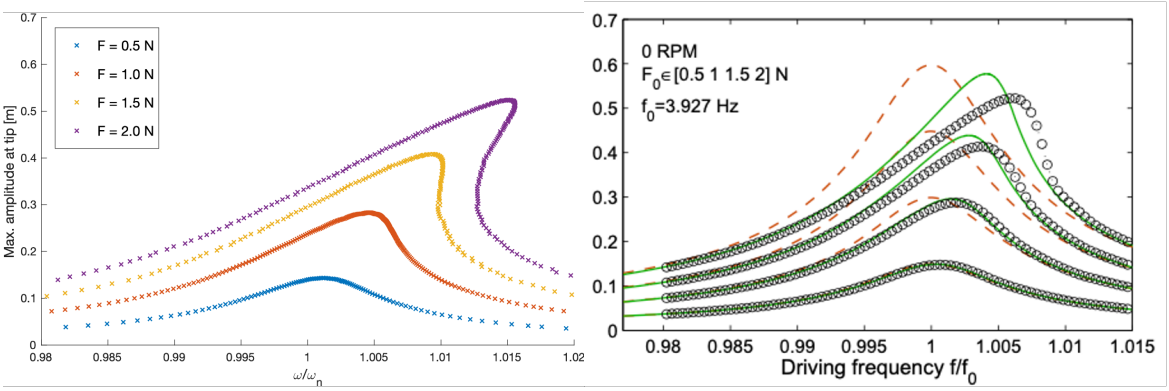
The forced frequency responses of the cantilevered beam generated from the FE model are also compared with literature works. Figure 3.14 presents the schematic model of the 3D beam used in the study. The physical parameters and the material properties used are also listed. Thomas et al. studied the large amplitude nonlinear vibratory behaviour of a cantilevered beam in [147]. Three different models were used to simulate the vibrations.



Parameters	
$b\ (m)$	0.1
$h\ (mm)$	5
$L\ (m)$	1
$E\ (GPa)$	104
$\rho\ (kg/m^3)$	4400
ν	0.31

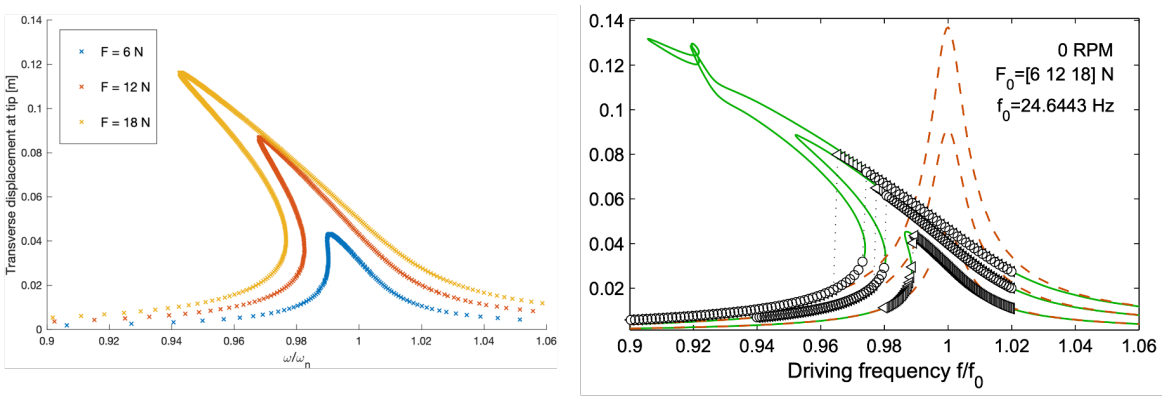
Fig. 3.14 *The schematic model the cantilevered beam.*

The first model (denoted VK), is based on the classical von Kármán assumptions which keeps only the first nonlinear flexural term in the axial strain. The second model (denoted Inxt.) is an extension of the classical elastica model in [30]. The third one is based on a FE discretisation with beam elements and integrated in time. The FRF results for the first and second bending mode of the 3D structure generated in [147] and the FE model with 3D TET10 elements are shown in Figure 3.15 and 3.16. A mass proportional damping matrix $[\mathbf{C}] = 0.005 * \omega_n * [\mathbf{M}]$ is employed in the computation. The nonlinear terms of the VK model stem from the coupling between the axial tension in the beam and its bending. Since the beam is free at its end, the VK model fails to represent the nonlinear dynamic behaviour of the cantilevered beam. Good alignment of the numerical results between the FE model with TET10 elements and the other two models presented by Thomas et al. can be observed. The geometric nonlinearity terms have stiffening effect on the first bending mode and softening effect on the second bending mode.



(a) FE Model with TET10 (b) Literature works [147]

Fig. 3.15 *First bending mode frequency response for various forcing amplitudes: (x) FE model with 3D solid elements, (○) FE model with beam elements, (−−) VK model, (—) Inxt. model.*



(a) FE Model with TET10 (b) Literature works [147]

Fig. 3.16 *Second bending mode frequency response for various forcing amplitudes:* (x) *FE model with 3D solid elements,* (○) *FE model with beam elements,* (−−) *VK model,* (—) *Inxt. model.*

Case Study I: Forced frequency response of the cantilevered beam

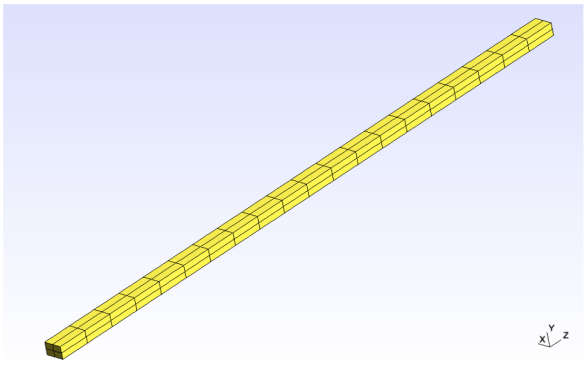


Fig. 3.17 *FEM mesh with HEX20 elements for numerical analysis.*

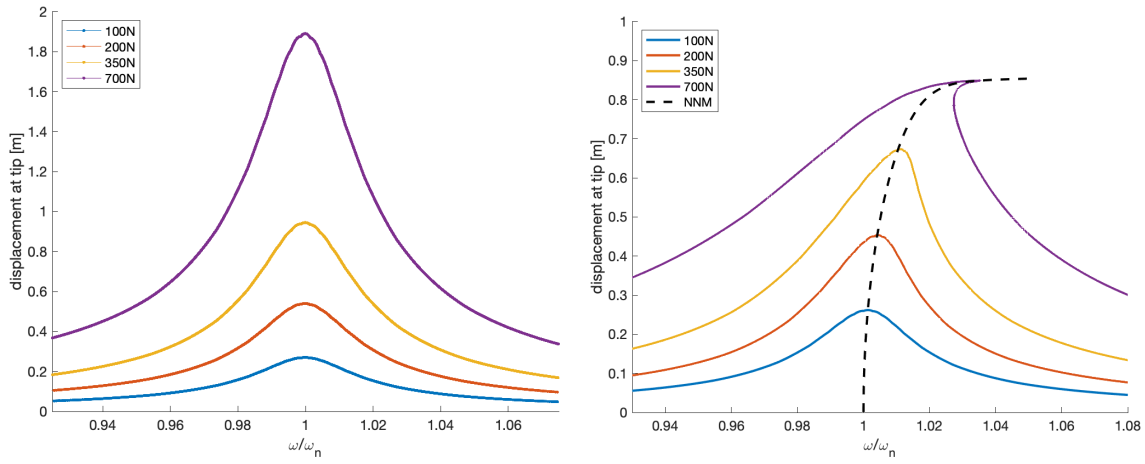
A 3D cantilevered beam model with dimension of 30mm $*$ 20mm $*$ 1000mm is used. Homogeneous material of Young's Modulus $E = 210$ GPa, density $\rho = 7800$ kg/m^3 and Poisson's ratio $\nu = 0.3$ is assumed. Parameters involved in the damping matrix are chosen to be $\alpha = 3$ and $\beta = 0$, i.e. a mass proportional damping matrix $[\mathbf{C}] = 3[\mathbf{M}]$. The periodic excitation force is applied at the free end of the beam. 3D 20-node hexahedron elements are used in the FE model (Figure 3.17). The mesh studied in this paper has 80 elements in total, with 20 elements along the axis and 2×2 elements on the cross-section. The mesh has a total of 1800 free DOFs. As can be seen from Appendix C, $[\mathbf{M}]$, $[\mathbf{C}]$ and $[\mathbf{K}_0]$ do not change throughout the simulation. These matrices can be computed before the loop. During the simulation, the element's nonlinear stiffness matrix are computed element by element in order. $[\mathbf{K}^e_{nl}]$ for each

element is then transferred into the global stiffness matrix. A sparse mapping which maps the $[\mathbf{K}_{nl}^{e}]$ to the global stiffness matrix $[\mathbf{K}_{nl}(\boldsymbol{u})]$ in CSR format need to be constructed before the loop. Hence the $\{\mathbf{IA}\}$ and $\{\mathbf{JA}\}$ vectors are computed beforehand. At each iteration, the entries of $[\mathbf{K}_{nl}^{e}]$ will automatically go to the exact locations in the $\{\mathbf{A}\}$ vector of $[\mathbf{K}_{nl}]$. Table 3.4 lists the computational time used in each pre-processing step for the cantilevered beam model.

	Pre-processing Steps	**Time** (*s*)
1	Read the mesh and compute element node coordinates $\hat{\boldsymbol{X}}_e$	6E-4
2	Construct the sparse mapping ($\{\mathbf{IA}\}$, $\{\mathbf{JA}\}$)	167
3	Compute the sparse matrices $[\mathbf{M}]$, $[\mathbf{C}]$ and $[\mathbf{K}_0]$	2E-2
4	Compute the smallest natural frequencies with FEAST algorithm	10

Table 3.4 *Computational time for the pre-processing steps*

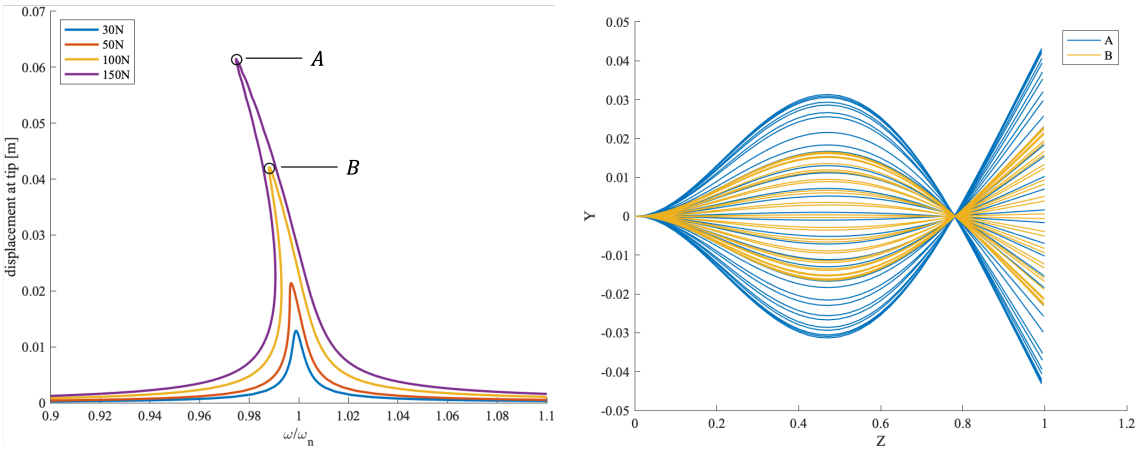
Figure 3.18 shows the forced frequency response of the first bending mode of the cantilevered beam under different level of periodic excitation force in the y direction. The backbone curve generated based on EPMC method is shown in the black dashed line. The excitation frequency on the x-axis is scaled by the natural frequency of the structure, $\omega_n = 16.80$ Hz. For the linear FRF shown in Figure 3.18a, only the linear stiffness matrix $[\mathbf{K}_0]$ is considered in the equation and $\{\boldsymbol{F}_{nl}(\boldsymbol{u})\}$ from Equation (3.45) is ignored. When taking into account the nonlinear stiffness matrix $[\mathbf{K}_{nl}]$, hardening effect of the nonlinear strain can be observed from the FRF plot in Figure 3.18b. For a small amplitude of oscillation, the response amplitudes are single-valued as in the linear case. As the forcing amplitude increases, the response curves start to bend to the right (hardening effect). When large deflection occurs, the hardening effect is more pronounced and the nonlinear dynamic system responses at a much more reasonable amplitude than the linear case. Linear model can only provide a good approximation when the deformation is small. For $F_y = 700 \cdot \cos(\omega t)$, the peak of the resonance curve reaches up to 1.9 m, which is physically impossible for a beam with a length of 1 m.



(a) Linear FRF (b) Nonlinear FRF

Fig. 3.18 *FRF of the 3D cantilevered beam under periodic point load (1st bending mode).*

Figure 3.19a shows the forced frequency response of the second bending mode of the cantilevered beam under different level of periodic excitation force in the y direction. The frequency on the x-axis is normalised by $\omega_n = 105.12$ Hz. The softening effect can be observed in this mode. No obvious negative terms can be found in the equation of the 3D model used in this research. This is because the internal responses within the structure are all included into the nonlinear stiffness matrix $\mathbf{K}_{nl}$. Nayfeh's paper [100] used nonlinear integro-differential equations of motion for an inextensional beam and showed that the negative nonlinear inertia term produces a softening effect and play a significant role in the planar responses of high-frequency modes. Whereas the geometric nonlinear terms produce a hardening effect and dominate the planar responses of low-frequency modes and non-planar responses for all modes. In the second bending mode of the cantilevered beam shown here, the softening effect overcomes the hardening terms. The overall nonlinear effect on the structures depends on the mode. Figure 3.19b shows the deformation shapes of the beam near the resonance peaks labelled in Figure 3.19a. For the simplicity of visualisation, only the deformation shapes of the centroid line in the YZ-plane are presented. Figure 3.20 shows the backbone curves for the second bending mode with different number of harmonics N_H used in the HBM. The softening effect can be observed on both cases. The bifurcation point for $N_H = 5$ vanished when more harmonics are considered.



(a) Nonlinear FRF (b) Dynamic shape at resonance

Fig. 3.19 *3D cantilevered beam under periodic point load around the 2nd bending mode.*

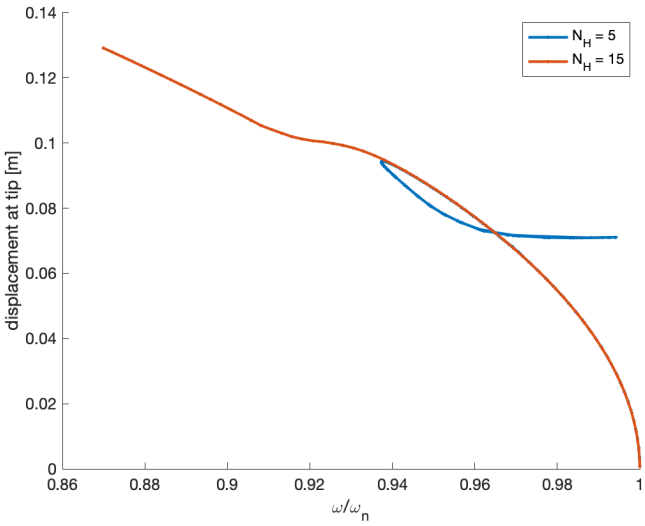


Fig. 3.20 *Backbone curves for the second bending mode with different number of harmonics used in HBM.*

Figure 3.21 shows the computational time consumed by different stages when generating Figure 3.18b with excitation force at an amplitude of 700 N. Intel MKL Pardiso solver is used for applying the Newton direction computation to solve Equation (3.65) in sparse matrices. Sparse matrix solver takes the majority of the computational time due to the size of the dynamic system. AFT and the assembly of matrix for Newton direction computation ranks second and third respectively in the computational time consumed. The computation of $\mathbf{F}(\omega, \tilde{\boldsymbol{q}})$ by manipulating the sparse matrices is efficient and takes negligible time. Step AFT corresponds to the time taken for the calculation of $\boldsymbol{F}_{nl}$ and the matrix $\partial \boldsymbol{F}_{nl}/\partial \boldsymbol{u}$ at each

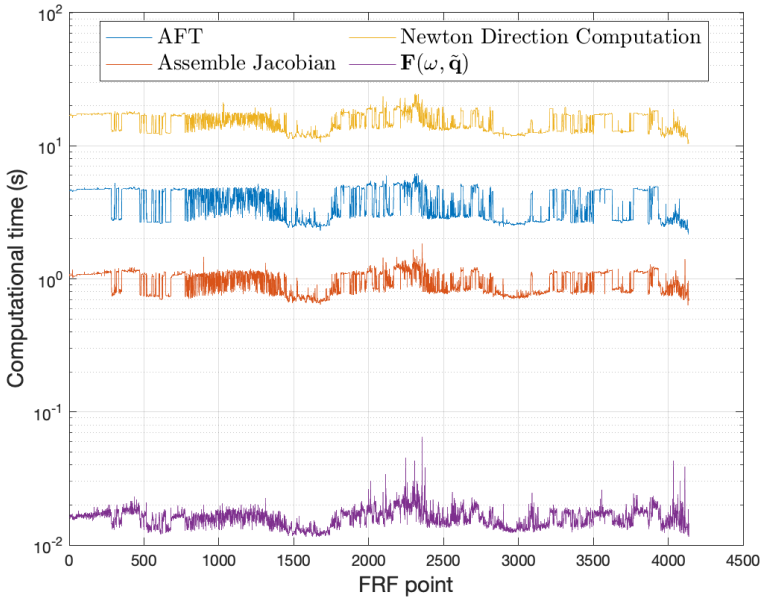


Fig. 3.21 *Computational time for points on the FRF plot.*

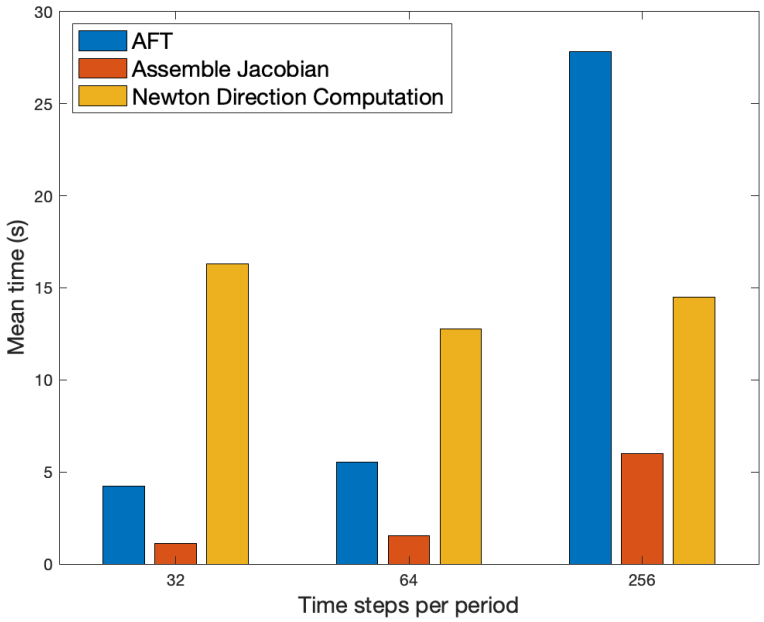
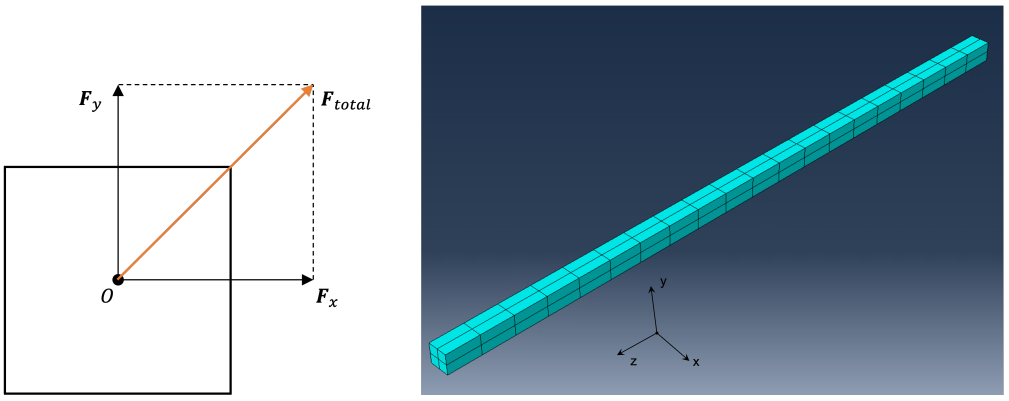


Fig. 3.22 *Computational time with different time steps per period.*

time step. The Fourier transformation of variables between the time and frequency domain is also included. The peaks on the plot are corresponding to the increase in the iteration numbers when solving the equations. Computational times arising from different time steps per period, N_t, used in DFT and IDFT are shown in Figure 3.22. Mean time taken by the most computational consuming procedures are compared. AFT is the most sensitive procedure to the time steps per period as expected. Second order 20-node hexahedron elements are used in this study. Higher order elements can increase the accuracy of the result however the increase in the total DOFs in the system and the number of Gaussian points used for constructing matrices, Equation (3.24) and (3.32), will cause the increase in the overall computation time. On the other hand, the lower order elements require much less computational power, but a compromise must be made for the accuracy of the results.

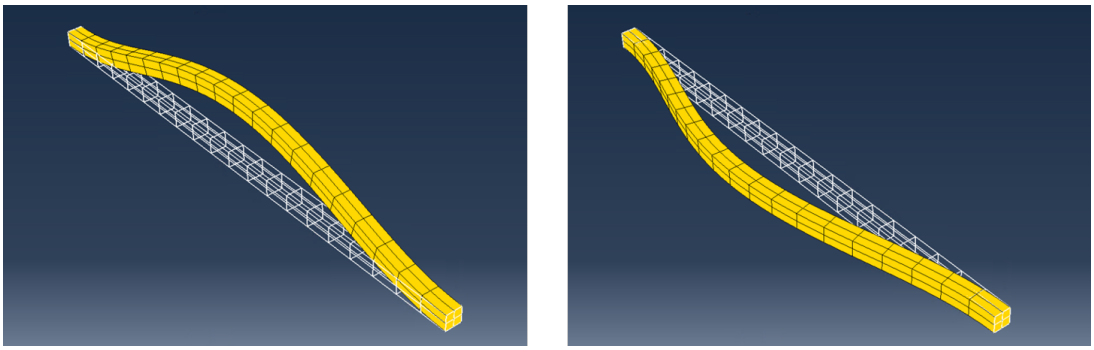
Case Study II: Forced frequency response of the clamped-clamped beam



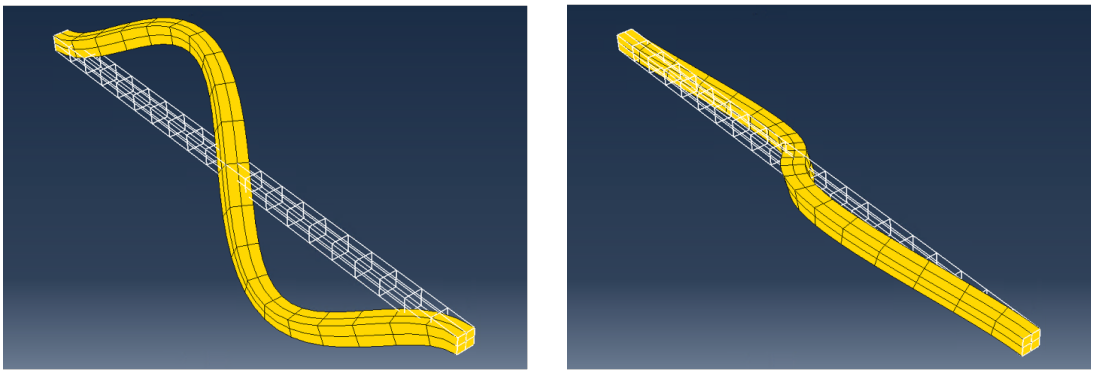
(a) Combined excitation (b) FEM mesh with 20-node hexahedron elements

Fig. 3.23 *3D clamped-clamped beam model used for numerical analysis.*

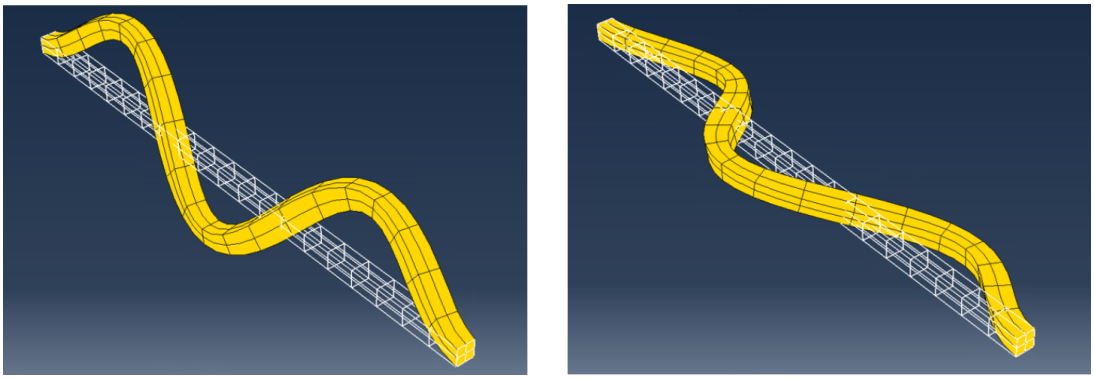
In order to test the mathemetical model's ability on capturing the couplings arising between the modes, a 3D clamped-clamped beam model with dimension of $30\text{mm} * 30\text{mm} * 1000\text{mm}$ is chosen. 3D 20-node hexahedron elements are used in the FE model (Figure 3.23b). The mesh studied in this paper has 80 elements in total, with 20 elements along the axis and 2×2 elements on the cross-section. Homogeneous material of Young's Modulus $E = 210$ GPa, density $\rho = 7800$ kg/m^3 and Poisson's ratio $\nu = 0.3$ is assumed. A mass proportional damping matrix $[\mathbf{C}] = 3[\mathbf{M}]$ is used in the computation. With the boundary DOFs removed, the mesh has a total of 1737 free DOFs in total. Two loading conditions are studied in this case. The first one has only vertical periodic excitation force F_y applied in the middle of



(a) The first vertical and lateral bending mode: $\omega_1 = \omega_2 = 159.90$ Hz



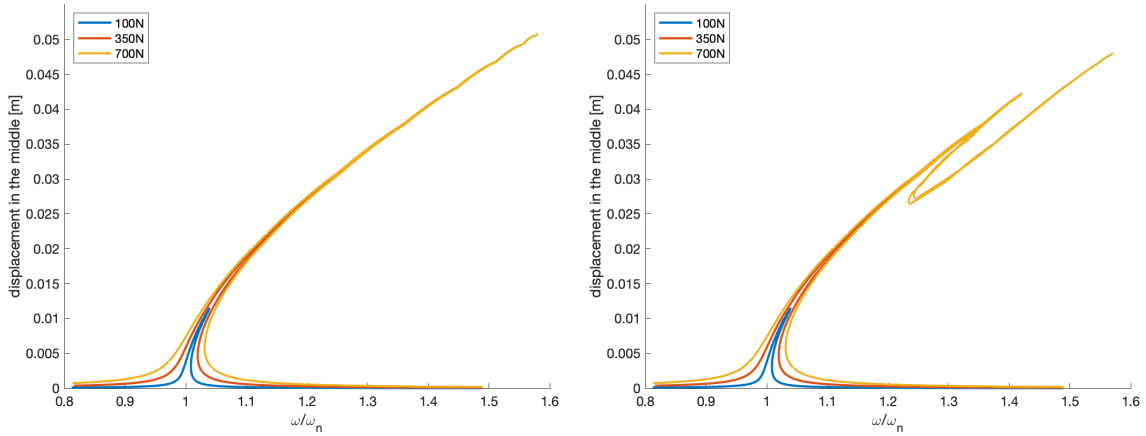
(b) The second vertical and lateral bending mode: $\omega_3 = \omega_4 = 437.39$ Hz



(c) The third vertical and lateral bending mode: $\omega_5 = \omega_6 = 848.87$ Hz

Fig. 3.24 *First 6 modes of the 3D clamped-clamped beam.*

the beam. The second one have periodic forces applied in two directions simultaneously, i.e. $F_x = F_y = 500\cos(\omega, t)$. As illustrated in Figure 3.23a, an inclined resultant force with an angle of 45 degree to the xz-plane is formed. Figure 3.24 shows the first 6 mode shapes of the clamped-clamped beam. Since the cross-section of the beam is a square, the vertical and the lateral bending modes are of the same natural frequency with $\omega_1 = \omega_2 = 159.90$ Hz, $\omega_3 = \omega_4 = 437.39$ Hz and $\omega_5 = \omega_6 = 848.87$ Hz.



(a) Nonlinear FRF with $N_H = 3$ (b) Nonlinear FRF with $N_H = 5$

Fig. 3.25 *FRF of the 3D clamped-clamped beam under periodic point load in y direction.*

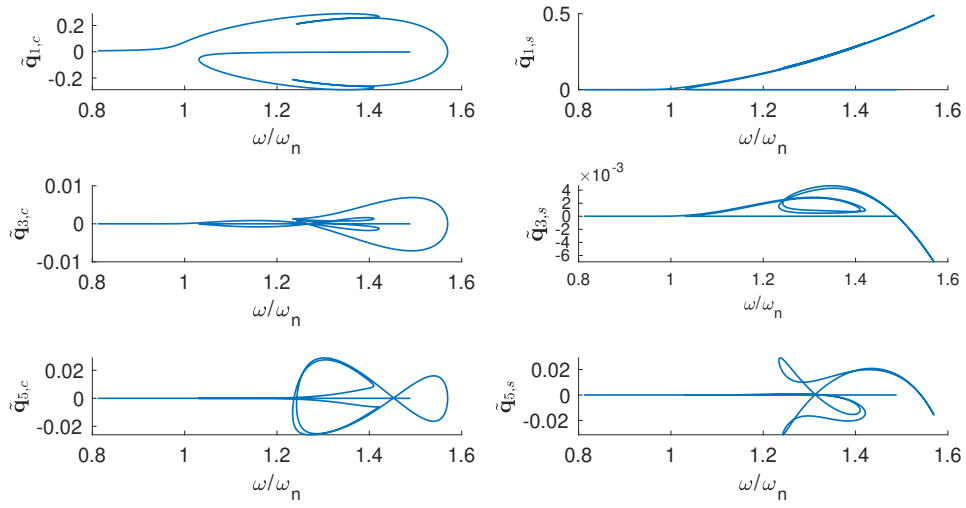


Fig. 3.26 *Fourier coefficient for u_y at the load point.*

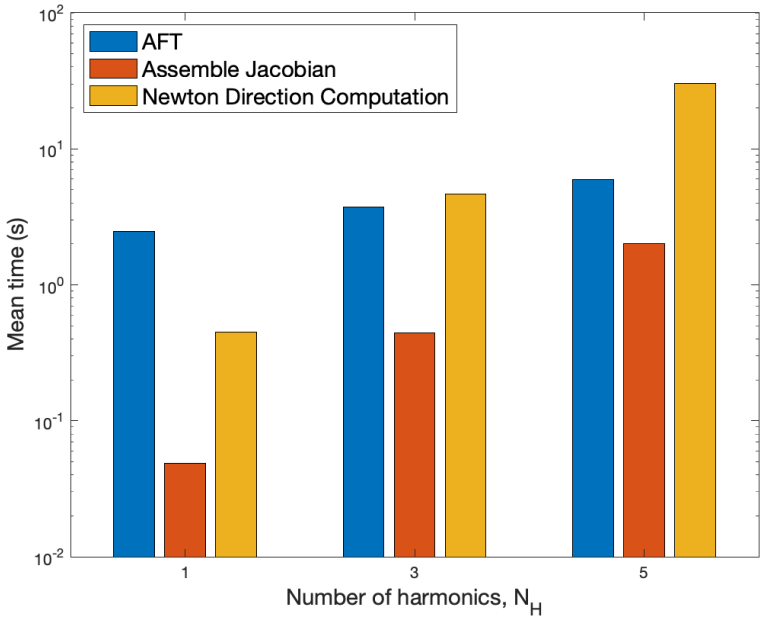
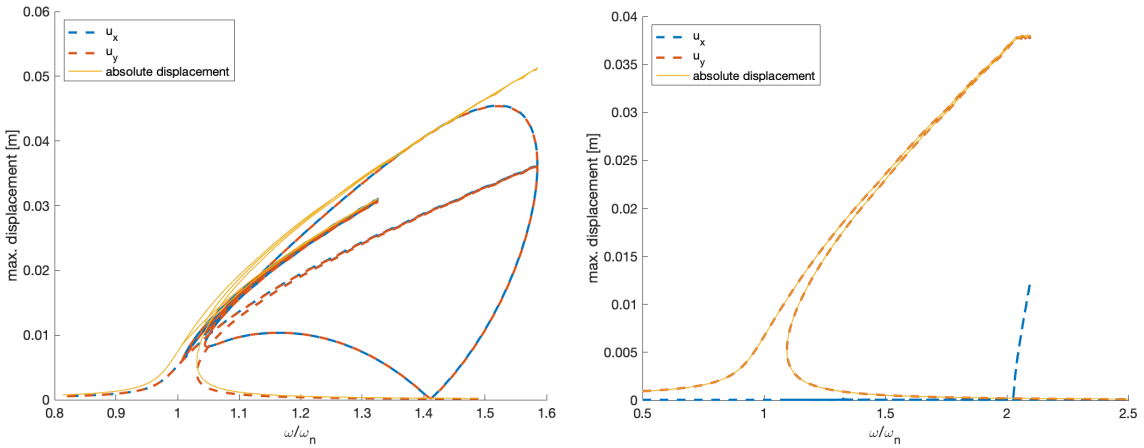


Fig. 3.27 *Computational time with different harmonics in HBM ($N_t = 32$).*

Figure 3.25 shows the forced frequency response of the first bending mode of the clamped-clamped beam with different number of harmonics employed in the HBM. The excitation frequency on the x-axis is scaled by the natural frequency of the structure, $\omega_n = 159.90$ Hz. Values on the y-axis are the vertical displacement of the beam at the location of load point. A periodic force in the vertical direction is applied in the middle of the beam. With more number of harmonics considered in the HBM, the modal interaction between the vertical bending modes can be observed on the FRF plot. As the frequency increases, the 5:1 ratio between the 3$^{\text{rd}}$ and the 1$^{\text{st}}$ bending mode in vertical direction is reached. The loop on Figure 3.25b represents the interaction between the two modes. Figure 3.26 shows the Fourier coefficient for the response in y-direction at the load point. The fifth harmonic of the response is excited at $\omega/\omega_n = 1.2$. A jump phenomenon can be observed on both FRF plots as ω reaching around $1.6\,\omega_n$. Figure 3.27 shows the computational times arising from different harmonics, N_H, used in the HBM. N_t is set to be 32 samples per period. Mean time taken by the most computational consuming procedures are compared. AFT dealing with the transformation between $\boldsymbol{F}_{nl}(t)$ and $\tilde{\boldsymbol{b}}_{nl}(\omega)$. $\tilde{\boldsymbol{b}}_{nl}(\omega)$ has a length of $(2H_N+1)\times\text{DOF}$. As the N_H increases, the length of the vector $\tilde{\boldsymbol{b}}_{nl}(\omega)$ increases. $\left[\dfrac{\partial \mathbf{Z}}{\partial \omega}\right]$ and $\mathbf{Z}$ has a dimension of $((2N_H+1)\times\text{DOF})*((2N_H+1)\times\text{DOF})$. Hence assembling the Jacobian matrix $\mathbf{F}'$ and solving the Equation (3.65) require more computational time when N_H increases. Computers are dealing with larger matrices. A fuller picture of the dynamic properties of the system can be captured with more harmonics considered in the HBM equations. However, this comes



(a) 30mm ∗ 30mm ∗ 1000mm (b) 15mm ∗ 60mm ∗ 1000mm

Fig. 3.28 *FRF of the clamped-clamped beam under periodic point load in both x and y direction.*

with the price of increasing the overall computational time.

Figure 3.28a shows the FRF of the clamped-clamped beam with a periodic force applied in two directions simultaneously, i.e. $F_x = F_y = 500\cos(\omega,t)$. Both the vertical and the lateral bending modes are initiated in this case. Values on the y-axis are the displacement of the beam at the location of load point. 3 harmonics are used in the HBM. For the beam with the symmetric cross-section, the response is in the same plane as the excitation force, i.e. the responses in the x and y directions are the same. The first and the second modes (Figure 3.24) of the beam has exactly the same resonance frequency, i.e. $\omega_1 = \omega_2 = 159.90$ Hz. The loops on the plot represent the modal interaction between the modes. The same load is applied onto the flat beam with dimension of 15mm ∗ 60mm ∗ 1000mm, Figure 3.28b. The material parameters are the same and the natural frequency for the clamped-clamped flat beam is $\omega_n = 80.66$ Hz. The vibration of the beam is mainly in the yz-plane up until $\omega/\omega_n = 2$. As the frequency increases, the amplitude of vibration in the xz-plane start to increase.

3.5 Concluding remarks

In this chapter, the finite element equations for the structure with geometric nonlinearities are presented. 3D solid elements are used in the FE model. Due to the high sparsity level of the FE matrices, the CSR format is chosen for storing and manipulating the matrices. The performances of the four commonly used elements are studied. The natural frequencies

calculated from the eigenvalue problem of the FE model are compared with the analytical values based on the Euler-Bernoulli beam theory. FE model using the higher-order elements provides more accurate results than using the lower-order elements. However, this comes with the price of higher computational cost, as more Gaussian integration points and shape functions of the elements need to be involved in the computation. For thin structures, the hexahedron elements tend to perform better than the tetrahedron element. Locking of the hexahedron elements can be avoided by introducing reduced integration. Hourglass control needs to be implemented for the 8-node hexahedron elements during meshing.

The HBM methodology has been proposed in order to solve the nonlinear dynamic equations. The nonlinear dynamic responses of the 3D structures computed from the proposed mathematical model are validated with works of literature. Good alignments between the numerical results and the experimental data are attained. For responses in lower amplitudes, the linear model can be used as an estimation for the dynamic behaviour. The effect of the geometric nonlinearities can be observed on the plots for the frequency-response functions (FRF). The geometric nonlinear terms can have hardening or softening effects on different modes. The effect is more significant when the structures respond at higher amplitudes. The computation methods for the backbone curved based on EPMC are also provided in this chapter. This method can be used on conservative systems. The backbone curves generated have a good match with the nonlinear FRF plots in the test cases.

Chapter 4

Application of Proposed Methods

The objective of this chapter is to apply the HBM and the NNM algorithms discussed in the previous chapters to rotating structures. Geometric nonlinearities are considered in the FEM model. The energy expressions for the rotating structures are derived first. The corresponding matrices in the FEM are then computed through the Euler–Lagrange equation. Additional terms i.e. the speed-dependent spin softening matrix, the centrifugal force vector, and the skew-symmetric speed-dependent matrix due to Coriolis forces need to be added to the equation of motion. Constant angular velocities are assumed and the effect of Coriolis forces is neglected in this research. When a structure undergoes rotation, the centrifugal force arises to account for the constant acceleration of the structure. The speed-dependent centrifugal force will bring the rotating structure into a pre-stressed configuration. The stiffening effect of the rotational speed on the linear vibration modes can hence be observed. The nonlinear forced frequency responses of the cantilevered beam under different rotational speeds are investigated. For large-amplitude vibrations, softening or hardening behaviour of the rotating systems can be observed on the bending modes.

To validate the methodologies proposed for the nonlinear vibration analysis, simulation results are compared with the experimental data. For the test cases shown in the previous chapters, an ideal point load is considered as the excitation force. A periodic point load is difficult to achieve in a real life system. Base excitation as an alternative loading method has been widely used in experiments. It is a powerful means of non-intrusive testing of vibration characteristics. Algorithms for the force vector due to the base excitation are derived in this chapter. The simulation results of a geometrically nonlinear structure under base excitation are compared with the experimental data.

4.1 Finite element analysis of Rotating Structures

4.1.1 Governing equation in the time domain

As discussed in section 3.1, the matrix format of the equation of motion can be achieved by applying the Euler–Lagrange equation (Equation (2.7)) onto the energy expressions of the system. For a rotating beam, the potential energy of a dynamic system is due to the deformation of the structure. The expression for the potential energy follows the procedures shown in section 3.1.1. This yields the stiffness matrix of the element, which can be expressed as the sum of linear and nonlinear stiffness matrix.

$$\begin{aligned}[\mathbf{K}_e] &= [\mathbf{K}_0^e] + [\mathbf{K}_{nl}^e] = \int \mathbf{S} : \mathrm{d}\boldsymbol{\varepsilon}^G \, \mathrm{d}V \\ &= \int [\mathbf{B}_0 + \mathbf{B}_1(\boldsymbol{u}_e)]^{\mathsf{T}} [\mathbf{D}] \left[\mathbf{B}_0 + \frac{1}{2}\mathbf{B}_1(\boldsymbol{u}_e)\right] \mathrm{d}V \end{aligned} \tag{4.1}$$

$$\textit{where}, \quad [\mathbf{K}_0^e] = \int [\mathbf{B}_0]^{\mathsf{T}} [\mathbf{D}] [\mathbf{B}_0] \, \mathrm{d}V \tag{4.2}$$

$$\begin{aligned}[\mathbf{K}_{nl}^e] &= \int \frac{1}{2} [\mathbf{B}_0]^{\mathsf{T}} [\mathbf{D}] [\mathbf{B}_1] \, \mathrm{d}V + \int [\mathbf{B}_1]^{\mathsf{T}} [\mathbf{D}] [\mathbf{B}_0] \, \mathrm{d}V + \frac{1}{2} \int [\mathbf{B}_1]^{\mathsf{T}} [\mathbf{D}] [\mathbf{B}_1] \, \mathrm{d}V \\ &= \frac{1}{2} [\mathbf{K}_1^e(\boldsymbol{u}_e)] + [\mathbf{K}_2^e(\boldsymbol{u}_e)] + \frac{1}{2} [\mathbf{K}_3^e(\boldsymbol{u}_e)] \end{aligned} \tag{4.3}$$

V stands for the volume of the 3D element. The nonlinear stiffness matrix $[\mathbf{K}_{nl}]$ contributes to the nonlinear force in the dynamic equation. The Jacobian of the nonlinear force is expressed as:

$$\begin{aligned}\frac{\partial \boldsymbol{F}_{nl}^e(\boldsymbol{u}_e)}{\partial \mathbf{a}_e} &= \int [\mathbf{B}_0]^T [\mathbf{D}] [\mathbf{B}_1(\boldsymbol{u}_e)] \, \mathrm{d}V + \int [\mathbf{B}_1(\boldsymbol{u}_e)]^T [\mathbf{D}] [\mathbf{B}_0] \, \mathrm{d}V \\ &\quad + \int [\mathbf{B}_1(\boldsymbol{u}_e)]^T [\mathbf{D}] [\mathbf{B}_1(\boldsymbol{u}_e)] \, \mathrm{d}V + \int [\mathbf{G}]^T [\boldsymbol{\Sigma}(\mathbf{S})] [\mathbf{G}] \, \mathrm{d}V \\ &= [\mathbf{K}_1^e(\boldsymbol{u}_e)] + [\mathbf{K}_2^e(\boldsymbol{u}_e)] + [\mathbf{K}_3^e(\boldsymbol{u}_e)] + [\mathbf{K}_4^e(\mathbf{S})] \end{aligned} \tag{4.4}$$

Details of the matrices shown in the equations above can be found in section 3.1.1.

4.1.2 Kinetic energy expression

For a rotating structure, the rotation vector can be expressed as $\boldsymbol{\Omega} = \{\Omega_x, \Omega_y, \Omega_z\}$. In this research, only constant rotational speed is considered. Ω_x, Ω_y and Ω_y represent the angular velocity in the x, y and z direction. Assuming that the origin of the co-rotating reference

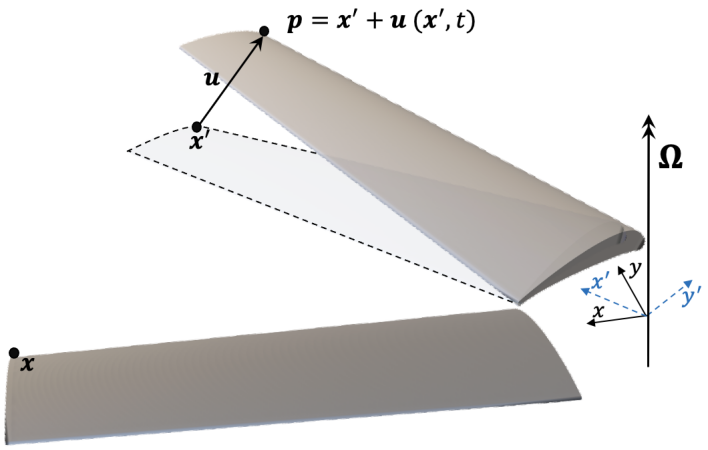


Fig. 4.1 Rotating structure within the co-rotating reference system.

system $\boldsymbol{x}'$ is located on the axis of rotation (Figure 4.1), the position of a certain point on the rotating structure within the co-rotating reference system is given by:

$$\begin{aligned}\boldsymbol{p}(\boldsymbol{x}',t) &= \boldsymbol{x}' + \boldsymbol{u}(\boldsymbol{x}',t) \\ &= \boldsymbol{x}' + \sum_{i=1}^{n} \phi_i\left(\boldsymbol{x}'\right) q_i^n\left(t\right) \\ &= \boldsymbol{x}' + \boldsymbol{\phi}\left(\boldsymbol{x}'\right)\boldsymbol{q}(t)\end{aligned} \tag{4.5}$$

where $\boldsymbol{x}'$ is the position of the point in the undeformed state and $\boldsymbol{u}(\boldsymbol{x}',t)$ is the displacement field. The displacement field can be approximated as the sum of the space-dependent shape functions ϕ_i multiplying their corresponding time-dependent amplitudes q_i. Taking into account the angular velocity vector $\boldsymbol{\Omega}$, the total velocity of a point of the rotating structure follows as:

$$\begin{aligned}\dot{\boldsymbol{p}}(\boldsymbol{x}',t) &= \boldsymbol{\Omega} \times \left(\boldsymbol{x}' + \boldsymbol{\phi}\left(\boldsymbol{x}'\right)\boldsymbol{q}(t)\right) + \boldsymbol{\phi}\left(\boldsymbol{x}'\right)\dot{\boldsymbol{q}}(t) \\ &= \boldsymbol{S}_\omega \boldsymbol{x}' + \boldsymbol{S}_\omega \boldsymbol{\phi}(\boldsymbol{x}')\boldsymbol{q}(t) + \boldsymbol{\phi}\left(\boldsymbol{x}'\right)\dot{\boldsymbol{q}}(t)\end{aligned} \tag{4.6}$$

The skew-symmetric matrix $\boldsymbol{S}_\omega$ is computed as:

$$\boldsymbol{S}_\omega = \begin{bmatrix} 0 & -\Omega_z & \Omega_y \\ \Omega_z & 0 & -\Omega_x \\ -\Omega_y & \Omega_x & 0 \end{bmatrix} \tag{4.7}$$

The kinetic energy of the dynamic system can thus be expressed as:

$$\begin{aligned} T &= \frac{1}{2}\int \dot{\boldsymbol{p}}^T(\boldsymbol{x}',t)\dot{\boldsymbol{p}}(\boldsymbol{x}',t)\,\mathrm{d}m \\ &= \frac{1}{2}\int (\boldsymbol{x}')^T \boldsymbol{S}_\omega^T \boldsymbol{S}_\omega \boldsymbol{x}'\,\mathrm{d}m + \frac{1}{2}\boldsymbol{q}^T(t)\int \boldsymbol{\phi}^T(\boldsymbol{x}')\boldsymbol{S}_\omega^T\boldsymbol{S}_\omega\boldsymbol{\phi}(\boldsymbol{x}')\,\mathrm{d}m\boldsymbol{q}(t) + \\ &\quad \frac{1}{2}\dot{\boldsymbol{q}}^T(t)\int \boldsymbol{\phi}^T(\boldsymbol{x}')\boldsymbol{\phi}(\boldsymbol{x}')\,\mathrm{d}m\dot{\boldsymbol{q}}(t) + \int (\boldsymbol{x}')^T\boldsymbol{S}_\omega^T\boldsymbol{S}_\omega\boldsymbol{\phi}(\boldsymbol{x}')\,\mathrm{d}m\boldsymbol{q}(t) + \\ &\quad \int (\boldsymbol{x}')^T\boldsymbol{S}_\omega^T\boldsymbol{\phi}(\boldsymbol{x}')\,\mathrm{d}m\dot{\boldsymbol{q}}(t) + \boldsymbol{q}^T(t)\int \boldsymbol{\phi}^T(\boldsymbol{x}')\boldsymbol{S}_\omega^T\boldsymbol{\phi}(\boldsymbol{x}')\,\mathrm{d}m\dot{\boldsymbol{q}}(t) \end{aligned} \tag{4.8}$$

m stands for the mass of the element. As discussed in the previous chapter, the displacement field variable for a 3D solid element can be expressed in terms of the shape functions N_i:

$$\boldsymbol{u}_e\left(\bar{\boldsymbol{\xi}}\right) = \left\{u_x \quad u_y \quad u_z\right\}^{\mathsf{T}} = \sum_{i=1}^{n} N_i\left(\bar{\boldsymbol{\xi}}\right)a_{e,i}(t) = \mathbf{N}\left(\bar{\boldsymbol{\xi}}\right)\cdot\mathbf{a}_e(t) \tag{4.9}$$

Hence, applying the Euler–Lagrange equation onto the kinetic energy equation yields the following matrices for each element:

Mass Matrix: $$\mathbf{M}_e = \rho\int \boldsymbol{N}^T(\bar{\boldsymbol{\xi}})\boldsymbol{N}(\bar{\boldsymbol{\xi}})\,\mathrm{d}V \tag{4.10}$$

Coriolis Matrix: $$\mathbf{G}_e = 2\rho\int \boldsymbol{N}^T(\bar{\boldsymbol{\xi}})\boldsymbol{S}_\omega^T\boldsymbol{N}(\bar{\boldsymbol{\xi}})\,\mathrm{d}V \tag{4.11}$$

Spin Softening Matrix: $$\mathbf{K}_s^e = -\rho\int \boldsymbol{N}^T(\bar{\boldsymbol{\xi}})\boldsymbol{S}_\omega^T\boldsymbol{S}_\omega\boldsymbol{N}(\bar{\boldsymbol{\xi}})\,\mathrm{d}V \tag{4.12}$$

Centrifugal Force Vector: $$\boldsymbol{Q}_c^e = \rho\int \boldsymbol{N}^T(\bar{\boldsymbol{\xi}})\boldsymbol{S}_\omega^T\boldsymbol{S}_\omega\boldsymbol{x}'\,\mathrm{d}V \tag{4.13}$$

The integral functions involved in Equation (4.10) - (4.13) can be estimated by employing the Gaussian quadrature rule as shown in section 3.1.1.

4.1.3 Equation of Motion for the Rotating 3D Structures

The matrices of each element derived in the previous sections need to be transferred back into the global domain of the structure to assemble the global matrices shown in Equation (4.14). $[\mathbf{M}]$ is the global mass matrix and $[\mathbf{C}]$ is the global damping matrix. $[\mathbf{K}_0]$ stands for the global linear stiffness matrix and $[\mathbf{K}_{nl}]$ represents the global nonlinear stiffness matrix due to large strain. $[\mathbf{K}_s]$ is the symmetric spin softening matrix due to rotation. $\{\boldsymbol{Q}_c\}$ represents the centrifugal force vector, and $\{\boldsymbol{F}_{ext}\}$ is the harmonic excitation force vector. The Coriolis force is proportional to the components of the vibrational velocity perpendicular to the

rotational axis. The skew-symmetric matrix for the Coriolis effect $[\mathbf{G}]$ is not included in this research as the structure is much stiffer in the plane of rotation than in the transverse plane. Both $[\mathbf{K}_s]$ and $\{\boldsymbol{Q}_c\}$ are quadratic functions of $\boldsymbol{\Omega}$.

$$[\mathbf{M}]\,\ddot{\boldsymbol{u}} + [\mathbf{C}]\,\dot{\boldsymbol{u}} + ([\mathbf{K}_0] + [\mathbf{K}_{nl}(\boldsymbol{u})] + [\mathbf{K}_s(\boldsymbol{\Omega})])\,\boldsymbol{u} = \{\boldsymbol{F}_{ext}(t)\} + \{\boldsymbol{Q}_c(\boldsymbol{\Omega})\} \tag{4.14}$$

Damping matrix of the structural expressed in terms of $[\mathbf{M}]$ and $[\mathbf{K}]$ can be assumed to ensure that the system will still possess the classic normal modes, i.e. $[\mathbf{C}] = \alpha\,[\mathbf{M}] + \beta\,[\mathbf{K}_0]$. In a rotating system, the centrifugal force will bring the system into a pre-stressed state. The static displacement, $\boldsymbol{x}_s$, caused by centrifugal force is computed as the solution of the following static problem:

$$([\mathbf{K}_0] + [\mathbf{K}_{nl}(\boldsymbol{x}_s)] + [\mathbf{K}_s(\boldsymbol{\Omega})]) \cdot \{\boldsymbol{x}_s\} = \{\boldsymbol{Q}_c(\boldsymbol{\Omega})\} \tag{4.15}$$

Newton direction computation can be used to solve the equation. The total response of the system $\boldsymbol{u}(t)$ can be expressed as sum of static displacement and dynamic response, i.e. $\boldsymbol{u}(t) = \boldsymbol{x}_s + \mathbf{x}_d(t)$. Hence, the governing equation for rotating structure is computed as:

$$[\mathbf{M}]\,\ddot{\boldsymbol{u}} + [\mathbf{C}]\,\dot{\boldsymbol{u}} + ([\mathbf{K}_0] + [\mathbf{K}_{nl}(\boldsymbol{u})] + [\mathbf{K}_s(\boldsymbol{\Omega})])\,\boldsymbol{u} = \{\boldsymbol{F}_{ext}(t)\} + \{\boldsymbol{Q}_c(\boldsymbol{\Omega})\} \tag{4.16}$$

$$\Downarrow$$

$$[\mathbf{M}]\,\ddot{\mathbf{x}}_d + [\mathbf{C}]\,\dot{\mathbf{x}}_d + [\mathbf{K}]\,\mathbf{x}_d + \{\boldsymbol{F}_{nl}(\boldsymbol{x}_s, \mathbf{x}_d)\} = \{\boldsymbol{F}_{ext}(t)\} \tag{4.17}$$

$$\begin{aligned} \textit{where}, \quad & [\mathbf{K}] = [\mathbf{K}_0] + [\mathbf{K}_s(\boldsymbol{\Omega})] \\ & \{\boldsymbol{F}_{nl}\} = [\mathbf{K}_{nl}(\boldsymbol{x}_s + \mathbf{x}_d)] \cdot \{\boldsymbol{x}_s + \mathbf{x}_d\} - [\mathbf{K}_{nl}(\boldsymbol{x}_s)] \cdot \{\boldsymbol{x}_s\} \end{aligned}$$

4.1.4 Linear modal analysis

The free response of an undamped rotating systems is expressed as:

$$[\mathbf{M}]\,\ddot{\mathbf{x}}_d + [\mathbf{C}]\,\dot{\mathbf{x}}_d + [\mathbf{K}(\boldsymbol{\Omega})]\,\mathbf{x}_d + \{\boldsymbol{F}_{nl}(\boldsymbol{x}_s, \mathbf{x}_d)\} = 0 \tag{4.18}$$

The resonance frequencies and the linear mode shapes of the centrifugally pre-stressed FE model can be computed by solving the eigenvalue problem in Equation (4.19), where ω_i is the i-th angular frequency and vector $\boldsymbol{\phi}_i$ is the i-th linear mode shape. Equation (4.19) is a linearised expression for Equation (4.18) at $\boldsymbol{u} = \boldsymbol{x}_s$.

$$\left([\mathbf{K}_T(\boldsymbol{x}_s, \boldsymbol{\Omega})] - \omega_i^2\,[\mathbf{M}]\right)\{\boldsymbol{\phi}_i\} = 0 \tag{4.19}$$

$[\mathbf{K}_T]$ is the tangential stiffness matrix computed at the pre-stressed displacement, i.e. $\boldsymbol{u} = \boldsymbol{x}_s$.

$$\begin{aligned}
\boldsymbol{F}(\boldsymbol{u}) &= [\mathbf{K}(\boldsymbol{\Omega})]\,\boldsymbol{u} + [\mathbf{K}_{nl}(\boldsymbol{u})]\,\boldsymbol{u} \\
[\mathbf{K}_T] &= \left.\frac{d\boldsymbol{F}(\boldsymbol{u})}{d\boldsymbol{u}}\right|_{\boldsymbol{u}=\boldsymbol{x}_s} \\
&= [\mathbf{K}(\boldsymbol{\Omega})] + \left.\frac{d\boldsymbol{F}_{nl}(\boldsymbol{x}_s, \mathbf{x}_d)}{d\mathbf{x}_d}\right|_{\boldsymbol{u}=\boldsymbol{x}_s} \\
&= [\mathbf{K}(\boldsymbol{\Omega})] + [\mathbf{K}_1(\boldsymbol{x}_s)] + [\mathbf{K}_2(\boldsymbol{x}_s)] + [\mathbf{K}_3(\boldsymbol{x}_s)] + [\mathbf{K}_4(\mathbf{S})]|_{\boldsymbol{u}=\boldsymbol{x}_s}
\end{aligned} \tag{4.20}$$

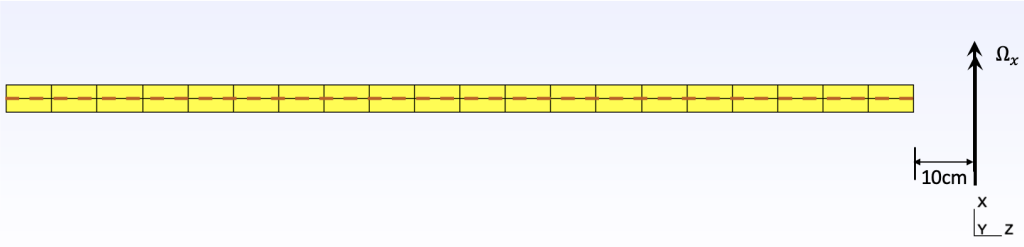
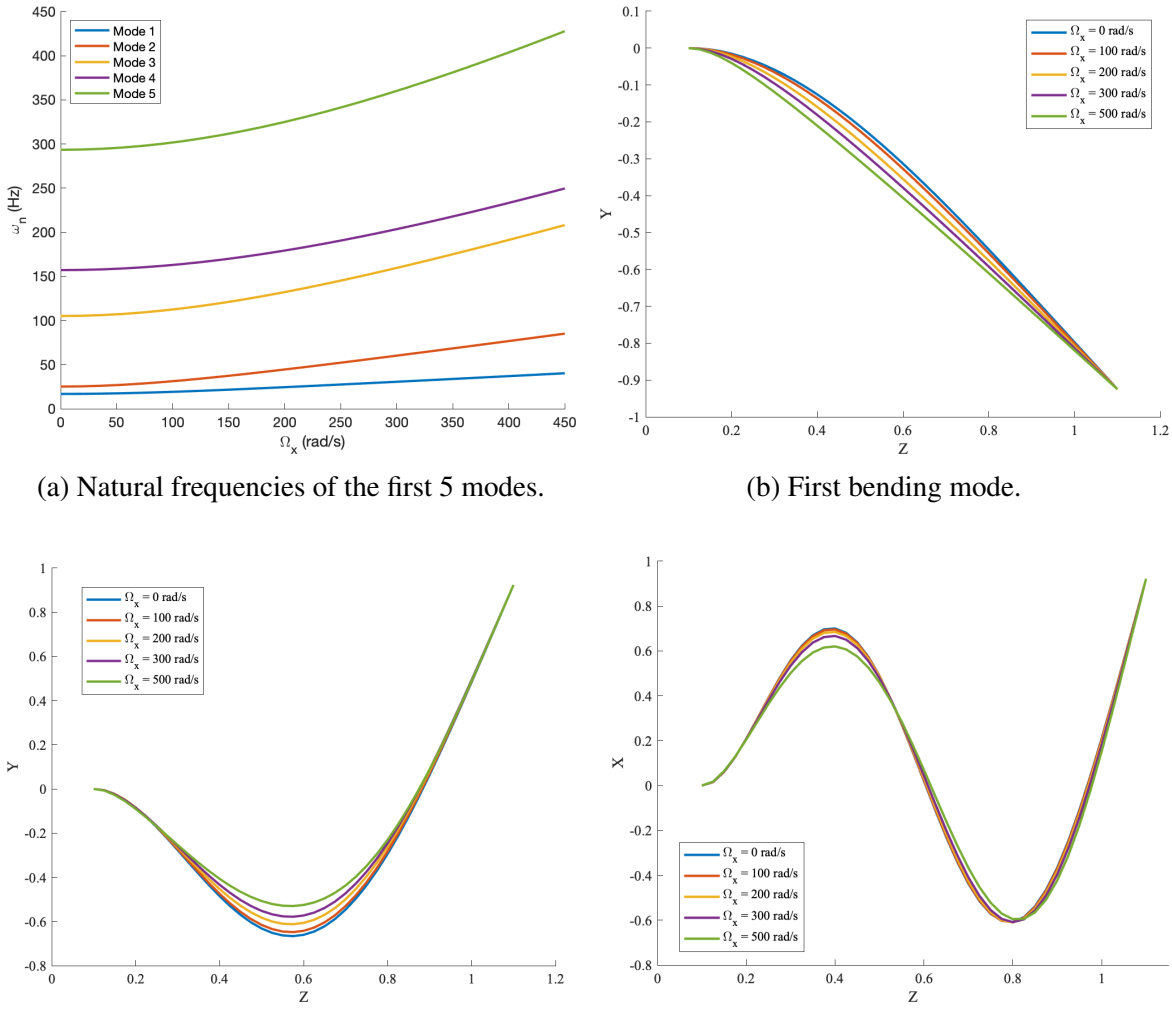


Fig. 4.2 *Rotating cantilevered beam with centre of rotation 10 cm apart from the clamped end.*

Figure 4.3a shows the effect of the rotational speed on the first 5 natural frequencies of the cantilevered beam model shown in Figure 3.17. As depicted in Figure 4.2, the centre of rotation is 10 cm apart from the clamped end of the cantilevered beam. The 3D structure has a dimension of $30\text{mm} * 20\text{mm} * 1000\text{mm}$. 3D 20-node hexahedron elements are used in the FE model with material parameters being: Young's Modulus $E = 210$ GPa, density $\rho = 7800$ kg/m^3 and Poisson's ratio $\nu = 0.3$. A mass proportional damping matrix $[\mathbf{C}] = 3[\mathbf{M}]$ is assumed. As the rotational speed Ω_x increases, the stiffening effect can be observed on all 5 modes investigated. This is due to the centrifugal force $\boldsymbol{Q}_c$ introduced when the beam is rotating. Centrifugal force is the outward force away from the centre of rotation. The force is caused by the motion of the rotating frame to account for the constant acceleration of the beam. It contributes to the restoring forces on the structure if it bends. The centrifugal force increases with the rotational speed, as in Equation (4.13), hence the stiffening effect becomes significant for large rotation. Figures 4.3b to 4.3d illustrate the effect of the rotational speed on the shape of the first 3 flapwise bending modes. A 3D FEM model is employed in this case. For the simplicity of visualisation, only the deformation shapes of the centroid line in the YZ-plane (dashed red line on Figure 4.2) are presented. For the 3D model under higher rotational speed, the mode shapes of the FE model become less flexible.



(a) Natural frequencies of the first 5 modes.

(b) First bending mode.

(c) Second bending mode.

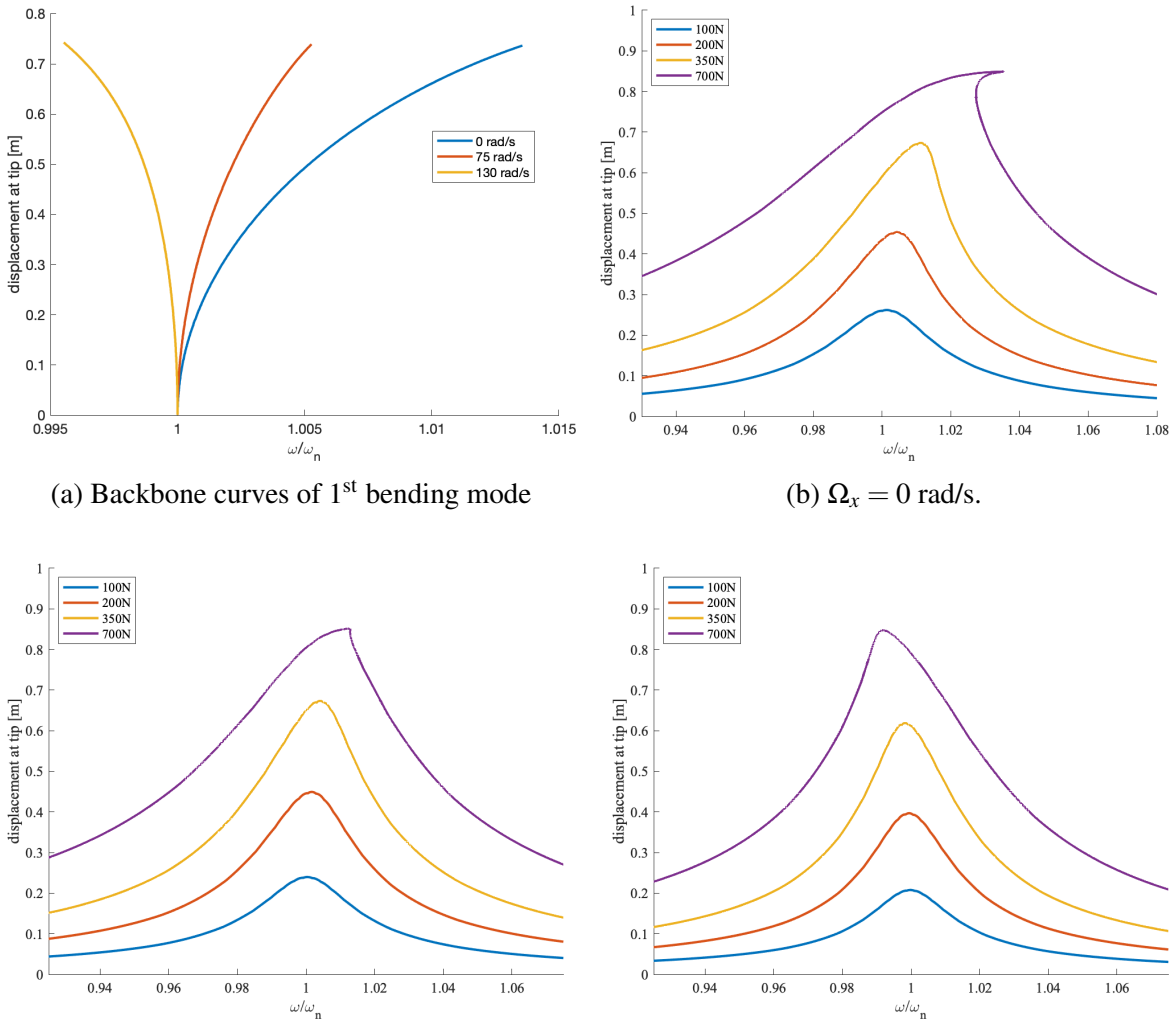
(d) Third bending mode.

Fig. 4.3 *Effect of rotational speed on the linear vibration modes.*

4.1.5 Free and forced vibration analysis of the 3D rotating structure

The nonlinear dynamic equation of motion for the rotating system is solved by using the HBM method together with the AFT. Readers are referred to Chapter 3 for the details of the algorithms used. For both the free and the forced analysis, 5 harmonics are considered in the HBM and 32 time steps were chosen for the AFT. Figure 4.4 shows the nonlinear FRF plots and the backbone curves for the first bending mode. For the forced vibration analysis, a periodic point load is applied at the tip of the cantilevered beam. The excitation frequency on the x-axis is scaled by the natural frequency of the structure. The values of ω_n are at 16.804 Hz, 18.207 Hz, and 20.594 Hz for $\Omega_x = 0$ rad/s, $\Omega_x = 75$ rad/s, and $\Omega_x = 130$ rad/s, respectively. Due to the centrifugal stiffening effect, the amplitude of the resonance peak

decreases as the rotational speed increases. For example, for the forcing amplitude at 350 N, the resonance peaks for $\Omega_x = 0$ rad/s and $\Omega_x = 130$ rad/s are at 0.6709 m and 0.6128 m, respectively. The static deflection caused by the centrifugal force introduces a softening effect on the 1st bending mode of the nonlinear system. This softening effect could overcome the hardening terms, i.e. $[\mathbf{K}_1]\boldsymbol{u}$, $[\mathbf{K}_2]\boldsymbol{u}$, and $[\mathbf{K}_3]\boldsymbol{u}$, if the static deflection is large or when the beam is very slender. At lower rotational speed, hardening effect caused by the nonlinear strain dominates. The softening behaviour can be seen once $\boldsymbol{\Omega}$ passed a critical value.



(a) Backbone curves of 1st bending mode

(b) $\Omega_x = 0$ rad/s.

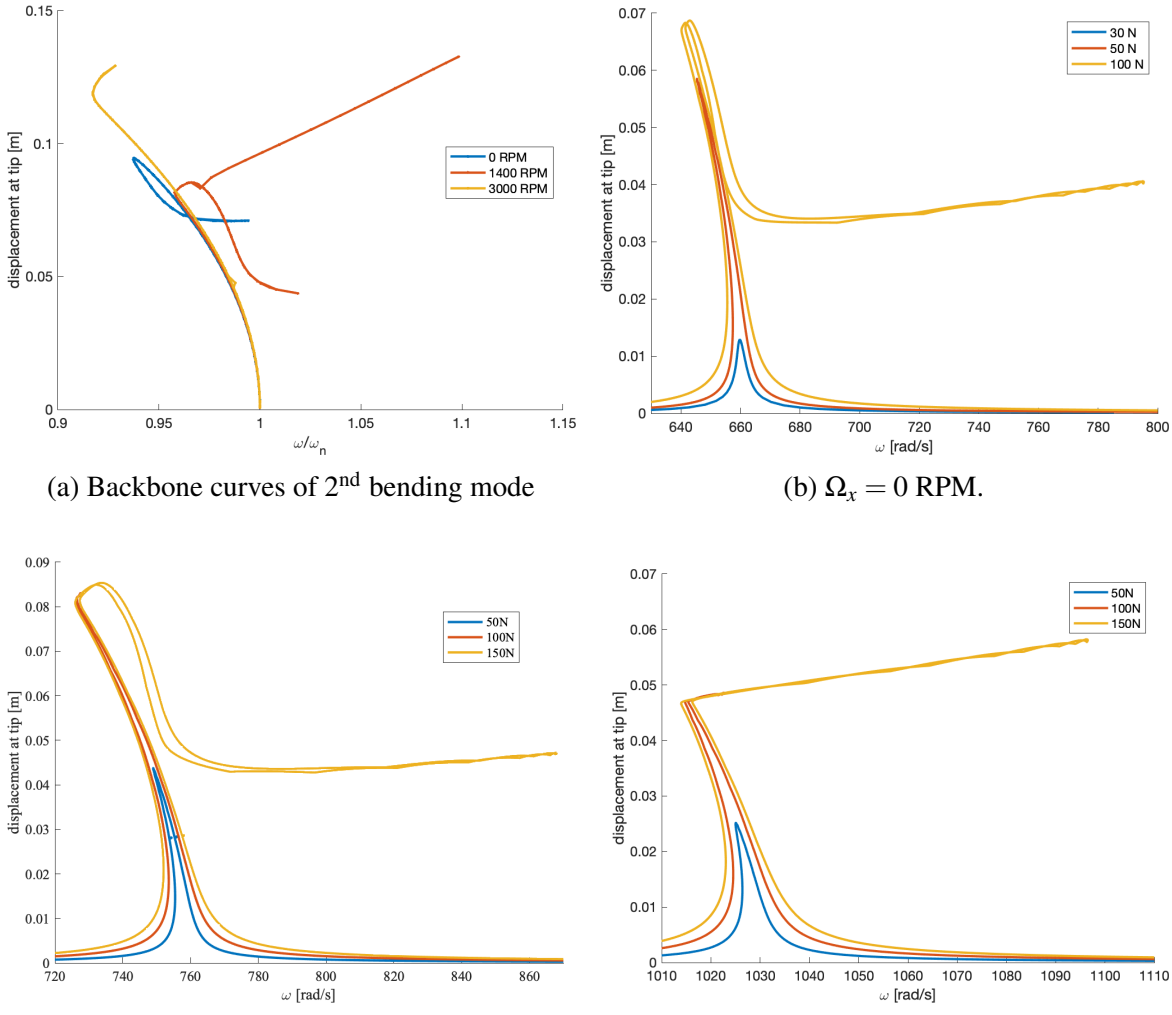
(c) $\Omega_x = 75$ rad/s.

(d) $\Omega_x = 130$ rad/s.

Fig. 4.4 *Backbone curves and FRF plots of the first bending mode for various rotational speed.*

Figure 4.5 shows the backbone curves and the nonlinear FRF plots of the 2nd bending mode for various rotational velocities. The rotational speed enforces a hardening effect on

the nonlinear system in this mode. The hardening effect is relatively weak on this mode compared to the softening effect on the first bending mode. When $\Omega_x = 1400$ RPM, the 4$^{\text{th}}$ flexural modes has a natural frequency of 3721 Hz. A 5:1 ratio between the 4$^{\text{th}}$ and the 2$^{\text{nd}}$ flexural modes can be found when ω reach 740 Hz. The branches on the backbone curve for $\Omega_x = 1400$ RPM represent the modal interaction between the two flexural modes. The damping parameter α is taken to be $\alpha = 2 \times 0.5\% \, \omega_n$ for the this mode. The branch on the $\Omega_x = 3000$ FRF plot is due to the 4:1 ratio between the 4$^{\text{th}}$ and the 2$^{\text{nd}}$ flexural modes. A 3:1 ratio between the 3$^{\text{rd}}$ and the 2$^{\text{nd}}$ flexural modes is found for the non-rotating case.



(a) Backbone curves of 2$^{\text{nd}}$ bending mode

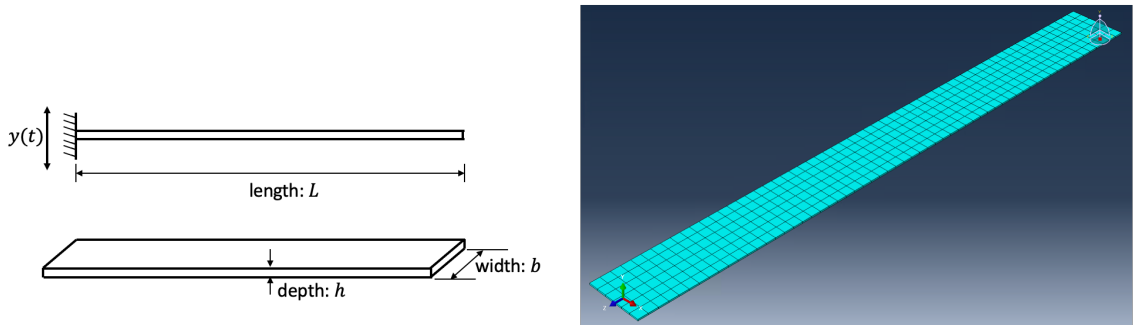
(b) $\Omega_x = 0$ RPM.

(c) $\Omega_x = 1400$ RPM.

(d) $\Omega_x = 3000$ RPM.

Fig. 4.5 *Backbone curves and FRF plots of the second bending mode for various rotational speed.*

4.2 Structure with base excitation



(a) Schematic Model (b) FEM mesh with 20-node hexahedron elements

Fig. 4.6 *3D cantilevered beam under periodic base excitation.*

In the previous analyses, a periodic point load is assumed. To validate the algorithms implemented for the nonlinear analysis, simulation results are compared with the experimental data. A periodic base excitation is used in the experiment setup. Base Excitation loading is a commonly used load type for studying the behaviour of a vibration isolation system. One or more structural supports are given a prescribed motion, causing the system to vibrate. This can be used to model a vehicle suspension system or the earthquake response of a structure. Figure 4.6b shows the cantilevered beam under transverse base excitationx, $y(t) = Y\sin(\omega t)$, with Y being the amplitude of the base excitation in m. An experiment on investigating the nonlinear behaviour of a catilevered beam was carried in ISAE Supméca (Institut supérieur de mécanique de Paris). The mesh for the 3D structure used in the experiment is presented in Figure 4.6b. 20-node hexahedron elements are selected for the simulation.

4.2.1 Equation of motion in time domain

As discussed in Chapter 3, the FEM motion equations for a geometrically nonlinear beam under periodic point load $\{\boldsymbol{F}_{ext}(\omega,t)\}$ are:

$$\begin{gathered}[\mathbf{M}]\ddot{\boldsymbol{u}}+[\mathbf{C}]\dot{\boldsymbol{u}}+([\mathbf{K}_0]+[\mathbf{K}_{nl}(\boldsymbol{u})])\,\boldsymbol{u}=\{\boldsymbol{F}_{ext}(\omega,t)\}\\ \Downarrow\\ [\mathbf{M}]\ddot{\boldsymbol{u}}+[\mathbf{C}]\dot{\boldsymbol{u}}+[\mathbf{K}(\boldsymbol{u})]\,\boldsymbol{u}=\{\boldsymbol{F}_{ext}(\omega,t)\}\end{gathered} \tag{4.21}$$

In the base excitation, the absolute response $\boldsymbol{u}^a$ can be partitioned into the known applied base movements $\boldsymbol{u}_b^a$ and the unknown internal movements $\boldsymbol{u}_i^a$. The FEM equation of motion

can hence be partitioned as:

$$\begin{bmatrix} \mathbf{M}_{ii} & \mathbf{M}_{ib} \\ \mathbf{M}_{bi} & \mathbf{M}_{bb} \end{bmatrix} \begin{Bmatrix} \ddot{\boldsymbol{u}}_i^a \\ \ddot{\boldsymbol{u}}_b^a \end{Bmatrix} + \begin{bmatrix} \mathbf{C}_{ii} & \mathbf{C}_{ib} \\ \mathbf{C}_{bi} & \mathbf{C}_{bb} \end{bmatrix} \begin{Bmatrix} \dot{\boldsymbol{u}}_i^a \\ \dot{\boldsymbol{u}}_b^a \end{Bmatrix} + \begin{bmatrix} \mathbf{K}_{ii} & \mathbf{K}_{ib} \\ \mathbf{K}_{bi} & \mathbf{K}_{bb} \end{bmatrix} \begin{Bmatrix} \boldsymbol{u}_i^a \\ \boldsymbol{u}_b^a \end{Bmatrix} = \begin{Bmatrix} 0 \\ \boldsymbol{F}_b \end{Bmatrix} \tag{4.22}$$

$\boldsymbol{F}_b$ is the external force applied to the support due to base acceleration. The first row of Equation (4.22) gives:

$$\mathbf{M}_{ii}\ddot{\boldsymbol{u}}_i^a + \mathbf{C}_{ii}\dot{\boldsymbol{u}}_i^a + \mathbf{K}_{ii}\boldsymbol{u}_i^a = -\mathbf{M}_{ib}\ddot{\boldsymbol{u}}_b^a - \mathbf{C}_{ib}\dot{\boldsymbol{u}}_b^a - \mathbf{K}_{ib}\boldsymbol{u}_b^a \tag{4.23}$$

The rigid body movement due to the base excitation $y(t)$ in the j-direction can be expressed as $\boldsymbol{\phi}^{(j)}y(t)$. For a system with n unconstrained nodes, $\boldsymbol{\phi}^{(x)}$ is a vector of length $3n$ computed as $\begin{Bmatrix} 1 & 0 & 0 & 1 & 0 & 0 & \dots & 1 & 0 & 0 \end{Bmatrix}^\mathsf{T}$. The relative response $\boldsymbol{u}^r$ of the structure to the base is expressed as:

$$\boldsymbol{u}_i^r = \boldsymbol{u}_i^a - \boldsymbol{\phi}^{(j)}y(t) \tag{4.24}$$

The rigid body movement does not cause any internal strain, hence $\mathbf{K}\phi^{(j)} = 0$. Knowing that $[\mathbf{C}]\dot{\boldsymbol{u}} = [\alpha\mathbf{M} + \beta\mathbf{K}]\dot{\boldsymbol{u}}$, the expression can be simplified to $[\mathbf{C}]\dot{\boldsymbol{u}} = \alpha\,[\mathbf{M}]\boldsymbol{\phi}^{(j)}\dot{y}$. Assuming that there is no coupling between the base DOFs and the internal DOFs in the mass matrix, i.e. $\mathbf{M}_{ib} = \mathbf{C}_{ib} = \mathbf{K}_{ib} = \vec{0}$. Equation (4.23) can hence be rearranged as:

$$\mathbf{M}_{ii}\ddot{\boldsymbol{u}}_i^r + \mathbf{C}_{ii}\dot{\boldsymbol{u}}_i^r + \mathbf{K}_{ii}\boldsymbol{u}_i^r = -\mathbf{M}_{ii}\boldsymbol{\phi}\,\ddot{y} - \alpha\,\mathbf{M}_{ii}\boldsymbol{\phi}\,\dot{y} \tag{4.25}$$

HBM coupling with AFT can be used to solve the equation of motion for the response relative to the base supports, Equation (3.54). The excitation force vector in the frequency domain depends on ω. For $y(t) = Y\cos(\omega t)$, the vector $\tilde{\boldsymbol{b}}_{ext}$ of length $(2N_H + 1) \times \text{DOF}$ and its derivative are:

$$\tilde{\boldsymbol{b}}_{ext}(\omega) = \begin{Bmatrix} O_{\text{DOF}} & \omega^2\mathbf{M}_{ii}\boldsymbol{\phi}Y & \omega\,\alpha\,\mathbf{M}_{ii}\boldsymbol{\phi}Y & O_{\text{DOF}} & \dots & O_{\text{DOF}} \end{Bmatrix}^\mathsf{T} \tag{4.26}$$

$$\frac{\partial\tilde{\boldsymbol{b}}_{ext}}{\partial\omega} = \begin{Bmatrix} O_{\text{DOF}} & 2\omega\mathbf{M}_{ii}\boldsymbol{\phi}Y & \alpha\,\mathbf{M}_{ii}\boldsymbol{\phi}Y & O_{\text{DOF}} & \dots & O_{\text{DOF}} \end{Bmatrix}^\mathsf{T} \tag{4.27}$$

4.2.2 Simulation results for the experiment setup

The beam used in the experiment has a dimension of $30\text{mm} * 8.1\text{mm} * 300\text{mm}$. Homogeneous material of Young's Modulus $E = 193$ GPa, density $\rho = 8000\ \text{kg/m}^3$ and Poisson's ratio $\nu = 0.3$ is assumed in the simulation. This gives the natural frequency of the first bending mode being as $\omega_n = 45.30$ rad/s. The material damping coefficient ξ is measured as 0.428%, hence the damping matrix is formulated as $[\mathbf{C}] = 2\xi \cdot \omega_n \cdot [\mathbf{M}]$. Base excitation is applied at

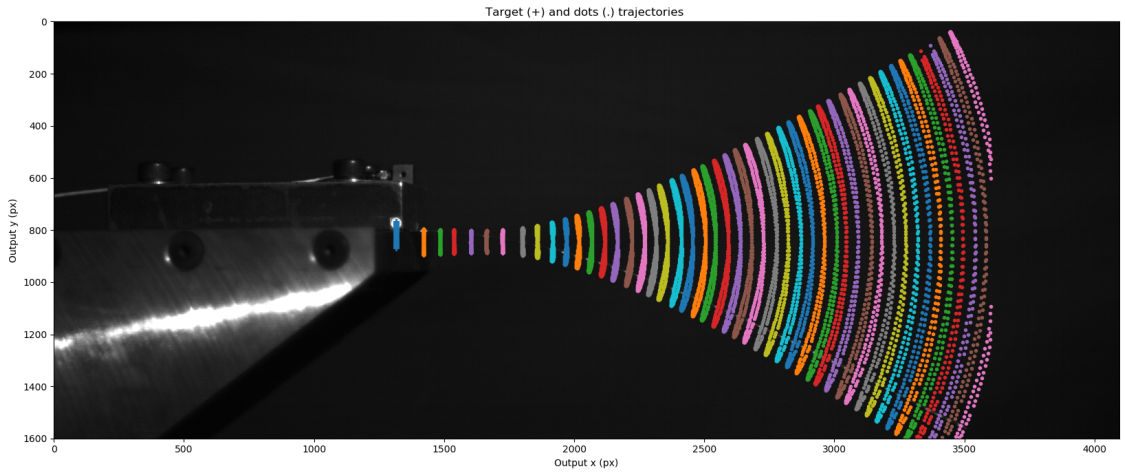
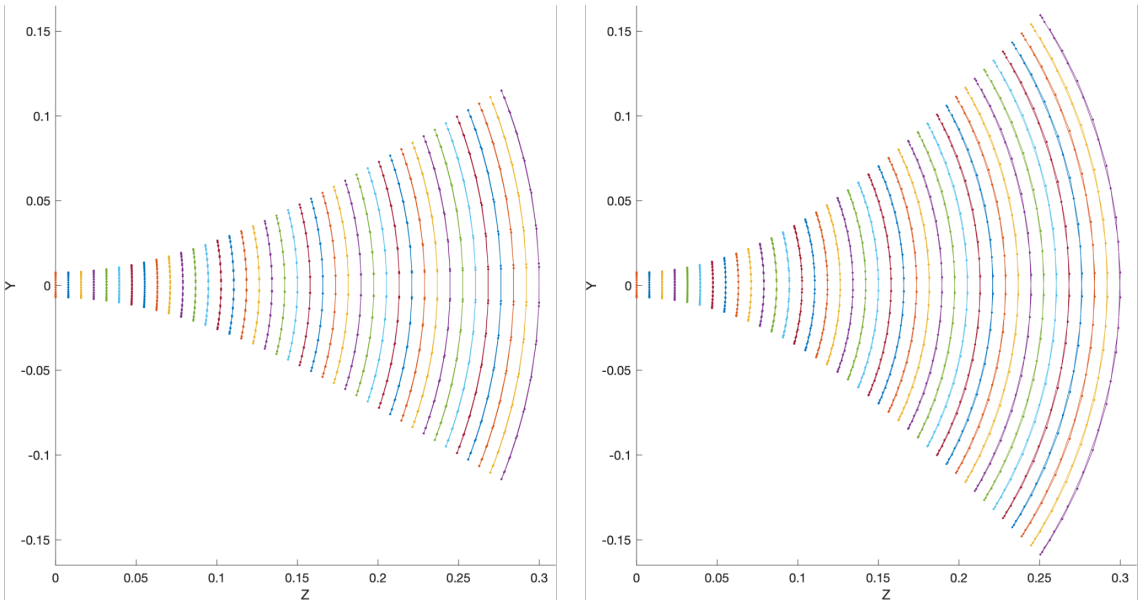


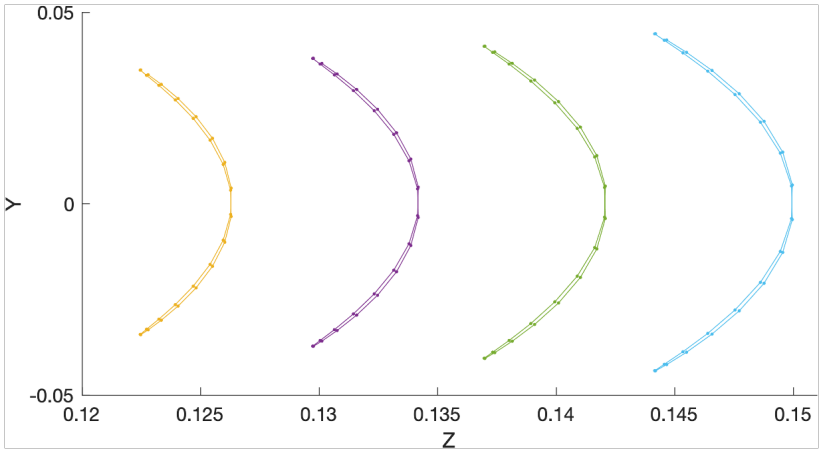
Fig. 4.7 *Dynamic response of the cantilevered beam under base excitation.*

the clamped end of the beam. Figure 4.7 shows the experimental set-up. The cantilevered beam is excited in the primary resonance region and the dynamic deformation of the beam is captured by camera. The experimental image shown in Figure 4.7 is in pixel (px). In this test, the magnitude of the base excitation was set as $Y = 7.25$ mm and the maximum responses at the tip was observed around 0.1145 m. Figure 4.9 shows the motion the beam in one period of oscillation predicted by the mathematical model. The axes show the coordinates of the nodes in YZ-plane. The coordinates of nodes on the clamped end are $Z = 0$. At the resonance frequency ($\omega = \omega_n$), the maximum transverse displacement at the beam tip reaches 0.1591 m. Maximum displacement of 0.1145 m is achieved when $\omega = 0.965\omega_n$ in the numerical prediction, Figure 4.8a. At each node, the dynamic response gives an ∞ shape as shown in both the experimental image and the simulation results (Figure 4.9a). This is due to the displacement of the shaker $y(t)$. Figure 4.9b presents the relative response ($\boldsymbol{u}^r$) of the beam with $Y = 7.25$ mm at $\omega = 0.965\omega_n$. In free vibration, the ∞ shape disappears. The simulation result responses at a higher amplitude with respect to the experimental data, which is due to several reasons. The cantilever was not placed in a vacuum chamber during the experiment. The neglect of air damping in the numerical model can lead to an overestimation on the dynamic response. Extracting the data slightly below the resonance frequency or an underestimated damping coefficient can also result in the mismatch between the experimental data and the simulation results. Figure 4.10 shows the FE model upward frequency sweep at different base excitation magnitudes. A noticeable difference in response amplitude can be detected with a slight deviation from the resonance frequency. The dynamic behaviours of beam with oscillations at large amplitudes are presented in Figure 4.11. The total displacements are around 80% of the beam length.

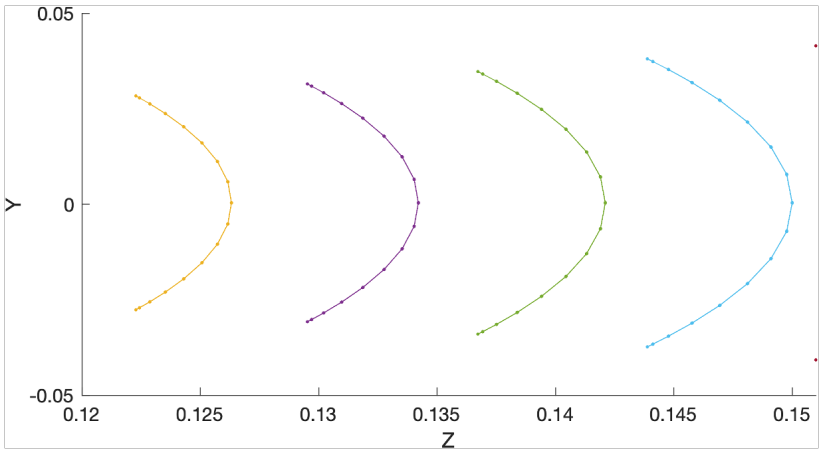


(a) $\omega = 0.965\omega_n$ (b) $\omega = \omega_n$

Fig. 4.8 *Dynamic response of the cantilevered beam from the numerical simulation with* $Y = 7.25$ *mm.*



(a) $\boldsymbol{u}^a$



(b) $\boldsymbol{u}^r$

Fig. 4.9 *Dynamic response of the cantilevered beam with* $Y = 7.25$ *mm and* $\omega = 0.965\omega_n$ *(zoomed): (a) absolute response, (b) relative response.*

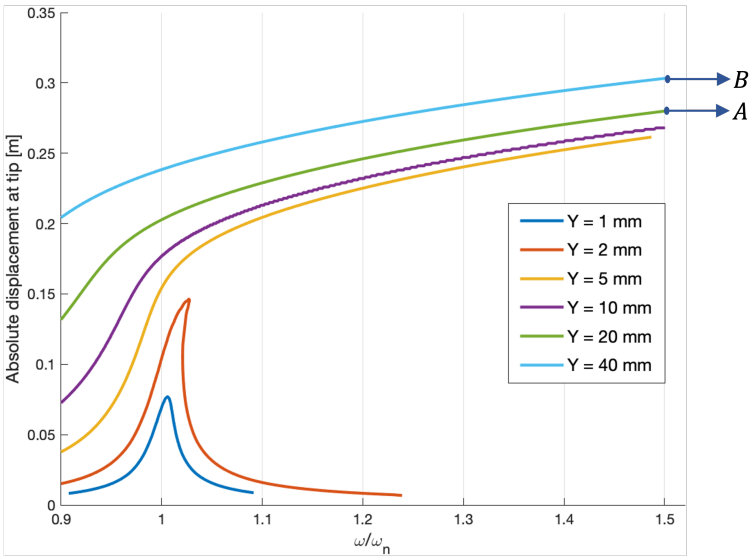
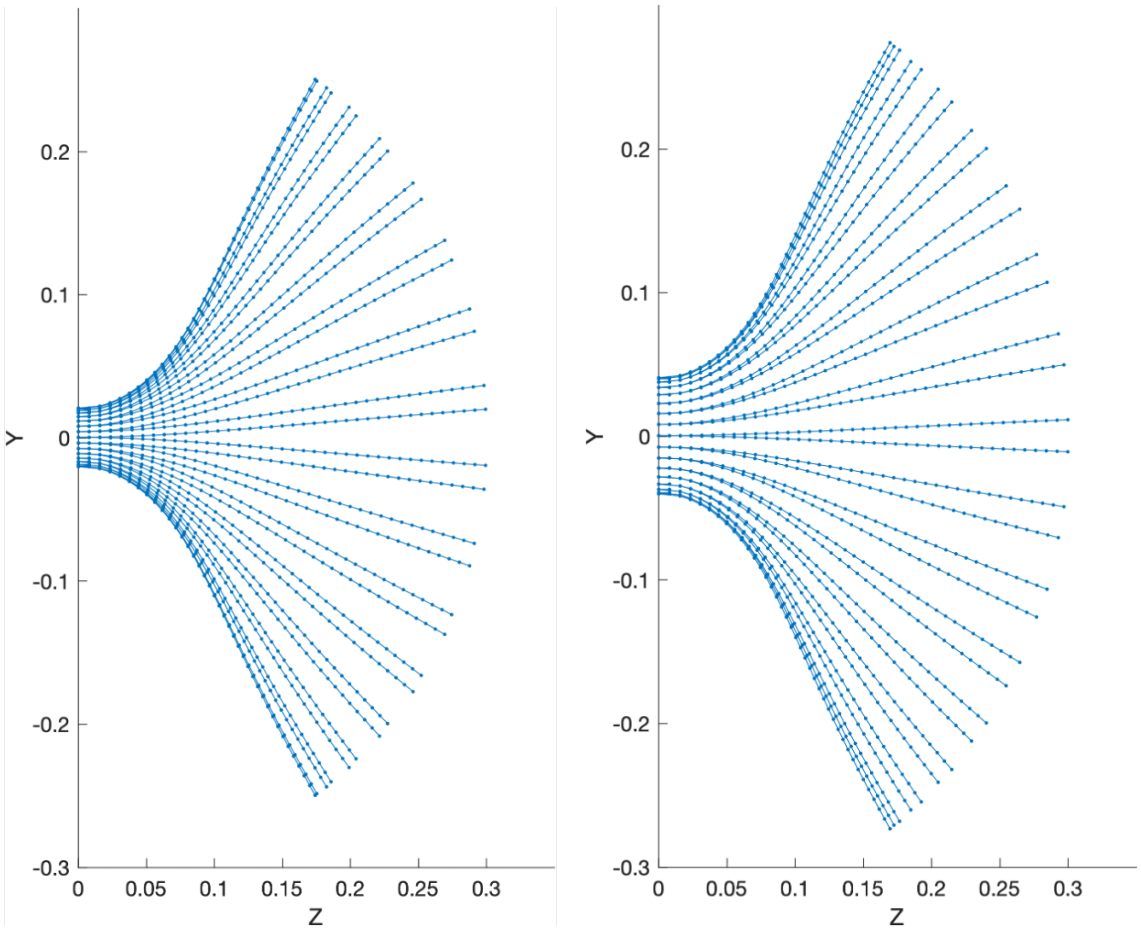


Fig. 4.10 *Upward frequency sweep of the cantilevered beam at different base excitation magnitudes.*



(a) $Y = 20$ mm (Point A) (b) $Y = 40$ mm (Point B)

Fig. 4.11 *Dynamic response of the cantilevered beam with extreme amplitude in one period of oscillation.*

4.3 Concluding remarks

In this chapter, the finite element equations for the rotating structure with geometric nonlinearities are presented. Uniform angular velocities are assumed and the effect of the Coriolis force is neglected in the algorithm. The combined effect of the rotational speed and geometric nonlinear terms are studied. The speed-dependent centrifugal force brings the rotating structure into a pre-stressed state. This causes the hardening effect on the linear natural frequencies. For the nonlinear modal analysis of the rotating cantilevered beam investigated in this chapter, the rotational speed can have softening/hardening effects, depending on the mode. The hardening effect can be seen on the FRF of the first bending mode when the rotational speed is low. Once the rotational speed passed a critical value, softening effect can be observed. Whereas for the second bending mode, the hardening effect is shown on the backbone curves at all rotational speeds.

Algorithms used in the numerical simulation for structures under base excitation are derived. The nonlinear dynamics of a cantilevered beam were examined experimentally and theoretically. In the experiment set-up, the cantilevered beam was base excited around the primary resonance region. The motion of the beam was captured by a camera. Numerical analyses of the 3D cantilevered beam under base excitation around the primary frequency were conducted. The overall dynamic behaviour predicted by the simulation has a good match with the experimental observation. However, the model gave a higher response amplitude than the experiment. This is mainly due to the neglect on air damping in the model. It was also shown that the nonlinear model is fully capable of capturing the extreme motions when oscillating at large amplitudes.

Chapter 5

Reduced order modelling based on intrusive method

The solution time of the system increases rapidly with the number of DOFs in the system. For complex engineering structures with thousands or millions of DOFs in the finite element model, the numerical analysis methods for solving the ODEs in the equations of motion become impossible. Model order reduction methods are used to decrease the complexity and computational effort for solving the equations by reducing the number of DOFs ($r \ll n$) and allowing the frequency analysis, i.e. HBM, to be applied on large-scale applications. A computationally efficient ROM model with a good approximation of the full-order model and the ability to retrieve nonlinear features is desired.

This chapter presents two projection-based reduced order modelling techniques for 3D structures with geometric nonlinearities. In the projection-based ROM methods, $\boldsymbol{\Gamma} \in \mathbb{R}^{n \times r}$ maps the full-order model with n DOFs to a reduced set of r generalised coordinates. The displacement vector of size n is approximated by:

$$\boldsymbol{u}(t) \approx \boldsymbol{\Gamma}(\boldsymbol{q}) \qquad \textit{and} \qquad \boldsymbol{V} = \left.\frac{\partial \boldsymbol{\Gamma}}{\partial \boldsymbol{q}}\right|_{\boldsymbol{q}=\boldsymbol{q}_0} \tag{5.1}$$

where vector $\boldsymbol{q} \in \mathbb{R}^r$ denotes the reduced set of generalised coordinates. The projection basis matrix $\boldsymbol{V}$ consists of r selected subspaces V_i, i.e. $[\boldsymbol{V}] = \begin{bmatrix} V_1 & V_2 & \dots & V_r \end{bmatrix}$. The selected subspace is used as a basis onto which the discrete equations describing the nonlinear dynamic system are projected. The choice of $\boldsymbol{V}$ is very critical in determining the accuracy of the reduced solution. The size of the basis is essential in determining the reduction in computation time. For the first approach presented, the motion equations of the full FEM model are projected onto a linear basis, which is consisted of the mass-normalised linear

modes. The second approach is based on nonlinear mapping. Static modal derivatives (SMDs) and the relevant vibration modes are used to construct the quadratic manifold (QM). The quadratic manifold defined is then used for nonlinear projectional reduction. In this chapter, a full-order model based on finite element and harmonic balance method is derived. The two ROM approaches are then implemented into the Finite Element framework in an intrusive way to predict the dynamic behaviour of the 3D geometrically nonlinear structure. The ROM techniques are also implemented onto the rotating structures to predict the correct hardening/softening behaviour of nonlinear systems. The convergences of the frequency response functions generated from the reduced models are investigated and the computational times taken by each method are compared.

5.1 Governing equations for a geometric nonlinear system

The equation of motion for the 3D FEM model with a total of n DOFs is expressed as:

$$[\mathbf{M}]\ddot{\boldsymbol{u}} + [\mathbf{C}]\dot{\boldsymbol{u}} + [\mathbf{K}]\boldsymbol{u} + \{\boldsymbol{F}_{nl}(\boldsymbol{u})\} = \{\boldsymbol{F}_{ext}(\omega, t)\} \tag{5.2}$$

$[\mathbf{M}]$ is the global mass matrix and $[\mathbf{K}]$ is the global linear stiffness matrix. $[\mathbf{C}]$ stands for the global damping matrix, which can be expressed as $[\mathbf{C}] = \alpha[\mathbf{M}] + \beta[\mathbf{K}]$. $\{\boldsymbol{F}_{nl}\}$ is the nonlinear force caused by the nonlinear strain-displacement relationship (geometric nonlinearity). $\{\boldsymbol{F}_{ext}\}$ is the harmonic excitation force vector and $\boldsymbol{u}$ is the dynamic response. For a non-rotating structure:

$$\begin{aligned}
&[\mathbf{K}] = [\mathbf{K}_0] \\
&\boldsymbol{F}_{nl} = [\mathbf{K}_{nl}]\boldsymbol{u} = \left(\frac{1}{2}[\mathbf{K}_1(\boldsymbol{u})] + [\mathbf{K}_2(\boldsymbol{u})] + \frac{1}{2}[\mathbf{K}_3(\boldsymbol{u})]\right)\boldsymbol{u}
\end{aligned}$$

For a rotating structure with $\boldsymbol{\Omega} = \{\Omega_x, \Omega_y, \Omega_z\}$ and static deformation $\boldsymbol{x}_s$:

$$\begin{aligned}
&[\mathbf{K}] = [\mathbf{K}_0] + [\mathbf{K}_s(\boldsymbol{\Omega})] \\
&\boldsymbol{F}_{nl} = [\mathbf{K}_{nl}(\boldsymbol{x}_s + \boldsymbol{u})] \cdot \{\boldsymbol{x}_s + \boldsymbol{u}\} - [\mathbf{K}_{nl}(\boldsymbol{x}_s)] \cdot \{\boldsymbol{x}_s\}
\end{aligned}$$

$\boldsymbol{x}_s$ is the static deformation caused by the centrifugal stiffening effect. Details of the computation for $\boldsymbol{x}_s$ and the FE matrices can be found in section 4.1.

5.2 ROM using linear modes

In the linear projection-based approach, the dynamic response of the rotating structure $\boldsymbol{u} \in \mathbb{R}^n$ can be expressed in the reduced coordinates as:

$$\boldsymbol{u}(\omega,t) = \sum_{i=1}^{r} \boldsymbol{\phi}_i \cdot q_i(t) = \boldsymbol{\Phi}\boldsymbol{q} \tag{5.3}$$

$\boldsymbol{\Phi} \in \mathbb{R}^{n\times r}$ is a collection of the selected eigenmodes of the system. The eigenmodes are computed as shown in section 4.1.4.

5.2.1 Reduced equation of motion for 3D nonlinear structures

The reduced equation of motion can then be achieved by substituting Equation (5.3) into Equation (5.2) and multiplying the equation by $\boldsymbol{\Phi}^\mathsf{T}$:

$$\begin{gathered}
\boldsymbol{\Phi}^\mathsf{T}[\mathbf{M}]\boldsymbol{\Phi}\ddot{\boldsymbol{q}} + \boldsymbol{\Phi}^\mathsf{T}[\mathbf{C}]\boldsymbol{\Phi}\dot{\boldsymbol{q}} + \boldsymbol{\Phi}^\mathsf{T}[\mathbf{K}]\boldsymbol{\Phi}\boldsymbol{q} + \boldsymbol{\Phi}^\mathsf{T}\{\boldsymbol{F}_{nl}(\boldsymbol{\Phi}\boldsymbol{q})\} = \boldsymbol{\Phi}^\mathsf{T}\{\boldsymbol{F}_{ext}(\omega,t)\} \\
\Downarrow \\
\left[\hat{\mathbf{M}}\right]\ddot{\boldsymbol{q}} + \left[\hat{\mathbf{C}}\right]\dot{\boldsymbol{q}} + \left[\hat{\mathbf{K}}\right]\boldsymbol{q} + \{\hat{\boldsymbol{F}}_{nl}(\boldsymbol{\Phi}\boldsymbol{q})\} = \{\hat{\boldsymbol{F}}_{ext}(t)\}
\end{gathered} \tag{5.4}$$

with the reduced matrices and vectors being as:

$$\begin{aligned}
&\left[\hat{\mathbf{M}}\right] = \boldsymbol{\Phi}^\mathsf{T}[\mathbf{M}]\boldsymbol{\Phi} \qquad &&\left[\hat{\mathbf{C}}\right] = \boldsymbol{\Phi}^\mathsf{T}[\mathbf{C}]\boldsymbol{\Phi} \qquad &&\left[\hat{\mathbf{K}}\right] = \boldsymbol{\Phi}^\mathsf{T}[\mathbf{K}]\boldsymbol{\Phi} \\
&\{\hat{\boldsymbol{F}}_{nl}\} = \boldsymbol{\Phi}^\mathsf{T}\boldsymbol{F}_{nl} \qquad &&\{\hat{\boldsymbol{F}}_{ext}\} = \boldsymbol{\Phi}^\mathsf{T}\{\hat{\boldsymbol{F}}_{ext}\}
\end{aligned} \tag{5.5}$$

Eigenvectors corresponding to the distinct eigenvalues of a symmetric matrix are mutually orthogonal to each other. The eigenvectors are normalised as:

$$\boldsymbol{\Phi}^\mathsf{T}\mathbf{M}\boldsymbol{\Phi} = \mathbf{I} \quad \textit{and} \quad \boldsymbol{\Phi}^\mathsf{T}\mathbf{K}_0\boldsymbol{\Phi} = \boldsymbol{\Lambda} \tag{5.6}$$

where $\boldsymbol{\Lambda} = \mathrm{diag}(\omega_1^2, \omega_2^2, \ldots, \omega_r^2)$ represents the collection of natural frequencies. The reduced linear stiffness term $\left[\hat{\mathbf{K}}\right]$ can hence be computed as:

$$\left[\hat{\mathbf{K}}\right] = \boldsymbol{\Lambda} + \boldsymbol{\Phi}^\mathsf{T}[\mathbf{K}_s(\boldsymbol{\Omega})]\boldsymbol{\Phi} \tag{5.7}$$

The reduced damping matrix $\left[\hat{\mathbf{C}}\right]$ is expressed as:

$$\left[\hat{\mathbf{C}}\right] = \alpha\left[\hat{\mathbf{M}}\right] + \beta\left[\hat{\mathbf{K}}\right] = \alpha\mathbf{I} + \beta\boldsymbol{\Lambda} + \beta\,\boldsymbol{\Phi}^\mathsf{T}[\mathbf{K}_s(\boldsymbol{\Omega})]\boldsymbol{\Phi} \tag{5.8}$$

By substituting the expression of the nonlinear stiffness matrix $[\mathbf{K}_{nl}]$ into the nonlinear term $\{\hat{\boldsymbol{F}}_{nl}(\boldsymbol{\Phi q})\}$ and expanding the function yields terms with $\boldsymbol{u}$ in different orders. The reduced nonlinear force can be expressed as:

$$\{\hat{\boldsymbol{F}}_{nl}(\boldsymbol{\Phi q})\} = \boldsymbol{L}(\boldsymbol{u}) + \boldsymbol{G}(\boldsymbol{u},\boldsymbol{u}) + \boldsymbol{H}(\boldsymbol{u},\boldsymbol{u},\boldsymbol{u}) \tag{5.9}$$

$\boldsymbol{L}^e(\boldsymbol{u})$ includes the linear terms of $\{\hat{\boldsymbol{F}}_{nl}\}$ for each FE element. The superscript e denotes the variables at the element level.

$$\boldsymbol{L}^e(\boldsymbol{u}) = \sum_{i=1}^{r} \boldsymbol{L}_i^e(\boldsymbol{\phi}_i) \cdot q_i \tag{5.10}$$

$$\begin{aligned}
\boldsymbol{L}_i^e(\boldsymbol{\phi}_i) = {} & \boldsymbol{\Phi}^{\mathsf{T}} \int [\mathbf{B}_0]^{\mathsf{T}} [\mathbf{D}] \left[\frac{1}{2}\mathbf{B}_1(\boldsymbol{x}_s)\right] \mathrm{d}V \cdot \boldsymbol{\phi}_i + \boldsymbol{\Phi}^{\mathsf{T}} \int [\mathbf{B}_0]^{\mathsf{T}} [\mathbf{D}] \left[\frac{1}{2}\mathbf{B}_1(\boldsymbol{\phi}_i)\right] \mathrm{d}V \cdot \boldsymbol{x}_s \\
& + \boldsymbol{\Phi}^{\mathsf{T}} \int [\mathbf{B}_1(\boldsymbol{x}_s)]^{\mathsf{T}} [\mathbf{D}] [\mathbf{B}_0] \mathrm{d}V \cdot \boldsymbol{\phi}_i + \boldsymbol{\Phi}^{\mathsf{T}} \int [\mathbf{B}_1(\boldsymbol{\phi}_i)]^{\mathsf{T}} [\mathbf{D}] [\mathbf{B}_0] \mathrm{d}V \cdot \boldsymbol{x}_s \\
& + \boldsymbol{\Phi}^{\mathsf{T}} \int [\mathbf{B}_1(\boldsymbol{\phi}_i)]^{\mathsf{T}} [\mathbf{D}] \left[\frac{1}{2}\mathbf{B}_1(\boldsymbol{x}_s)\right] \mathrm{d}V \cdot \boldsymbol{x}_s \\
& + \boldsymbol{\Phi}^{\mathsf{T}} \int [\mathbf{B}_1(\boldsymbol{x}_s)]^{\mathsf{T}} [\mathbf{D}] \left[\frac{1}{2}\mathbf{B}_1(\boldsymbol{\phi}_i)\right] \mathrm{d}V \cdot \boldsymbol{x}_s \\
& + \boldsymbol{\Phi}^{\mathsf{T}} \int [\mathbf{B}_1(\boldsymbol{x}_s)]^{\mathsf{T}} [\mathbf{D}] \left[\frac{1}{2}\mathbf{B}_1(\boldsymbol{x}_s)\right] \mathrm{d}V \cdot \boldsymbol{\phi}_i
\end{aligned} \tag{5.11}$$

The quadratic terms for each FE element are computed as:

$$\boldsymbol{G}^e(\boldsymbol{u},\boldsymbol{u}) = \sum_{i=1}^{r}\sum_{j=1}^{r} \boldsymbol{G}_{ij}^e(\boldsymbol{\phi}_i,\boldsymbol{\phi}_j) \cdot q_i \cdot q_j \tag{5.12}$$

$$\begin{aligned}
\boldsymbol{G}_{ij}^e(\boldsymbol{\phi}_i,\boldsymbol{\phi}_j) = {} & \boldsymbol{\Phi}^{\mathsf{T}} \int [\mathbf{B}_0]^{\mathsf{T}} [\mathbf{D}] \left[\frac{1}{2}\mathbf{B}_1(\boldsymbol{\phi}_i)\right] \mathrm{d}V \cdot \boldsymbol{\phi}_j + \boldsymbol{\Phi}^{\mathsf{T}} \int [\mathbf{B}_1(\boldsymbol{\phi}_i)]^{\mathsf{T}} [\mathbf{D}] [\mathbf{B}_0] \mathrm{d}V \cdot \boldsymbol{\phi}_j \\
& + \boldsymbol{\Phi}^{\mathsf{T}} \int [\mathbf{B}_1(\boldsymbol{x}_s)]^{\mathsf{T}} [\mathbf{D}] \left[\frac{1}{2}\mathbf{B}_1(\boldsymbol{\phi}_i)\right] \mathrm{d}V \cdot \boldsymbol{\phi}_j \\
& + \boldsymbol{\Phi}^{\mathsf{T}} \int [\mathbf{B}_1(\boldsymbol{\phi}_i)]^{\mathsf{T}} [\mathbf{D}] \left[\frac{1}{2}\mathbf{B}_1(\boldsymbol{x}_s)\right] \mathrm{d}V \cdot \boldsymbol{\phi}_j \\
& + \boldsymbol{\Phi}^{\mathsf{T}} \int [\mathbf{B}_1(\boldsymbol{\phi}_i)]^{\mathsf{T}} [\mathbf{D}] \left[\frac{1}{2}\mathbf{B}_1(\boldsymbol{\phi}_j)\right] \mathrm{d}V \cdot \boldsymbol{x}_s
\end{aligned} \tag{5.13}$$

The cubic terms for each FE element are computed as:

$$\boldsymbol{H}^e(\boldsymbol{u},\boldsymbol{u},\boldsymbol{u}) = \sum_{i=1}^{r}\sum_{j=1}^{r}\sum_{k=1}^{r}\boldsymbol{H}^e_{ijk}(\boldsymbol{\phi}_i,\boldsymbol{\phi}_j,\boldsymbol{\phi}_k)\cdot q_i\cdot q_j\cdot q_k \tag{5.14}$$

$$\boldsymbol{H}^e_{ijk}(\boldsymbol{\phi}_i,\boldsymbol{\phi}_j,\boldsymbol{\phi}_k) = \boldsymbol{\Phi}^{\mathsf{T}}\int\left[\mathbf{B}_1\left(\boldsymbol{\phi}_i\right)\right]^{\mathsf{T}}[\mathbf{D}]\left[\frac{1}{2}\mathbf{B}_1\left(\boldsymbol{\phi}_j\right)\right]\mathrm{d}V\cdot\boldsymbol{\phi}_k \tag{5.15}$$

Substituting Equations (5.7) - (5.15) into Equation (5.4), the reduced equation of motion for the rotating structure reads:

$$\ddot{\boldsymbol{q}}+[\alpha\mathbf{I}+\beta\boldsymbol{\Lambda}+\beta\boldsymbol{\Phi}^{\mathsf{T}}[\mathbf{K}_s(\boldsymbol{\Omega})]\boldsymbol{\Phi}]\dot{\boldsymbol{q}}+\boldsymbol{\Lambda}\boldsymbol{q}+\boldsymbol{L}(\boldsymbol{u})+\boldsymbol{G}(\boldsymbol{u},\boldsymbol{u})+\boldsymbol{H}(\boldsymbol{u},\boldsymbol{u},\boldsymbol{u})=\hat{\boldsymbol{F}}_{ext} \tag{5.16}$$

For a non-rotating structure, the $\boldsymbol{\Omega}$ and $\boldsymbol{x}_s$ terms in the equation of motion are eliminated. $\boldsymbol{L}_i$, $\boldsymbol{G}_{ij}$, and $\boldsymbol{H}_{ijk}$ are the coefficient tensors in the reduced equation of motion, which can be computed in the pre-processing stage to save the computational power.

5.2.2 Harmonic balance method for vibration analysis

HBM coupled with AFT method can be used to solve the reduced dynamic equation in frequency domain, Equation (5.17). The derivation of $\mathbf{Z}(\omega)$ can be found in Equation (2.73), with $\mathbf{M}=\mathbf{I}$, $\mathbf{C}=\alpha\mathbf{I}+\beta\boldsymbol{\Lambda}+\beta\boldsymbol{\Phi}^{\mathsf{T}}[\mathbf{K}_s(\boldsymbol{\Omega})]\boldsymbol{\Phi}$, and $\mathbf{K}=\boldsymbol{\Lambda}$. Parameters $\tilde{\boldsymbol{q}}$, $\tilde{\boldsymbol{b}}_{nl}$ and $\tilde{\boldsymbol{b}}_{ext}$ are $\boldsymbol{q}$, $\hat{\boldsymbol{F}}_{nl}(\boldsymbol{\Phi}\boldsymbol{q})$ and $\hat{\boldsymbol{F}}_{ext}$ in the frequency domain respectively.

$$\mathbf{R}(\omega,\tilde{\boldsymbol{q}})\equiv\mathbf{Z}(\omega)\tilde{\boldsymbol{q}}+\tilde{\boldsymbol{b}}_{nl}(\tilde{\boldsymbol{q}})-\tilde{\boldsymbol{b}}_{ext}=0 \tag{5.17}$$

AFT methodology is used to compute $\tilde{\boldsymbol{b}}_{nl}$. The response $\tilde{\boldsymbol{q}}$ is transformed into the time domain by applying IDFT. DFT is then followed to compute the resulting nonlinear force in frequency domain $\tilde{\boldsymbol{b}}_{nl}$.

$$\tilde{\boldsymbol{q}}\xrightarrow{\text{IDFT: }[\mathscr{F}]^{-1}}\underline{\boldsymbol{q}}(t)\rightarrow\underline{\hat{\boldsymbol{F}}}_{nl}(t)\xrightarrow{\text{DFT: }[\mathscr{F}]}\tilde{\boldsymbol{b}}_{nl}(\tilde{\boldsymbol{q}}) \tag{5.18}$$

The expressions of $[\mathscr{F}]$, $[\mathscr{F}]^{-1}$, $\underline{\boldsymbol{q}}(t)$, and $\underline{\hat{\boldsymbol{F}}}_{nl}(t)$ are defined in section 3.4.2. The Jacobian matrix for the nonlinear force is required in the Newton direction computation when solving the nonlinear equations. The derivative of $\tilde{\boldsymbol{b}}_{nl}$ with respect to $\tilde{\boldsymbol{q}}$ can be computed as:

$$\frac{\partial\tilde{\boldsymbol{b}}_{nl}}{\partial\tilde{\boldsymbol{q}}}=\frac{\partial\tilde{\boldsymbol{b}}_{nl}}{\partial\underline{\hat{\boldsymbol{F}}}_{nl}}\frac{\partial\underline{\hat{\boldsymbol{F}}}_{nl}}{\partial\underline{\boldsymbol{q}}}\frac{\partial\underline{\boldsymbol{q}}}{\partial\tilde{\boldsymbol{q}}}=[\mathscr{F}]\frac{\partial\underline{\boldsymbol{F}}_{nl}}{\partial\underline{\boldsymbol{q}}}[\mathscr{F}]^{-1} \tag{5.19}$$

The full expression for the $\dfrac{\partial \hat{\boldsymbol{F}}_{nl}}{\partial \boldsymbol{q}}$ matrix in each element is:

$$\frac{\partial \hat{\boldsymbol{F}}^e_{nl}}{\partial \boldsymbol{q}} = \boldsymbol{\Phi}^{\mathsf{T}} \frac{\partial \left[\boldsymbol{F}^e_{nl}(\boldsymbol{x}_s+\boldsymbol{u})\right]}{\partial \boldsymbol{u}} \boldsymbol{\Phi}$$

$$\begin{aligned}\frac{\partial \boldsymbol{F}^e_{nl}}{\partial \boldsymbol{u}} = &\int [\mathbf{B}_0]^{\mathsf{T}} [\mathbf{D}] [\mathbf{B}_1(\boldsymbol{x}_s+\boldsymbol{\Phi}\boldsymbol{q})] \, \mathrm{d}V + \int [\mathbf{B}_1(\boldsymbol{x}_s+\boldsymbol{\Phi}\boldsymbol{q})]^{\mathsf{T}} [\mathbf{D}] [\mathbf{B}_0] \, \mathrm{d}V \\ &+ \int [\mathbf{B}_1(\boldsymbol{x}_s+\boldsymbol{\Phi}\boldsymbol{q})]^{\mathsf{T}} [\mathbf{D}] [\mathbf{B}_1(\boldsymbol{x}_s+\boldsymbol{\Phi}\boldsymbol{q})] \, \mathrm{d}V + \int [\mathbf{G}]^{\mathsf{T}} [\boldsymbol{\Sigma}(\mathbf{S})] [\mathbf{G}] \, \mathrm{d}V \end{aligned} \tag{5.20}$$

The second Piola-Kirchoff stress vector $\mathbf{S}(\boldsymbol{q})$ can be expressed as:

$$\mathbf{S} = \boldsymbol{S}_0 + \sum_{i=1}^{r} \boldsymbol{S}_1(\boldsymbol{\phi}_i) \cdot q_i + \sum_{i=1}^{r}\sum_{j=1}^{r} \boldsymbol{S}_2(\boldsymbol{\phi}_i, \boldsymbol{\phi}_j) \cdot q_i \cdot q_j \tag{5.21}$$

with :

$$\mathbf{S}_0 = [\mathbf{D}] [\mathbf{B}_0] \{\boldsymbol{x}_s\} + [\mathbf{D}] \left[\frac{1}{2}\mathbf{B}_1(\boldsymbol{x}_s)\right] \{\boldsymbol{x}_s\} \tag{5.22}$$

$$\mathbf{S}_1 = [\mathbf{D}] [\mathbf{B}_0] \{\boldsymbol{\phi}_i\} + [\mathbf{D}] \left[\frac{1}{2}\mathbf{B}_1(\boldsymbol{\phi}_i)\right] \{\boldsymbol{x}_s\} + [\mathbf{D}] \left[\frac{1}{2}\mathbf{B}_1(\boldsymbol{x}_s)\right] \{\boldsymbol{\phi}_i\} \tag{5.23}$$

$$\mathbf{S}_2 = [\mathbf{D}] \left[\frac{1}{2}\mathbf{B}_1(\boldsymbol{\phi}_i)\right] \{\boldsymbol{\phi}_j\} \tag{5.24}$$

Hence the Jacobian matrix $\dfrac{\partial \boldsymbol{F}^e_{nl}}{\partial \boldsymbol{u}}$ is a function of $\boldsymbol{q}$ up to order 2.

$$\frac{\partial \boldsymbol{F}^e_{nl}}{\partial \boldsymbol{u}} = \boldsymbol{J}^e_0 + \sum_{i=1}^{r} \boldsymbol{J}^e_1(\boldsymbol{\phi}_i) \cdot q_i + \sum_{i=1}^{r}\sum_{j=1}^{r} \boldsymbol{J}^e_2(\boldsymbol{\phi}_i, \boldsymbol{\phi}_j) \cdot q_i \cdot q_j \tag{5.25}$$

with the constant term $\boldsymbol{J}^e_0$ being as:

$$\begin{aligned}\boldsymbol{J}^e_0 = &\int [\mathbf{B}_0]^{\mathsf{T}} [\mathbf{D}] [\mathbf{B}_1(\boldsymbol{x}_s)] \, \mathrm{d}V + \int [\mathbf{B}_1(\boldsymbol{x}_s)]^{\mathsf{T}} [\mathbf{D}] [\mathbf{B}_0] \, \mathrm{d}V \\ &+ \int [\mathbf{B}_1(\boldsymbol{x}_s)]^{\mathsf{T}} [\mathbf{D}] [\mathbf{B}_1(\boldsymbol{x}_s)] \, \mathrm{d}V + \int [\mathbf{G}]^{\mathsf{T}} [\boldsymbol{\Sigma}(\mathbf{S}_0)] [\mathbf{G}] \, \mathrm{d}V \end{aligned} \tag{5.26}$$

The linear term $\boldsymbol{J}^e_1(\boldsymbol{\phi}_i)$ being as:

$$\begin{aligned}\boldsymbol{J}^e_1 = &\int [\mathbf{B}_0]^{\mathsf{T}} [\mathbf{D}] [\mathbf{B}_1(\boldsymbol{\phi}_i)] \, \mathrm{d}V + \int [\mathbf{B}_1(\boldsymbol{\phi}_i)]^{\mathsf{T}} [\mathbf{D}] [\mathbf{B}_0] \, \mathrm{d}V \\ &+ \int [\mathbf{B}_1(\boldsymbol{x}_s)]^{\mathsf{T}} [\mathbf{D}] [\mathbf{B}_1(\boldsymbol{\phi}_i)] \, \mathrm{d}V + \int [\mathbf{B}_1(\boldsymbol{\phi}_i)]^{\mathsf{T}} [\mathbf{D}] [\mathbf{B}_1(\boldsymbol{x}_s)] \, \mathrm{d}V \\ &+ \int [\mathbf{G}]^{\mathsf{T}} [\boldsymbol{\Sigma}(\mathbf{S}_1)] [\mathbf{G}] \, \mathrm{d}V \end{aligned} \tag{5.27}$$

The quadratic term $\boldsymbol{J}_2^e(\boldsymbol{\phi}_i, \boldsymbol{\phi}_j)$ being as:

$$\boldsymbol{J}_2^e = \int [\mathbf{B}_1(\boldsymbol{\phi}_i)]^\mathsf{T} [\mathbf{D}] \left[\mathbf{B}_1(\boldsymbol{\phi}_j)\right] \mathrm{d}V + \int [\mathbf{G}]^\mathsf{T} [\boldsymbol{\Sigma}(\mathbf{S}_2)] [\mathbf{G}] \mathrm{d}V \tag{5.28}$$

The bar chart shown in Figure 5.1 is the comparison of time used to compute the coefficient tensors with different number of reduced basis (r) selected in the linear projection method. The 3D mesh shown in Figure 3.23 is used as an example here.

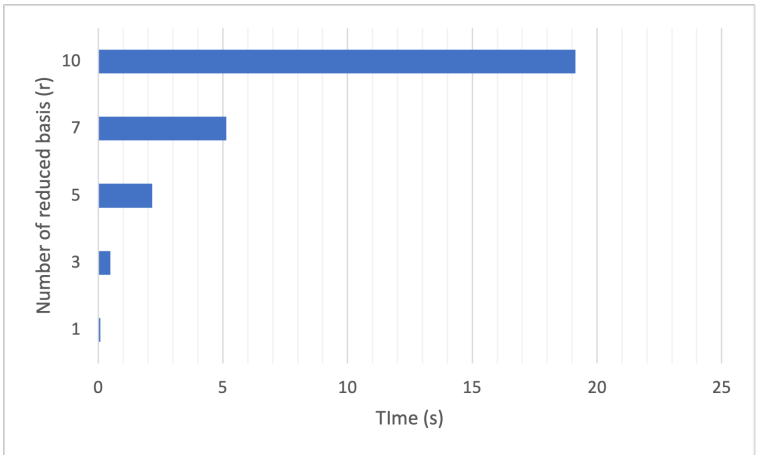


Fig. 5.1 *Time to compute the coefficient tensors with different number of reduced basis selected.*

5.3 ROM with static modal derivatives and quadratic manifold

In the quadratic manifold approach, the dynamic response of the 3D structure $\boldsymbol{u} \in \mathbb{R}^n$ can be approximated by applying the Taylor expansion up to quadratic order [156]. Hence, $\boldsymbol{u}$ is expressed in the reduced coordinates as:

$$\begin{aligned} \boldsymbol{u}(\omega,t) = \boldsymbol{\Gamma}(\boldsymbol{q}) &= \sum_{i=1}^{r} \boldsymbol{\phi}_i \cdot q_i(t) + \frac{1}{2} \sum_{i=1}^{r} \sum_{j=1}^{r} \boldsymbol{\Theta}_{ij} \cdot q_i \cdot q_j \\ &= \boldsymbol{\Phi}\boldsymbol{q} + \boldsymbol{\Theta}\boldsymbol{q}\boldsymbol{q} \end{aligned} \tag{5.29}$$

with $\boldsymbol{q} \in \mathbb{R}^r$ being the reduced generalized coordinates. $\boldsymbol{\Gamma} : \mathbb{R}^r \to \mathbb{R}^n$ represents the nonlinear mapping from the reduced generalized coordinates to the physical coordinates. $\boldsymbol{\Phi} \in \mathbb{R}^{n \times r}$ is a collection of the selected linear eigenmodes of the system. $\boldsymbol{\Theta} \in \mathbb{R}^{n \times r \times r}$ is the static modal derivative. $\boldsymbol{\Theta}_{ij}$ is defined as the derivative of $\boldsymbol{\phi}_i$ with respect to $\boldsymbol{q}_j$, i.e. the j-th coordinate

used for the reduced basis. In this approach, the nonlinear mapping is tangent to the subspace spanned by the selected linear modes, and its curvature is provided by the modal derivatives.

5.3.1 Static modal derivatives

In the nonlinear system, the eigenvector and its eigenfrequency have a dependence on the amplitude. With $\boldsymbol{F}(\boldsymbol{x}_s,\boldsymbol{u})$ being the total internal force, the eigenvalue problem of the nonlinear system becomes:

$$\left(\frac{d\boldsymbol{F}(\boldsymbol{x}_s,\boldsymbol{u})}{d\boldsymbol{u}} - \omega_i^2(\boldsymbol{u})\,[\mathbf{M}]\right)\{\boldsymbol{\phi}_i(\boldsymbol{u})\} = 0$$
$$\left(\mathbf{K}_T - \omega_i^2(\boldsymbol{u})\,[\mathbf{M}]\right)\{\boldsymbol{\phi}_i(\boldsymbol{u})\} = 0 \tag{5.30}$$

$\mathbf{K}_T$ is the tangential stiffness matrix. The mass matrix is assumed to be independent of the amplitude. The eigenvectors of a symmetric matrix are mutually orthogonal to each other. The eigenvectors are normalised as:

$$\boldsymbol{\phi}_i^{\mathsf{T}}(\boldsymbol{u})\;[\mathbf{M}]\;\boldsymbol{\phi}_i(\boldsymbol{u}) = 1 \tag{5.31}$$

Differentiate Equation (5.30) and (5.31) with respect to $\boldsymbol{q}_j$, yields:

$$\left(\mathbf{K}_T(\boldsymbol{x}_s,\boldsymbol{u}) - \omega_i^2(\boldsymbol{u})\,[\mathbf{M}]\right)\frac{d\boldsymbol{\phi}_i(\boldsymbol{u})}{d\boldsymbol{q}_j} + \left(\frac{d\mathbf{K}_T(\boldsymbol{x}_s,\boldsymbol{u})}{d\boldsymbol{q}_j} - \left[\frac{\omega_i^2(\boldsymbol{u})}{d\boldsymbol{q}_j}\mathbf{M}\right]\right)\{\boldsymbol{\phi}_i(\boldsymbol{u})\} = 0 \tag{5.32}$$

$$\boldsymbol{\phi}_i^{\mathsf{T}}(\boldsymbol{u})\;[\mathbf{M}]\;\frac{d\boldsymbol{\phi}_i(\boldsymbol{u})}{d\boldsymbol{q}_j} = 0 \tag{5.33}$$

Thus,

$$\begin{bmatrix} \left(\mathbf{K}_T - \omega_i^2(\boldsymbol{u})\,[\mathbf{M}]\right) & -[\mathbf{M}]\,\{\boldsymbol{\phi}_i(\boldsymbol{u})\} \\ \boldsymbol{\phi}_i^{\mathsf{T}}(\boldsymbol{u})\;[\mathbf{M}] & 0 \end{bmatrix} \begin{bmatrix} \boldsymbol{\Theta}_{ij} \\ \frac{\omega_i^2(\boldsymbol{u})}{d\boldsymbol{q}_j} \end{bmatrix} = \begin{bmatrix} -\frac{d\mathbf{K}_T(\boldsymbol{x}_s,\boldsymbol{u})}{d\boldsymbol{q}_j}\,\boldsymbol{\phi}_i(\boldsymbol{u}) \\ 0 \end{bmatrix} \tag{5.34}$$

The static modal derivative of $\boldsymbol{\phi}_i$ with respect to $\boldsymbol{q}_j$ for a rotating system at the equilibrium position ($\boldsymbol{u} = 0$) is computed as:

$$\boldsymbol{\Theta}_{ij} = \frac{\partial\boldsymbol{\phi}_i}{\partial\boldsymbol{q}_j} = -\left[\mathbf{K}_T(\boldsymbol{x}_s)\right]^{-1}\frac{\partial}{\partial\boldsymbol{q}_j}\left(\frac{\partial\mathbf{F}_{nl}}{\partial\boldsymbol{u}}\right)\Bigg|_{q_j=0}\boldsymbol{\phi}_i$$
$$= -\left[\mathbf{K}_T(\boldsymbol{x}_s)\right]^{-1}\cdot\boldsymbol{J}_1(\boldsymbol{\phi}_j)\cdot\boldsymbol{\phi}_i \tag{5.35}$$

Expression for $\boldsymbol{J}_1(\boldsymbol{\phi}_j)$ is shown in Equation (5.27). The tangential stiffness matrix at the equilibrium position is:

$$[\mathbf{K}_T(\boldsymbol{x}_s)] = [\mathbf{K}(\boldsymbol{\Omega})] + [\mathbf{K}_1(\boldsymbol{x}_s)] + [\mathbf{K}_2(\boldsymbol{x}_s)] + [\mathbf{K}_3(\boldsymbol{x}_s)] + [\mathbf{K}_4(\mathbf{S})] \tag{5.36}$$

Figure 5.3 demonstrates the linear vibration modes $\boldsymbol{\phi}_i$ and their corresponding modal derivatives $\boldsymbol{\Theta}_{ij}$ of a cantilevered beam. Modal derivatives describe the change in the vibration mode $\boldsymbol{\phi}_i$ corresponding to a displacement given in the direction of vibration mode $\boldsymbol{\phi}_j$. The static modal derivatives are symmetric, i.e. $\boldsymbol{\Theta}_{ij} = \boldsymbol{\Theta}_{ji}$. Since $\boldsymbol{\Theta}_{ij}$ depends on the static deformation caused by angular velocities. Figure 5.4 shows the effect of rotational speed on the modal derivative $\boldsymbol{\Theta}_{23}$. The stretching effect due to the centrifugal force can be observed on the modal derivative. The bar chart shown in Figure 5.2 is the comparison of time used to compute the static modal derivatives $\boldsymbol{\Theta}_{ij}$ with different number of reduced basis (r) selected in the ROM. The 3D mesh shown in Figure 3.23 is used as an example here.

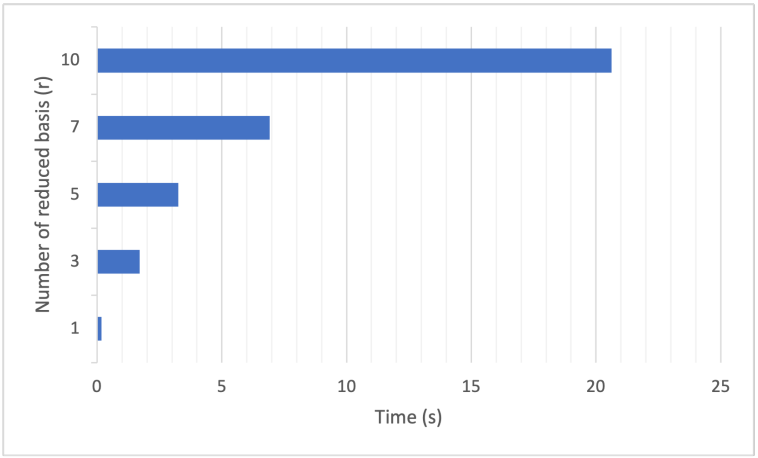


Fig. 5.2 *Time to compute $\boldsymbol{\Theta}_{ij}$ with different number of reduced basis selected in linear projection method.*

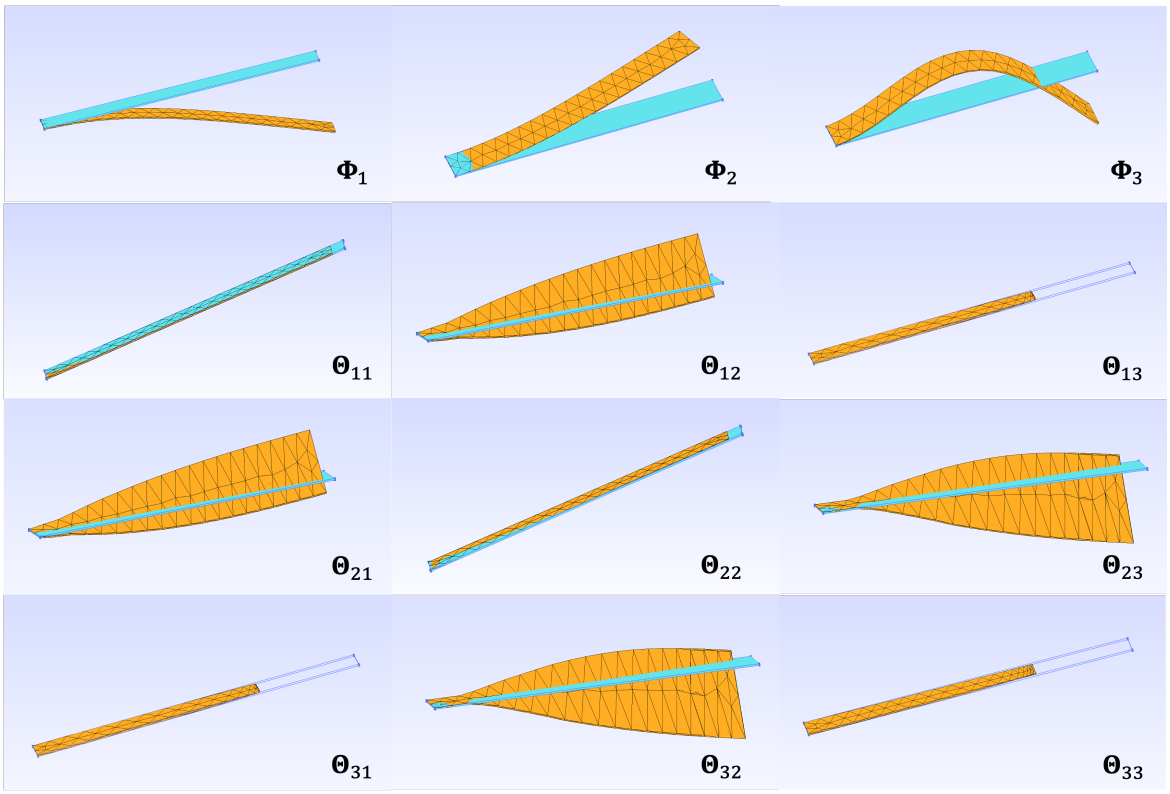
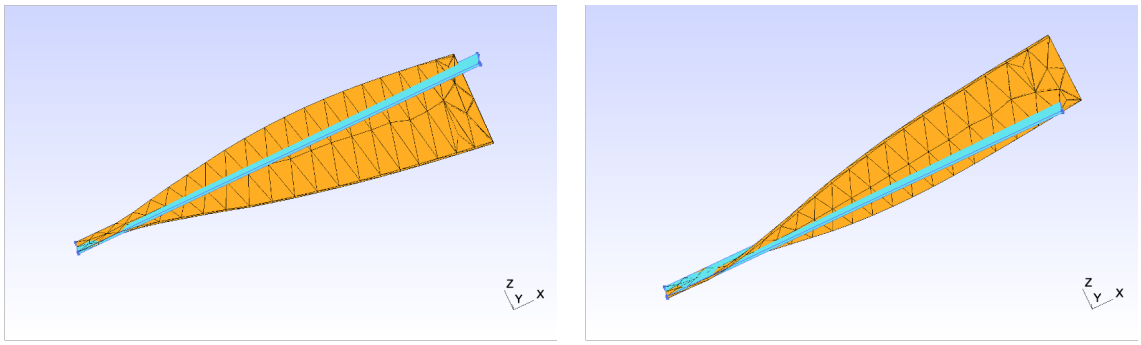


Fig. 5.3 *Linear modes* $\boldsymbol{\phi}$ *of the cantilevered beam and the corresponding modal derivatives* $\boldsymbol{\Theta}$.



(a) $\Omega_z = 0$ rad/s (b) $\Omega_z = 300$ rad/s

Fig. 5.4 *Effect of rotational speed on the modal derivative* $\boldsymbol{\Theta}_{23}$

5.3.2 Reduced equation of motion for 3D nonlinear structures

The derivatives of the nonlinear mapping $\boldsymbol{\Gamma}(\boldsymbol{q})$ shown in the quadratic manifold equation are:

$$\mathbf{P}_{\boldsymbol{\Gamma}} = \frac{\partial \boldsymbol{\Gamma}}{\partial \boldsymbol{q}} = \boldsymbol{\Phi} + \boldsymbol{\Theta}\boldsymbol{q} \tag{5.37}$$

$$\dot{\boldsymbol{\Gamma}} = \mathbf{P}_{\boldsymbol{\Gamma}}\,\dot{\boldsymbol{q}} = \boldsymbol{\Phi}\dot{\boldsymbol{q}} + \boldsymbol{\Theta}\boldsymbol{q}\dot{\boldsymbol{q}} \tag{5.38}$$

$$\ddot{\boldsymbol{\Gamma}} = \mathbf{P}_{\boldsymbol{\Gamma}}\,\ddot{\boldsymbol{q}} + \boldsymbol{\Theta}\,\dot{\boldsymbol{q}}\,\dot{\boldsymbol{q}} = \boldsymbol{\Phi}\ddot{\boldsymbol{q}} + \boldsymbol{\Theta}\boldsymbol{q}\ddot{\boldsymbol{q}} + \boldsymbol{\Theta}\,\dot{\boldsymbol{q}}\,\dot{\boldsymbol{q}} \tag{5.39}$$

Substitute Equations (5.29) and (5.37-5.39) into Equation (5.2) and multiplying the equation by $\mathbf{P}_{\boldsymbol{\Gamma}}^{\mathsf{T}}$, yields the dynamic equation of the rotating structure in the reduced basis:

$$\left[\hat{\mathbf{M}}\right]\ddot{\boldsymbol{q}} + \left[\hat{\mathbf{C}}\right]\dot{\boldsymbol{q}} + \{\hat{\mathbf{p}}\} + \{\hat{\mathbf{F}}(\boldsymbol{\Gamma}(\boldsymbol{q}))\} = \{\hat{\mathbf{F}}_{ext}(t)\} \tag{5.40}$$

with:

$$\begin{aligned}
\left[\hat{\mathbf{M}}\right] &= \mathbf{P}_{\boldsymbol{\Gamma}}^{\mathsf{T}}[\mathbf{M}]\,\mathbf{P}_{\boldsymbol{\Gamma}} & \{\hat{\mathbf{F}}\} &= \mathbf{P}_{\boldsymbol{\Gamma}}^{\mathsf{T}}[\mathbf{K}]\,\{\boldsymbol{\Gamma}(\boldsymbol{q})\} + \mathbf{P}_{\boldsymbol{\Gamma}}^{\mathsf{T}}\{\mathbf{F}_{nl}(\boldsymbol{x}_s, \boldsymbol{\Gamma}(\boldsymbol{q}))\} \\
\left[\hat{\mathbf{C}}\right] &= \mathbf{P}_{\boldsymbol{\Gamma}}^{\mathsf{T}}[\mathbf{C}]\,\mathbf{P}_{\boldsymbol{\Gamma}} & \{\hat{\mathbf{F}}_{ext}\} &= \mathbf{P}_{\boldsymbol{\Gamma}}^{\mathsf{T}}\{\hat{\mathbf{F}}_{ext}\} \\
\{\hat{\mathbf{p}}\} &= \mathbf{P}_{\boldsymbol{\Gamma}}^{\mathsf{T}}[\mathbf{M}]\boldsymbol{\Theta}\,\dot{\boldsymbol{q}}\,\dot{\boldsymbol{q}}
\end{aligned}$$

When expanding $\hat{\mathbf{F}}(\boldsymbol{\Gamma}(\boldsymbol{q}))$, the $\boldsymbol{q}$ terms in the expression can go up to order of seven. Since the dynamic response $\boldsymbol{u}$ is estimated up to the second order, only terms with order up to three are considered in the dynamic equation. The reduced equation of motion can be expressed in a simplified format as:

$$\ddot{\boldsymbol{q}} + [\alpha\mathbf{I} + \beta\boldsymbol{\Lambda} + \beta\,\boldsymbol{\Phi}^{\mathsf{T}}[\mathbf{K}_s(\boldsymbol{\Omega})]]\,\dot{\boldsymbol{q}} + \hat{\boldsymbol{F}}_{nl}(\boldsymbol{q}, \dot{\boldsymbol{q}}, \ddot{\boldsymbol{q}}) = \hat{\mathbf{F}}_{ext}(t) \tag{5.41}$$

with:

$$\begin{aligned}
\hat{\boldsymbol{F}}_{nl}(\boldsymbol{q}, \dot{\boldsymbol{q}}, \ddot{\boldsymbol{q}}) = &\sum_{i}^{r}\sum_{j}^{r} \boldsymbol{P}_{ij} \cdot \dot{q}_i \cdot \dot{q}_j + \sum_{i}^{r}\sum_{j}^{r}\sum_{k}^{r} \boldsymbol{Q}_{ijk} \cdot q_i \cdot \dot{q}_j \cdot \dot{q}_k + \sum_{i}^{r} \boldsymbol{A}_i(\boldsymbol{x}_s, \boldsymbol{\phi}_i) \cdot q_i \\
&+ \sum_{i}^{r}\sum_{j}^{r} \boldsymbol{B}_{ij}(\boldsymbol{x}_s, \boldsymbol{\phi}_i, \boldsymbol{\phi}_j) \cdot q_i \cdot q_j + \sum_{i}^{r}\sum_{j}^{r}\sum_{k}^{r} \boldsymbol{C}_{ijk}(\boldsymbol{x}_s, \boldsymbol{\phi}_i, \boldsymbol{\phi}_j, \boldsymbol{\phi}_k) \cdot q_i \cdot q_j \cdot q_k \\
&+ \sum_{i}^{r}\sum_{j}^{r} \boldsymbol{D}_{ij}(\boldsymbol{\phi}_i, \boldsymbol{\phi}_j) \cdot q_i \cdot \dot{q}_j + \sum_{i}^{r}\sum_{j}^{r} \boldsymbol{M}_{ij}(\boldsymbol{\phi}_i, \boldsymbol{\phi}_j) \cdot q_i \cdot \ddot{q}_j \\
&+ \sum_{i}^{r}\sum_{j}^{r}\sum_{k}^{r} \boldsymbol{N}_{ijk} \cdot q_i \cdot q_j \cdot \ddot{q}_k + \sum_{i}^{r}\sum_{j}^{r}\sum_{k}^{r} \boldsymbol{G}_{ijk} \cdot q_i \cdot q_j \cdot \dot{q}_k
\end{aligned} \tag{5.42}$$

$\boldsymbol{P}_{ij}$, $\boldsymbol{Q}_{ijk}$, $\boldsymbol{A}_i$, $\boldsymbol{B}_{ij}$, $\boldsymbol{C}_{ijk}$, $\boldsymbol{D}_{ij}$, $\boldsymbol{M}_{ij}$, $\boldsymbol{N}_{ijk}$ and $\boldsymbol{G}_{ijk}$ are the coefficient tensors in the reduced equation of motion. The explicit expressions of the tensors are presented in Equations (5.43) to (5.51). For a non-rotating structure, the $\boldsymbol{x}_s$ terms in the equations are removed.

$$\boldsymbol{P}_{ij} = \boldsymbol{\Phi}^{\mathsf{T}}[\mathbf{M}]\ \{\boldsymbol{\Theta}(:,i,j)\} \tag{5.43}$$

$$\boldsymbol{Q}_{ijk} = [\boldsymbol{\Theta}(:,:,i)]^{\mathsf{T}}[\mathbf{M}]\ \{\boldsymbol{\Theta}(:,j,k)\} \tag{5.44}$$

$$\begin{aligned}\boldsymbol{A}_i = &\frac{1}{2}\boldsymbol{\Phi}^{\mathsf{T}}\int[\mathbf{B}_0+\mathbf{B}_1(\boldsymbol{x}_s)]^{\mathsf{T}}[\mathbf{D}]\,[\mathbf{B}_1(\boldsymbol{\phi}_i)]\mathrm{d}V\,\{\boldsymbol{x}_s\}\\ &+\boldsymbol{\Phi}^{\mathsf{T}}\int[\mathbf{B}_1(\boldsymbol{\phi}_i)]^{\mathsf{T}}[\mathbf{D}]\,[\mathbf{B}_0]\mathrm{d}V\,\{\boldsymbol{x}_s\}\\ &+\boldsymbol{\Phi}^{\mathsf{T}}\int[\mathbf{B}_1(\boldsymbol{\phi}_i)]^{\mathsf{T}}[\mathbf{D}]\left[\mathbf{B}_0+\frac{1}{2}\mathbf{B}_1(\boldsymbol{x}_s)\right]\mathrm{d}V\,\{\boldsymbol{x}_s\}\\ &+\boldsymbol{\Phi}^{\mathsf{T}}[\mathbf{K}_0]\,\{\boldsymbol{\phi}_i\}+\boldsymbol{\Phi}^{\mathsf{T}}[\mathbf{K}_{nl}(\boldsymbol{x}_s)]\,\{\boldsymbol{\phi}_i\}\end{aligned} \tag{5.45}$$

$$\begin{aligned}\boldsymbol{B}_{ij} = &\frac{1}{2}[\boldsymbol{\Theta}(:,:,i)]^{\mathsf{T}}\int[\mathbf{B}_0+\mathbf{B}_1(\boldsymbol{x}_s)]^{\mathsf{T}}[\mathbf{D}]\,[\mathbf{B}_1(\boldsymbol{\phi}_j)]\mathrm{d}V\,\{\boldsymbol{x}_s\}\\ &+[\boldsymbol{\Theta}(:,:,i)]^{\mathsf{T}}\int[\mathbf{B}_1(\boldsymbol{\phi}_j)]^{\mathsf{T}}[\mathbf{D}]\left[\mathbf{B}_0+\frac{1}{2}\mathbf{B}_1(\boldsymbol{x}_s)\right]\mathrm{d}V\,\{\boldsymbol{x}_s\}\\ &+\frac{1}{2}\boldsymbol{\Phi}^{\mathsf{T}}\int[\mathbf{B}_0+\mathbf{B}_1(\boldsymbol{x}_s)]^{\mathsf{T}}[\mathbf{D}]\,[\mathbf{B}_1(\boldsymbol{\phi}_i)]\mathrm{d}V\,\{\boldsymbol{\phi}_j\}\\ &+\boldsymbol{\Phi}^{\mathsf{T}}\int[\mathbf{B}_1(\boldsymbol{\phi}_i)]^{\mathsf{T}}[\mathbf{D}]\left[\frac{1}{2}\mathbf{B}_0+\mathbf{B}_1(\boldsymbol{x}_s)\right]\mathrm{d}V\,\{\boldsymbol{\phi}_j\}\\ &+\frac{1}{2}\boldsymbol{\Phi}^{\mathsf{T}}\int[\mathbf{B}_0+\mathbf{B}_1(\boldsymbol{x}_s)]^{\mathsf{T}}[\mathbf{D}]\left[\mathbf{B}_1\left(\frac{1}{2}\boldsymbol{\Theta}(:,i,j)\right)\right]\mathrm{d}V\,\{\boldsymbol{x}_s\}\\ &+\boldsymbol{\Phi}^{\mathsf{T}}\int\left[\mathbf{B}_1\left(\frac{1}{2}\boldsymbol{\Theta}(:,i,j)\right)\right]^{\mathsf{T}}[\mathbf{D}]\left[\mathbf{B}_0+\frac{1}{2}\mathbf{B}_1(\boldsymbol{x}_s)\right]\mathrm{d}V\,\{\boldsymbol{x}_s\}\\ &+\frac{1}{2}\boldsymbol{\Phi}^{\mathsf{T}}\int[\mathbf{B}_1(\boldsymbol{\phi}_i)]^{\mathsf{T}}[\mathbf{D}]\left[\mathbf{B}_1\left(\boldsymbol{\phi}_j\right)\right]\mathrm{d}V\,\{\boldsymbol{x}_s\}\\ &+[\boldsymbol{\Theta}(:,:,i)]^{\mathsf{T}}[\mathbf{K}_0+\mathbf{K}_{nl}(\boldsymbol{x}_s)]\,\boldsymbol{\phi}_j+\boldsymbol{\Phi}^{\mathsf{T}}[\mathbf{K}_0+\mathbf{K}_{nl}(\boldsymbol{x}_s)]\left\{\frac{1}{2}\boldsymbol{\Theta}(:,i,j)\right\}\end{aligned} \tag{5.46}$$

$$\boldsymbol{D}_{ij} = [\boldsymbol{\Theta}(:,:,i)]^{\mathsf{T}}[\mathbf{C}]\,\{\boldsymbol{\phi}_j\}+\boldsymbol{\Phi}^{\mathsf{T}}[\mathbf{C}]\,\{\boldsymbol{\Theta}(:,i,j)\} \tag{5.47}$$

$$\boldsymbol{M}_{ij} = [\boldsymbol{\Theta}(:,:,i)]^{\mathsf{T}}[\mathbf{M}]\{\boldsymbol{\phi}_j\} + \boldsymbol{\Phi}^{\mathsf{T}}[\mathbf{M}]\{\boldsymbol{\Theta}(:,i,j)\} \tag{5.48}$$

$$\boldsymbol{N}_{ijk} = [\boldsymbol{\Theta}(:,:,i)]^{\mathsf{T}}[\mathbf{M}]\{\boldsymbol{\Theta}(:,j,k)\} \tag{5.49}$$

$$\boldsymbol{G}_{ijk} = [\boldsymbol{\Theta}(:,:,i)]^{\mathsf{T}}[\mathbf{C}]\{\boldsymbol{\Theta}(:,j,k)\} \tag{5.50}$$

$$\begin{aligned}
\boldsymbol{C}_{ijk} = {} & \frac{1}{2}[\boldsymbol{\Theta}(:,:,i)]^{\mathsf{T}} \int [\mathbf{B}_0 + \mathbf{B}_1(\boldsymbol{x}_s)]^{\mathsf{T}}[\mathbf{D}][\mathbf{B}_1(\boldsymbol{\phi}_j)]\mathrm{d}V\{\boldsymbol{\phi}_k\} \\
& + [\boldsymbol{\Theta}(:,:,i)]^{\mathsf{T}} \int [\mathbf{B}_1(\boldsymbol{\phi}_j)]^{\mathsf{T}}[\mathbf{D}]\left[\mathbf{B}_0 + \frac{1}{2}\mathbf{B}_1(\boldsymbol{x}_s)\right]\mathrm{d}V\{\boldsymbol{\phi}_k\} \\
& \frac{1}{2}\boldsymbol{\Phi}^{\mathsf{T}} \int [\mathbf{B}_0 + \mathbf{B}_1(\boldsymbol{x}_s)]^{\mathsf{T}}[\mathbf{D}][\mathbf{B}_1(\boldsymbol{\phi}_i)]\mathrm{d}V\left\{\frac{1}{2}\boldsymbol{\Theta}(:,j,k)\right\} \\
& + \boldsymbol{\Phi}^{\mathsf{T}} \int [\mathbf{B}_1(\boldsymbol{\phi}_i)]^{\mathsf{T}}[\mathbf{D}]\left[\mathbf{B}_0 + \frac{1}{2}\mathbf{B}_1(\boldsymbol{x}_s)\right]\mathrm{d}V\left\{\frac{1}{2}\boldsymbol{\Theta}(:,j,k)\right\} \\
& + \frac{1}{2}[\boldsymbol{\Theta}(:,:,i)]^{\mathsf{T}} \int [\mathbf{B}_0 + \mathbf{B}_1(\boldsymbol{x}_s)]^{\mathsf{T}}[\mathbf{D}]\left[\mathbf{B}_1\left(\frac{1}{2}\boldsymbol{\Theta}(:,j,k)\right)\right]\mathrm{d}V\{\boldsymbol{x}_s\} \\
& + [\boldsymbol{\Theta}(:,:,i)]^{\mathsf{T}} \int \left[\mathbf{B}_1\left(\frac{1}{2}\boldsymbol{\Theta}(:,j,k)\right)\right]^{\mathsf{T}}[\mathbf{D}]\left[\mathbf{B}_0 + \frac{1}{2}\mathbf{B}_1(\boldsymbol{x}_s)\right]\mathrm{d}V\{\boldsymbol{x}_s\} \\
& + \frac{1}{2}[\boldsymbol{\Theta}(:,:,i)]^{\mathsf{T}} \int [\mathbf{B}_1(\boldsymbol{\phi}_j]^{\mathsf{T}}[\mathbf{D}][\mathbf{B}_1(\boldsymbol{\phi}_k)]\,\mathrm{d}V\{\boldsymbol{x}_s\} \\
& + \frac{1}{2}\boldsymbol{\Phi}^{\mathsf{T}} \int [\mathbf{B}_0 + \mathbf{B}_1(\boldsymbol{x}_s)]^{\mathsf{T}}[\mathbf{D}]\left[\mathbf{B}_1\left(\frac{1}{2}\boldsymbol{\Theta}(:,i,j)\right)\right]\mathrm{d}V\{\boldsymbol{\phi}_k\} \\
& + \boldsymbol{\Phi}^{\mathsf{T}} \int \left[\mathbf{B}_1\left(\frac{1}{2}\boldsymbol{\Theta}(:,i,j)\right)\right]^{\mathsf{T}}[\mathbf{D}]\left[\mathbf{B}_0 + \frac{1}{2}\mathbf{B}_1(\boldsymbol{x}_s)\right]\mathrm{d}V\{\boldsymbol{\phi}_k\} \\
& + \frac{1}{2}\boldsymbol{\Phi}^{\mathsf{T}} \int [\mathbf{B}_1(\boldsymbol{\phi}_i)]^{\mathsf{T}}[\mathbf{D}]\left[\mathbf{B}_1\left(\boldsymbol{\phi}_j\right)\right]\mathrm{d}V\{\boldsymbol{\phi}_k\} \\
& + \frac{1}{2}\boldsymbol{\Phi}^{\mathsf{T}} \int [\mathbf{B}_1(\boldsymbol{\phi}_i)]^{\mathsf{T}}[\mathbf{D}]\left[\mathbf{B}_1\left(\frac{1}{2}\boldsymbol{\Theta}(:,j,k)\right)\right]\mathrm{d}V\{\boldsymbol{x}_s\} \\
& + \frac{1}{2}\boldsymbol{\Phi}^{\mathsf{T}} \int \left[\mathbf{B}_1\left(\frac{1}{2}\boldsymbol{\Theta}(:,i,j)\right)\right]^{\mathsf{T}}[\mathbf{D}][\mathbf{B}_1(\boldsymbol{\phi}_k)]\,\mathrm{d}V\{\boldsymbol{x}_s\} \\
& + [\boldsymbol{\Theta}(:,:,i)]^{\mathsf{T}}[\mathbf{K}_0 + \mathbf{K}_{nl}(\boldsymbol{x}_s)]\left\{\frac{1}{2}\boldsymbol{\Theta}(:,j,k)\right\}
\end{aligned} \tag{5.51}$$

5.3.3 Harmonic balance method for vibration analysis

HBM coupled with AFT method can be used to solve the reduced dynamic equation in frequency domain, Equation (5.52). Arc-length continuation scheme is used.

$$\mathbf{F}(\omega,\tilde{\boldsymbol{q}}) = \begin{bmatrix} \boldsymbol{R}(\omega,\tilde{\boldsymbol{q}}) \\ r(\omega,\tilde{\boldsymbol{q}}) \end{bmatrix} = \begin{bmatrix} \mathbf{Z}(\omega)\tilde{\boldsymbol{q}} + \tilde{\boldsymbol{b}}_{nl}(\tilde{\boldsymbol{q}}) - \tilde{\boldsymbol{b}}_{ext} \\ (\tilde{\boldsymbol{q}} - \tilde{\boldsymbol{q}}_0)^2 + (\omega - \omega_0)^2 - \Delta s^2 \end{bmatrix} = 0 \tag{5.52}$$

The derivation of $\mathbf{Z}(\omega)$ can be found in Equation (2.73), with $\mathbf{M} = \mathbf{I}$, $\mathbf{C} = \alpha\mathbf{I} + \beta\boldsymbol{\Lambda} + \beta\boldsymbol{\Phi}^{\intercal}[\mathbf{K}_s(\boldsymbol{\Omega})]\boldsymbol{\Phi}$, and $\mathbf{K} = [0]_{r\times r}$. Parameters $\tilde{\boldsymbol{q}}$, $\tilde{\boldsymbol{b}}_{nl}$, and $\tilde{\boldsymbol{b}}_{ext}$ are $\boldsymbol{q}$, $\hat{\boldsymbol{F}}_{nl}$, and $\hat{\boldsymbol{F}}_{ext}$ in the frequency domain respectively. AFT methodology is used to compute $\tilde{\boldsymbol{b}}_{nl}$. The response $\tilde{\boldsymbol{q}}$ is transformed into the time domain by applying IDFT. DFT is then followed to compute the resulting nonlinear force in frequency domain $\tilde{\boldsymbol{b}}_{nl}$.

$$\tilde{\boldsymbol{q}} \xrightarrow[\text{IDFT}]{[\mathscr{F}]^{-1},\ [\dot{\mathscr{F}}]^{-1},\ [\ddot{\mathscr{F}}]^{-1}} \underline{\boldsymbol{q}}(t), \underline{\dot{\boldsymbol{q}}}(t), \underline{\ddot{\boldsymbol{q}}}(t) \rightarrow \underline{\hat{\boldsymbol{F}}}_{nl}(\boldsymbol{q},\dot{\boldsymbol{q}},\ddot{\boldsymbol{q}}) \xrightarrow{\text{DFT: } [\mathscr{F}]} \tilde{\boldsymbol{b}}_{nl}(\tilde{\boldsymbol{q}}) \tag{5.53}$$

The expressions of $[\mathscr{F}]$, $[\mathscr{F}]^{-1}$, $\underline{\boldsymbol{q}}(t)$, and $\underline{\hat{\boldsymbol{F}}}_{nl}(t)$ are defined in section 3.4.2. The time derivatives of the IDFT, which transforms $\tilde{\boldsymbol{q}} \rightarrow \underline{\dot{\boldsymbol{q}}}(t)$ and $\tilde{\boldsymbol{q}} \rightarrow \underline{\ddot{\boldsymbol{q}}}(t)$, are defined as:

$$\left[\dot{\mathscr{F}}\right]^{-1}: \quad \underline{\dot{q}}_i(t_n) = -\sum_{k=1}^{N_H} (k\omega)\cdot c_k^i \cdot \sin\left(kn\frac{2\pi}{N_t}\right) + \sum_{k=1}^{N_H} (k\omega)\cdot s_k^i \cdot \cos\left(kn\frac{2\pi}{N_t}\right) \tag{5.54}$$

$$\left[\ddot{\mathscr{F}}\right]^{-1}: \quad \underline{\ddot{q}}_i(t_n) = -\sum_{k=1}^{N_H} (k\omega)^2\cdot c_k^i \cdot \cos\left(kn\frac{2\pi}{N_t}\right) - \sum_{k=1}^{N_H} (k\omega)^2\cdot s_k^i \cdot \sin\left(kn\frac{2\pi}{N_t}\right) \tag{5.55}$$

c_k^i and s_k^i are the Fourier coefficient of $\tilde{\boldsymbol{q}}$ as shown in Equation (3.59). For $\boldsymbol{z} = \{\tilde{\boldsymbol{q}},\omega\}^{\intercal}$, equation $\mathbf{F}(\boldsymbol{z})$ can be solved by using Newton direction computation. The Jacobian matrix $\mathbf{F}'(\boldsymbol{z})$ is required:

$$\mathbf{F}'(\boldsymbol{z}) = \begin{bmatrix} \dfrac{\partial \boldsymbol{R}}{\partial \tilde{\boldsymbol{q}}} & \dfrac{\partial \boldsymbol{R}}{\partial \omega} \\ \dfrac{\partial r}{\partial \tilde{\boldsymbol{q}}} & \dfrac{\partial r}{\partial \omega} \end{bmatrix} = \begin{bmatrix} \mathbf{Z}(\omega) + \dfrac{\partial \tilde{\boldsymbol{b}}_{nl}}{\partial \tilde{\boldsymbol{q}}} & \dfrac{\partial \mathbf{Z}}{\partial \omega}\cdot\tilde{\boldsymbol{q}} \\ 2(\tilde{\boldsymbol{q}} - \tilde{\boldsymbol{q}}_0) & 2(\omega - \omega_0) \end{bmatrix} \tag{5.56}$$

Expression for $\dfrac{\partial \mathbf{Z}}{\partial \omega}$ can be found in Equation (3.71). Equation (5.42) shows that the nonlinear force vector in this ROM case depends not only on the displacements, but also on the velocities and the accelerations of the DOFs. The derivative of $\tilde{\boldsymbol{b}}_{nl}$ with respect to $\tilde{\boldsymbol{q}}$ can

hence be computed as:

$$\begin{aligned}\frac{\partial \tilde{\boldsymbol{b}}_{nl}}{\partial \tilde{\boldsymbol{q}}} &= \frac{\partial \tilde{\boldsymbol{b}}_{nl}}{\partial \underline{\hat{\boldsymbol{F}}}_{nl}} \frac{\partial \underline{\hat{\boldsymbol{F}}}_{nl}}{\partial \underline{\boldsymbol{q}}} \frac{\partial \underline{\boldsymbol{q}}}{\partial \tilde{\boldsymbol{q}}} + \frac{\partial \tilde{\boldsymbol{b}}_{nl}}{\partial \underline{\hat{\boldsymbol{F}}}_{nl}} \frac{\partial \underline{\hat{\boldsymbol{F}}}_{nl}}{\partial \underline{\dot{\boldsymbol{q}}}} \frac{\partial \underline{\dot{\boldsymbol{q}}}}{\partial \tilde{\boldsymbol{q}}} + \frac{\partial \tilde{\boldsymbol{b}}_{nl}}{\partial \underline{\hat{\boldsymbol{F}}}_{nl}} \frac{\partial \underline{\hat{\boldsymbol{F}}}_{nl}}{\partial \underline{\ddot{\boldsymbol{q}}}} \frac{\partial \underline{\ddot{\boldsymbol{q}}}}{\partial \tilde{\boldsymbol{q}}} \\ &= [\mathscr{F}] \frac{\partial \underline{\hat{\boldsymbol{F}}}_{nl}}{\partial \underline{\boldsymbol{q}}} [\mathscr{F}]^{-1} + [\mathscr{F}] \frac{\partial \underline{\hat{\boldsymbol{F}}}_{nl}}{\partial \underline{\dot{\boldsymbol{q}}}} [\dot{\mathscr{F}}]^{-1} + [\mathscr{F}] \frac{\partial \underline{\hat{\boldsymbol{F}}}_{nl}}{\partial \underline{\ddot{\boldsymbol{q}}}} [\ddot{\mathscr{F}}]^{-1}\end{aligned} \tag{5.57}$$

The full expression for the $\dfrac{\partial \hat{\boldsymbol{F}}_{nl}}{\partial \boldsymbol{q}}$ matrix in each element is:

$$\begin{aligned}\frac{\partial \hat{\boldsymbol{F}}^e_{nl}}{\partial \boldsymbol{q}} =& J^e_0(\boldsymbol{x}_s) + \sum_{i=1}^{r} J^e_1(\boldsymbol{\phi}_i)\cdot\boldsymbol{q} + \sum_{i=1}^{r} C^e_1(\boldsymbol{\phi}_i)\cdot\dot{\boldsymbol{q}} + \sum_{i=1}^{r} M^e_1(\boldsymbol{\phi}_i)\cdot\ddot{\boldsymbol{q}} + \sum_{i=1}^{r}\sum_{j=1}^{r} J^e_2(\boldsymbol{\phi}_i,\boldsymbol{\phi}_j)\cdot\boldsymbol{q}\cdot\boldsymbol{q} \\ &+ \sum_{i=1}^{r}\sum_{j=1}^{r} C^e_2(\boldsymbol{\phi}_i,\boldsymbol{\phi}_j)\cdot\boldsymbol{q}\cdot\dot{\boldsymbol{q}} + \sum_{i=1}^{r}\sum_{j=1}^{r} M^e_2(\boldsymbol{\phi}_i,\boldsymbol{\phi}_j)\cdot\boldsymbol{q}\cdot\ddot{\boldsymbol{q}} \\ &+ \sum_{i=1}^{r}\sum_{j=1}^{r} M^e_3(\boldsymbol{\phi}_i,\boldsymbol{\phi}_j)\cdot\dot{\boldsymbol{q}}\cdot\dot{\boldsymbol{q}}\end{aligned} \tag{5.58}$$

Details of the computation for the coefficient tensors in Euqation (5.58) are delivered in Appendix D. The expression for the $\dfrac{\partial \hat{\boldsymbol{F}}_{nl}}{\partial \dot{\boldsymbol{q}}}$ matrix in each element is:

$$\begin{aligned}\frac{\partial \hat{\boldsymbol{F}}^e_{nl}}{\partial \dot{\boldsymbol{q}}} =& \sum_{i=1}^{r} Q^e_1(\boldsymbol{\phi}_i)\cdot\boldsymbol{q} + \sum_{i=1}^{r} Q^e_2(\boldsymbol{\phi}_i)\cdot\dot{\boldsymbol{q}} \\ &+ \sum_{i=1}^{r}\sum_{j=1}^{r} Q^e_3(\boldsymbol{\phi}_i,\boldsymbol{\phi}_j)\cdot\boldsymbol{q}\cdot\boldsymbol{q} + \sum_{i=1}^{r}\sum_{j=1}^{r} Q^e_4(\boldsymbol{\phi}_i,\boldsymbol{\phi}_j)\cdot\boldsymbol{q}\cdot\dot{\boldsymbol{q}}\end{aligned} \tag{5.59}$$

with:

$$Q^e_1 = [\boldsymbol{\Theta}(:,:,i)]^{\mathsf{T}}[\mathbf{C}]\boldsymbol{\Phi} + \boldsymbol{\Phi}^{\mathsf{T}}[\mathbf{C}]\,[\boldsymbol{\Theta}(:,:,i)] \tag{5.60}$$

$$Q^e_2 = 2\boldsymbol{\Phi}^{\mathsf{T}}[\mathbf{M}]\,[\boldsymbol{\Theta}(:,:,i)] \tag{5.61}$$

$$Q^e_3 = [\boldsymbol{\Theta}(:,:,i)]^{\mathsf{T}}[\mathbf{C}]\,[\boldsymbol{\Theta}(:,:,i)] \tag{5.62}$$

$$Q^e_4 = 2\,[\boldsymbol{\Theta}(:,:,i)]^{\mathsf{T}}[\mathbf{M}]\,[\boldsymbol{\Theta}(:,:,i)] \tag{5.63}$$

The expression for the $\dfrac{\partial \hat{\boldsymbol{F}}_{nl}}{\partial \ddot{\boldsymbol{q}}}$ matrix in each element is:

$$\frac{\partial \hat{\boldsymbol{F}}^e_{nl}}{\partial \ddot{\boldsymbol{q}}} = \sum_{i=1}^{r} P^e_1(\boldsymbol{\phi}_i)\cdot\boldsymbol{q} + \sum_{i=1}^{r}\sum_{j=1}^{r} P^e_2(\boldsymbol{\phi}_i,\boldsymbol{\phi}_j)\cdot\boldsymbol{q}\cdot\boldsymbol{q} + \sum_{i=1}^{r}\sum_{j=1}^{r} P^e_3(\boldsymbol{\phi}_i,\boldsymbol{\phi}_j)\cdot\dot{\boldsymbol{q}}\cdot\dot{\boldsymbol{q}} \tag{5.64}$$

with:

$$P_1^e = [\boldsymbol{\Theta}(:,:,i)]^\mathsf{T}[\mathbf{M}]\boldsymbol{\Phi} + \boldsymbol{\Phi}^\mathsf{T}[\mathbf{M}]\,[\boldsymbol{\Theta}(:,:,i)] \tag{5.65}$$

$$P_2^e = [\boldsymbol{\Theta}(:,:,i)]^\mathsf{T}[\mathbf{M}]\,[\boldsymbol{\Theta}(:,:,i)] \tag{5.66}$$

$$P_3^e = \boldsymbol{\Phi}^\mathsf{T}[\mathbf{M}]\,[\boldsymbol{\Theta}(:,i,j)] \tag{5.67}$$

Substituting the Equations (5.58) - (5.67) into Equation (5.57) yields the matrix for the derivative of the nonlinear force in frequency domain with respect to $\tilde{\boldsymbol{q}}$. The $\boldsymbol{x}_s$ terms are eliminated in the Jacobin matrix for a non-rotating structure. The coefficient tensors for both the nonlinear force and the Jacobian matrix are computed in the pre-processing stage to save the computational power. The bar chart shown in Figure 5.5 is the comparison of time used to compute the coefficient tensors with different number of reduced basis (r) selected in the ROM. The 3D mesh with 80 elements shown in Figure 3.23 is used as an example here. The reduced equations can catch a better picture of the nonlinear dynamic behaviour with more basis selected, however the number of SMDs and the coefficient tensors that involved in the numerical analysis is also increased significantly.

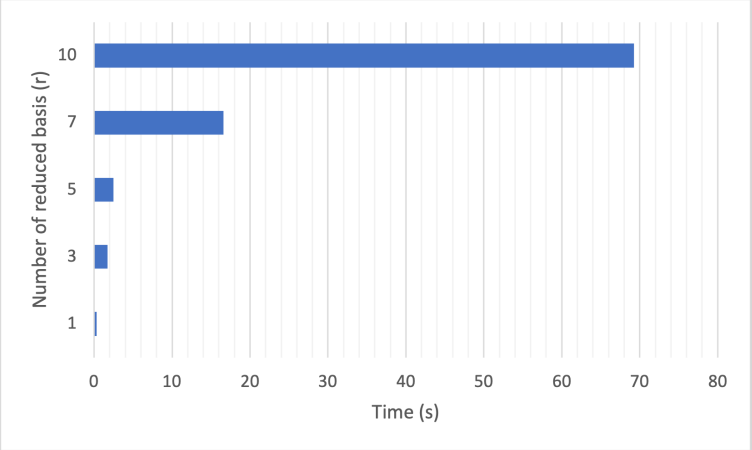


Fig. 5.5 *Time to compute the coefficient tensors with different number of reduced basis selected in SMD-QM.*

5.4 Numerical results

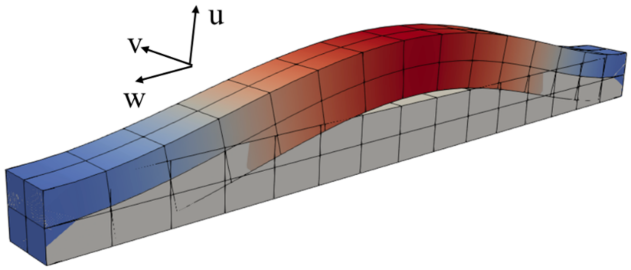
The convergence and the computational cost of the two ROM techniques are investigated on both the rotating and non-rotating 3D structures. The performance of the SMD-QM technique is compared with other model-order reduction methods, i.e. the implicit condensation and expansion (ICE) method, the direct normal form (DNF), and the quadratic manifold

computed from modal derivatives (MD). The nonlinear FRF plots generated from the full FE model are used as references to assess the ROM results. The ability of the ROM techniques on predicting the nonlinear phenomenon, i.e, modal interaction, hardening/softening effect, are studied.

5.4.1 3D non-rotating clamped-clamped beam

The performance of the ROM techniques on a non-rotating clamped-clamped beam are investigated in this section. Two different cases were studied. In the first case, the frequency-response functions of a straight beam with an un-symmetric cross-section are computed. There is a detuning of 4.92% between the first two eigenfrequencies. The ROM results are compared with the benchmark used in literature. In the second case, the 3D beam have a perfect square cross-section. Hence there is no detuning between the eigenfrequencies of the two polarizations of the first two bending modes.

Clamped-clamped beam with un-symmetric cross-section

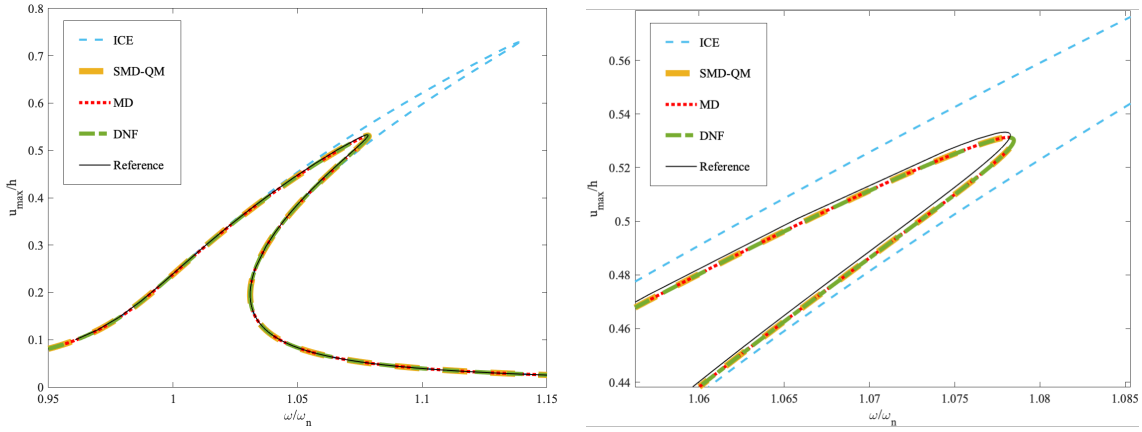


Parameters	
$b\ (m)$	0.0315
$h\ (m)$	0.03
$L\ (m)$	1
$E\ (GPa)$	104
$\rho\ (kg/m^3)$	4400
ν	0.3

Fig. 5.6 *The clamped-clamped beam under investigation in [131].*

Shen et al. worked on the numerical comparisons of ROM methods for the geometrically nonlinear structures in [131]. SMD-QM method is tested first on a non-rotating clamped-clamped beam. The performance of SMD-QM is compared with the ROM results generated in [131]. Figure 5.6 shows the 3D beam under investigation in [131]. The figure illustrates the mesh used and the deformed shape of the first bending mode. The physical parameters and the material properties are listed. Homogeneous material is assumed and stiffness-proportional damping is taken into account i.e. $[\mathbf{C}] = \frac{2\times 0.5\%}{\omega_n}[\mathbf{K}]$. A total of 80 HEX20R elements are used in the mesh, i.e. 20 on the length and (2×2) on the cross-section. A periodic point load with an amplitude of 300 N is applied at the middle of the beam in the u-direction.

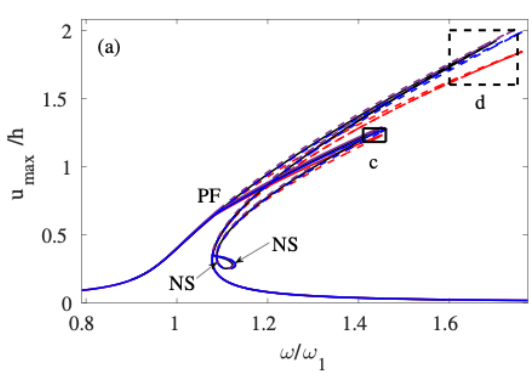
Figure 5.7 shows the convergence of the nonlinear ROM methods. The frequency on the horizontal axis is normalised by the first linear frequency $\omega_n = 941.373$ rad/s. The FRF computed from the full FEM model is used as a reference. The FRF results computed from different nonlinear ROM techniques, i.e. ICE, MD, and DNF, are obtained by Shen et al. in [131]. The methodologies involved in the nonlinear ROM methods used can be found in [44] for the ICE method, [94] for the DNF method, and [61] for the MD method. For the clamped-clamped beam case, the first two linear modes are selected as the reduced basis. With only the damping of the master mode considered in the ICE method, the ROM result shows an underestimation of the damping. A slow/fast assumption between the master and slave coordinates as proposed in [48] needs to be fulfilled in ICE to produce accurate ROM result. The results computed with the rest nonlinear ROM techniques demonstrate a good agreement with the reference solution.



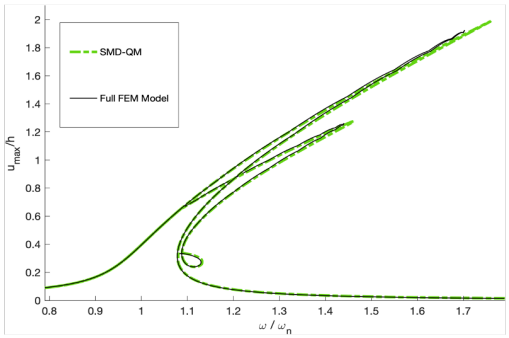
(a) FRFs of 1st Mode (b) FRFs near resonance peak

Fig. 5.7 *Convergence of the nonlinear ROM methods. Blue: ICE, orange: SMD-QM, red: MD, green: DNF, black: full FEM model.*

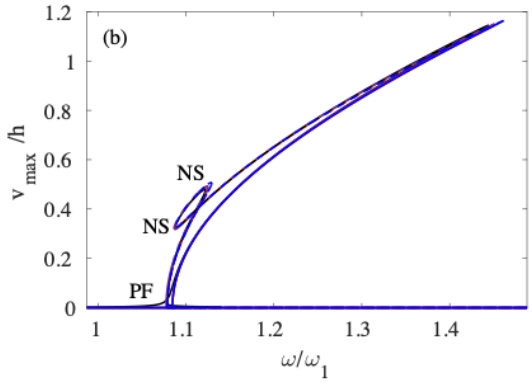
In order to have more insights on the coupled branch solution, a periodic point-load with higher amplitude (1500 N) is applied on the structure. The FE methodology implemented in this research does not have the ability to locate pitchfork bifurcation points. A small forcing in the v direction, with an amplitude selected as 1% of the amplitude in the u direction, is also imposed. This allows the continuation method to retrieve the coupled branch. Figure 5.8 presents the ROM results computed with the four different nonlinear techniques. A mass-proportional damping matrix is employed in this case, i.e. $[\mathbf{C}] = 2 \times 0.5\% \, \omega_n \, [\mathbf{M}]$. All of the ROM methods generate very good results. The pitchfork bifurcation point and the two Neimark–Sacker bifurcation points along the branch of coupled solution are captured by all techniques. For mass-proportional damping, the damping ratios decrease with increasing



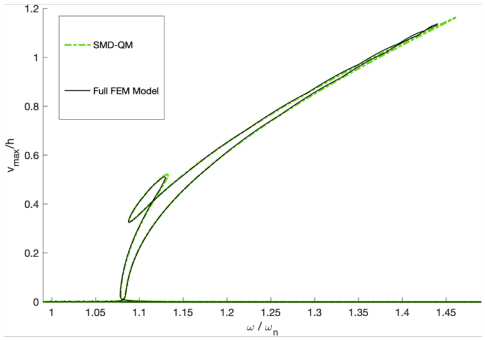
(a) ICE, MD, DNF (u_{max}) [131]



(b) SMD-QM (u_{max})



(c) ICE, MD, DNF (v_{max}) [131]



(d) SMD-QM (v_{max})

Fig. 5.8 *FRFs of the clamped-clamped beam with $F = 1500$ N. Full FEM model (black) compared to ROMs obtained with the ICE method (purple), the DNF method (red), the MD method (blue), and the SMD-QM (light green). PF: pitchfork bifurcation point. NS: Neimark–Sacker bifurcation.*

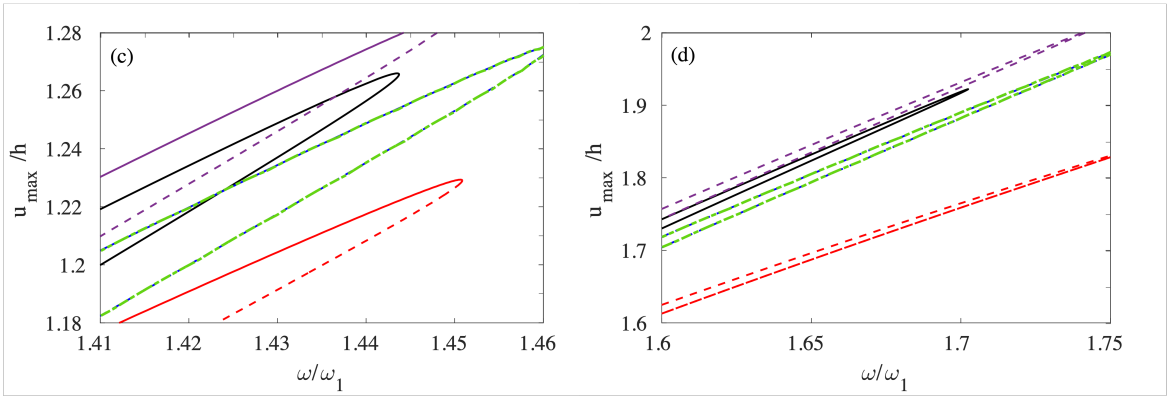
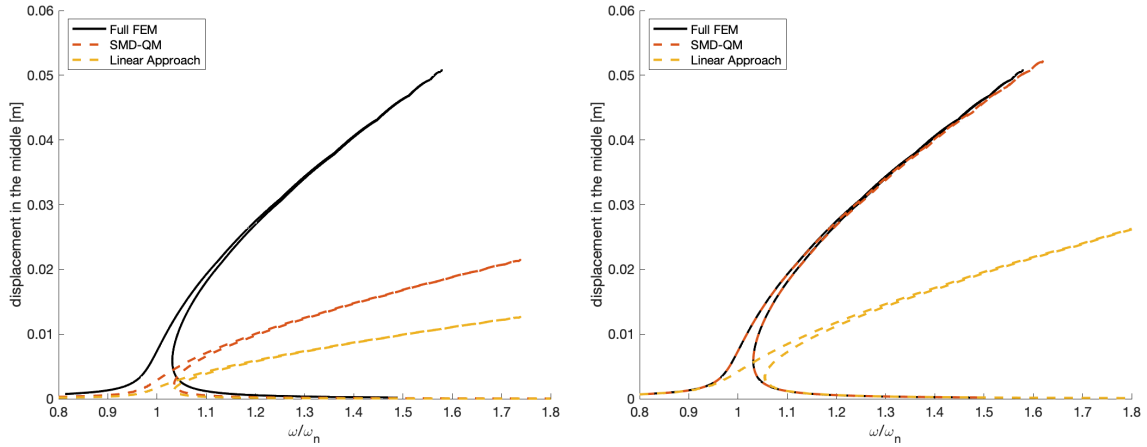


Fig. 5.9 *Zoomed views of Figure 5.8. Full FEM model (black), ICE (purple), DNF (red), MD (blue), and SMD-QM (light green).*

frequencies. The damping issue of the ICE method is eased in this case, as the damping values of the slave modes are smaller. SMD-QM is a simplified version of MD. In this simple straight beam case, the FRF plots of the two ROM techniques overlap.

Clamped-clamped beam with symmetric cross-section



(a) r = 1 (b) r = 2

Fig. 5.10 *Convergence of the SMD-QM and the linear approach with the full FE model.*

The clamped-clamped beam with a symmetric cross-section with mesh shown in Figure 5.6 is investigated. The new dimension of beam is $30\text{mm} * 30\text{mm} * 1000\text{mm}$. Homogeneous material of Young's Modulus $E = 210$ GPa, density $\rho = 7800\ \text{kg/m}^3$ and Poisson's ratio $\nu = 0.3$ is assumed. A mass proportional damping matrix $[\mathbf{C}] = 3[\mathbf{M}]$ is employed. A periodic point load is applied at the middle of the beam in the vertical-direction, i.e. $F_y = 700 \cdot \cos(\omega t)$. Figure 5.10 shows the the nonlinear FRF plots for the first bending mode generated by using a full FEM model and the reduced models. The maximum displacement in the y-direction at the load point is shown on the y-axis of the plots. The frequency on the x-axis is normalised by the natural frequency $\omega_n = 159.90$ Hz. The full FEM model has a total of 1737 free DOFs. With 3 Harmonics considering in the HBM equations, the numerical analysis need to deal with a total of $12159 = (2 \times 3 + 1) * 1737$ equations. Figure 5.10a shows the nonlinear FRF plot generated by using the reduced model with $r = 1$. For $r = 1$, only the first linear eigenmode $\boldsymbol{\phi}_1$ is selected in the reduced basis for the linear approach. $\boldsymbol{\phi}_1$ and its modal derivative $\boldsymbol{\Theta}_{11}$ are considered in the reduced basis of SMD-QM. The large dynamic system is reduced to a single-DOF system in this case. Figure 5.10b shows the nonlinear FRF plot generated by using the reduced model with $r = 2$. The mass normalised linear modes $\boldsymbol{\phi}_1$

and $\boldsymbol{\phi}_2$ are considered in the linear approach. The additional mode and its derivatives, i.e. $\boldsymbol{\phi}_2$, $\boldsymbol{\Theta}_{12}$, and $\boldsymbol{\Theta}_{22}$, are considered in the SMD-QM approach. For both ROM techniques, 5 harmonics are considered in the HBM analysis.

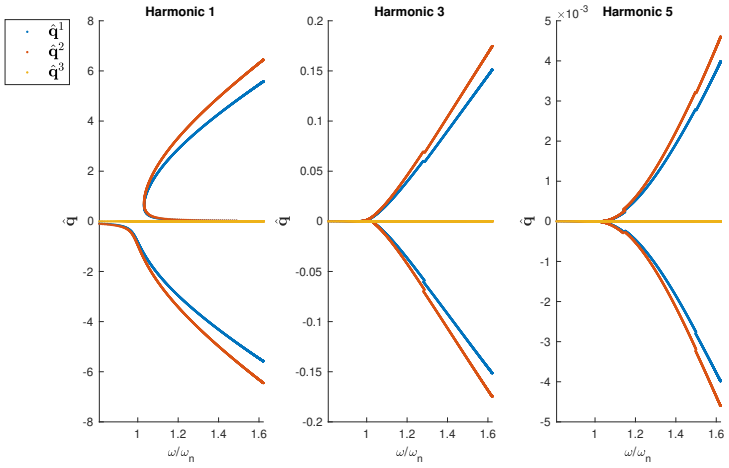


Fig. 5.11 *Response of the reduced basis $\hat{\boldsymbol{q}}$ in odd harmonics ($r = 3$).*

The response of the reduce basis $\hat{\boldsymbol{q}}$ at the i-th harmonic can be expressed as:

$$\hat{\boldsymbol{q}}^i = \tilde{\boldsymbol{q}}_c^i \cos(\omega t) + \tilde{\boldsymbol{q}}_s^i \sin(\omega t) \tag{5.68}$$

$\tilde{\boldsymbol{q}}_c^i$ and $\tilde{\boldsymbol{q}}_s^i$ are the Fourier coefficients shown in Equation (3.59). The amplitude of the response of the odd harmonics with $r = 3$ are presented in Figure 5.11. The first two modes have equal significance to the overall response of the nonlinear structure and the contribution of the 3$^{\text{rd}}$ mode is negligible. Since the cross-section of the beam is a perfect square, the mass-normalised modes $\boldsymbol{\phi}_1$ and $\boldsymbol{\phi}_2$ are of the same shape. The two mode shapes are in planes which are inclined with a 45° angle from the YZ-plane. When a vertical force applied to the beam, both modes are initiated. SMD-QM method has a much better convergence with compared to the linear approach. To achieve a better convergence with the linear approach, additional modes need to be included in the reduce basis. The Fourier coefficients can be used as a guideline for mode(s) selection. Figure 5.12 shows the total time taken for the nonlinear dynamic analysis shown in Figure 5.10b. Both ROM methods require much less computational power than the full FEM model. The linear approach uses slightly less time than the SMD-QM, but lower convergence.

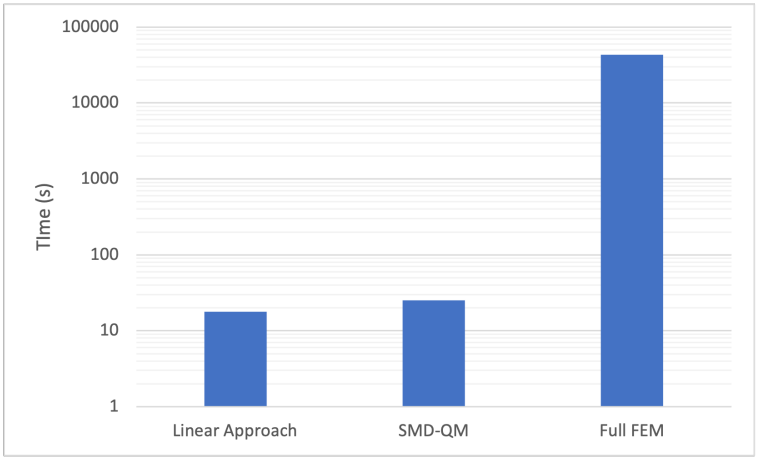
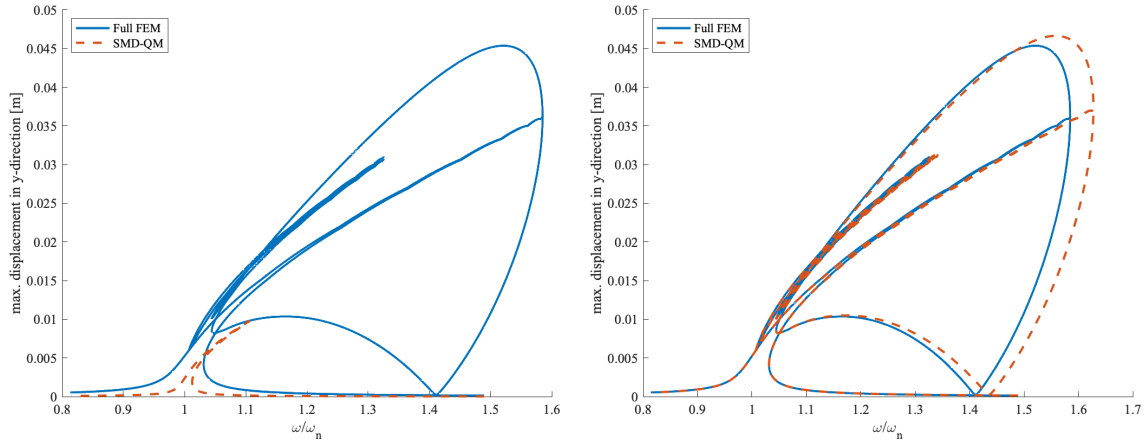


Fig. 5.12 *Computation time taken for the dynamic analysis.*



(a) r = 1 (b) r = 2

Fig. 5.13 *Comparison of the results from the SMD-QM approach and the full FEM with* $F_x = F_y = 500 \cdot \cos(\omega t)$.

For the same clamped-clamped beam mesh, a periodic point load with an inclined angle is applied at the middle of the beam. The force is applied in the plane that is inclined on 45° with respect to *xz* and *yz* planes, i.e. $F_x = F_y = 500 \cdot \cos(\omega t)$. Both vertical and lateral bending modes are activated in this case. Figure 5.13 shows the comparison of the nonlinear FRF plots generated by using a full FEM model and a reduced modal based on SMD-QM. The response of the beam with square cross-section has an equal response in both *x* and *y* direction, Figure 3.28a. Hence only the maximum displacement in the *y*-direction at the load point is shown. Since the first 2 modes are activated by the excitation force, reduced basis with only the first mode considered is not enough to attain the full picture. With the additional mode and its derivatives considered into the reduced basis, the modal interaction between

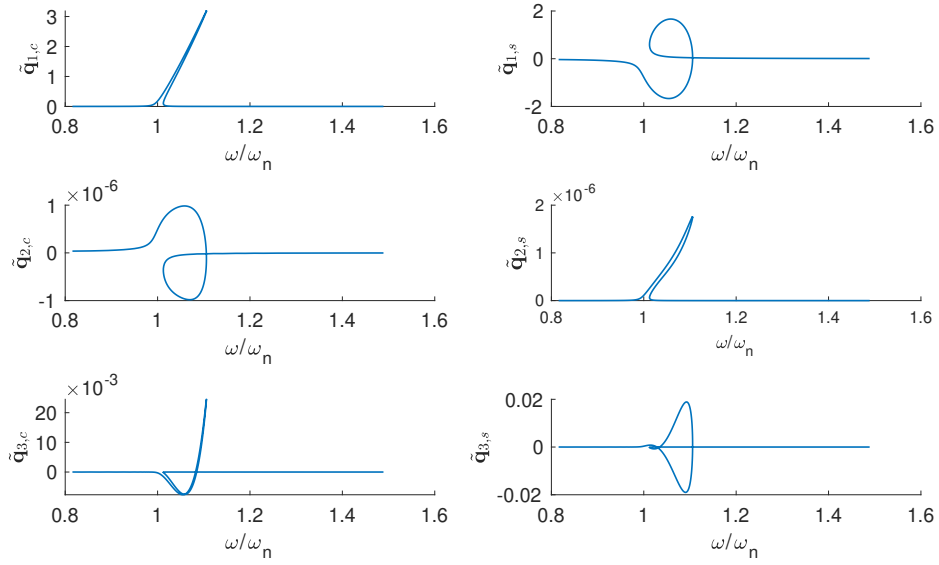


Fig. 5.14 *Fourier coefficients in* $\tilde{\boldsymbol{q}}$ *with* $r = 1$.

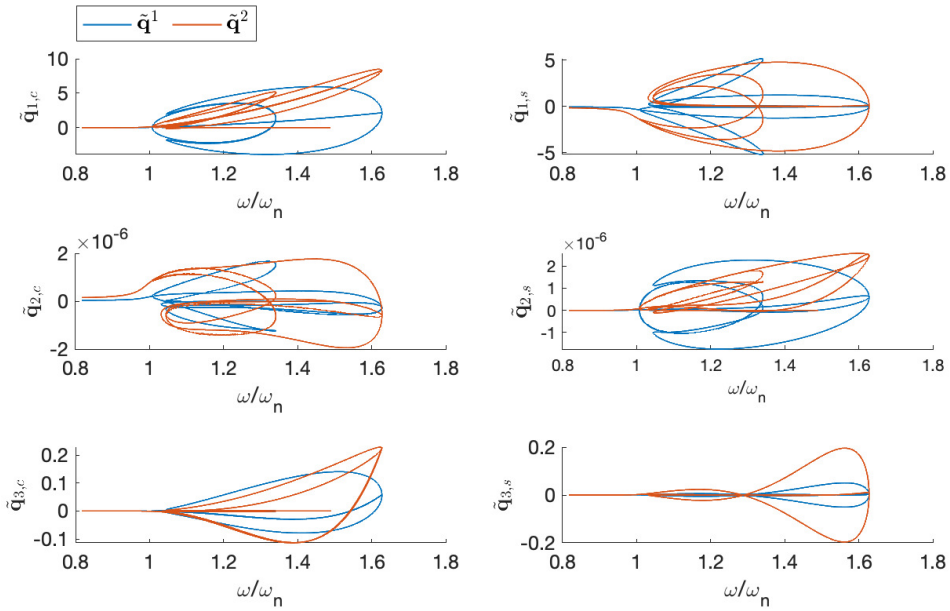
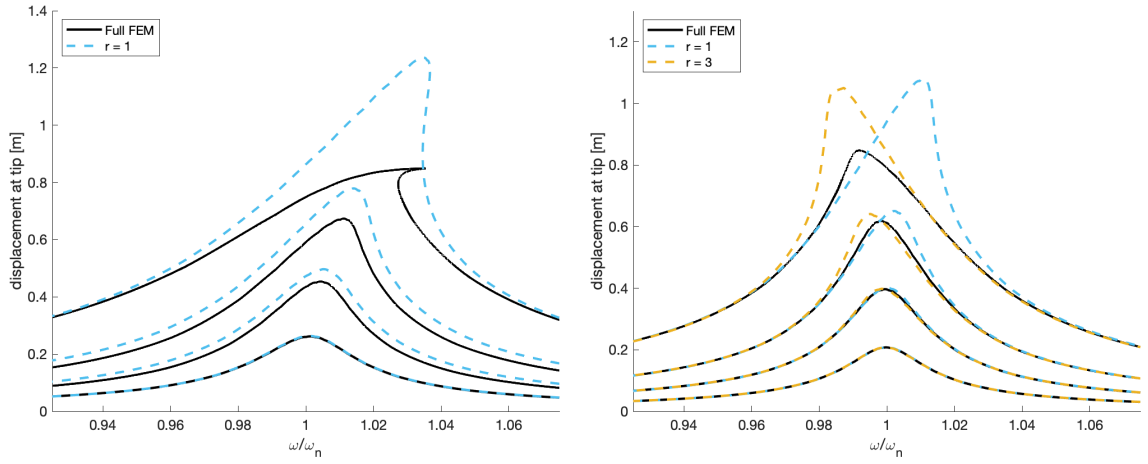


Fig. 5.15 *Fourier coefficients in* $\tilde{\boldsymbol{q}}$ *with* $r = 2$.

the first 2 bending modes can be captured by the SMD-QM approach. Figure 5.14 and 5.15 shows the Fourier coefficients in $\tilde{\boldsymbol{q}}$ with $r = 1$ and $r = 2$, respectively. The contribution of the even harmonics are negligible compared to the odd harmonics. The 3$^{\text{rd}}$ harmonics start to take part into the dynamic response when 2 modes are considered into the reduced basis. The branches on Figure 5.15 represent the bifurcation of the system. The result demonstrates the potential of the SMD-QM method to predict the nonlinear dynamic behaviour of the system with the right mode(s) selected.

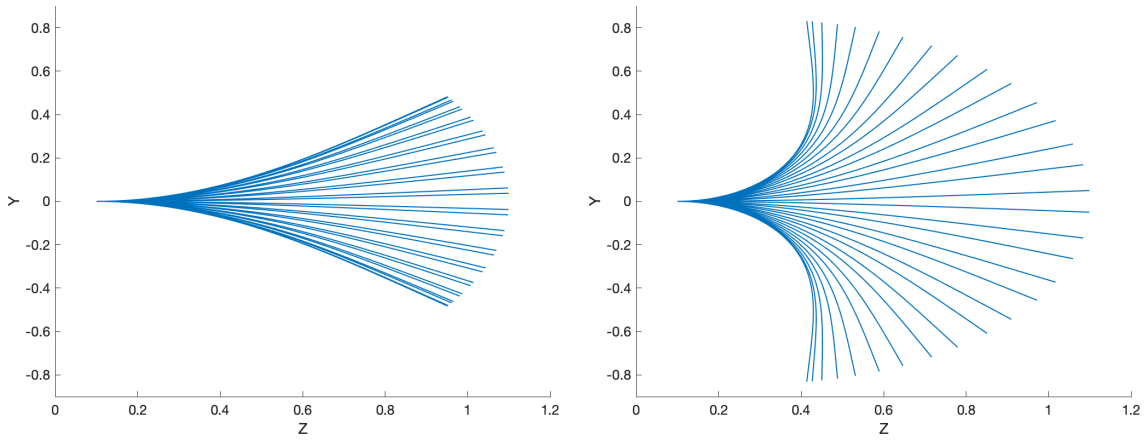
5.4.2 Rotating 3D cantilevered beam



(a) $\Omega_x = 0$ rad/s (b) $\Omega_x = 130$ rad/s

Fig. 5.16 *FRF of the first bending mode from the SMD-QM model and the full FEM for a rotating cantilevered beam.*

The effects of rotational speed on the cantilevered mesh shown in Figure 4.2 are investigated. 20-node hexahedron elements are chosen in the FE model with the same material parameters as the clamped-clamped beam. The 3D structure has a dimension of $30\text{mm} * 20\text{mm} * 1000\text{mm}$. The centre of rotation Ω_x is 10 cm apart from the clamped end of the cantilevered beam. A harmonic force is applied at the end of the beam in vertical direction. Figure 5.16b shows the nonlinear FRF plots of the full FE model and the reduced model based on SMD-QM. 5 harmonics are used in the HBM analysis for both the full and the reduced equations. The force amplitudes of 100N, 200N, 350N and 700N, are investigated. For the responses with lower amplitudes, reduced model with only the first linear mode and its derivative ($r = 1$) can provide good predictions for the dynamic behaviours. For $F_y = 700$ N, the maximum response reaches about 80% of the total length. With only the first bending mode and its derivative considered into the reduced basis of SMD-QM, the responses under higher forcing



(a) $F = 200$ N (b) $F = 700$ N

Fig. 5.17 *Dynamic shape of the cantilevered beam.*

amplitude are overestimated in both cases. The dynamic deformation shapes of the beam at $F_y = 200$ N and $F_y = 700$ N are depicted on Figure 5.17 for the non-rotating case. The cantilevered beam is bent by 90° under $F_y = 200$ N. The SMD-QM method finds its limitation on describing this kind of deformation.

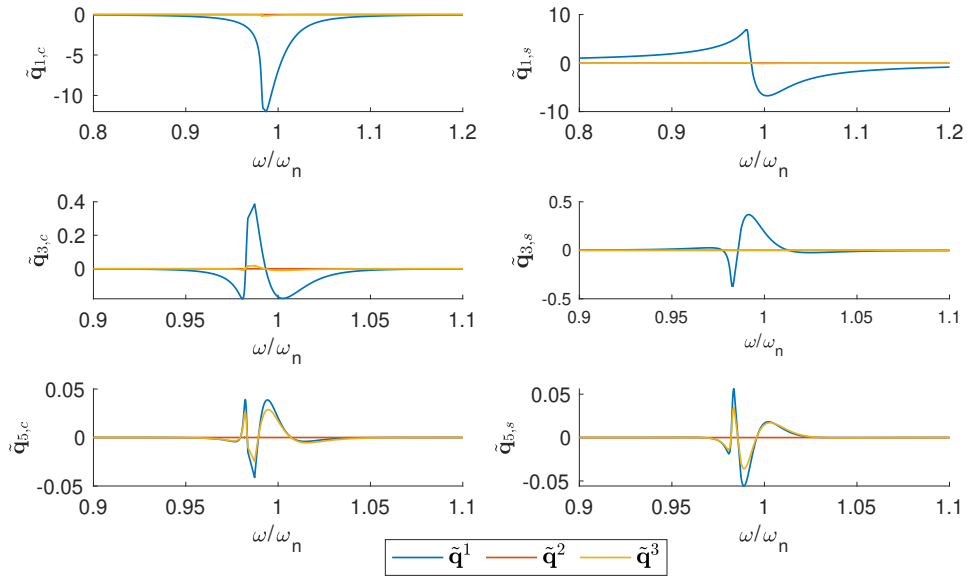
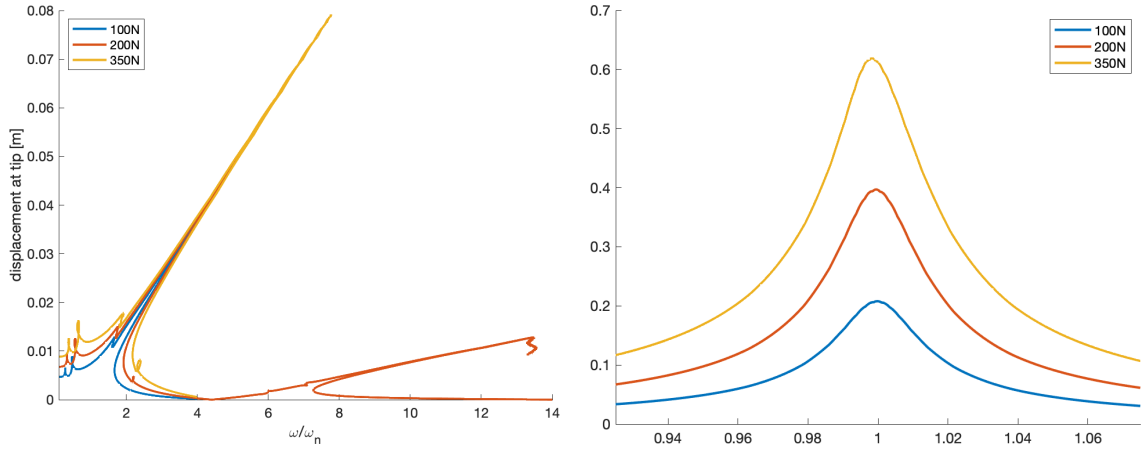


Fig. 5.18 *Fourier coefficients in* $\tilde{\boldsymbol{q}}$ *with* $r = 3$.

The softening effect due to the rotational speed is captured by the reduced model with $r = 3$ for $\Omega_x = 130$ rad/s. $\boldsymbol{\phi}_1$, $\boldsymbol{\phi}_2$ and $\boldsymbol{\phi}_3$ are considered in the $r = 3$ case. Figure 5.18 shows the

Fourier coefficients of the odd harmonics for the three reduced basis used in the rotating case. The second eigenmode (lateral bending mode) has a limited contribution to the overall response. The first eigenmode dominates at the first and the third harmonic. Mode 3 (second vertical bending mode) is excited on the fifth harmonic. Mode 1 and mode 3 in this harmonic response at the same amplitude level.

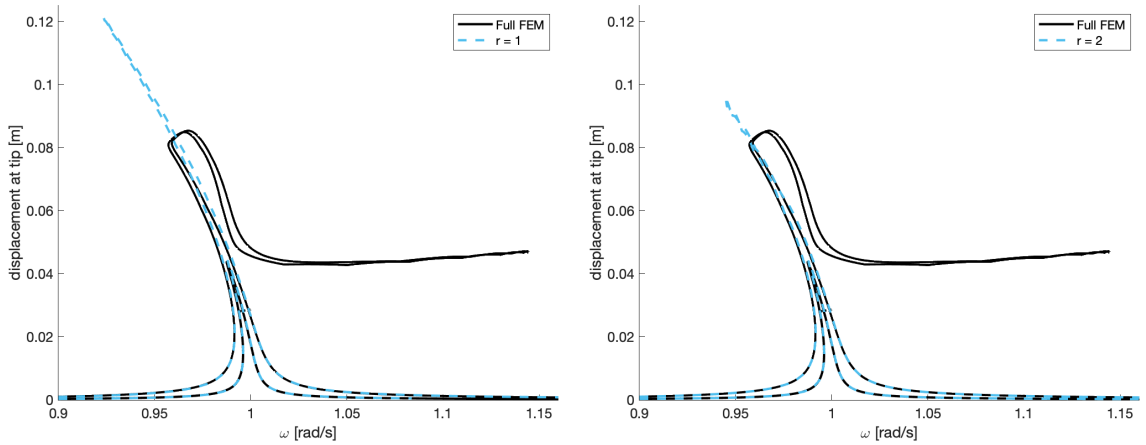
Since less nodes are constrained in a cantilevered beam, the dynamic behaviour of the structure is more complex. The linear ROM approach which based on the linear eigenmodes only cannot provide good predictions for the dynamic behaviour with few modes included, Figure 5.20a. The first 20 bending modes are selected as the reduced basis. The ROM results have a very strong stiffening effect on the FRF plots with compared to the full FE model. Additional relevant modes are required to be included into the reduced basis for a better convergence of the ROM results. In paper [155], the authors illustrated the modes required to capture the full dynamic picture of the first bending mode with ROM based on the linear eigenmodes only. The poisson modes that taking into account the radial deformation of the structure need to be included. These modes are within the high frequency range. The selection of the modes is critical to the performance of the linear approach. To find all the relevant modes required can be impractical for large-scale systems. The paper also shows that the modal derivatives in the SMD-QM technique automatically included these Poisson modes. SMD-QM is a better choice in this case.



(a) Linear-based ROM with $\Omega_x = 0$ rad/s (b) Full FEM with $\Omega_x = 0$ rad/s

Fig. 5.19 *3D cantilevered beam: FRF of the first bending mode from the ROM based on linear subspaces ($r = 20$).*

The performance of SMD-QM on the second bending mode with $\Omega_x = 1400$ RPM are studied in Figure 5.20. $F_y = 50$ N and $F_y = 150$ N are studied. The damping matrix used in this mode is set to be $[\mathbf{C}] = 2 \times 0.5\% \, \omega_n \cdot [\mathbf{M}]$. Reduced model based on SMD-QM with $r = 1$ and $r = 2$ is used for the analysis. For $r = 1$, the second bending mode $\boldsymbol{\phi}_3$ and its SMD are considered in the nonlinear mapping $\boldsymbol{\Gamma}$. Aa discussed in section 4.1.5, there is a modal interaction between the second and the fourth flexural modes. For $r = 2$, the 2$^{\text{nd}}$ and the 4$^{\text{th}}$ flexural modes, i.e. $\boldsymbol{\phi}_3$ and $\boldsymbol{\phi}_7$, together with their SMDs ($\boldsymbol{\Theta}_{33}$, $\boldsymbol{\Theta}_{37}$, and $\boldsymbol{\Theta}_{77}$) are included in the mapping. 15 harmonics are considered in the HBM. The prediction results converge better with $r = 2$. The branch on the full FEM is due to the modal interaction of higher modes. The dynamic behaviour of the modal interaction can be isolated from other modes in the reduced system.



(a) $r = 1$ (b) $r = 2$

Fig. 5.20 *FRF of the second bending mode from the SMD-QM model and the full FEM for a rotating cantilevered beam ($\Omega_x = 1400$ RPM).*

5.5 Concluding remarks

The reduced-order models based on linear decomposition and quadratic manifold are presented in this chapter. Both methods are used to study the dynamic behaviour of the 3D structure with geometric nonlinearities. The 3D structures are discretised by the FE method and the ROM methods are applied to the discretised system. For the linear approach, the full FE model is projected onto the linear eigenmode(s) of the system. For the nonlinear mapping, both the eigenmode(s) and the SMD(s) are included in the reduced basis. Computational details for both approaches are provided and a full algorithm has been presented. A methodology has been proposed to take into account the effects of the rotational speeds

in the ROM so as to produce the FRFs. The computational time for the FRF has been reduced significantly by both methods in comparison to the full FE model. SMDs are used to describe the curvature of the subspace in the directions of the reduced co-ordinates. By considering the SMDs on top of the linear modes in the reduced basis, the convergence of the results is improved significantly. A much lower number of reduced basis are required for the SMD-QM than the linear approach. With the correctly selected reduced basis, it has been shown that the SMD-QM can recover the internal resonance loops and retrieve the bifurcation points due to the fulfilment of an exact commensurability of nonlinear frequencies. The hardening/softening effect due to the rotational speed on the cantilevered beam can also be captured by the ROM.

Chapter 6

Conclusions and Future Works

6.1 Conclusions for research work

The present research has been focused on the dynamic modelling of 3D structures with emphasis on the geometric nonlinearity and rotational effect. The nonlinear numerical methodologies for the discretised system are developed and validated. The steady-state responses of the 3D structure with respect to various performance attributes can be computed more efficiently with the implementation of the reduced order modelling techniques. Three dimensional solid finite elements have been used throughout the research. In comparison to the lower-order elements, 3D solid elements are geometrically exact. This makes them well-suited for academic studies and standard industrial applications. Furthermore, they are better suited for the discretisation of complex geometries.

6.1.1 Conclusions on nonlinear modal analysis

In continuum mechanics, finite strain theory deals with deformation problems that involve large strains and large rotations. When structures vibrate with large amplitudes, the significant difference between the initial and the current configuration of the continuum model makes the assumptions in the infinitesimal strain theory no longer suitable. As presented by the research, a great deal of nonlinear couplings between lower-frequency bending modes and higher-frequency modes are involved in the dynamic behaviour of simple structures like straight beams. The Green-Lagrange strain measures are employed in this research to express the nonlinear relationship between displacement and strain. This is a rotational-independent tensor that quantifies the change in length and direction of an infinitesimal material fibre. In this research, the structure's material is assumed to be elastic, homogeneous, and isotropic. The constitutive relationship between the Green-Lagrange strain and its work conjugate, i.e.

Second Piola-Kirchoff stress tensor, is described by the linear 3D Saint Venant–Kirchhoff material law.

The continuum structures are discretised in space by using the Finite Element Method. A finite element modelling code has been developed for the 3D structures with geometric nonlinearities. The governing equation in the time domain for 3D structure with geometric nonlinearity is derived from the energy expressions. The motion and the deformation of the structure over time are described with respect to its initial configuration (Total Lagrangian Descriptions). The FE matrices in the equations of motion are yielded by applying the Euler–Lagrange equation to the energy expressions. Gauss-Legendre quadrature formulations are applied to approximate the definite integrals of the polynomial functions involved in the energy expressions. 3D solid elements are used in the FE model. The absence of the rotational degree of freedom on the nodes makes the elements suitable for structures with large displacement and rotation. The performance and properties of different 3D element types were investigated in this research. For flat/thin structures, hexahedron elements perform better than tetrahedron elements. The first-order tetrahedron elements have the simplest formulation among all, however, they tend to give much stiffer results. The convergence rate of the first-order tetrahedron elements is very slow. Unless a very fine mesh is employed, the results are far from the real values. Reduced integration is engaged on the hexahedron elements to prevent locking. Especially for the first-order hexahedron elements, the development of the artificial shear strain within the element is more significant without the reduced integration. This is due to the inability to bend the element edge. Additional control procedures for preventing hourglassing in the first-order hexahedron elements need to take. Structures discretised with the first-order elements are extremely stiff in the coarse mesh. The accuracies of the results increase with the refinement of the mesh. Higher-order elements give more accurate results even with a coarser mesh. The 20-node hexahedron elements have the best performance overall. However, the increases in the number of shape functions and the Gauss–Legendre quadrature points involved cause the increase in the overall computational time.

The derived equations of motion in the time domain are solved in the frequency domain by using the Harmonic Balance Method (HBM) coupling with the Alternating Fourier Transformation (AFT). In the HBM, the periodic responses are estimated as a truncated Fourier series to the N_H-th harmonic. The more harmonics considered in the HBM, the more detailed dynamic behaviours can be described by the solution. However, the size of the motion equations in the frequency domain and the number of samples per period in the AFT will

also increase, which causes an increase in the computational time for solving the equations. The dynamic analyses are done on two test cases with a periodic point load applied, i.e. clamped-clamped beam and cantilevered beam. The Frequency Response Function (FRF) plots illustrate the steady-state responses of the 3D structure to the harmonic forces with different excitation levels. The geometric nonlinear terms have a hardening or softening effect on the forced response of the structure, depending on the mode. The algorithms used for computing the nonlinear normal modes based on the Extended Periodic Motion Concept (EPMC) are also presented. The backbone curve constructed shows the peak locations of the FRF plots under different forcing levels. The backbone curves are valuable tools for quantifying active nonlinearities whilst highlighting the interactions that may occur within the system. Both the FRF plots and the backbone curves are able to capture the nonlinear features of the dynamic behaviour, such as modal interaction. The simulation results from the mathematical model proposed are validated with the experimental data. The model demonstrates its capability on representing real-world dynamic responses. The methodologies developed are applicable to 3D structures with complex or more advanced shapes.

6.1.2 Conclusions on the effect of rotation

The finite element equations for the 3D rotating structures with geometric nonlinearities are derived from the energy expressions. The expressions are defined in the co-rotating reference system, i.e. the reference frame is located on the axis of rotation and is rotating with the structures. Additional speed-dependent terms need to be added to the equation of motion. Uniform angular velocities are assumed and the effect of Coriolis forces is neglected in this research. The centrifugal forces caused by the angular velocities bring the rotating structure into a pre-stressed state, which leads to a higher bending stiffness as compared to the case of a non-rotating structure. The centrifugal stiffening effect can be observed in the linear modes. The natural frequencies increase with the angular velocities. The nonlinear forced frequency responses of the cantilevered beam under different rotational speeds are investigated. For large-amplitude vibrations, softening or hardening behaviour of the rotating systems can be observed. For the first bending mode, the hardening effect can be observed in the forced response at lower rotational speeds. The softening effect of the rotation dominates once the rotational speed passes a critical value. On the other hand, the hardening effect can be observed in the second bending mode at any rotational speed.

6.1.3 Conclusions on the reduced order modelling techniques

Two intrusive reduced order modelling techniques for nonlinear dynamics are introduced in this research. Both techniques are projection-based. The first ROM method projects the full FEM onto the linear eigenmode(s) of the system. There is a linear mapping between the reduced basis and the full model. Whereas the second quadratic manifold (QM) method has a nonlinear mapping, which includes both the linear mode(s) and the static modal derivatives (SMD) in the reduced basis. SMDs are used to describe the curvature of the subspace in the directions of the reduced co-ordinates. Both ROM methods can decrease the complexity of the equations by reducing the number of DOFs from n to r, with $r \ll n$. Computational details for the two approaches are provided and a full algorithm has been presented. FRF plots of the reduced systems are compared with the full FE model. The nonlinear features of the dynamic and the hardening/softening effect of rotation can be captured by both techniques. The SMD-QM method has much better convergence than the linear-based ROM. With only the modes of interest and their derivatives included, the SMD-QM method can reproduce the nonlinear behaviour of the system. However, this is not the case for linear ROM. For structures undergoing complex dynamics, the ROM results diverge from the full model with only the linear eigenmode(s) involved. Eigenmodes within the higher frequency range need to be included to improve the accuracy of the prediction. These modes are automatically included in the SMDs. For a large-scale application, finding all the relevant modes for the linear ROM becomes impractical. The performance of the SMD-QM method is also compared with other nonlinear ROM techniques, i.e. the implicit condensation and expansion (ICE) method, the direct normal form (DNF), and the quadratic manifold computed from modal derivatives (MD). All four nonlinear methods demonstrate good results in the non-rotating case. The bifurcation points on the branch of coupled solution can be captured by all methods. Although the SMD-QM method has a good convergence, it still finds its limit when the 3D structure undergoes extreme deformation. The mode shapes and the derivatives are not able to describe the deformation shape in this case. The overall complexity and the computational effort for solving the equations are reduced significantly by the ROM methods, which makes the dynamic analysis for large-scale systems possible. Another feature of the ROM is that the mode(s) of interest can be isolated from all others. This permits the study of single nonlinear mode behaviour or multiple modes behaviour in the case of internal resonances.

6.2 Scientific contributions

- A full 3D FEM model with the implementation of 3D solid elements is developed. The distributed geometric nonlinearities and the effect of rotation are both considered in the model. The steady-state response of the structure can be achieved. The geometric exact solid elements make the model capable of performing accurate nonlinear dynamic analysis on structures with complex or more advanced shapes, such as large curvatures and twists.
- Intrusive ROM methods are implemented in the numerical model. The ROM methods provided can capture the effect of both the geometric nonlinearities and the rotational effect. The computational time for solving the dynamic equations has been reduced significantly. This permits the application of the code to large-scale structures.
- The methodologies developed can be applied to different types of blades to determine the important parameters for design and the influences of nonlinearities on the dynamic responses of the blades.

6.3 Future works

In the future, the following works can be carried forward to make the numerical model more comprehensive or complete:

- Application of the codes developed on industrial models can be carried out to test the capabilities and limitations of the numerical method. Parallelisation can be implemented into the codes to make them run more efficiently.
- To make the model more complete, other types of nonlinearities can be included in the code, such as material nonlinearity, contact friction etc. When studying the effect of rotation, the Coriolis effect is neglected and angular velocities are assumed to be uniform in this research. These assumptions can be withdrawn by adding the skew-symmetric Coriolis matrix and the Euler force into the equations.
- Comparison studies of ROM methods for geometric nonlinearities can be considered as future work to explore other possibilities.
- In a nonlinear system, there exist multiple solutions that could be found. Algorithms for determining the local stability of a steady-state periodic solution can be useful.

References

[1] Abramowitz, M. and Stegun, I. A. (1972). *Handbook of Mathematical Functions with Formulas, Graphs, and Mathematical Tables. National Bureau of Standards Applied Mathematics Series 55. Tenth Printing.* ERIC.

[2] Aghababaei, O., Nahvi, H., and Ziaei-Rad, S. (2010). Dynamic bifurcation and sensitivity analysis of non-linear non-planar vibrations of geometrically imperfect cantilevered beams. *International Journal of Non-Linear Mechanics*, 45(2):121–139.

[3] Anand, L. and Govindjee, S. (2020). *Continuum mechanics of solids*. Oxford University Press.

[4] Andrade, L., Awruch, A., and Morsch, I. (2007). Geometrically nonlinear analysis of laminate composite plates and shells using the eight-node hexahedral element with one-point integration. *Composite Structures*, 79(4):571–580.

[5] Bäker, M. (2018). How to get meaningful and correct results from your finite element model. *arXiv preprint arXiv:1811.05753*.

[6] Banerjee, J. (2000). Free vibration of centrifugally stiffened uniform and tapered beams using the dynamic stiffness method. *Journal of Sound and Vibration*, 233(5):857–875.

[7] Banerjee, J. (2001). Dynamic stiffness formulation and free vibration analysis of centrifugally stiffened timoshenko beams. *Journal of Sound and Vibration*, 247(1):97–115.

[8] Barbic, J. and James, D. L. (2007). *Real-time reduced large-deformation models and distributed contact for computer graphics and haptics*. PhD thesis, PhD thesis, Carnegie Mellon University.

[9] Bauchau, O. A. and Nikishkov, Y. G. (2001). An implicit transition matrix approach to stability analysis of flexible multi-body systems. *Multibody System Dynamics*, 5(3):279–301.

[10] Bayat, H. R., Wulfinghoff, S., Kastian, S., and Reese, S. (2018). On the use of reduced integration in combination with discontinuous galerkin discretization: application to volumetric and shear locking problems. *Advanced Modeling and Simulation in Engineering Sciences*, 5(1):1–16.

[11] Bazoune, A., Khulief, Y., and Stephen, N. (1999). Further results for modal characteristics of rotating tapered timoshenko beams. *Journal of Sound and Vibration*, 219(1):157–174.

[12] Bazoune, A., Khulief, Y., Stephen, N., and Mohiuddin, M. (2001). Dynamic response of spinning tapered timoshenko beams using modal reduction. *Finite Elements in Analysis and Design*, 37(3):199–219.

[13] Bellman, R. (2008). *Stability theory of differential equations*. Courier Corporation.

[14] Belytschko, T., Liu, W. K., Moran, B., and Elkhodary, K. (2014). *Nonlinear finite elements for continua and structures*. John wiley & sons.

[15] Ben-Israel, A. (1966). A newton-raphson method for the solution of systems of equations. *Journal of Mathematical analysis and applications*, 15(2):243–252.

[16] Benson, D. A., Huntington, G. T., Thorvaldsen, T. P., and Rao, A. V. (2006). Direct trajectory optimization and costate estimation via an orthogonal collocation method. *Journal of Guidance, Control, and Dynamics*, 29(6):1435–1440.

[17] Bonet, J., Gil, A. J., and Wood, R. D. (2016a). *Nonlinear solid mechanics for finite element analysis: statics*. Cambridge University Press.

[18] Bonet, J., Gil, A. J., and Wood, R. D. (2016b). *Nonlinear solid mechanics for finite element analysis: statics*. Cambridge University Press.

[19] Cameron, T. and Griffin, J. (1989). An alternating frequency/time domain method for calculating the steady-state response of nonlinear dynamic systems. *Journal of applied mechanics*, 56(1):149–154.

[20] Campbell, F. C. (2010). *Structural composite materials*. ASM international.

[21] Cardona, A., Lerusse, A., and Géradin, M. (1998). Fast fourier nonlinear vibration analysis. *Computational Mechanics*, 22(2):128–142.

[22] Carr, J. (2012). *Applications of centre manifold theory*, volume 35. Springer Science & Business Media.

[23] Carrera, E., Pagani, A., and Petrolo, M. (2013). Use of lagrange multipliers to combine 1d variable kinematic finite elements. *Computers & Structures*, 129:194–206.

[24] Caughey, T. and O'Kelly, M. (1965). Classical normal modes in damped linear dynamic systems. *Journal of Applied Mechanics*, 32(3):583.

[25] Chandiramani, N., Librescu, L., and Shete, C. (2002). On the free-vibration of rotating composite beams using a higher-order shear formulation. *Aerospace Science and Technology*, 6(8):545–561.

[26] Chandiramani, N. K., Shete, C. D., and Librescu, L. I. (2003). Vibration of higher-order-shearable pretwisted rotating composite blades. *International Journal of Mechanical Sciences*, 45(12):2017–2041.

[27] Chung, J. and Yoo, H. H. (2002). Dynamic analysis of a rotating cantilever beam by using the finite element method. *Journal of Sound and vibration*, 249(1):147–164.

[28] Combescure, D. and Lazarus, A. (2008). Refined finite element modelling for the vibration analysis of large rotating machines: Application to the gas turbine modular helium reactor power conversion unit. *Journal of Sound and Vibration*, 318(4-5):1262–1280.

[29] Cowper, G. (1966). The shear coefficient in timoshenko's beam theory. *Journal of applied mechanics*, 33(2):335–340.

[30] Crespo da Silva, M. (1980). On the whirling of a base-excited cantilever beam. *The Journal of the Acoustical Society of America*, 67(2):704–706.

[31] Curry, J. (1980). An algorithm for finding closed orbits. In *Global theory of dynamical systems*, pages 111–120. Springer.

[32] De Vivo, L. and de Sciarra, F. M. (1999). The b-bar method and the limitation principles. *International journal of solids and structures*, 36(34):5177–5206.

[33] Demo, N., Tezzele, M., and Rozza, G. (2019). A non-intrusive approach for the reconstruction of pod modal coefficients through active subspaces. *Comptes Rendus Mécanique*, 347(11):873–881.

[34] Detroux, T., Renson, L., Masset, L., and Kerschen, G. (2015a). The harmonic balance method for bifurcation analysis of large-scale nonlinear mechanical systems. *Computer Methods in Applied Mechanics and Engineering*, 296:18–38.

[35] Detroux, T., Renson, L., Masset, L., and Kerschen, G. (2015b). The harmonic balance method for bifurcation analysis of large-scale nonlinear mechanical systems. *Computer Methods in Applied Mechanics and Engineering*, 296:18–38.

[36] Dokumaci, E., Thomas, J., and Carnegie, W. (1967). Matrix displacement analysis of coupled bending-bending vibrations of pretwisted blading. *Journal of Mechanical Engineering Science*, 9(4):247–254.

[37] Ewins, D. J. (2009). *Modal testing: theory, practice and application*. John Wiley & Sons.

[38] Flügge, S. (2013). *Principles of Classical Mechanics and Field Theory/Prinzipien der Klassischen Mechanik und Feldtheorie*. Springer-Verlag.

[39] Fox, C. and Burdess, J. (1979). The natural frequencies of a thin rotating cantilever with offset root. *Journal of Sound and Vibration*, 65(2):151–158.

[40] Friedmann, P., Hammond, C., and Woo, T.-H. (1977). Efficient numerical treatment of periodic systems with application to stability problems. *International Journal for Numerical Methods in Engineering*, 11(7):1117–1136.

[41] Fu, Z.-F. and He, J. (2001). *Modal analysis*. Elsevier.

[42] Gent, A. (1996). A new constitutive relation for rubber. *Rubber chemistry and technology*, 69(1):59–61.

[43] Ghosh, S., Lee, K., and Raghavan, P. (2001). A multi-level computational model for multi-scale damage analysis in composite and porous materials. *International journal of solids and structures*, 38(14):2335–2385.

[44] Gordon, R. and Hollkamp, J. (2006). Reduced-order modeling of random response of curved beams using implicit condensation. In *47th AIAA/ASME/ASCE/AHS/ASC Structures, Structural Dynamics, and Materials Conference 14th AIAA/ASME/AHS Adaptive Structures Conference 7th*, page 1926.

[45] Griewank, A. and Reddien, G. (1983). The calculation of hopf points by a direct method. *IMA Journal of Numerical Analysis*, 3(3):295–303.

[46] Gunda, J. B., Singh, A. P., Chhabra, P. S., and Ganguli, R. (2007). Free vibration analysis of rotating tapered blades using fourier-p superelement. *Structural Engineering and Mechanics*, 27(2):243–258.

[47] Guo, Q., Yao, W., Li, W., and Gupta, N. (2020). Constitutive models for the structural analysis of composite materials for the finite element analysis: A review of recent practices. *Composite Structures*, page 113267.

[48] Haller, G. and Ponsioen, S. (2017). Exact model reduction by a slow–fast decomposition of nonlinear mechanical systems. *Nonlinear Dynamics*, 90(1):617–647.

[49] Hamilton, S. W. R. (1834). *On a general method in dynamics*. Richard Taylor.

[50] Han, S. and Feeny, B. (2002). Enhanced proper orthogonal decomposition for the modal analysis of homogeneous structures. *Journal of Vibration and control*, 8(1):19–40.

[51] Haselbach, F. (2015). Next generation of large civil aircraft engines-concepts & technologies. In *11 th European Conference on Turbomachinery Fluid dynamics & Thermodynamics*. EUROPEAN TURBOMACHINERY SOCIETY.

[52] Haussy, B. and Ganghoffer, J.-F. (2005). Instability analysis in pressurized transversely isotropic saint-venant–kirchhoff and neo-hookean cylindrical thick shells. *Archive of Applied Mechanics*, 74(9):600–617.

[53] Hoa, S. (1979). Vibration of a rotating beam with tip mass. *Journal of sound and vibration*, 67(3):369–381.

[54] Hodges, D. H. and Rutkowski, M. J. (1981). Free-vibration analysis of rotating beams by a variable-order finite-element method. *AIAA Journal*, 19(11):1459–1466.

[55] Hollkamp, J. J. and Gordon, R. W. (2008). Reduced-order models for nonlinear response prediction: Implicit condensation and expansion. *Journal of Sound and Vibration*, 318(4-5):1139–1153.

[56] Hu, Q., Xia, Y., Natarajan, S., Zilian, A., Hu, P., and Bordas, S. (2020). Isogeometric analysis of thin reissner–mindlin shells: locking phenomena and b-bar method. *Computational Mechanics*, 65(5):1323–1341.

[57] Hughes, P. J. and Kuether, R. J. (2021). Nonlinear interface reduction for time-domain analysis of hurty/craig-bampton superelements with frictional contact. *Journal of Sound and Vibration*, 507:116154.

[58] Hughes, T. J. (2012). *The finite element method: linear static and dynamic finite element analysis*. Courier Corporation.

[59] Hulbert, G. M. (1992). Time finite element methods for structural dynamics. *International Journal for Numerical Methods in Engineering*, 33(2):307–331.

[60] Imakura, A., Du, L., and Sakurai, T. (2015). A map of contour integral-based eigensolvers for solving generalized eigenvalue problems. *arXiv preprint arXiv:1510.02572*.

[61] Jain, S., Tiso, P., Rutzmoser, J. B., and Rixen, D. J. (2017). A quadratic manifold for model order reduction of nonlinear structural dynamics. *Computers & Structures*, 188:80–94.

[62] Jaśkowiec, J. and Sukumar, N. (2020). High-order cubature rules for tetrahedra. *International Journal for Numerical Methods in Engineering*, 121(11):2418–2436.

[63] Jeffreys, H. and Jeffreys, B. (1988). Lagrange's interpolation formula. *Methods of mathematical physics*, 3:260.

[64] Karkar, S., Cochelin, B., and Vergez, C. (2014). A comparative study of the harmonic balance method and the orthogonal collocation method on stiff nonlinear systems. *Journal of Sound and Vibration*, 333(12):2554–2567.

[65] Kee, Y.-J. and Shin, S.-J. (2015). Structural dynamic modeling for rotating blades using three dimensional finite elements. *Journal of Mechanical Science and Technology*, 29(4):1607–1618.

[66] Keller, H. B. (1975). Numerical solution of boundary value problems for ordinary differential equations: survey and some recent results on difference methods. In *Numerical solutions of boundary value problems for ordinary differential equations*, pages 27–88. Elsevier.

[67] Kerschen, G., Peeters, M., Golinval, J.-C., and Vakakis, A. F. (2009). Nonlinear normal modes, part i: A useful framework for the structural dynamicist. *Mechanical Systems and Signal Processing*, 23(1):170–194.

[68] Kim, B., Lee, S. B., Lee, J., Cho, S., Park, H., Yeom, S., and Park, S. H. (2012). A comparison among neo-hookean model, mooney-rivlin model, and ogden model for chloroprene rubber. *International Journal of Precision Engineering and Manufacturing*, 13(5):759–764.

[69] Kim, J. H., Lee, M.-G., Barlat, F., Wagoner, R., and Chung, K. (2008). An elasto-plastic constitutive model with plastic strain rate potentials for anisotropic cubic metals. *International Journal of Plasticity*, 24(12):2298–2334.

[70] King, M. and Vakakis, A. (1996). An energy-based approach to computing resonant nonlinear normal modes. *Journal of Applied Mechanics*, 63(3):810.

[71] Kondou, T., Tamura, H., and Sueoka, A. (1986). On a method of higher approximation and determination of stability criterion for steady oscillations in nonlinear systems. *Bulletin of JSME*, 29(248):525–532.

[72] Krack, M. (2015). Nonlinear modal analysis of nonconservative systems: Extension of the periodic motion concept. *Computers & Structures*, 154:59–71.

[73] Krack, M. and Gross, J. (2019). *Harmonic balance for nonlinear vibration problems*, volume 1. Springer.

[74] Krack, M., Salles, L., and Thouverez, F. (2017). Vibration prediction of bladed disks coupled by friction joints. *Archives of Computational Methods in Engineering*, 24(3):589–636.

[75] Krajcinovic, D. (1983). Creep of structures—a continuous damage mechanics approach. *Journal of structural mechanics*, 11(1):1–11.

[76] Krattiger, D., Wu, L., Zacharczuk, M., Buck, M., Kuether, R. J., Allen, M. S., Tiso, P., and Brake, M. R. (2019). Interface reduction for hurty/craig-bampton substructured models: Review and improvements. *Mechanical Systems and Signal Processing*, 114:579–603.

[77] Krylov, N. M. and Bogoliubov, N. N. (2016). *Introduction to Non-Linear Mechanics.(AM-11)*, volume 11. Princeton University Press.

[78] Kuo, Y. H., Wu, T. H., and Lee, S. Y. (1992). Bending vibrations of a rotating non-uniform beam with tip mass and an elastically restrained root. *Computers & structures*, 42(2):229–236.

[79] Langtangen, H. P. and Pedersen, G. K. (2016). *Scaling of differential equations*. Springer.

[80] Laxalde, D., Thouverez, F., Sinou, J.-J., and Lombard, J.-P. (2007). Qualitative analysis of forced response of blisks with friction ring dampers. *European Journal of Mechanics-A/Solids*, 26(4):676–687.

[81] Lazarus, A. and Thomas, O. (2010). A harmonic-based method for computing the stability of periodic solutions of dynamical systems. *Comptes Rendus Mécanique*, 338(9):510–517.

[82] Leissa, A., Lee, J., and Wang, A. (1981). Rotating blade vibration analysis using shells. In *Turbo Expo: Power for Land, Sea, and Air*, volume 79641, page V004T13A005. American Society of Mechanical Engineers.

[83] Lin, S. and Hsiao, K. (2001). Vibration analysis of a rotating timoshenko beam. *Journal of Sound and Vibration*, 240(2):303–322.

[84] Mahdiabadi, M. K., Tiso, P., Brandt, A., and Rixen, D. J. (2021). A non-intrusive model-order reduction of geometrically nonlinear structural dynamics using modal derivatives. *Mechanical Systems and Signal Processing*, 147:107126.

[85] McEwan, M., Wright, J., Cooper, J., and Leung, A. (2001). A finite element/modal technique for nonlinear plate and stiffened panel response prediction. In *19th AIAA Applied Aerodynamics Conference*, page 1595.

[86] McEwan, M. I. (2001). *A combined modal/finite element technique for the non-linear dynamic simulation of aerospace structures*. PhD thesis, The University of Manchester.

[87] Mooney, M. (1940). A theory of large elastic deformation. *Journal of applied physics*, 11(9):582–592.

[88] Moore, G. (2005). Floquet theory as a computational tool. *SIAM journal on numerical analysis*, 42(6):2522–2568.

[89] Moore, G. and Spence, A. (1980). The calculation of turning points of nonlinear equations. *SIAM Journal on Numerical Analysis*, 17(4):567–576.

[90] Morris, B. and Grizzle, J. W. (2005). A restricted poincaré map for determining exponentially stable periodic orbits in systems with impulse effects: Application to bipedal robots. In *Proceedings of the 44th IEEE Conference on Decision and Control*, pages 4199–4206. IEEE.

[91] Morrison, D. D., Riley, J. D., and Zancanaro, J. F. (1962). Multiple shooting method for two-point boundary value problems. *Communications of the ACM*, 5(12):613–614.

[92] Muravyov, A. A. and Rizzi, S. A. (2003). Determination of nonlinear stiffness with application to random vibration of geometrically nonlinear structures. *Computers & Structures*, 81(15):1513–1523.

[93] Nagtegaal, J. C., Parks, D. M., and Rice, J. (1974). On numerically accurate finite element solutions in the fully plastic range. *Computer methods in applied mechanics and engineering*, 4(2):153–177.

[94] Nasir, A., Sims, N., and Wagg, D. (2021). Direct normal form analysis of oscillators with different combinations of geometric nonlinear stiffness terms. *Journal of Applied and Computational Mechanics*, 7(Special Issue):1167–1182.

[95] Nayfeh, A. H. (1995). On direct methods for constructing nonlinear normal modes of continuous systems. *Journal of Vibration and Control*, 1(4):389–430.

[96] Nayfeh, A. H. and Balachandran, B. (2008). *Applied nonlinear dynamics: analytical, computational, and experimental methods*. John Wiley & Sons.

[97] Nelson, H. (1980). A finite rotating shaft element using timoshenko beam theory. *Journal of Mechanical Design*, 102:793.

[98] Ogden, R. W. (1972). Large deformation isotropic elasticity–on the correlation of theory and experiment for incompressible rubberlike solids. *Proc. R. Soc. Lond. A*, 326(1567):565–584.

[99] Ozgumus, O. O. and Kaya, M. O. (2007). Energy expressions and free vibration analysis of a rotating double tapered timoshenko beam featuring bending–torsion coupling. *International journal of engineering science*, 45(2-8):562–586.

[100] Pai, P. F. and Nayfeh, A. H. (1990). Non-linear non-planar oscillations of a cantilever beam under lateral base excitations. *International Journal of Non-Linear Mechanics*, 25(5):455–474.

[101] Papangelo, A., Fontanela, F., Grolet, A., Ciavarella, M., and Hoffmann, N. (2018). Multistability and localization in forced cyclic symmetric structures modelled by weakly-coupled duffing oscillators. *Journal of Sound and Vibration*.

[102] Parker, R. (2009). From blue skies to green skies: engine technology to reduce the climate-change impacts of aviation. *Technology Analysis & Strategic Management*, 21(1):61–78.

[103] Parker, T. S. and Chua, L. (2012). *Practical numerical algorithms for chaotic systems*. Springer Science & Business Media.

[104] Peeters, M., Viguié, R., Sérandour, G., Kerschen, G., and Golinval, J.-C. (2009). Nonlinear normal modes, part ii: Toward a practical computation using numerical continuation techniques. *Mechanical systems and signal processing*, 23(1):195–216.

[105] Peletan, L., Baguet, S., Torkhani, M., and Jacquet-Richardet, G. (2013). A comparison of stability computational methods for periodic solution of nonlinear problems with application to rotordynamics. *Nonlinear dynamics*, 72(3):671–682.

[106] Pernot, S. and Lamarque, C.-H. (2003). A wavelet-balance method to investigate the vibrations of nonlinear dynamical systems. *Nonlinear Dynamics*, 32(1):33–70.

[107] Pesheck, E., Pierre, C., and Shaw, S. (2002a). A new galerkin-based approach for accurate non-linear normal modes through invariant manifolds. *Journal of sound and vibration*, 249(5):971–993.

[108] Pesheck, E., Pierre, C., and Shaw, S. W. (2002b). Modal reduction of a nonlinear rotating beam through nonlinear normal modes. *J. Vib. Acoust.*, 124(2):229–236.

[109] Peter Tang, P. T. and Polizzi, E. (2014). Feast as a subspace iteration eigensolver accelerated by approximate spectral projection. *SIAM Journal on Matrix Analysis and Applications*, 35(2):354–390.

[110] Petyt, M. (2010). *Introduction to finite element vibration analysis*. Cambridge university press.

[111] Pierre, C., Ferri, A., and Dowell, E. (1985). Multi-harmonic analysis of dry friction damped systems using an incremental harmonic balance method. *Journal of applied mechanics*, 52(4):958–964.

[112] Raghothama, A. and Narayanan, S. (1999). Non-linear dynamics of a two-dimensional airfoil by incremental harmonic balance method. *Journal of Sound and Vibration*, 226(3):493–517.

[113] Rand, R. H. (1971). A higher order approximation for non-linear normal modes in two degree of freedom systems. *International Journal of Non-Linear Mechanics*, 6(4):545–547.

[114] Rand, R. H. (1973). The geometrical stability of non-linear normal modes in two degree of freedom systems. *International Journal of Non-Linear Mechanics*, 8(2):161–168.

[115] Rathod, H., Venkatesudu, B., Nagaraja, K., and Islam, M. S. (2007). Gauss legendre–gauss jacobi quadrature rules over a tetrahedral region. *Applied mathematics and computation*, 190(1):186–194.

[116] Rayleigh, L. (1877). Theory of sound f 109. *Ed*, 1(93):128.

[117] Ribeiro, P. (2004). Non-linear forced vibrations of thin/thick beams and plates by the finite element and shooting methods. *Computers & structures*, 82(17-19):1413–1423.

[118] Rosendahl, P., Staudt, Y., Schneider, A., Schneider, J., and Becker, W. (2019). Nonlinear elastic finite fracture mechanics: Modeling mixed-mode crack nucleation in structural glazing silicone sealants. *Materials & Design*, 182:108057.

[119] Salles, L., Staples, B., Hoffmann, N., and Schwingshackl, C. (2016). Continuation techniques for analysis of whole aeroengine dynamics with imperfect bifurcations and isolated solutions. *Nonlinear Dynamics*, 86(3):1897–1911.

[120] Samoĭlenko, A. M. and Ronto, N. I. (1979). *Numerical-analytic methods of investigating periodic solutions*. Imported Pubn.

[121] Sarrouy, E. and Sinou, J.-J. (2011). Non-linear periodic and quasi-periodic vibrations in mechanical systems-on the use of the harmonic balance methods. In *Advances in Vibration Analysis Research*. InTech.

[122] Scheel, M., Peter, S., Leine, R. I., and Krack, M. (2018). A phase resonance approach for modal testing of structures with nonlinear dissipation. *Journal of Sound and Vibration*, 435:56–73.

[123] Schilhansl, M. (1958). Bending frequency of a rotating cantilever beam. *Journal of Applied Mechanics*, 25(1):28–30.

[124] Seydel, R. (2009). *Practical bifurcation and stability analysis*, volume 5. Springer Science & Business Media.

[125] Shang, H., Machado, R., and Abdalla Filho, J. (2016). Dynamic analysis of euler–bernoulli beam problems using the generalized finite element method. *Computers & Structures*, 173:109–122.

[126] Shaw, S. (1985). The dynamics of a harmonically excited system having rigid amplitude constraints, part 1: Subharmonic motions and local bifurcations. *Journal of Applied Mechanics*, 52(2):453–458.

[127] Shaw, S. and Pierre, C. (1991). Non-linear normal modes and invariant manifolds. *Journal of sound and Vibration*, 150(1):170–173.

[128] Shaw, S. W. and Pierre, C. (1993). Normal modes for non-linear vibratory systems. *Journal of sound and vibration*, 164(1):85–124.

[129] Shaw, S. W. and Pierre, C. (1999). Modal analysis-based reduced-order models for nonlinear structures: An invariant manifold approach. *The shock and vibration digest*, 31(1):3–16.

[130] Shen, Y. (2021). *Reduced-order models for geometrically nonlinear vibrations of thin structures*. PhD thesis, Institut Polytechnique de Paris.

[131] Shen, Y., Vizzaccaro, A., Kesmia, N., Yu, T., Salles, L., Thomas, O., and Touzé, C. (2021). Comparison of reduction methods for finite element geometrically nonlinear beam structures. *Vibration*, 4(1):175–204.

[132] Sin, Y.-J., Jy, Y.-C., Yun, J.-H., and Yoo, Y.-C. (2007). Free vibration analysis of a rotating cantilever beam by using differential transformation method. *Transactions of the Korean Society of Mechanical Engineers A*, 31(3):331–337.

[133] Sinha, S. and Wu, D.-H. (1991). An efficient computational scheme for the analysis of periodic systems. *Journal of Sound and Vibration*, 151(1):91–117.

[134] Sipp, D., de Pando, M. F., and Schmid, P. J. (2020). Nonlinear model reduction: a comparison between pod-galerkin and pod-deim methods. *Computers & Fluids*, 208:104628.

[135] Slaats, P., De Jongh, J., and Sauren, A. (1995a). Model reduction tools for nonlinear structural dynamics. *Computers & structures*, 54(6):1155–1171.

[136] Slaats, P., De Jongh, J., and Sauren, A. (1995b). Model reduction tools for nonlinear structural dynamics. *Computers & structures*, 54(6):1155–1171.

[137] Southwell, R. V. and Gough, B. S. (1922). *On the free transverse vibrations of airscrew blades*. HM Stationery Office.

[138] Spiess, H. (2006). *Reduction methods in finite element analysis of nonlinear structural dynamics*. Inst. f. Baumechanik u. Numerische Mechanik, Univ. Hannover.

[139] Stewart, G. W. (2002a). Addendum to" a krylov–schur algorithm for large eigenproblems". *SIAM journal on matrix analysis and applications*, 24(2):599–601.

[140] Stewart, G. W. (2002b). A krylov–schur algorithm for large eigenproblems. *SIAM Journal on Matrix Analysis and Applications*, 23(3):601–614.

[141] Sun, X., Pan, X., and Choi, J.-I. (2019). A non-intrusive reduced-order modeling method using polynomial chaos expansion. *arXiv preprint arXiv:1903.10202*.

[142] Szemplinska, W. (1990). *The Behaviour of Nonlinear Vibrating Systems: Volume II: Advanced Concepts and Applications to Multi-Degree-of-Freedom Systems*, volume 12. Springer Science & Business Media.

[143] Tesi, A., Abed, E. H., Genesio, R., and Wang, H. O. (1996). Harmonic balance analysis of period-doubling bifurcations with implications for control of nonlinear dynamics. *Automatica*, 32(9):1255–1271.

[144] Tessler, A. and Spangler, J. L. (2004). Inverse fem for full-field reconstruction of elastic deformations in shear deformable plates and shells. In *2nd European Workshop on Structural Health Monitoring*.

[145] Thomas, J. and Abbas, B. (1975a). Finite element model for dynamic analysis of timoshenko beam. *Journal of Sound and Vibration*, 41(3):291–299.

[146] Thomas, J. and Abbas, B. (1975b). Finite element model for dynamic analysis of timoshenko beam. *Journal of Sound and Vibration*, 41(3):291–299.

[147] Thomas, O., Sénéchal, A., and Deü, J.-F. (2016). Hardening/softening behavior and reduced order modeling of nonlinear vibrations of rotating cantilever beams. *Nonlinear dynamics*, 86(2):1293–1318.

[148] Tian, J., Su, J., Zhou, K., and Hua, H. (2018). A modified variational method for nonlinear vibration analysis of rotating beams including coriolis effects. *Journal of Sound and Vibration*, 426:258–277.

[149] Timoshenko, S. P. (1921). Lxvi. on the correction for shear of the differential equation for transverse vibrations of prismatic bars. *The London, Edinburgh, and Dublin Philosophical Magazine and Journal of Science*, 41(245):744–746.

[150] Truesdell, C. and Noll, W. (2013). *The Non-Linear Field Theories of Mechanics/Die Nicht-Linearen Feldtheorien der Mechanik*, volume 2. Springer Science & Business Media.

[151] Turhan, Ö. and Bulut, G. (2009). On nonlinear vibrations of a rotating beam. *Journal of sound and vibration*, 322(1-2):314–335.

[152] Urabe, M. (1965). Galerkin's procedure for nonlinear periodic systems. *Archive for Rational Mechanics and Analysis*, 20(2):120–152.

[153] Vakakis, A. (1997). Non-linear normal modes (nnms) and their applications in vibration theory: an overview. *Mechanical systems and signal processing*, 11(1):3–22.

[154] Van Gorder, R. A. (2012). Analytical method for the construction of solutions to the föppl–von kármán equations governing deflections of a thin flat plate. *International Journal of Non-Linear Mechanics*, 47(3):1–6.

[155] Vizzaccaro, A., Givois, A., Longobardi, P., Shen, Y., Deü, J.-F., Salles, L., Touzé, C., and Thomas, O. (2020). Non-intrusive reduced order modelling for the dynamics of geometrically nonlinear flat structures using three-dimensional finite elements. *Computational Mechanics*, 66(6):1293–1319.

[156] Vizzaccaro, A., Salles, L., and Touzé, C. (2021). Comparison of nonlinear mappings for reduced-order modelling of vibrating structures: normal form theory and quadratic manifold method with modal derivatives. *Nonlinear Dynamics*, 103(4):3335–3370.

[157] Volovoi, V. V., Hodges, D. H., Cesnik, C. E., and Popescu, B. (2001). Assessment of beam modeling methods for rotor blade applications. *Mathematical and computer modelling*, 33(10-11):1099–1112.

[158] Wagg, D. and Neild, S. (2009). *Nonlinear vibration with control*. Springer.

[159] Watson, L. T. (1986). Numerical linear algebra aspects of globally convergent homotopy methods. *SIAM review*, 28(4):529–545.

[160] Weeger, O., Wever, U., and Simeon, B. (2013). Isogeometric analysis of nonlinear euler–bernoulli beam vibrations. *Nonlinear Dynamics*, 72(4):813–835.

[161] Weeger, O., Wever, U., and Simeon, B. (2014). Nonlinear frequency response analysis of structural vibrations. *Computational Mechanics*, 54(6):1477–1495.

[162] Weinstein, A. (1973). Normal modes for nonlinear hamiltonian systems. *Inventiones mathematicae*, 20(1):47–57.

[163] Wilson, E. L., Yuan, M.-W., and Dickens, J. M. (1982). Dynamic analysis by direct superposition of ritz vectors. *Earthquake Engineering & Structural Dynamics*, 10(6):813–821.

[164] Witherden, F. D. and Vincent, P. E. (2015). On the identification of symmetric quadrature rules for finite element methods. *Computers & Mathematics with Applications*, 69(10):1232–1241.

[165] Wolfe, H. F., Shroyer, C. A., Brown, D. L., and Simmons, L. W. (1995). An experimental investigation of nonlinear behaviour of beam an plates excited to high levels of dynamic response. Technical report, WRIGHT LAB WRIGHT-PATTERSON AFB OH FLIGHT DYNAMICS DIRECTORATE.

[166] Wriggers, P. (2016). Discretization methods for solids undergoing finite deformations. In *Advanced Finite Element Technologies*, pages 17–51. Springer.

[167] Wright, A., Smith, C., Thresher, R., and Wang, J. (1982). Vibration modes of centrifugally stiffened beams. *Journal of Applied Mechanics*, 49(1):197.

[168] Xiao, D. et al. (2016). *Non-intrusive reduced order models and their applications*. PhD thesis, Imperial College London.

[169] Xiao, H. and Gimbutas, Z. (2010). A numerical algorithm for the construction of efficient quadrature rules in two and higher dimensions. *Computers & mathematics with applications*, 59(2):663–676.

[170] Yeoh, O. (1993). Some forms of the strain energy function for rubber. *Rubber Chemistry and technology*, 66(5):754–771.

[171] Yokoyama, T. (1988). Free vibration characteristics of rotating timoshenko beams. *International Journal of Mechanical Sciences*, 30(10):743–755.

[172] Yoo, H. H., Park, J. H., and Park, J. (2001). Vibration analysis of rotating pre-twisted blades. *Computers & Structures*, 79(19):1811–1819.

[173] Zaoutsos, S. P., Papanicolaou, G. C., and Cardon, A. (1998). On the non-linear viscoelastic behaviour of polymer-matrix composites. *Composites Science and Technology*, 58(6):883–889.

[174] Zeng, Q., Liu, Z., Xu, D., Wang, H., and Zhuang, Z. (2016). Modeling arbitrary crack propagation in coupled shell/solid structures with x-fem. *International Journal for Numerical Methods in Engineering*, 106(12):1018–1040.

[175] Zhang, L., Cui, T., and Liu, H. (2009). A set of symmetric quadrature rules on triangles and tetrahedra. *Journal of Computational Mathematics*, pages 89–96.

[176] Zhang, X., Chen, Z., and Liu, Y. (2016). *The material point method: a continuum-based particle method for extreme loading cases*. Academic Press.

[177] Zhou, Z., Gill, A. S., Qian, D., Mannava, S., Langer, K., Wen, Y., and Vasudevan, V. K. (2011). A finite element study of thermal relaxation of residual stress in laser shock peened in718 superalloy. *International Journal of Impact Engineering*, 38(7):590–596.

[178] Zhu, S.-P., Yue, P., Yu, Z.-Y., and Wang, Q. (2017). A combined high and low cycle fatigue model for life prediction of turbine blades. *Materials*, 10(7):698.

[179] Zhu, T. and Atluri, S. (1998). A modified collocation method and a penalty formulation for enforcing the essential boundary conditions in the element free galerkin method. *Computational Mechanics*, 21(3):211–222.

Appendix A

3D Solid Elements in the Reference Coordinates

A.1 Shape functions of the 3D solid elements

The shape function of the four commonly used 3D solid elements are listed in this section with $\gamma = 1 - \xi - \zeta - \eta$.

A.1.1 4-node Tetrahedron Element

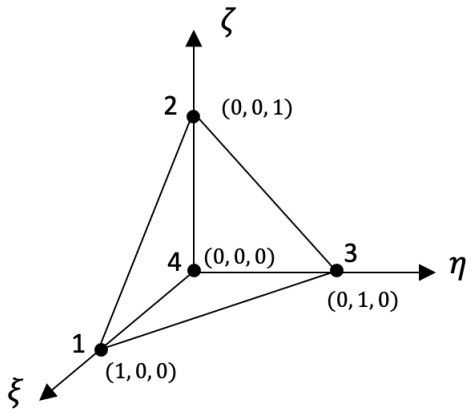


Fig. A.1 *Reference 4-node tetrahedron element.*

$$N_1 = \xi \qquad N_2 = \zeta \qquad N_3 = \eta \qquad N_4 = \gamma$$

A.1.2 10-node Tetrahedron Element

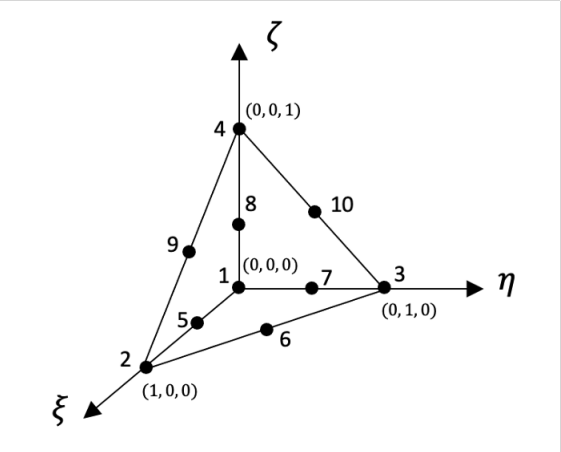


Fig. A.2 *Reference 10-node tetrahedron element.*

$$N_1 = \gamma(2\gamma-1) \qquad N_2 = \xi\,(2\xi-1) \qquad N_3 = \eta\,(2\eta-1) \qquad N_4 = \zeta\,(2\zeta-1)$$
$$N_5 = 4\,\xi\,\gamma \qquad N_6 = 4\,\xi\,\eta \qquad N_7 = 4\,\eta\,\gamma \qquad N_8 = 4\,\zeta\,\gamma$$
$$N_9 = 4\,\xi\,\zeta \qquad N_{10} = 4\,\eta\,\zeta$$

A.1.3 8-node Hexahedron Element

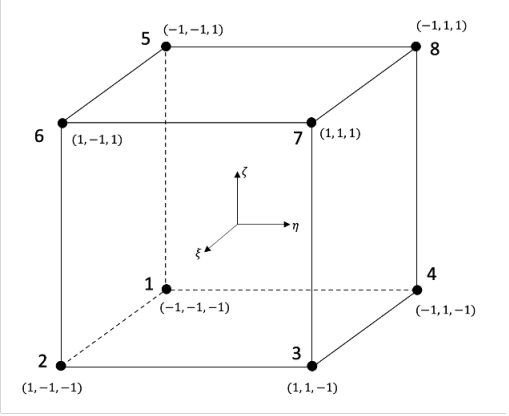


Fig. A.3 *Reference 8-node hexahedron element.*

$$N_1 = (1-\xi)(1-\eta)(1-\zeta)/8 \qquad N_2 = (1+\xi)(1-\eta)(1-\zeta)/8 \qquad N_3 = (1+\xi)(1+\eta)(1-\zeta)/8$$
$$N_4 = (1-\xi)(1+\eta)(1-\zeta)/8 \qquad N_5 = (1-\xi)(1-\eta)(1+\zeta)/8 \qquad N_6 = (1+\xi)(1-\eta)(1+\zeta)/8$$
$$N_7 = (1+\xi)(1+\eta)(1+\zeta)/8 \qquad N_8 = (1-\xi)(1+\eta)(1+\zeta)/8$$

A.1.4 20-node Hexahedron Element

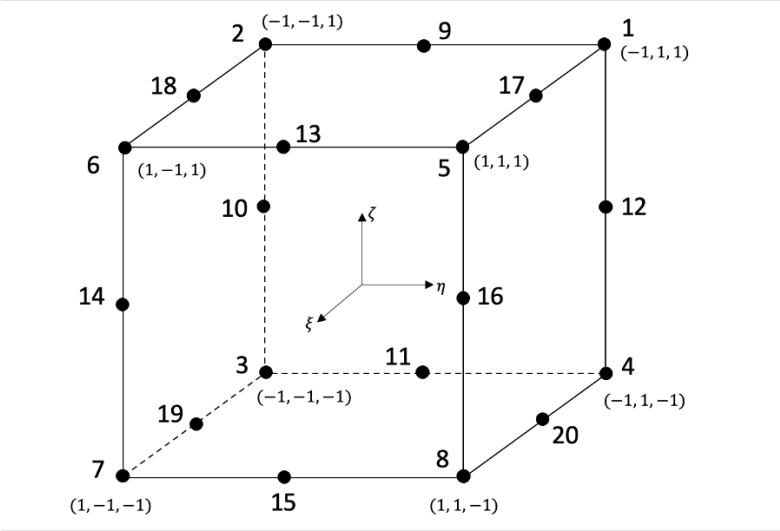


Fig. A.4 *Reference 8-node hexahedron element.*

$$N_1 = (1-\xi)(1+\eta)(1+\zeta)(-2-\xi+\eta+\zeta)/8$$
$$N_2 = (1-\xi)(1-\eta)(1+\zeta)(-2-\xi-\eta+\zeta)/8$$
$$N_3 = (1-\xi)(1-\eta)(1-\zeta)(-2-\xi-\eta-\zeta)/8$$
$$N_4 = (1-\xi)(1+\eta)(1-\zeta)(-2-\xi+\eta-\zeta)/8$$
$$N_5 = (1+\xi)(1+\eta)(1+\zeta)(-2+\xi+\eta+\zeta)/8$$
$$N_6 = (1+\xi)(1-\eta)(1+\zeta)(-2+\xi-\eta+\zeta)/8$$
$$N_7 = (1+\xi)(1-\eta)(1-\zeta)(-2+\xi-\eta-\zeta)/8$$
$$N_8 = (1+\xi)(1+\eta)(1-\zeta)(-2+\xi+\eta-\zeta)/8$$
$$N_9 = (1-\xi)(1-\eta^2)(1+\zeta)/4 \qquad N_{10} = (1-\xi)(1-\eta^2)(1+\zeta)/4$$
$$N_{11} = (1-\xi)(1-\eta^2)(1-\zeta)/4 \qquad N_{12} = (1-\xi)(1+\eta)(1-\zeta^2)/4$$
$$N_{13} = (1+\xi)(1-\eta^2)(1+\zeta)/4 \qquad N_{14} = (1+\xi)(1-\eta)(1-\zeta^2)/4$$
$$N_{15} = (1+\xi)(1-\eta^2)(1-\zeta)/4 \qquad N_{16} = (1+\xi)(1+\eta)(1-\zeta^2)/4$$
$$N_{17} = (1-\xi^2)(1+\eta)(1+\zeta)/4 \qquad N_{18} = (1-\xi^2)(1-\eta)(1+\zeta)/4$$
$$N_{19} = (1-\xi^2)(1-\eta)(1-\zeta)/4 \qquad N_{20} = (1-\xi^2)(1+\eta)(1-\zeta)/4$$

A.2 Local derivative of the shape functions for the 3D solid elements

The local derivative of the shape functions matrix has a size of $n \times 3$, with n being the total number of nodes in the solid element. $\frac{\partial \mathbf{\Psi}}{\partial \bar{\boldsymbol{\xi}}}$ can be expressed in the form of:

$$\frac{\partial \mathbf{\Psi}}{\partial \bar{\boldsymbol{\xi}}} = \begin{bmatrix} \frac{\partial N_1}{\partial \xi} & \frac{\partial N_2}{\partial \xi} & \frac{\partial N_3}{\partial \xi} & \cdots & \frac{\partial N_n}{\partial \xi} \\ \frac{\partial N_1}{\partial \eta} & \frac{\partial N_2}{\partial \eta} & \frac{\partial N_3}{\partial \eta} & \cdots & \frac{\partial N_n}{\partial \eta} \\ \frac{\partial N_1}{\partial \zeta} & \frac{\partial N_2}{\partial \zeta} & \frac{\partial N_3}{\partial \zeta} & \cdots & \frac{\partial N_n}{\partial \zeta} \end{bmatrix}^{\mathsf{T}} \tag{A.1}$$

A.2.1 4-node Tetrahedron Element

$$\frac{\partial \mathbf{\Psi}}{\partial \bar{\boldsymbol{\xi}}} = \begin{bmatrix} 1 & 0 & 0 & -1 \\ 0 & 0 & 1 & -1 \\ 0 & 1 & 0 & -1 \end{bmatrix}^{\mathsf{T}} \tag{A.2}$$

A.2.2 10-node Tetrahedron Element

With $\gamma = 1 - \xi - \zeta - \eta$:

$$\frac{\partial \mathbf{\Psi}}{\partial \bar{\boldsymbol{\xi}}} = \begin{bmatrix} 1-4\gamma & 1-4\gamma & 1-4\gamma \\ 4\xi-1 & 0 & 0 \\ 0 & 4\eta-1 & 0 \\ 0 & 0 & 4\zeta-1 \\ 4(\gamma-\xi) & -4\xi & -4\xi \\ 4\eta & 4\xi & 0 \\ -4\eta & 4(\gamma-\eta) & -4\eta \\ -4\zeta & -4\zeta & 4(\gamma-\zeta) \\ 4\zeta & 0 & 4\xi \\ 0 & 4\zeta & 4\eta \end{bmatrix} \tag{A.3}$$

A.2.3 8-node Hexahedron Element

$$\frac{\partial \boldsymbol{\Psi}}{\partial \bar{\boldsymbol{\xi}}} = \frac{1}{8}\begin{bmatrix} -(1-\eta)(1-\zeta) & -(1-\xi)(1-\zeta) & -(1-\xi)(1-\eta) \\ (1-\eta)(1-\zeta) & -(1+\xi)(1-\zeta) & -(1+\xi)(1-\eta) \\ (1+\eta)(1-\zeta) & (1+\xi)(1-\zeta) & -(1+\xi)(1+\eta) \\ -(1+\eta)(1-\zeta) & (1-\xi)(1-\zeta) & -(1-\xi)(1+\eta) \\ -(1-\eta)(1+\zeta) & -(1-\xi)(1+\zeta) & (1-\xi)(1-\eta) \\ (1-\eta)(1+\zeta) & -(1+\xi)(1+\zeta) & (1+\xi)(1-\eta) \\ (1+\eta)(1+\zeta) & (1+\xi)(1+\zeta) & (1+\xi)(1+\eta) \\ -(1+\eta)(1+\zeta) & (1-\xi)(1+\zeta) & (1-\xi)(1+\eta) \end{bmatrix} \tag{A.4}$$

A.2.4 20-node Hexahedron Element

$$\frac{\partial \boldsymbol{\Psi}}{\partial \bar{\boldsymbol{\xi}}} = \tag{A.5}$$

$$\frac{1}{4}\begin{bmatrix} \frac{(1+\eta)(1+\zeta)(1+2\xi-\eta-\zeta)}{2} & \frac{(1-\xi)(1+\zeta)(-1-\xi+2\eta+\zeta)}{2} & \frac{(1-\xi)(1+\eta)(-1-\xi+\eta+2\zeta)}{2} \\ \frac{(1-\eta)(1+\zeta)(1+2\xi+\eta-\zeta)}{2} & \frac{(1-\xi)(1+\zeta)(1+\xi+2\eta-\zeta)}{2} & \frac{(1-\xi)(1-\eta)(-1-\xi-\eta+2\zeta)}{2} \\ \frac{(1-\eta)(1-\zeta)(1+2\xi+\eta+\zeta)}{2} & \frac{(1-\xi)(1-\zeta)(1+\xi+2\eta+\zeta)}{2} & \frac{(1-\xi)(1-\eta)(1+\xi+\eta+2\zeta)}{2} \\ \frac{(1+\eta)(1-\zeta)(1+2\xi-\eta+\zeta)}{2} & \frac{(1-\xi)(1-\zeta)(-1-\xi+2\eta-\zeta)}{2} & \frac{(1-\xi)(1+\eta)(1+\xi-\eta+2\zeta)}{2} \\ \frac{(1+\eta)(1+\zeta)(2\xi+\eta+\zeta-1)}{2} & \frac{(1+\xi)(1+\zeta)(-1+\xi+2\eta+\zeta)}{2} & \frac{(1+\xi)(1+\eta)(-1+\xi+\eta+2\zeta)}{2} \\ \frac{(1-\eta)(1+\zeta)(2\xi-\eta+\zeta-1)}{2} & \frac{(1+\xi)(1+\zeta)(1-\xi+2\eta-\zeta)}{2} & \frac{(1+\xi)(1-\eta)(-1+\xi-\eta+2\zeta)}{2} \\ \frac{(1-\eta)(1-\zeta)(2\xi-\eta-\zeta-1)}{2} & \frac{(1+\xi)(1-\zeta)(1-xi+2\eta+\zeta)}{2} & \frac{(1+\xi)(1-\eta)(1-\xi+\eta+2\zeta)}{2} \\ \frac{(1+\eta)(1-\zeta)(2\xi+\eta-\zeta-1)}{2} & \frac{(1+\xi)(1-\zeta)(-1+\xi+2\eta-\zeta)}{2} & \frac{(1+\xi)(1+\eta)(1-\xi-\eta+2\zeta)}{2} \\ -(1-\eta^2)(1+\zeta) & -2\eta(1-\xi)(1+\zeta) & (1-\xi)(1-\eta^2) \\ -(1-\eta)(1-\zeta^2) & -(1-\xi)(1-\zeta^2) & -2\zeta(1-\xi)(1-\eta) \\ -(1-\eta^2)(1-\zeta) & -2\eta(1-\xi)(1-\zeta) & -(1-\xi)(1-\eta^2) \\ -(1+\eta)(1-\zeta^2) & (1-\xi)(1-\zeta^2) & -2\zeta(1-\xi)(1+\eta) \\ (1-\eta^2)(1+\zeta) & -2\eta(1+\xi)(1+\zeta) & (1+\xi)(1-\eta^2) \\ (1-\eta)(1-\zeta^2) & -(1+\xi)(1-\zeta^2) & -2\zeta(1+\xi)(1-\eta) \\ (1-\eta^2)(1-\zeta) & -2\eta(1+\xi)(1-\zeta) & -(1+\xi)(1-\eta^2) \\ (1+\eta)(1-\zeta^2) & (1+\xi)(1-\zeta^2) & -2\zeta(1+\xi)(1+\eta) \\ -2\xi(1+\eta)(1+\zeta) & (1-\xi^2)(1+\zeta) & (1-\xi^2)(1+\eta) \\ -2\xi(1-\eta)(1+\zeta) & -(1-\xi^2)(1+\zeta) & (1-\xi^2)(1-\eta) \\ -2\xi(1-\eta)(1-\zeta) & -(1-\xi^2)(1-\zeta) & -(1-\xi^2)(1-\eta) \\ -2\xi(1+\eta)(1-\zeta) & (1-\xi^2)(1-\zeta) & -(1-\xi^2)(1+\eta) \end{bmatrix} \tag{A.6}$$

Appendix B

Gaussian Quadrature for 3D Elements

B.1 3D tetrahedron element

Table B.1 *Gaussian quadrature points and the weights for 3D tetrahedron element.*

Order	**No. of Points**	**Integration Point**				**Weight**
		i	ξ_i	η_i	ζ_i	w_i
1	1	1	0.25	0.25	0.25	1/6
2	4	1	0.58541020	0.13819660	0.13819660	1/24
		2	0.13819660	0.58541020	0.13819660	1/24
		3	0.13819660	0.13819660	0.58541020	1/24
		4	0.13819660	0.13819660	0.13819660	1/24
3	5	1	0.25	0.25	0.25	-2/15
		2	0.5	1/6	1/6	3/40
		3	1/6	0.5	1/6	3/40
		4	1/6	1/6	0.5	3/40
		5	1/6	1/6	1/6	3/40
4	11	1	0.25	0.25	0.25	-0.0131555556
		2	0.7857428571	0.0714285714	0.0714285714	0.0076222222
		3	0.0714285714	0.7857428571	0.0714285714	0.0076222222
		4	0.0714285714	0.0714285714	0.7857428571	0.0076222222
		5	0.0714285714	0.0714285714	0.0714285714	0.0076222222
		6	0.3994035762	0.1005964238	0.3994035762	0.0248888889
		7	0.3994035762	0.1005964238	0.1005964238	0.0248888889

Order	No. of Points	Integration Point				Weight
		i	ξ_i	η_i	ζ_i	w_i
		8	0.3994035762	0.3994035762	0.1005964238	0.0248888889
		9	0.1005964238	0.1005964238	0.3994035762	0.0248888889
		10	0.1005964238	0.3994035762	0.3994035762	0.0248888889
		11	0.1005964238	0.3994035762	0.1005964238	0.0248888889

B.2 3D hexahedron element

No. of Points	Integration Point				Weight
	i	ξ_i	η_i	ζ_i	w_i
1	1	0	0	0	8
8	1 - 8	$\pm\frac{1}{\sqrt{3}}$	$\pm\frac{1}{\sqrt{3}}$	$\pm\frac{1}{\sqrt{3}}$	1
27	1 - 8	$\pm\frac{1}{\sqrt{3}}$	$\pm\frac{1}{\sqrt{3}}$	$\pm\frac{1}{\sqrt{3}}$	$(\frac{5}{9})^3$
	9 - 12	$\pm\frac{1}{\sqrt{3}}$	$\pm\frac{1}{\sqrt{3}}$	0	$(\frac{5}{9})^2 \cdot (\frac{8}{9})$
	13 - 16	$\pm\frac{1}{\sqrt{3}}$	0	$\pm\frac{1}{\sqrt{3}}$	$(\frac{5}{9})^2 \cdot (\frac{8}{9})$
	17 - 20	0	$\pm\frac{1}{\sqrt{3}}$	$\pm\frac{1}{\sqrt{3}}$	$(\frac{5}{9})^2 \cdot (\frac{8}{9})$
	21 - 22	0	0	$\pm\frac{1}{\sqrt{3}}$	$(\frac{5}{9}) \cdot (\frac{8}{9})^2$
	23 - 24	0	$\pm\frac{1}{\sqrt{3}}$	0	$(\frac{5}{9}) \cdot (\frac{8}{9})^2$
	25 - 26	$\pm\frac{1}{\sqrt{3}}$	0	0	$(\frac{5}{9}) \cdot (\frac{8}{9})^2$
	27	0	0	0	$(\frac{8}{9})^3$

Table B.2 *Gaussian quadrature points and the weights for 3D hexahedron element.*

Appendix C

Newton Direction Computation for Harmonic Balance Method

1: Pre-assembly $\mathbf{M}$, $\mathbf{C}$, $\mathbf{K}_0$ matrices and vector $\tilde{\boldsymbol{b}}_{ext}$.

2: Set tolerance ε_r

3: Initial Guess $(\omega_0, \tilde{\boldsymbol{q}}_0)$

4: Set $\omega = \omega_0$ and $\tilde{\boldsymbol{q}} = \tilde{\boldsymbol{q}}_0$

5: **REPEAT**

6: **for** $n = 0, \ldots, (N_t - 1)$ **do**

7: IDFT: $\boldsymbol{u}(t_n) = \frac{1}{2}\tilde{\boldsymbol{q}}^{0,c} + \sum_{n=1}^{N_H} \tilde{\boldsymbol{q}}^{n,c} \cdot \cos\left(\frac{2\pi}{N_t} \cdot kn\right) + \tilde{\boldsymbol{q}}^{n,s} \cdot \sin\left(\frac{2\pi}{N_t} \cdot kn\right)$

8: $\boldsymbol{u}(t_n) \rightarrow \mathbf{K}_{nl}(\boldsymbol{u})$ and $\frac{\partial \boldsymbol{F}_{nl}}{\partial \boldsymbol{u}}(t_n)$

9: $\mathbf{K}_{nl}(\boldsymbol{u}) \rightarrow \boldsymbol{F}_{nl}(t_n) \rightarrow \underline{\boldsymbol{F}}_{nl}(t)$

10: **end for**

11: $\underline{\boldsymbol{F}}_{nl}(t) \xrightarrow{\text{DFT: } [\mathscr{F}]} \tilde{\boldsymbol{b}}_{nl}$

for $k = 1, \ldots, (N_H)$ **do**

$\tilde{\boldsymbol{b}}_{nl}^{k,c} = \frac{2}{N_t} \times \sum_{n=0}^{N_t-1} \boldsymbol{F}_{nl}(t_n) \cdot \cos\left(\frac{2\pi}{N_t} \cdot k \cdot n\right)$

$\tilde{\boldsymbol{b}}_{nl}^{k,s} = \frac{2}{N_t} \times \sum_{n=0}^{N_t-1} \boldsymbol{F}_{nl}(t_n) \cdot \sin\left(\frac{2\pi}{N_t} \cdot k \cdot n\right)$

end for

12: Compute $\mathbf{Z}(\omega)$

13: $\boldsymbol{R}(\omega,\tilde{\boldsymbol{q}}) \equiv \mathbf{Z}(\omega)\tilde{\boldsymbol{q}} + \tilde{\boldsymbol{b}}_{nl}(\tilde{\boldsymbol{q}}) - \tilde{\boldsymbol{b}}_{ext} = 0$

14: Arc Length Constraint $\rightarrow r(\omega,\tilde{\boldsymbol{q}}) \equiv (\tilde{\boldsymbol{q}} - \tilde{\boldsymbol{q}}_0)\cdot(\tilde{\boldsymbol{q}} - \tilde{\boldsymbol{q}}_0) + (\omega_1 - \omega_0)^2 - \Delta s^2 = 0$

15: Equation of motion in frequency domain $\mathbf{F}(\omega,\tilde{\boldsymbol{q}}) = \begin{bmatrix}\boldsymbol{R} & r\end{bmatrix}^{\mathsf{T}} = 0$

16: Jacobian Matrix: $\left(\frac{\partial \boldsymbol{F}_{nl}}{\partial \boldsymbol{u}}(t_n),\ \frac{\partial r}{\partial \tilde{\boldsymbol{q}}},\ \frac{\partial \boldsymbol{R}}{\partial \omega},\ \frac{\partial r}{\partial \omega}\right) \xrightarrow{DFT} \mathbf{F}'$

17: Newton Direction Computation:

$$\mathbf{F}'(\omega,\tilde{\boldsymbol{q}})\cdot\Delta = -\mathbf{F}(\omega,\tilde{\boldsymbol{q}})$$

$$(\omega_1,\tilde{\boldsymbol{q}}_1) = \Delta + (\omega,\tilde{\boldsymbol{q}})$$

18: Update: $\omega = \omega_1$ and $\tilde{\boldsymbol{q}} = \tilde{\boldsymbol{q}}_1$

19: Evaluate Residual: $res = max|\mathbf{F}(\omega,\tilde{\boldsymbol{q}})|$

20: **UNTIL** $res \leq \varepsilon_r$

21: Return value $(\omega,\tilde{\boldsymbol{q}})$

22: Predict next point $(\omega_1,\tilde{\boldsymbol{q}}_1)$ with Secant Method: $(\omega_1,\ \tilde{\boldsymbol{q}}_1) = (\omega,\tilde{\boldsymbol{q}}) + \Delta s\,((\omega,\tilde{\boldsymbol{q}}) - (\omega_0,\tilde{\boldsymbol{q}}_0))$

N_H is the total number of harmonics considered in HBM and N_t is the total number of samples taken per period for DFT and IDFT.

Step 6 to 11 correspond to procedure AFT in the flowchart shown in Figure 3.11. Step 12 to 13 correspond to assembly of $\mathbf{F}(\omega,\tilde{\boldsymbol{q}})$, computation of Jacobian matrix $\mathbf{F}'$ and Newton direction computation are shown in step 14 and 16 respectively.

Appendix D

Jacobian Matrix for the Reduced Equation of Motion in SMD

The full expression for the Jacobian matrix $\frac{\partial \hat{\boldsymbol{F}}_{nl}}{\partial \boldsymbol{q}}$ in each element is:

$$\begin{aligned}\frac{\partial \hat{\boldsymbol{F}}^e_{nl}}{\partial \boldsymbol{q}} =& J^e_0(\boldsymbol{x}_s) + \sum_{i=1}^{r} J^e_1(\boldsymbol{\phi}_i)\cdot\boldsymbol{q} + \sum_{i=1}^{r} C^e_1(\boldsymbol{\phi}_i)\cdot\dot{\boldsymbol{q}} + \sum_{i=1}^{r} M^e_1(\boldsymbol{\phi}_i)\cdot\ddot{\boldsymbol{q}} + \sum_{i=1}^{r}\sum_{j=1}^{r} J^e_2(\boldsymbol{\phi}_i,\boldsymbol{\phi}_j)\cdot\boldsymbol{q}\cdot\boldsymbol{q} \\ &+ \sum_{i=1}^{r}\sum_{j=1}^{r} C^e_2(\boldsymbol{\phi}_i,\boldsymbol{\phi}_j)\cdot\boldsymbol{q}\cdot\dot{\boldsymbol{q}} + \sum_{i=1}^{r}\sum_{j=1}^{r} M^e_2(\boldsymbol{\phi}_i,\boldsymbol{\phi}_j)\cdot\boldsymbol{q}\cdot\ddot{\boldsymbol{q}} \\ &+ \sum_{i=1}^{r}\sum_{j=1}^{r} M^e_3(\boldsymbol{\phi}_i,\boldsymbol{\phi}_j)\cdot\dot{\boldsymbol{q}}\cdot\dot{\boldsymbol{q}} \end{aligned} \tag{D.1}$$

where the coefficient tensors are:

$$C^e_1 = \boldsymbol{\Theta}^\intercal[\mathbf{C}]\boldsymbol{\phi}_i + \boldsymbol{\Phi}^\intercal[\mathbf{C}][\boldsymbol{\Theta}(:,:,i)] \tag{D.2}$$

$$M^e_1 = \boldsymbol{\Theta}^\intercal[\mathbf{M}]\boldsymbol{\phi}_i + \boldsymbol{\Phi}^\intercal[\mathbf{M}][\boldsymbol{\Theta}(:,:,i)] \tag{D.3}$$

$$C^e_2 = \boldsymbol{\Theta}^\intercal[\mathbf{C}]\{\boldsymbol{\Theta}(:,i,j)\} + [\boldsymbol{\Theta}(:,:,i)]^\intercal[\mathbf{C}][\boldsymbol{\Theta}(:,:,j)] \tag{D.4}$$

$$M^e_2 = \boldsymbol{\Theta}^\intercal[\mathbf{M}]\{\boldsymbol{\Theta}(:,i,j)\} + [\boldsymbol{\Theta}(:,:,i)]^\intercal[\mathbf{M}][\boldsymbol{\Theta}(:,:,j)] \tag{D.5}$$

$$M^e_3 = \boldsymbol{\Theta}^\intercal[\mathbf{M}]\{\boldsymbol{\Theta}(:,i,j)\} \tag{D.6}$$

$$J_0^e = \frac{1}{2}\boldsymbol{\Phi}^\mathsf{T}\int [\mathbf{B}_0 + \mathbf{B}_1(\boldsymbol{x}_s)]^\mathsf{T}[\mathbf{D}]\,[\mathbf{B}_1(\boldsymbol{x}_s)]\,\mathrm{d}V\,\boldsymbol{\Phi} + \boldsymbol{\Phi}^\mathsf{T}\int [\mathbf{G}]^\mathsf{T}[\Sigma(\mathbf{S}_0)]\,[\mathbf{G}]\mathrm{d}V\,\boldsymbol{\Phi}$$
$$+ \boldsymbol{\Phi}^\mathsf{T}[\mathbf{K}(\Omega)]\boldsymbol{\Phi} + \boldsymbol{\Phi}^\mathsf{T}[\mathbf{K}_{nl}(\boldsymbol{x}_s)]\boldsymbol{\Phi} \tag{D.7}$$

$$J_1^e = \frac{1}{2}[\boldsymbol{\Theta}(:,:,i)]^\mathsf{T}\int [\mathbf{B}_0 + \mathbf{B}_1(\boldsymbol{x}_s)]^\mathsf{T}[\mathbf{D}]\,[\mathbf{B}_1(\boldsymbol{x}_s)]\,\mathrm{d}V\,\boldsymbol{\Phi} + [\boldsymbol{\Theta}(:,:,i)]^\mathsf{T}\int [\mathbf{G}]^\mathsf{T}[\Sigma(\mathbf{S}_0)]\,[\mathbf{G}]\mathrm{d}V\,\boldsymbol{\Phi}$$
$$+ \boldsymbol{\Theta}^\mathsf{T}\int [\mathbf{B}_1(\boldsymbol{\phi}_i)]^\mathsf{T}[\mathbf{D}]\left[\mathbf{B}_0 + \frac{1}{2}[\mathbf{B}_1(\boldsymbol{x}_s)]\right]\mathrm{d}V\,\{\boldsymbol{x}_s\} + \frac{1}{2}\boldsymbol{\Theta}^\mathsf{T}\int [\mathbf{B}_0 + \mathbf{B}_1(\boldsymbol{x}_s)]^\mathsf{T}[\mathbf{D}]\,[\mathbf{B}_1(\boldsymbol{\phi}_i)]\mathrm{d}V\,\{\boldsymbol{x}_s\}$$
$$+ [\boldsymbol{\Theta}(:,:,i)]^\mathsf{T}[\mathbf{K}_{nl}(\boldsymbol{x}_s)]\boldsymbol{\Phi} + \boldsymbol{\Theta}^\mathsf{T}[\mathbf{K}_{nl}(\boldsymbol{x}_s)]\boldsymbol{\phi}_i$$
$$+ \boldsymbol{\Phi}^\mathsf{T}\int [\mathbf{B}_1(\boldsymbol{\phi}_i)]^\mathsf{T}[\mathbf{D}]\left[\mathbf{B}_0 + \frac{1}{2}[\mathbf{B}_1(\boldsymbol{x}_s)]\right]\mathrm{d}V\,\boldsymbol{\Phi} + \frac{1}{2}\boldsymbol{\Phi}^\mathsf{T}\int [\mathbf{B}_0 + \mathbf{B}_1(\boldsymbol{x}_s)]^\mathsf{T}[\mathbf{D}]\,[\mathbf{B}_1(\boldsymbol{\phi}_i)]\mathrm{d}V\,\boldsymbol{\Phi}$$
$$+ \boldsymbol{\Phi}^\mathsf{T}\int [\mathbf{G}]^\mathsf{T}[\Sigma(\mathbf{S}_1)]\,[\mathbf{G}]\mathrm{d}V\,\boldsymbol{\Phi} + \frac{1}{2}\boldsymbol{\Phi}^\mathsf{T}\int [\mathbf{B}_0 + \mathbf{B}_1(\boldsymbol{x}_s)]\,[\mathbf{D}]\,[\mathbf{B}_1(\boldsymbol{\phi}_i)]\mathrm{d}V\,\boldsymbol{\Phi}$$
$$+ \boldsymbol{\Phi}^\mathsf{T}[\mathbf{K}_{nl}(\boldsymbol{x}_s)]\,[\boldsymbol{\Theta}(:,:,i)] + \boldsymbol{\Theta}^\mathsf{T}[\mathbf{K}(\Omega)]\,\boldsymbol{\phi}_i + [\boldsymbol{\Theta}(:,:,i)]^\mathsf{T}[\mathbf{K}(\Omega)]\boldsymbol{\Phi}$$
$$+ \boldsymbol{\Phi}^\mathsf{T}[\mathbf{K}(\Omega)]\,[\boldsymbol{\Theta}(:,:,i)] + \frac{1}{2}\boldsymbol{\Phi}^\mathsf{T}\int [\mathbf{B}_0 + \mathbf{B}_1(\boldsymbol{x}_s)]^\mathsf{T}[\mathbf{D}]\,[\mathbf{B}_1(\boldsymbol{x}_s)]\,\mathrm{d}V\,[\boldsymbol{\Theta}(:,:,i)]$$
$$+ \boldsymbol{\Phi}^\mathsf{T}\int [\mathbf{G}]^\mathsf{T}[\Sigma(\mathbf{S}_0)]\,[\mathbf{G}]\mathrm{d}V\,[\boldsymbol{\Theta}(:,:,i)] + \frac{1}{2}\boldsymbol{\Phi}^\mathsf{T}\int [\mathbf{B}_1(\boldsymbol{\phi}_i)]^\mathsf{T}[\mathbf{D}]\,[\mathbf{B}_1(\boldsymbol{x}_s)]\,\mathrm{d}V\,\boldsymbol{\Phi} \tag{D.8}$$

$$
\begin{aligned}
J_2^e = & \frac{1}{2}\boldsymbol{\Theta}^{\mathsf{T}} \int [\mathbf{B}_0 + \mathbf{B}_1(\boldsymbol{x}_s)]^{\mathsf{T}} [\mathbf{D}] \, [\mathbf{B}_1(\boldsymbol{\phi}_i)] \mathrm{d}V \, \boldsymbol{\phi}_j + \boldsymbol{\Theta}^{\mathsf{T}} \int [\mathbf{B}_1(\boldsymbol{\phi}_i)]^{\mathsf{T}} [\mathbf{D}] \left[\mathbf{B}_0 + \frac{1}{2}\mathbf{B}_1(\boldsymbol{x}_s) \right] \mathrm{d}V \, \boldsymbol{\phi}_j \\
& + \frac{1}{2} [\boldsymbol{\Theta}(:,:,i)]^{\mathsf{T}} \int [\mathbf{B}_0 + \mathbf{B}_1(\boldsymbol{x}_s)]^{\mathsf{T}} [\mathbf{D}] \, [\mathbf{B}_1(\boldsymbol{\phi}_j)] \mathrm{d}V \, \boldsymbol{\Phi} \\
& + [\boldsymbol{\Theta}(:,:,i)]^{\mathsf{T}} \int [\mathbf{B}_1(\boldsymbol{\phi}_j)]^{\mathsf{T}} [\mathbf{D}] \left[\mathbf{B}_0 + \frac{1}{2}\mathbf{B}_1(\boldsymbol{x}_s) \right] \mathrm{d}V \, \boldsymbol{\Phi} \\
& + \frac{1}{2} [\boldsymbol{\Theta}(:,:,i)]^{\mathsf{T}} \int [\mathbf{B}_0 + \mathbf{B}_1(\boldsymbol{x}_s)]^{\mathsf{T}} [\mathbf{D}] \, [\mathbf{B}_1(\boldsymbol{\phi}_j)] \mathrm{d}V \, \boldsymbol{\Phi} + [\boldsymbol{\Theta}(:,:,i)]^{\mathsf{T}} \int [\mathbf{G}]^{\mathsf{T}} [\Sigma(\mathbf{S}_1)] \, [\mathbf{G}] \mathrm{d}V \, \boldsymbol{\Phi} \\
& + \frac{1}{2} \boldsymbol{\Phi}^{\mathsf{T}} \int [\mathbf{B}_0 + \mathbf{B}_1(\boldsymbol{x}_s)]^{\mathsf{T}} [\mathbf{D}] \, [\mathbf{B}_1(\boldsymbol{\phi}_i)] \mathrm{d}V \, [\boldsymbol{\Theta}(:,:,j)] \\
& + \boldsymbol{\Phi}^{\mathsf{T}} \int [\mathbf{B}_1(\boldsymbol{\phi}_i)]^{\mathsf{T}} [\mathbf{D}] \left[\mathbf{B}_0 + \frac{1}{2}\mathbf{B}_1(\boldsymbol{x}_s) \right] \mathrm{d}V \, [\boldsymbol{\Theta}(:,:,j)] \\
& + \frac{1}{2} \boldsymbol{\Phi}^{\mathsf{T}} \int [\mathbf{B}_0 + \mathbf{B}_1(\boldsymbol{x}_s)]^{\mathsf{T}} [\mathbf{D}] \left[\mathbf{B}_1 \left(\frac{1}{2}\boldsymbol{\Theta}(:,i,j) \right) \right] \mathrm{d}V \, \boldsymbol{\Phi} + \boldsymbol{\Phi}^{\mathsf{T}} \int [\mathbf{G}]^{\mathsf{T}} [\Sigma(\mathbf{S}_2)] \, [\mathbf{G}] \mathrm{d}V \, \boldsymbol{\Phi} \\
& + \boldsymbol{\Theta}^{\mathsf{T}} [\mathbf{K}_{nl}(\boldsymbol{x}_s)] \{ \frac{1}{2}\boldsymbol{\Theta}(:,i,j) \} + [\boldsymbol{\Theta}(:,:,i)]^{\mathsf{T}} [\mathbf{K}_{nl}(\boldsymbol{x}_s)] \, [\boldsymbol{\Theta}(:,:,j)] \\
& + \frac{1}{2} \boldsymbol{\Theta}^{\mathsf{T}} \int [\mathbf{B}_0 + \mathbf{B}_1(\boldsymbol{x}_s)]^{\mathsf{T}} [\mathbf{D}] \left[\mathbf{B}_1 \left(\frac{1}{2}\boldsymbol{\Theta}(:,i,j) \right) \right] \mathrm{d}V \, \{\boldsymbol{x}_s\} \\
& + \boldsymbol{\Theta}^{\mathsf{T}} \int \left[\mathbf{B}_1 \left(\frac{1}{2}\boldsymbol{\Theta}(:,i,j) \right) \right]^{\mathsf{T}} [\mathbf{D}] \left[\mathbf{B}_0 + \frac{1}{2}\mathbf{B}_1(\boldsymbol{x}_s) \right] \mathrm{d}V \, \{\boldsymbol{x}_s\} \\
& + \frac{1}{2} \boldsymbol{\Theta}^{\mathsf{T}} \int [\mathbf{B}_1(\boldsymbol{\phi}_i)]^{\mathsf{T}} [\mathbf{D}] \, [\mathbf{B}_1(\boldsymbol{\phi}_j)] \mathrm{d}V \, \{\boldsymbol{x}_s\} \\
& + \frac{1}{2} [\boldsymbol{\Theta}(:,:,i)]^{\mathsf{T}} \int [\mathbf{B}_0 + \mathbf{B}_1(\boldsymbol{x}_s)]^{\mathsf{T}} [\mathbf{D}] \, [\mathbf{B}_1(\boldsymbol{x}_s)] \, \mathrm{d}V \, [\boldsymbol{\Theta}(:,:,j)] \\
& + [\boldsymbol{\Theta}(:,:,i)]^{\mathsf{T}} \int [\mathbf{G}]^{\mathsf{T}} [\Sigma(\mathbf{S}_0)] \, [\mathbf{G}] \mathrm{d}V \, [\boldsymbol{\Theta}(:,:,j)] \\
& + \frac{1}{2} [\boldsymbol{\Theta}(:,:,i)]^{\mathsf{T}} \int [\mathbf{B}_1(\boldsymbol{\phi}_j)]^{\mathsf{T}} [\mathbf{D}] \, [\mathbf{B}_1(\boldsymbol{x}_s)] \mathrm{d}V \, \boldsymbol{\Phi} \\
& + \frac{1}{2} \boldsymbol{\Phi}^{\mathsf{T}} \int [\mathbf{B}_0 + \mathbf{B}_1(\boldsymbol{x}_s)]^{\mathsf{T}} [\mathbf{D}] \, [\mathbf{B}_1(\boldsymbol{\phi}_i)] \mathrm{d}V \, [\boldsymbol{\Theta}(:,:,j)] + \boldsymbol{\Phi}^{\mathsf{T}} \int [\mathbf{G}]^{\mathsf{T}} [\Sigma(\mathbf{S}_1)] \, [\mathbf{G}] \mathrm{d}V \, [\boldsymbol{\Theta}(:,:,j)] \\
& + \frac{1}{2} \boldsymbol{\Phi}^{\mathsf{T}} \int [\mathbf{B}_0 + \mathbf{B}_1(\boldsymbol{x}_s)]^{\mathsf{T}} [\mathbf{D}] \left[\mathbf{B}_1 \left(\frac{1}{2}\boldsymbol{\Theta}(:,i,j) \right) \right] \mathrm{d}V \, \boldsymbol{\Phi} \\
& + \boldsymbol{\Phi}^{\mathsf{T}} \int \left[\mathbf{B}_1 \left(\frac{1}{2}\boldsymbol{\Theta}(:,i,j) \right) \right]^{\mathsf{T}} [\mathbf{D}] \left[\mathbf{B}_0 + \frac{1}{2}\mathbf{B}_1(\boldsymbol{x}_s) \right] \mathrm{d}V \, \boldsymbol{\Phi} \\
& + \boldsymbol{\Phi}^{\mathsf{T}} \int [\mathbf{B}_1(\boldsymbol{\phi}_i)]^{\mathsf{T}} [\mathbf{D}] \, [\mathbf{B}_1(\boldsymbol{\phi}_j)] \mathrm{d}V \, \boldsymbol{\Phi} + \boldsymbol{\Phi}^{\mathsf{T}} \int [\mathbf{G}]^{\mathsf{T}} [\Sigma(\mathbf{S}_2)] \, [\mathbf{G}] \mathrm{d}V \, \boldsymbol{\Phi} \\
& + \frac{1}{2} \boldsymbol{\Phi}^{\mathsf{T}} \int [\mathbf{B}_1(\boldsymbol{\phi}_i)]^{\mathsf{T}} [\mathbf{D}] \, [\mathbf{B}_1(\boldsymbol{x}_s)] \mathrm{d}V \, [\boldsymbol{\Theta}(:,:,j)] + \boldsymbol{\Phi}^{\mathsf{T}} \int \left[\mathbf{B}_1 \left(\frac{1}{2}\boldsymbol{\Theta}(:,i,j) \right) \right]^{\mathsf{T}} [\mathbf{D}] \, [\mathbf{B}_1(\boldsymbol{x}_s)] \mathrm{d}V \, \boldsymbol{\Phi} \\
& + \frac{1}{2} \boldsymbol{\Theta}^{\mathsf{T}} [\mathbf{K}(\boldsymbol{\Omega})] \{ \boldsymbol{\Theta}(:,i,j) \} + [\boldsymbol{\Theta}(:,:,i)]^{\mathsf{T}} [\mathbf{K}(\boldsymbol{\Omega})] [\boldsymbol{\Theta}(:,:,j)] \qquad \text{(D.9)}
\end{aligned}
$$

$\mathbf{S}_0$, $\mathbf{S}_1$, and $\mathbf{S}_2$ correspond to the terms in the second Piola-Kirchoff stress vector $\mathbf{S}(\boldsymbol{q})$:

$$\mathbf{S} = \boldsymbol{S}_0 + \sum_{i=1}^{r} \boldsymbol{S}_1(\boldsymbol{\phi}_i) \cdot q_i + \sum_{i=1}^{r} \sum_{j=1}^{r} \boldsymbol{S}_2(\boldsymbol{\phi}_i, \boldsymbol{\phi}_j) \cdot q_i \cdot q_j \tag{D.10}$$

$$with: \quad \mathbf{S}_0 = [\mathbf{D}]\,[\mathbf{B}_0]\,\{\boldsymbol{x}_s\} + \frac{1}{2}[\mathbf{D}]\,[\mathbf{B}_1(\boldsymbol{x}_s)]\,\{\boldsymbol{x}_s\} \tag{D.11}$$

$$\mathbf{S}_1 = [\mathbf{D}]\,[\mathbf{B}_0]\,\{\boldsymbol{\phi}_i\} + \frac{1}{2}[\mathbf{D}]\,[\mathbf{B}_1(\boldsymbol{\phi}_i)]\,\{\boldsymbol{x}_s\} + \frac{1}{2}[\mathbf{D}]\,[\mathbf{B}_1(\boldsymbol{x}_s)]\,\{\boldsymbol{\phi}_i\} \tag{D.12}$$

$$\mathbf{S}_2 = \frac{1}{2}[\mathbf{D}]\,[\mathbf{B}_0]\,\{\boldsymbol{\Theta}(:,i,j)\} + \frac{1}{2}[\mathbf{D}]\,[\mathbf{B}_1(\boldsymbol{\phi}_i)]\,\{\boldsymbol{\phi}_j\} + \frac{1}{2}[\mathbf{D}]\left[\mathbf{B}_1\left(\frac{1}{2}\boldsymbol{\Theta}(:,i,j)\right)\right]\{\boldsymbol{x}_s\} \tag{D.13}$$